The Dissertation Committee for Chirag A. Gokani
certifies that this is the approved version of the following dissertation:

Scattering and Diffraction of Acoustic Waves in Three Problems with Broken Symmetry

Committee:

Michael R. Haberman, Co-supervisor

Mark F. Hamilton, Co-supervisor

Preston S. Wilson

Andrea Alù

Scattering and Diffraction of Acoustic Waves in Three Problems with Broken Symmetry

by

Chirag A. Gokani

Dissertation

Presented to the Faculty of the Graduate School of

The University of Texas at Austin

in Partial Fulfillment

of the Requirements

for the Degree of

Doctor of Philosophy

The University of Texas at Austin

May 2026

Dedication

For my beloved Mother

to whose truthfulness, purity, and love I aspire.

May I always tell the truth.

May I not find fault with others and rather see my own faults.

May I have a pure heart and see the world as my family.

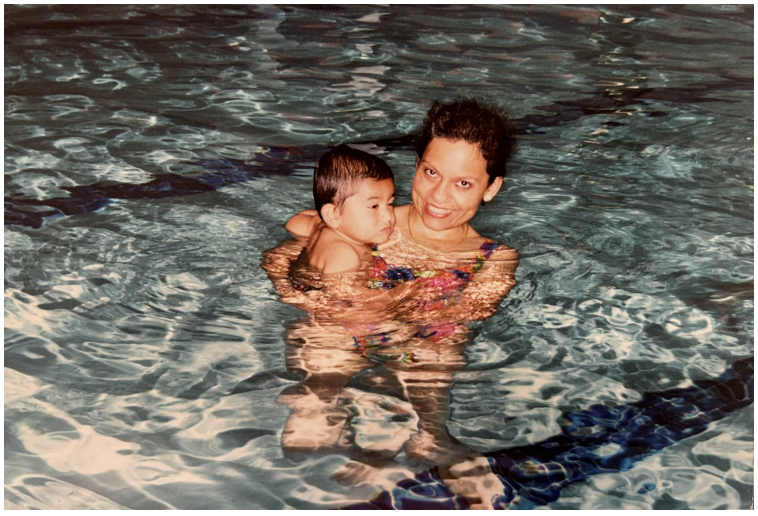

Scattering, interference, refraction, and caustics (April 2000)

Epigraph

All things must pass…
All things must pass away…

—George Harrison[1]

[1] G. Harrison. *All Things Must Pass.* Apple Records, London. 1970, Side 3, Track 5.

Acknowledgments

I have enjoyed studying the beautiful motion of waves. I am very grateful to:

- The Applied Research Laboratories for the Chester M. McKinney Graduate Fellowship in Acoustics
- The Cockrell School of Engineering for the T. W. Whaley, Jr. Friends of Alec Endowed Scholarship
- M. R. Haberman for co-advising me, guiding Chaps. 2 and 3, helping initiate the study that led to Chap. 4, and conducting the literature review in Sec. 4.1
- M. F. Hamilton for co-advising me, developing Chap. 4, and introducing me to topics discussed in Apps. B, C, and E.
- P. S. Wilson and A. Alù for providing feedback as members of my committee
- S. P. Wallen, B. M. Goldsberry, J. M. Cormack, J. Li, K. S. Spratt, S. P. Blackstock, O. A. Sapozhnikov, J. M. Izen, L. A. Ostrovsky, and P. L. Marston for their insights
- R. P. Williams for help with Sec. 4.2 and thoughts on diffraction
- T. S. Jerome for code used in Sec. 2.4 and thoughts on radiation force
- A. J. Lawrence for advice on Chaps. 2 and 3 and help creating Figs. D.1–D.3
- J. S. Hallveld for obtaining Eq. (4.22) from Eq. (4.13) and suggesting that Eqs. (4.24) and (E.20) are equivalent
- My respected academic brothers and sisters, who always remind me of my ideals.

Chirag

Abstract

Scattering and Diffraction of Acoustic Waves in Three Problems with Broken Symmetry

Chirag A. Gokani, Ph.D.
The University of Texas at Austin, 2026

SUPERVISORS: Michael R. Haberman, Mark F. Hamilton

The effects of asymmetry in acoustic scattering and diffraction phenomena are investigated across the frequency spectrum, simplifying the modeling of waves used for particle manipulation, sensing, and communications. Considered first is the steady force exerted by traveling waves on scatterers that are smaller than a wavelength. Asymmetric material distributions are found to experience forces that are two orders of magnitude weaker than forces exerted on symmetric distributions. Considered next is the aggregate effect of subwavelength asymmetric piezoelectric scatterers suspended periodically in a fluid. The asymmetry couples the effective acoustic and electrodynamic constitutive relations, which are shown to conserve energy and obey reciprocity. Attention is finally turned to acoustic fields with helicoidal wavefronts that break axisymmetry. Analytical expressions of such waves are obtained for all frequencies, yielding scaling laws and geometric descriptions of the fields. In the absence of asymmetry, the findings of this dissertation simplify to previous results for scattering and diffraction from symmetric objects.

Table of Contents

Chapter 1: Introduction

1.1 Asymmetry, inhomogeneity, and anisotropy

Symmetry is "the existence of different viewpoints from which [a] system appears the same" [1, p. 394]. Many classical results of wave physics involve an assumption of symmetry. In the study of scattering, Lord Rayleigh explained why the sky is blue by treating atmospheric molecules as homogeneous spheres [2]. Gor'kov used the analogous solution in acoustics to calculate radiation forces exerted by progressive and standing waves on spheres [3, Eqs. (10) and (13)]. In the study of diffraction, Fresnel derived an approximation for the axial field transmitted through a circular aperture [4]. Axisymmetric solutions in the Fresnel approximation continue to be employed heavily both in optics [5, Eq. (8.40a)] and acoustics [6, Eqs. (8.19) and (8.37)].

Objects bearing an axis of symmetry are often discussed "to avoid excessive entanglement in the techniques of mathematical analysis" [7, p. 2]. For example, Griffiths limits the discussion of solving the Laplace equation to spheres with azimuthal symmetry in his introductory electrodynamics text [8, p. 137], and Blackstock derives solutions of the spherical wave equation by gradually introducing dependencies on polar and azimuthal coordinates in his introductory acoustics text [9, pp. 336–337].

Symmetric objects are also used to represent more general objects when considering randomly oriented sources or scatterers. For example, Rayleigh acknowledged that if atmospheric molecules were asymmetric, the random orientation of the molecules would negate the effects of asymmetry at the macroscopic scale [2, pp. 382–383]:

> In the electromagnetic theory we have treated the molecules as spherical continuous bodies differing from the rest of the medium merely in the value of their dielectric constant. If we abandon the restriction as to sphericity, the results will be modified in a manner that cannot be precisely defined until the shape is specified. On the whole, however, it does not appear probable that this consideration would greatly affect the calculation as to transparency,

> since the particles must be supposed to be oriented in all directions indifferently.

Rayleigh's comment suggests that the effects of asymmetry become relevant when a certain degree of randomness is suppressed. Modern studies show that the effects of asymmetry become observable when scatterers and sources are considered in isolation [10, 11] or in periodic arrays [12–14].

Pierre Curie was among the first to emphasize the importance of asymmetry across physical domains [15], noting that [16, pp. 25, 34]

> ...it would be useful to introduce symmetry considerations known to crystallographers into the study of physical phenomena. For example, an isotropic body can be set in a rectilinear or a rotary motion; a fluid can be a medium of vortex motions; a solid can be compressed or twisted; it may be in an electric or magnetic field; electric current or heat may flow through it; natural light or light that is rectilinearly, circularly, elliptically, etc. polarized can pass through it. In all these cases, the occurrence of some characteristic dissymmetry is necessary, in every point of the body. ...When certain effects exhibit a certain dissymmetry, this dissymmetry must manifest itself in the causes that generated these effects.

The causes of asymmetry can be understood in terms of *inhomogeneity*—the variation of a system at different positions—and *anisotropy*—the variation in different directions. The present work explores how inhomogeneity and anisotropy affect acoustic scattering and diffraction phenomena, the motivation for which is described in Sec. 1.3. Section 1.2 first contextualizes scattering and diffraction phenomena across the frequency spectrum by introducing the parameter ka.

1.2 The parameter ka

The acoustic frequency spectrum shown in Fig. 1.1 is quantified by the dimensionless parameter ka, where k is the wavenumber and a is the characteristic size of the scatterer or

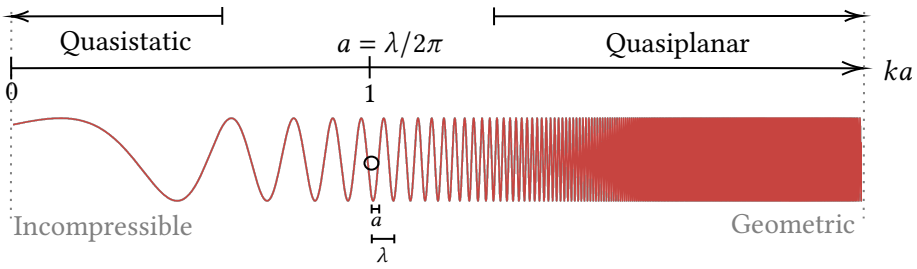

Figure 1.1: The acoustic spectrum quantified by ka, where $k = 2\pi/\lambda$ and λ is the wavelength. The zero-frequency limit corresponds to the suppression of wave motion due to incompressibility. The quasistatic limit $ka \ll 1$ describes spherically spreading waves. Shown near the center of the figure is a scatterer representing $ka \simeq 1$. The limit $ka \gg 1$ describes quasiplanar waves. The infinite-frequency limit corresponds to geometrical acoustics, in which waves are reduced to rays.

source of sound. If an acoustic wave varies harmonically in time, then its spatial dependence satisfies the Helmholtz equation given by Eq. (A.1), which is accurate for all values of ka [7, Eq. (3.1.7)].

A scatterer or source that is vanishingly small compared to a wavelength $\lambda = 2\pi/k$ corresponds to the limit $ka \to 0$, as shown on the left-hand side of Fig. 1.1. The zero-frequency limit describes an object in an incompressible medium, for which wavelengths are so much larger than the object that acoustic wave motion is negligible. The pressure in the limit $ka \to 0$ is static over a, although wave motion may occur over larger length scales. Mathematically, the Helmholtz equation reduces to the Laplace equation given by Eq. (A.4) in the zero-frequency limit. An acoustic wave phenomenon that can be described in the limit $ka \to 0$ is infrasound generated by natural sources like avalanches and tornadoes. An infrasonic wave with a frequency of 1 Hz has a wavelength of 343 m in air, which at the length scale of an ordinary microphone corresponds to ka on the order of 10^{-4}. Measuring infrasonic waves therefore requires sensors to be deployed in arrays on the order of 6 m [17, p. 36 and Fig. 5], increasing ka to the order of 10^{-1}.

The parameter range $0 < ka \ll 1$ shown in Fig. 1.1 is called the *quasistatic limit* [7, p. 490] because the period of the wave is much greater than a/c_0, where c_0 is the wave speed. Three-dimensional waves spread spherically from scatterers and sources of sound

in the quasistatic limit [9, p. 44], which is sometimes called the *Rayleigh limit* in reference to Rayleigh's pioneering work on both the electromagnetic [2, 18, 19] and acoustic [20] scattering problems. The quasistatic approximation is also called the *subwavelength* [21], *lumped-element* [9, pp. 144–156], or *low-frequency* approximation [22, Chap. 7].

The middle region of Fig. 1.1 depicting moderate values of ka is sometimes called the Mie regime [23, Chap. 9], in reference to Mie's solution of Maxwell's equations for electromagnetic scattering from a sphere in terms of spherical wave expansions [24]. While the solution is valid for all values of ka, the moderate values of ka have become associated with Mie because exact solutions of the wave equation are required to accurately describe scattering and diffraction when λ is on the order of a. A familiar example of electromagnetic Mie scattering is the interaction between sunlight and water droplets in clouds [25]. A brief history of Rayleigh and Mie scattering is provided by Caruthers [26].

The limit $ka \gg 1$ shown in Fig. 1.1 represents a scatterer or source that is much larger than a wavelength. Wavefronts are *quasiplanar* for $ka \gg 1$, warranting the use of the relation $p = \rho_0 c_0 v$, where ρ_0 is the ambient density of the fluid and v is the magnitude of the fluid velocity vector $\mathbf{v}$ [9, p. 44]. The limit is called the *paraxial approximation* in the study of diffraction because wavefronts are quasiplanar in the vicinity of the propagation axis for $ka \gg 1$ [6, pp. 58–60, 319–320]. The paraxial approximation is also called the *Fresnel approximation* in reference to Fresnel's original treatment of the limit [4], a history of which is provided by Silliman [27]. Mathematically, the Helmholtz equation reduces to the paraxial equation [Eq. (A.25)] in the Fresnel approximation.

The right-hand side of Fig. 1.1 represents the limit $ka \to \infty$, which corresponds to a scatterer or source that is infinitely large compared to a wavelength. The field in this limit consists of *rays*, which are plane waves that do not interfere [9, p. 284]. The study of sound in the limit of infinite frequency is referred to as *geometrical acoustics* or *ray theory* due to the suppression of diffraction and the reduction of wave functions to trajectories. For example, rays travel in straight lines in homogeneous media, and they follow circular trajectories in media in which the sound speed varies linearly in depth

[22, Sec. 8.3.2]. Geometrical acoustics is often used to model acoustic propagation in the ocean [9, pp. 284–293]. Mathematically, the Helmholtz equation reduces to the eikonal and transport equations in the infinite-frequency limit [Eqs. (A.37) and (A.42)].

The mathematical simplifications of the Helmholtz equation described above are presented in Sec. A.1, and a conceptual depiction of the frequency spectrum is offered in Sec. A.2. Motivation for the dissertation is developed in Sec. 1.3, which proceeds in order of increasing ka.

1.3 Motivation

In the quasistatic limit, interest in broken symmetry is motivated by particle manipulation with applications to acoustofluidics [28, 29]. Radiation forces and torques due to standing waves incident on asymmetric scatterers have been investigated [30–32], but radiation forces due to progressive waves on such scatterers have only recently garnered interest [32–37]. The development of analytical expressions for radiation force exerted by progressive waves is relevant to the acoustical transportation of subwavelength particles over large distances [38–40]. The present study is partially motivated by inconsistencies between Ref. 33 and the widely cited result published by Gor'kov for progressive waves more than a half century earlier [3, Eq. (10)].

The study of subwavelength scattering from asymmetric objects is also motivated by the desire to create materials with unconventional effective properties [41]. Willis media—materials with constitutive properties that emerge due to asymmetric subwavelength scatterers—have been investigated theoretically [13, 42–50] and experimentally [51–55], but the modeling of unit cells that constitute such media remains challenging [49]. Several studies use finite element modeling to determine the acoustic polarizabilities of unit cells [14, 56–58], but these calculations, which solve the inverse scattering problem [59], do not easily lend themselves to analysis and physical insights. The lack of a simple analytical formulation towards calculating polarizabilities partially motivates the present study.

Willis media have recently been generalized to include asymmetric subwavelength piezoelectric scatterers [60]. The resulting constitutive relations couple electrostatics to elastodynamics via an effect called *electromomentum coupling*. The coupling between electric displacement and velocity is relevant to the realization of advanced sensors, and attempts have been made to measure the effect [61]. The majority of studies analyze electromomentum coupling in the electrostatic regime [62–66]. To account for energy carried by electromagnetic waves, however, the electrostatic approximation must be abandoned [67, 68], and the fully elasto-electrodynamic system must be considered. While constraints due to reciprocity and passivity have been derived for the bianisotropic, piezoelectric, and electromomentum coupling tensors [60, 69, 70], the constraints on the piezomagnetic and magnetomomentum coupling tensors must be determined.

In diffraction phenomena, acoustic vortices constitute a broad class of sound beams that break axisymmetry [71]. Acoustic vortex beams have been applied to particle manipulation [72–81], biomedical ultrasound [82–84], underwater communications [85–91], and sound diffusion [92], but their modeling remains challenging. Many studies utilize finite element [78, 89, 93–99] and angular spectrum [79, 100] methods to calculate vortex fields, while others resort to the direct numerical evaluation of the Rayleigh integral [101–104]. All of these approaches are formally equivalent, but none of them provides analytical insight into the structure of the field. Laguerre-Gaussian eigenfunctions are sometimes used to obtain analytical solutions for vortex beams [10], but an infinite number of eigenfunctions is needed to match realistic source conditions [105–107]. The eigenfunctions converge slowly for even idealized source conditions, and the large number of terms required to describe fields radiated by these sources limits their utility. Closed-form analytical solutions exist for Bessel-vortex sources [108–112], but these solutions are mainly of theoretical relevance because Bessel beams require infinite energy to generate [113]. The lack of analytical descriptions of vortex beams radiated by more realistic source conditions motivates the present work.

In the infinite-frequency limit, the effects of breaking axisymmetry have been discussed in optics [114–118] but not acoustics. While the relationship between diffraction

and ray theory has been outlined formally in optics by Gloge and Marcuse [119], the relationship between the wavenumber k and orbital number ℓ, which quantify linear and angular momentum, respectively, has not been explored from the perspective of geometrical acoustics.

Additional perspectives on scattering from inhomogeneous media, Willis and electromomentum coupling, and vortex beam diffraction are provided by Yves et al. [120], who discuss symmetry-breaking wave phenomena in the context of artificial phononic media.

1.4 Overview of dissertation

The dissertation is organized in order of increasing ka. In Chap. 2, the acoustic radiation force exerted by plane progressive waves is calculated in the Born approximation using Westervelt's far-field integral [121, Eq. (2)]. In the subwavelength limit $ka \ll 1$ of the Born approximation [122, Eq. (8.1.20)], closed-form analytical expressions for the radiation force are obtained in terms of *acoustic polarizabilities*, which represent the response of the scatterer to dipole order. For subwavelength scatterers with relative compressibilities and densities that are even functions about the centroid, Gor'kov's force on the order of $(ka)^4$ is recovered [3, Eq. (10)], while the radiation force on scatterers characterized by odd distributions is on the order of $(ka)^6$. Radiation forces on homogeneous and inhomogeneous spheres and cubes are considered as examples, for which the analytical expressions agree with solutions based on spherical wave expansions and Fourier transforms for $ka \lesssim 0.8$. The results of Chap. 2 complement the volume integral obtained by Jerome and Hamilton [11, Eq. (16)] for the radiation force exerted by standing waves in the subwavelength limit of the Born approximation. The formulas for acoustic polarizability in combination with the homogenization theory of Sieck et al. [13] also provide a description of Willis media consisting of Born scatterers.

The effects of low-ka scattering in a piezoelectric metamaterial are considered in Chap. 3. A periodic array of asymmetric piezoelectric scatterers is homogenized, leading to effective constitutive relations that fully couple continuum mechanics to classical

electrodynamics. The dynamic homogenization is simplified by considering compressional waves in one dimension. Constraints due to reciprocity and passivity are derived for the medium's constitutive relations, which are shown to be consistent with the effective constitutive relations obtained from the homogenization. The piezomagnetic and magnetomomentum tensors are found to bear symmetries similar to those of the electromomentum and piezoelectric tensors, respectively. The symmetries of the constitutive tensors are explained by considering how the fields and displacements transform under time reversal. Limiting cases of the constraints recover previous results that neglect elastodynamics [69, Eqs. (8) and (23)], piezoelectricity [70, Eqs. (3.10)–(3.17)], and magnetism [123, Eqs. (18), (20), (33), and (42)]. The insights gained in Chap. 3 may help guide the design of devices that measure stress and velocity fields simultaneously.

Vortex beam diffraction is considered in Chap. 4. The vortex field radiated by a circular piston is represented for all ka as an infinite sum of Bessel beams. Closed-form analytical solutions are derived in the paraxial approximation for focused and unfocused vortex fields radiated by sources with uniform circular and Gaussian amplitude shadings. The utility of the analytical solutions is demonstrated by calculating the vortex ring radius, and the validity of the paraxial approximation is assessed by comparison with the exact solution of the Helmholtz equation. In the limit that ka is infinite, the effects of diffraction are suppressed, leading to a geometrical description of how the field depends on ℓ. In the absence of orbital motion ($\ell = 0$), the exact, paraxial, and ray solutions recover known descriptions of axisymmetric beams [6, Eqs. (8.19) and (8.37)]. The analytical solutions and scaling laws derived in Chap. 4 simplify the modeling of vortex fields.

Chapter 5 summarizes the scientific contributions of the dissertation and offers suggestions for future research.

Chapter 2: Radiation force due to progressive waves on inhomogeneous objects

2.1 Introduction

Radiation force is the time-averaged force exerted by waves on scatterers. The force arises due to momentum conservation at quadratic order in the solution of the wave equation [124]. Both progressive and standing waves are capable of exerting radiation forces, but the forces differ in their dependence on both position and frequency [3]. For plane waves, the differences can be understood qualitatively by noting that progressive waves carry time-averaged intensity, whereas standing waves do not. Meanwhile, standing waves form time-averaged gradients of energy, while progressive waves do not.

Perhaps the first observation of radiation force in nature was the force exerted by progressive waves of sunlight on the tails of comets. Chinese astronomers noted that comet tails point away from the Sun in 66 AD [125], when the appearance of Halley's Comet was first recorded accurately [126]. Tycho Brahe wrote that the Great Comet of 1577 "had its tail turned directly away from the Sun, as all other comets, those observed many years ago by Regiomontanus, Apian, Gemma Frisius, and Fracastoro, have also done" [127], indicating that the phenomenon was known in the West as early as Regiomontanus's observation of the Great Comet of 1472 [128, p. 104]. Johannes Kepler, who witnessed the Great Comet of 1577 at the age of six [129, p. 232], concluded following his observations of Halley's Comet in 1607 and the Great Comet of 1618 that "a comet's tail is formed by matter that the Sun's rays chase through their impulses outside the comet's body" [130, 131]. Euler explained the phenomenon by analogy to acoustics,

The content of Chap. 2 has been accepted for publication in the *Journal of the Acoustical Society of America* and is currently in press. The author's contributions include combining Westervelt's integral [121, Eq. (2)] with the scattering theory of Morse and Ingard [122, pp. 407–414] and the polarizabilities of Sieck et al. [13, Eqs. (16)], obtaining analytical expressions of radiation forces, comparing the results to known solutions, generating figures, and writing the manuscript.

noting that "a sound vigorously excites not only a vibratory motion in the air particles" but also causes "a real motion in small, very light dust particles which tumble in the air" [132, 133]. Forces due to progressive electromagnetic waves were subsequently described mathematically by Maxwell [134] and Poynting [135, 136], and the analogous acoustical problem was described by Rayleigh [137].

Interest in radiation forces exerted by standing waves began with Kundt's report of a powder in a tube accumulating near the nodes of a standing acoustic wave field [138]. Rayleigh [139] and Brillouin [140] calculated forces exerted by oscillations of a pendulum and standing waves on a string before considering the more involved acoustical problem, as reviewed by Beyer [133]. A discussion of the history, calculation, and applications of forces exerted by standing acoustic waves is provided by Bruus [29].

As mentioned in Sec. 1.3, current interest in radiation forces exerted by both standing and progressive waves is largely motivated by acoustofluidics [28, 141, 142]. Contributions by Mishra et al. [143], Jerome et al. [144], Lima and Silva [30], and Ekeroth et al. [145] have facilitated the calculation of forces exerted by standing waves on asymmetric [146] and/or inhomogeneous [11] objects. While forces exerted by progressive waves have been considered for the purpose of particle manipulation [39, 147–150] and transport over long distances [32, 38, 40], closed-form expressions for such forces on asymmetric and/or inhomogeneous objects remain unavailable [36, 37]. The goal of the present work is to obtain analytical expressions for the force exerted by progressive waves analogous to those obtained by Jerome et al. for standing waves [11, 144].

Jerome et al. showed that the radiation force exerted by a standing wave on a scatterer can be obtained by integrating differential radiation forces over the volume of a scatterer [144, Eq. (13)]. While radiation forces are proportional to the squares of the total acoustic fields and therefore do not generally superpose [3], the superposition principle underlying the integration is justified in the Born approximation, which neglects the effects of multiple scattering [22, Sec. 9.2.2]. The Born approximation itself requires that the scattered field be much weaker than the incident field, a condition that is satisfied if the

relative phase shift is small compared with an incident wave that misses the scatterer. The same conditions underlie the Rayleigh-Gans approximation in electromagnetic scattering [23, p. 80]. The Born approximation is therefore satisfied if contrasts between the material properties of the scatterer and the background medium are much smaller than unity [122, pp. 413–414] and if the products of the relative contrasts and the characteristic size a of the scatterer are much smaller than a wavelength $2\pi/k$ [22, 23, 151]. In practice, the forces calculated by Jerome et al. converge to exact solutions for $ka \lesssim 1$, with a number of examples transcending that limit for sufficiently weak material contrasts [144, Fig. 1(a)].

The integral for the radiation force is calculated by Jerome et al. by noting that in standing waves, the differential force is proportional to the scatterer's differential volume dV_s [11]. However, the approach does not apply to progressive waves, for which the differential force is proportional to $(dV_\mathrm{s})^2$, prohibiting integration over a scatterer's finite volume [144]. To calculate forces exerted by progressive waves, the present work makes approximations on the same order as those made by Jerome et al., but at different stages of the calculation. The Born and subwavelength approximations are invoked not as justifications to superpose differential radiation forces but rather as a means to solve the linear scattering problem.

The radiation force parallel to the unit vector $\mathbf{e}_\mathrm{i}$, which indicates the direction of the incident wave, is obtained by inserting the directivity Φ of the scattered wave into Westervelt's integral [121, Eq. (2)],

$$F_\parallel = \frac{p_0^2}{2\rho_0 c_0^2} \oint |\Phi|^2 (1 - \mathbf{e}_\mathrm{i} \cdot \mathbf{e}_r)\, d\Omega\,, \tag{2.1}$$

where p_0 is the incident pressure amplitude, ρ_0 is the density of the background fluid, $\mathbf{e}_r$ is the spherical radial unit vector, and $d\Omega$ is the differential solid angle, e.g., $\sin\theta\, d\theta\, d\phi$ in spherical coordinates, where θ and ϕ are the spherical polar and azimuthal angles, respectively. The relationship between $\mathbf{e}_\mathrm{i}$ and $\mathbf{e}_r$ is shown in Fig. 2.1 with respect to the incident progressive wave and scatterer. The speed of sound c_0 in the background fluid equals $1/\sqrt{\beta_0\rho_0}$, where β_0 is the compressibility of the fluid. Expressions for the

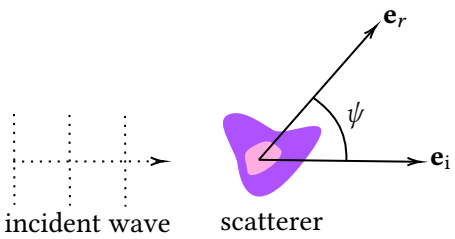

Figure 2.1: Spherical radial unit vector $\mathbf{e}_r$, incident wave unit vector $\mathbf{e}_\mathrm{i}$, and scattering angle $\psi = \arccos(\mathbf{e}_\mathrm{i} \cdot \mathbf{e}_r)$ shown with respect to the incident plane progressive wave and scatterer.

directivity Φ appearing in Eq. (2.1) are obtained by appealing to the Born and subwavelength approximations in Secs. 2.2 and 2.3, respectively. Equation (2.1) is evaluated for homogeneous and inhomogeneous spheres and cubes in Sec. 2.4, in which the resulting analytical expressions for $F_{\|}$ are compared with solutions in terms of spherical wave expansions and Fourier transforms. Equation (2.1) is derived from first principles in App. B [see Eq. (B.113)], where the final step of Westervelt's 1957 derivation [121] is clarified by appealing to energy conservation, and a qualitative derivation of Eq. (2.1) in terms of the scattering cross section is provided by van de Hulst [23, pp. 13–14]. While Eq. (2.1) is applicable to lossless scattering, the effect of absorption is discussed by Westervelt [121] and Zhang and Marston [110]. An alternative perspective on Eq. (2.1) is provided in the framework of momentum by Zhang and Marston in terms of phase shifts [152].

2.2 Far field of Born approximation

The propagation of time-harmonic acoustic waves in an inhomogeneous medium is described by [122, Eq. (8.1.12)][1]

$$\nabla^2 \tilde{p} + k^2 \tilde{p} = -k^2 \gamma_\beta \tilde{p} + \boldsymbol{\nabla} \cdot (\gamma_\rho \boldsymbol{\nabla} \tilde{p}) \,, \tag{2.2}$$

where the pressure field is related to $\tilde{p}$ by Eq. (A.3), $\mathbf{r}$ is the position vector, and k is the wavenumber. The functions γ_β and γ_ρ in Eq. (2.2) are Morse and Ingard's dimensionless

[1] In Morse and Ingard's corresponding Eq. (8.1.12), the second term on the right-hand side should be added to, not subtracted from, the equation.

contrast factors [122, p. 409]

$$\gamma_\beta(\mathbf{r}) = \frac{\beta_\mathrm{s}(\mathbf{r})}{\beta_0} - 1\,, \qquad \gamma_\rho(\mathbf{r}) = 1 - \frac{\rho_0}{\rho_\mathrm{s}(\mathbf{r})}\,, \tag{2.3}$$

where β_s and ρ_s are the scatterer's compressibility and density as functions of position within the scatterer, respectively. Equations (2.3) are defined such that $\gamma_\beta = \gamma_\rho = 0$ outside the region occupied by the scatterer. A derivation of Eq. (2.2) is provided in Sec. C.3.

While Morse and Ingard's contrast factors are convenient for the present analysis, studies of acoustic radiation force more frequently describe the material properties of scatterers in terms of Gor'kov's contrast factors [3, 11]

$$f_\beta(\mathbf{r}) = 1 - \frac{\beta_\mathrm{s}(\mathbf{r})}{\beta_0}\,, \qquad f_\rho(\mathbf{r}) = \frac{2[\rho_\mathrm{s}(\mathbf{r}) - \rho_0]}{2\rho_\mathrm{s}(\mathbf{r}) + \rho_0}\,, \tag{2.4}$$

which are related to Eqs. (2.3) through

$$f_\beta = -\gamma_\beta\,, \qquad f_\rho = \frac{2\gamma_\rho}{3 - \gamma_\rho}\,, \tag{2.5}$$

and therefore $\gamma_\beta = -f_\beta$ and $\gamma_\rho = 3f_\rho/(2+f_\rho)$. Morse and Ingard's contrast factors are used in the present section and in Sec. 2.3, but Gor'kov's contrast factors are used to describe scatterers in Sec. 2.4 for ease of comparison with previous studies.

The integral form of the inhomogeneous Helmholtz equation given by Eq. (2.2) is [122, Eq. (8.1.13)]

$$\tilde{p}(\mathbf{r}) = \tilde{p}_\mathrm{i}(\mathbf{r}) + \tilde{p}_\mathrm{s}(\mathbf{r})\,, \tag{2.6}$$

where $\tilde{p}_\mathrm{i}(\mathbf{r})$ represents the incident pressure and

$$\tilde{p}_\mathrm{s}(\mathbf{r}) = \int \left[k^2\gamma_\beta(\mathbf{r}_\mathrm{s})\tilde{p}(\mathbf{r}_\mathrm{s})g(\mathbf{r}|\mathbf{r}_\mathrm{s}) + \gamma_\rho(\mathbf{r}_\mathrm{s})\boldsymbol{\nabla}_\mathrm{s}\tilde{p}(\mathbf{r}_\mathrm{s}) \cdot \boldsymbol{\nabla}_\mathrm{s} g(\mathbf{r}|\mathbf{r}_\mathrm{s})\right] dV_\mathrm{s} \tag{2.7}$$

represents the scattered pressure, and

$$g(\mathbf{r}|\mathbf{r}_\mathrm{s}) = \frac{e^{ik|\mathbf{r}-\mathbf{r}_\mathrm{s}|}}{4\pi|\mathbf{r} - \mathbf{r}_\mathrm{s}|} \tag{2.8}$$

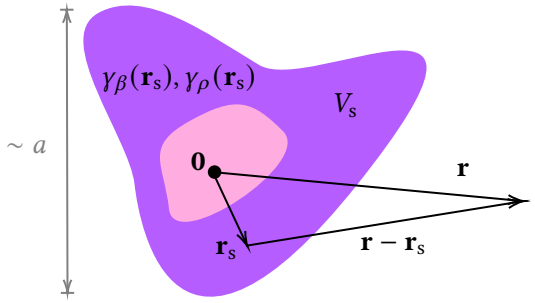

Figure 2.2: Geometry of scatterer of characteristic size a, volume V_s, and material properties given by Eqs. (2.3). The origin $\mathbf{0}$ is defined by Eq. (2.9) to be the centroid of the scatterer.

is the free-space Green's function of the Helmholtz equation. While the domain of integration in Eq. (2.7) is over all space, the evaluation of Eq. (2.7) amounts to a volume integral over the body of the scatterer because γ_β and γ_ρ vanish beyond the scatterer's boundary. Equations (2.2) and (2.7) are given by Eqs. (8.1.12) and (8.1.13) of Ref. 122, respectively, the derivations of which are reviewed in App. C. Equation (2.8) is derived in Sec. C.1.

The relationship between the integration coordinate $\mathbf{r}_s$ and the observation coordinate $\mathbf{r}$ with respect to the origin

$$\mathbf{0} = \frac{\int_{V_s} \mathbf{r}_s \, dV_s}{\int_{V_s} dV_s} \tag{2.9}$$

is shown in Fig. 2.2, where V_s denotes the region occupied by the scatterer. The identification of the origin as the centroid given by Eq. (2.9), as opposed to the center of mass, is consistent with previous scattering formulations [7, 11, 144] and is discussed further in Sec. 2.3.

For an incident plane progressive wave $\tilde{p}_i = p_0 e^{i\mathbf{k}_i \cdot \mathbf{r}}$, where $\mathbf{k}_i = k\mathbf{e}_i$ is the incident wave vector, the scattered wave given by Eq. (2.7) reduces in the far field of the Born

approximation to

$$\tilde{p}_\mathrm{s}(\mathbf{r}) = p_0 \frac{e^{ikr}}{r} \Phi(\mathbf{k}_\mathrm{s}) \,, \tag{2.10}$$

where $\mathbf{k}_\mathrm{s} = k\mathbf{e}_r$ is the scattered wave vector and $r = |\mathbf{r}|$. Equation (2.10) represents a spherically spreading scattered wave with directivity [122, Eq. (8.1.14)]

$$\Phi(\mathbf{k}_\mathrm{s}) = \frac{k^2}{4\pi} \left[\mathcal{F}_\mathrm{3D} \left\{ \gamma_\beta(\mathbf{r}_\mathrm{s}) e^{i\mathbf{k}_\mathrm{i}\cdot\mathbf{r}_\mathrm{s}} \right\} + \mathcal{F}_\mathrm{3D} \left\{ \gamma_\rho(\mathbf{r}_\mathrm{s}) e^{i\mathbf{k}_\mathrm{i}\cdot\mathbf{r}_\mathrm{s}} \right\} \mathbf{e}_\mathrm{i} \cdot \mathbf{e}_r \right] , \tag{2.11}$$

where the three-dimensional Fourier transform pair is defined by

$$\mathcal{F}_\mathrm{3D}\{f(\mathbf{r}_\mathrm{s})\} = \int f(\mathbf{r}_\mathrm{s}) e^{-i\mathbf{k}_\mathrm{s}\cdot\mathbf{r}_\mathrm{s}} dV_\mathrm{s} \,, \tag{2.12}$$

$$\mathcal{F}^{-1}_\mathrm{3D}\{F(\mathbf{k}_\mathrm{s})\} = \frac{1}{8\pi^3} \int F(\mathbf{k}_\mathrm{s}) e^{i\mathbf{k}_\mathrm{s}\cdot\mathbf{r}_\mathrm{s}} dW_\mathrm{s} \,, \tag{2.13}$$

and dV_s and dW_s are differential volume elements in position and wavenumber space, respectively, where the domains of integration are infinite. Equations (2.10) and (2.11) follow from Eq. (2.7) upon noting that Eq. (2.8) and its gradient approximately equal [153, Eq. (11.73)]

$$g(\mathbf{r}|\mathbf{r}_\mathrm{s}) \simeq \frac{e^{ikr}}{4\pi r} e^{-i\mathbf{k}_\mathrm{s}\cdot\mathbf{r}_\mathrm{s}} \,, \qquad \boldsymbol{\nabla}_\mathrm{s} g(\mathbf{r}|\mathbf{r}_\mathrm{s}) \simeq -i\mathbf{k}_\mathrm{s} g(\mathbf{r}|\mathbf{r}_\mathrm{s}) \tag{2.14}$$

in the far field, the conditions for which are discussed in the following paragraph. Evaluation of Westervelt's integral given by Eq. (2.1) for Φ given by Eq. (2.11) results in the Born approximation of the radiation force exerted by plane progressive waves on scatterers of arbitrary size with respect to a wavelength. While Westervelt's integral in combination with Eq. (2.11) is used simply to benchmark the subwavelength limit of the Born approximation in Sec. 2.4, the combination is valuable in its own right because its evaluation is considerably more simple than calculating radiation forces using partial wave expansions or the finite element method [36, 37, 154]. The study of how the Born approximation beyond the subwavelength limit compares to other methods falls beyond the scope of the present work but may be pursued in the future.

The far-field approximation leading to the scattered pressure given by Eq. (2.10) is based on the assumption that the spherical radial field coordinate r is much larger than the characteristic scatterer size a, allowing for the phase $k|\mathbf{r}-\mathbf{r}_s|$ of the Green's function to be approximated as $k(r-\mathbf{e}_r\cdot\mathbf{r}_s+r_s^2/2r)$, where $k|\mathbf{r}_s| = kr_s = O(ka)$. Thus for $r/a \gg ka$, one obtains

$$k|\mathbf{r}-\mathbf{r}_s| = k(r-\mathbf{e}_r\cdot\mathbf{r}_s)\,. \tag{2.15}$$

The far-field approximation is therefore always valid in the study of scattering for $ka \ll 1$ considered in Sec. 2.3 because the inequality $r/a \gg ka$ is satisfied for $r > a$. The far-field approximation is also on equal footing with Westervelt's integral, which requires that the scattered intensity be proportional to r^{-2}, as can be seen in Eq. (B.115). The far-field approximation as it pertains to the calculation of radiation force does "not introduce any approximation…in the idealized case of loss-less media" [155], though the limiting procedure leading to Westervelt's integral is "not straightforward" [156].

Conditions for the validity of the Born approximation leading to Φ given by Eq. (2.11) are more subtle. As stated in Sec. 2.1, while weak material contrast ($|\gamma_\beta|, |\gamma_\rho| \ll 1$) often satisfies the Born approximation, weak scattering may also be achieved if the scatterer is sufficiently small ($ka \ll 1$), provided that the frequency of the incident wave is not in the proximity of the resonance frequency of the scatterer [157–159]. A very small scatterer with large material contrast may therefore satisfy the Born approximation as well as a much larger scatterer with sufficiently small material contrast, as discussed in Sec. 2.4. The interrelated nature of the low-contrast and low-ka conditions is summarized by Pierce, who denotes $\Delta_1 = 1-\rho_0/\rho(\mathbf{r}) = \gamma_\rho$ and $\Delta_2 = 1-\beta(\mathbf{r})/\beta_0 = -\gamma_\beta$ [22, p. 507]:

> Although [the Born approximation] requires in general that the scattered wave in the steady state be much weaker than the incident wave wherever the dominant inhomogeneities occur, no simple criteria involving magnitudes of Δ_1 and Δ_2 establish the upper limits of the approximation's validity. It should, however, yield a good estimate of the scattered field if $|\Delta_1| \ll 1$ and $|\Delta_2| \ll 1$ and if the path integrals of both $k|\Delta_1|$ and $k|\Delta_2|$ are small compared with unity.

The interdependence between low contrast and long wavelength and its effect on the validity of the Born approximation is evident in Fig. 1(a) of Jerome et al. [144], in which the contrast is sufficiently weak that the radiation force predicted by the Born approximation agrees with the full expression of the force based on spherical wave expansions [160] for $ka = O(10)$. A similar interdependence is reported in Refs. 23, 151, and 59, and a more detailed discussion of how the validity of the Born approximation depends on frequency is provided in Ref. 161. For the present work, it suffices to note that Westervelt's integral in terms of Φ given by Eq. (2.11) is accurate for $ka > O(1)$ only if the sound speed within the scatterer is sufficiently close to that of the background medium such that the cumulative error due to propagation at a different phase speed within the scatterer can be neglected.

2.3 Subwavelength limit

The present section is devoted to obtaining the subwavelength limit of Φ given by Eq. (2.11), for which the Born approximation is more broadly satisfied, and for which evaluation of Westervelt's integral yields closed-form analytical expressions. Begin by noting that $|\mathbf{k}_\mathrm{i}| = |\mathbf{k}_\mathrm{s}| = k$ and $|\mathbf{r}_\mathrm{s}| = O(a)$. The products $\mathbf{k}_\mathrm{i} \cdot \mathbf{r}_\mathrm{s}$ and $\mathbf{k}_\mathrm{s} \cdot \mathbf{r}_\mathrm{s}$ are therefore $O(ka)$. Assuming $ka \ll 1$ therefore warrants the expansion of the complex exponentials in Eqs. (2.10)–(2.13) to linear order:

$$e^{i\mathbf{k}_\mathrm{i}\cdot\mathbf{r}_\mathrm{s}} \simeq 1 + i\mathbf{k}_\mathrm{i} \cdot \mathbf{r}_\mathrm{s}\,, \tag{2.16}$$

$$e^{-i\mathbf{k}_\mathrm{s}\cdot\mathbf{r}_\mathrm{s}} \simeq 1 - i\mathbf{k}_\mathrm{s} \cdot \mathbf{r}_\mathrm{s}\,. \tag{2.17}$$

Equation (2.11) in terms of Eqs. (2.12), (2.16), and (2.17) becomes

$$\Phi(\mathbf{k}_\mathrm{s}) = \frac{1}{4\pi} \int [k^2 \gamma_\beta(\mathbf{r}_\mathrm{s}) + \mathbf{k}_\mathrm{s} \cdot \mathbf{k}_\mathrm{i} \gamma_\rho(\mathbf{r}_\mathrm{s})][1 + i(\mathbf{k}_\mathrm{i} - \mathbf{k}_\mathrm{s}) \cdot \mathbf{r}_\mathrm{s}] dV_\mathrm{s}\,, \tag{2.18}$$

where terms proportional to $(\mathbf{k}_\mathrm{i} \cdot \mathbf{r}_\mathrm{s})(\mathbf{k}_\mathrm{s} \cdot \mathbf{r}_\mathrm{s}) = O[(ka)^2]$ have been neglected.

The retention of the linear terms in Eqs. (2.16) and (2.17) restricts the accuracy of the scattered pressure given by Eq. (2.10) combined with Eq. (2.18) to dipole order, as can

be shown by alternatively expressing Eq. (2.10) as the pressure field scattered by a point located at the origin $\mathbf{0}$ [13, Eq. (19)]:

$$\tilde{p}_\mathrm{s}(\mathbf{r}) = -k^2\rho_0 c_0^2 m g(\mathbf{r}|\mathbf{0}) + ikc_0\mathbf{d}\cdot\boldsymbol{\nabla} g(\mathbf{r}|\mathbf{0})\,. \tag{2.19}$$

The scalar m in Eq. (2.19) is the monopole strength, and the vector $\mathbf{d}$ is the acoustic dipole moment. Equation (2.19) is consistent with the dipole-order expansion of Sieck et al. given by Eqs. (19) and (20) of Ref. 13, and a derivation of Eq. (2.19) from first principles is presented in Sec. C.5. While several other conventions of dipole-order expansions appear in the literature [7, 22, 56, 57], the expansion given by Eq. (2.19) is conducive to the present study because it can be interpreted as the Born approximation for a point scatterer of the exact scattered field given by Eq. (2.7). The relationship between Eqs. (2.7) and (2.19) is reminiscent of the relationship between the full radiation force exerted by a standing wave on a compressible sphere and its point scattering approximation, given by Eqs. (3) and (6), respectively, of Jerome et al. [144]. Monopolar and dipolar fields were discussed previously in the context of radiation force by Fan and Zhang [162], whose analysis is based on the phase-shift-related expressions developed by Zhang and Marston [152], and by Sepehrirahnama et al. [33–35], whose results are discussed at the end of the present section.

The monopole strength and dipole moment appearing in Eq. (2.19) are related to the incident pressure and fluid velocity fields by acoustic polarizabilities, which represent the combined influence of the geometry and composition of a scatterer in the long-wavelength limit. The concept of polarizability originated in electromagnetism [8, 12]. An introduction to the electric polarizability tensor is provided by Feynman [163, Vol. II, Chap. 31], and an accessible discussion of the use of polarizability in subwavelength electromagnetic scattering is provided by van de Hulst [23, pp. 63–65]. Polarizability was introduced in acoustics by Senior [164] to describe scattering in the static limit, for which the Helmholtz equation reduces to the Laplace equation. Acoustic polarizabilities have since been discussed in Refs. 13, 22, 33, 34, 56, 57 and 35, and a recent review of the use of

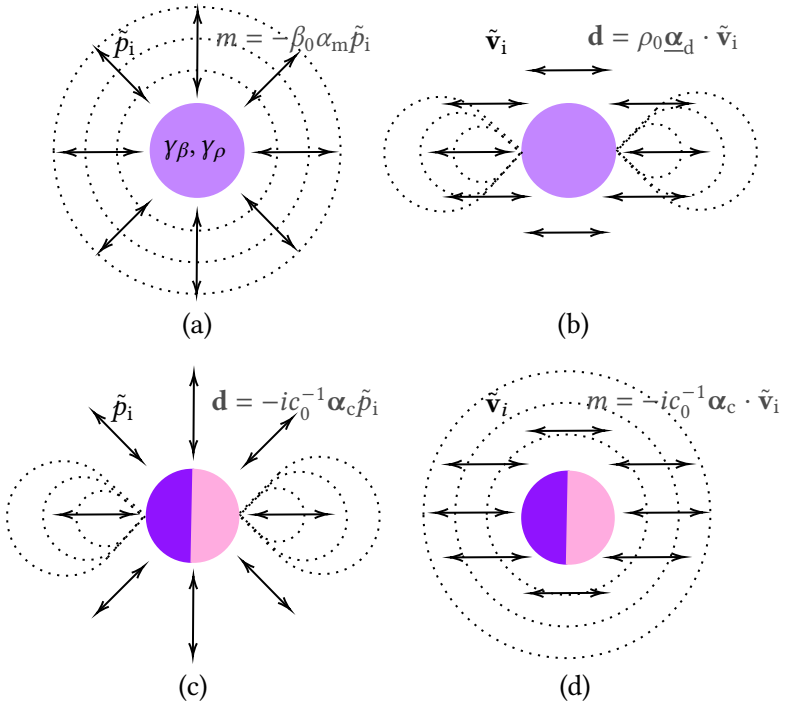

Figure 2.3: Time-harmonic field scattered by a homogeneous subwavelength object insonified by an incident (a) pressure field and (b) velocity field, yielding monopole and dipole scattered fields, respectively. This is shown in contrast to the field scattered by an inhomogeneous subwavelength object with an antisymmetric property distribution insonified by an incident (c) pressure field and (d) velocity field, yielding dipole and monopole scattered fields, respectively.

acoustic polarizability in the study of subwavelength scattering is provided by Lawrence [14, Sec. 2.2]. The present work employs the coupled linear equations

$$m = -\beta_0 \alpha_\mathrm{m} \tilde{p}_\mathrm{i} - ic_0^{-1} \boldsymbol{\alpha}_\mathrm{c} \cdot \tilde{\mathbf{v}}_\mathrm{i} \,, \tag{2.20}$$

$$\mathbf{d} = -ic_0^{-1} \boldsymbol{\alpha}_\mathrm{c} \tilde{p}_\mathrm{i} + \rho_0 \underline{\boldsymbol{\alpha}}_\mathrm{d} \cdot \tilde{\mathbf{v}}_\mathrm{i} \tag{2.21}$$

introduced by Sieck et al. [13, Eqs. (16)], where the volumetric quantities α_m, $\underline{\boldsymbol{\alpha}}_\mathrm{d}$, and $\boldsymbol{\alpha}_\mathrm{c}$ are the monopolar, dipolar, and coupled polarizabilities, respectively. The monopolar polarizability α_m is a scalar that linearly relates a time-harmonic incident pressure field to the monopole strength of the scattered field, as shown in Fig. 2.3(a). The dipolar polarizability $\underline{\boldsymbol{\alpha}}_\mathrm{d}$ is a rank-2 tensor that relates a time-harmonic incident velocity field to the dipole moment of the scattered field, as shown in Fig. 2.3(b). The coupled polarizability $\boldsymbol{\alpha}_\mathrm{c}$

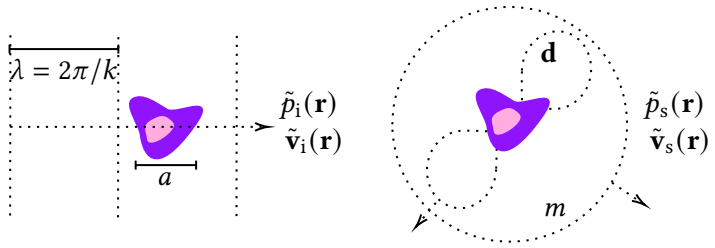

(a) incident plane waves (b) scattered spherical waves

Figure 2.4: (a) Incident plane progressive waves consist of both time-harmonic pressure and velocity fields given by $\tilde{p}_\mathrm{i} = p_0 e^{i\mathbf{k}_\mathrm{i}\cdot\mathbf{r}}$ and $\tilde{\mathbf{v}}_\mathrm{i}(\mathbf{r}) = p_0\mathbf{k}_\mathrm{i}e^{i\mathbf{k}_\mathrm{i}\cdot\mathbf{r}}/k\rho_0 c_0$, respectively. (b) The monopole, dipole, and coupling polarizabilities defined by Eqs. (2.20) and (2.21) therefore contribute to the scattered fields.

is a vector representing the asymmetry of the scatterer that relates the incident pressure and velocity fields to the dipole moment and monopole strength, respectively, as shown in Figs. 2.3(c) and (d).

Incident plane waves consist of both time-harmonic pressure and velocity fields [9, p. 39], so the field scattered by a subwavelength object generally includes contributions from α_m, $\underline{\boldsymbol{\alpha}}_\mathrm{d}$, and $\boldsymbol{\alpha}_\mathrm{c}$, as shown in Fig. 2.4. Since the incident field equals $\tilde{p}_\mathrm{i} = p_0 e^{i\mathbf{k}_\mathrm{i}\cdot\mathbf{r}}$, the incident pressure and velocity fields at $\mathbf{r} = \mathbf{0}$ are

$$\tilde{p}_\mathrm{i} = p_0\,, \qquad \tilde{\mathbf{v}}_\mathrm{i} = \mathbf{k}_\mathrm{i}p_0/k\rho_0 c_0\,, \tag{2.22}$$

where the second equation is obtained by inserting $\tilde{p}_\mathrm{i}$ into the time-harmonic form of the linearized momentum equation $\tilde{\mathbf{v}}_\mathrm{i}(\mathbf{r}) = \boldsymbol{\nabla}\tilde{p}_\mathrm{i}(\mathbf{r})/ik\rho_0 c_0$. In terms of Eq. (2.22), the monopole strength and dipole moment defined by Eqs. (2.20) and (2.21) become

$$m = -\beta_0\alpha_\mathrm{m}p_0 - i\boldsymbol{\alpha}_\mathrm{c}\cdot\mathbf{k}_\mathrm{i}p_0/k\rho_0 c_0^2\,, \tag{2.23}$$

$$\mathbf{d} = -i\boldsymbol{\alpha}_\mathrm{c}p_0/c_0 + \underline{\boldsymbol{\alpha}}_\mathrm{d}\cdot\mathbf{k}_\mathrm{i}p_0/kc_0\,. \tag{2.24}$$

The far-field limit $r \gg a$ of the scattered pressure is obtained by combining Eqs. (2.14) and (2.19):

$$\tilde{p}_\mathrm{s}(\mathbf{r}) = \frac{e^{ikr}}{4\pi r}(-k^2\rho_0 c_0^2 m + kc_0\mathbf{d}\cdot\mathbf{k}_\mathrm{s})\,. \tag{2.25}$$

Insertion of Eqs. (2.23) and (2.24) into Eq. (2.25) and comparison with the far-field pressure given by Eq. (2.10) yields the scattered directivity in terms of the polarizabilities:

$$\Phi(\mathbf{k}_\mathrm{s}) = \frac{k^2}{4\pi}[\alpha_\mathrm{m} + i\boldsymbol{\alpha}_\mathrm{c} \cdot (\mathbf{e}_\mathrm{i} - \mathbf{e}_r) + \mathbf{e}_r \cdot \underline{\boldsymbol{\alpha}}_\mathrm{d} \cdot \mathbf{e}_\mathrm{i}]\,. \tag{2.26}$$

Comparing Eq. (2.26) with Φ given by Eq. (2.18) identifies

$$\alpha_\mathrm{m} = \int \gamma_\beta(\mathbf{r}_\mathrm{s})\, dV_\mathrm{s}\,, \tag{2.27}$$

$$\underline{\boldsymbol{\alpha}}_\mathrm{d} = \underline{\mathbf{I}} \int \gamma_\rho(\mathbf{r}_\mathrm{s})\, dV_\mathrm{s} = \underline{\mathbf{I}}\alpha_\mathrm{d}\,, \tag{2.28}$$

$$\boldsymbol{\alpha}_\mathrm{c} = k\left[\int \gamma_\beta(\mathbf{r}_\mathrm{s})\mathbf{r}_\mathrm{s}\, dV_\mathrm{s} + \mathbf{e}_\mathrm{i} \cdot \mathbf{e}_r \int \gamma_\rho(\mathbf{r}_\mathrm{s})\mathbf{r}_\mathrm{s}\, dV_\mathrm{s}\right], \tag{2.29}$$

where $\underline{\mathbf{I}}$ is the identity tensor. The radiation force exerted by plane progressive waves on subwavelength scatterers satisfying the Born approximation is obtained by evaluating Westervelt's integral given by Eq. (2.1) for

$$|\Phi|^2 = \frac{k^4}{16\pi^2}\left\{\alpha_\mathrm{m}^2 + 2\alpha_\mathrm{m}\alpha_\mathrm{d}\cos\psi + [\boldsymbol{\alpha}_\mathrm{c} \cdot (\mathbf{e}_\mathrm{i} - \mathbf{e}_r)]^2 + \alpha_\mathrm{d}^2\cos^2\psi\right\}, \tag{2.30}$$

where $\mathbf{e}_\mathrm{i} \cdot \mathbf{e}_r = \cos\psi$, as shown in Fig. 2.1. In the special case that $\boldsymbol{\alpha}_\mathrm{c} = \mathbf{0}$, Westervelt's integral reduces to

$$F_\parallel = \frac{p_0^2}{2\rho_0 c_0^2}\frac{k^4}{4\pi}\left(\alpha_\mathrm{m}^2 - \tfrac{2}{3}\alpha_\mathrm{m}\alpha_\mathrm{d} + \tfrac{1}{3}\alpha_\mathrm{d}^2\right), \tag{2.31}$$

a result that is compared with solutions based on spherical wave expansions and Fourier transforms in Sec. 2.4. In such cases, perpendicular components of the radiation force vanish, as can be seen by inserting $|\Phi|^2$ given by Eq. (2.30) for $\boldsymbol{\alpha}_\mathrm{c} = \mathbf{0}$ into [121, Eq. (16)]

$$F_\perp = -\frac{p_0^2}{2\rho_0 c_0^2}\oint |\Phi|^2\, \mathbf{e}_m \cdot \mathbf{e}_r\, d\Omega\,, \tag{2.32}$$

where $\mathbf{e}_m$ is a unit vector perpendicular to $\mathbf{e}_\mathrm{i}$. For $\boldsymbol{\alpha}_\mathrm{c} = \mathbf{0}$, Eq. (2.31) therefore equals the magnitude of the total radiation force $\mathbf{F}$ exerted by progressive waves.

The far field of the scattered pressure given by Eq. (2.10) combined with Φ given by Eq. (2.26) is to leading order proportional to $(ka)^2$, a result that is consistent with

Rayleigh scattering [19, 20]. If Eqs. (2.16) and (2.17) were instead approximated to zeroth order as $e^{i\mathbf{k}_\mathrm{i}\cdot\mathbf{r}_\mathrm{s}} \simeq e^{i\mathbf{k}_\mathrm{s}\cdot\mathbf{r}_\mathrm{s}} \simeq 1$, then the quantity $i(\mathbf{k}_\mathrm{i} - \mathbf{k}_\mathrm{s}) \cdot \mathbf{r}_\mathrm{s}$ would not appear in Φ given by Eq. (2.18), which when combined with Eq. (2.10) would reduce to Morse and Ingard's Eq. (8.1.21) [122] and Ginsberg's Eq. (12.3.1) [7]:

$$\tilde{p}_\mathrm{s}(\mathbf{r}) = p_0 k^2 \frac{e^{ikr}}{4\pi r}(\alpha_\mathrm{m} + \alpha_\mathrm{d}\mathbf{e}_\mathrm{i} \cdot \mathbf{e}_r) \,. \tag{2.33}$$

The electromagnetic analog of Eq. (2.33) was originally obtained by Rayleigh to explain why the sky is blue [18]. Since Eq. (2.33) is based on the assumption that "the phase of any long-wavelength signal will be essentially constant over the extent of the body" [7, p. 490], it does not account for the effect of a scatterer's material asymmetry.

The present work generalizes Rayleigh scattering by approximating the phase over the body to linear order. Expansions in powers of ka were previously considered by Stevenson for electromagnetic scattering problems [165]. More recently, Marston and Zhang considered leading-order corrections to Rayleigh scattering to study scattering from, and radiation forces on, spheres in progressive wave fields [166]. Marston also developed expansions in powers of ka to describe acoustic radiation forces exerted by standing waves on spheres [167, 168]. Background concerning these expansions is provided in Refs. 169 and 170.

The fact that $\underline{\boldsymbol{\alpha}}_\mathrm{d}$ given by Eq. (2.28) is proportional to the identity tensor reflects that "the dipole is aligned in the direction of the incident wave" [7, p. 491] in the Born approximation. The same result was reported by Marston for scattering due to evanescent incident waves from an infinite fluid cylinder [171]. Had the Born approximation not been made, the second term of the integrand of Eq. (2.7) would be proportional to $\mathbf{k}_\mathrm{s} \cdot \boldsymbol{\nabla}_\mathrm{s}[\tilde{p}_\mathrm{i}(\mathbf{r}_\mathrm{s}) + \tilde{p}_\mathrm{s}(\mathbf{r}_\mathrm{s})]$ in the far field, revealing for plane-wave incidence ($\tilde{p}_\mathrm{i} = p_0 e^{i\mathbf{k}_\mathrm{i}\cdot\mathbf{r}}$) that $\underline{\boldsymbol{\alpha}}_\mathrm{d} \neq \alpha_\mathrm{d}\underline{\mathbf{I}}$ only when the gradient of the scattered pressure is oriented in a direction other than $\mathbf{k}_\mathrm{i}$. Since $\tilde{p}_\mathrm{s}$ is neglected altogether in the Born approximation, the quantity $\mathbf{k}_\mathrm{s} \cdot \boldsymbol{\nabla}_\mathrm{s}\tilde{p}_\mathrm{i}(\mathbf{r}_\mathrm{s})$ is proportional to $\mathbf{e}_r \cdot \mathbf{e}_\mathrm{i}$, comparison of which to the last term of Φ given by Eq. (2.26) shows that $\underline{\boldsymbol{\alpha}}_\mathrm{d}$ is proportional to the identity tensor. Methods of obtaining matrix

representations of $\underline{\boldsymbol{\alpha}}_\mathrm{d} \neq \alpha_\mathrm{d}\underline{\mathbf{I}}$ when the scatterer does not satisfy the Born approximation are provided in the quasistatic approximation by Senior [164], Pierce [22, Sec. 9.1.1], and Ginsberg [7, Sec. 12.3.3]. While such scatterers lie beyond the scope of Chap. 2, the results of Ref. 164 are used to calculate radiation forces on oblate and prolate rigid spheroids in Sec. C.6, revealing sizable transverse radiation forces when symmetry about the axis of incident-wave propagation is broken. Cases in which $\underline{\boldsymbol{\alpha}}_\mathrm{d} \neq \alpha_\mathrm{d}\underline{\mathbf{I}}$ are also encountered in anisotropic subwavelength structures [53, 56, 172], although resonance effects preclude such structures from being studied in the Born approximation [173].

The coupled polarizability given by Eq. (2.29) differs in several ways from α_m and $\underline{\boldsymbol{\alpha}}_\mathrm{d}$ given by Eqs. (2.27) and (2.28), respectively. For one thing, $\boldsymbol{\alpha}_\mathrm{c}$ is proportional to the wavenumber $k = \omega/c_0$, suggesting that it arises due to a dynamic effect [13, 51, 70]. The factor of k in $\boldsymbol{\alpha}_\mathrm{c}$ combined with the factor of $-i$ in Eqs. (2.20) and (2.21) forms the product $-ik = -i\omega/c_0$, which is suggestive of the time derivative of a harmonic quantity. Equations (2.20) and (2.21) therefore suggest that the coupled polarizability relates pressure to acceleration $\partial\mathbf{v}/\partial t$, not velocity itself, an interpretation that is consistent with the principle of Galilean invariance [174, Sec. 14.2] and the time-domain form of the macroscopic Willis constitutive relations expressed by Sieck et al [13, Eqs. (40)]. When combined with the far field of the scattered pressure given by Eqs. (2.10) and (2.26), the coupled polarizability therefore contributes to the scattered field at $O[(ka)^3]$ rather than at $O[(ka)^2]$, as in the case for scattering associated with α_m and $\underline{\boldsymbol{\alpha}}_\mathrm{d}$. Since the polarizabilities appear in $|\Phi|^2$ in quadratic combinations, it is anticipated that α_m^2 and α_d^2 contribute to Westervelt's integral at $O[(ka)^4]$, while $|\boldsymbol{\alpha}_\mathrm{c}|^2$ contributes at $O[(ka)^6]$, as will be shown in Sec. 2.4.

Another difference between $\boldsymbol{\alpha}_\mathrm{c}$ and the monopole and dipole polarizabilities is that the volume integrals in Eq. (2.29) for $\boldsymbol{\alpha}_\mathrm{c}$ are taken not over the contrast factors but over their moments, $\gamma_\beta(\mathbf{r}_\mathrm{s})\mathbf{r}_\mathrm{s}$ and $\gamma_\rho(\mathbf{r}_\mathrm{s})\mathbf{r}_\mathrm{s}$, indicating that $\boldsymbol{\alpha}_\mathrm{c}$ vanishes if $\gamma_\beta(\mathbf{r}_\mathrm{s}) = \gamma_\beta(-\mathbf{r}_\mathrm{s})$ and $\gamma_\rho(\mathbf{r}_\mathrm{s}) = \gamma_\rho(-\mathbf{r}_\mathrm{s})$ over a symmetric domain. The form of Eq. (2.29) indicates that $\boldsymbol{\alpha}_\mathrm{c}$ is nonzero when the contrast factors are not even functions of $\mathbf{r}_\mathrm{s}$.

Finally, it is noted that while Eqs. (2.27)–(2.29) are independent of coordinate sys-

tems, Eq. (2.29) *does* depend on the choice of the origin. The origin $\mathbf{0}$ is defined by Eq. (2.9) to be the centroid of the scatterer because it is desired that $\boldsymbol{\alpha}_c$ be "nonzero when the inhomogeneity has some form of asymmetry" [13]. The use of the centroid as the origin is consistent with previous studies of radiation force [11] and Willis coupling [13]. The relationship between the choice of the origin and the uniqueness of dynamic homogenization schemes is discussed in Refs. 175 and 176.

Expressions for acoustic polarizabilities that depend explicitly on material properties are generally unavailable without relying on approximations like those leading to Eqs. (2.27)–(2.29). Previous polarizability formulations are based on inverse scattering, in which the polarizabilities are expressed in terms of scattered fields [13, 53, 56, 57]. While such formulations can account for resonant phenomena and strong scattering, their generality comes at the expense of simplicity and physical insight. An appreciation of the complexity of previous studies of acoustic polarizability can be gained by inspecting Eq. (16) of Ref. 57, which itself is based on a formulation that is "significantly simpler than that of [Ref. 56]" [57]. In contrast, the present work provides expressions for the scattered field in terms of acoustic polarizabilities, which are calculated by integrating the material properties over the volume of the scatterer. The simplicity of the present formulation is due to the far-field and Born approximations, which limit the generality of the present work.

Sepehrirahnama et al. [33–35] employed the inverse scattering formulation of the acoustic polarizabilities derived by Quan et al. [56] to calculate the radiation force exerted by both standing and progressive waves on subwavelength scatterers. The present work provides a solution of the corresponding forward problem for the radiation force exerted by progressive waves, although the results presented here differ from those reported by Sepehrirahnama et al. The discrepancy appears to result from the claim that "the primary radiation force acting on a scatterer corresponds to the incident-scattering portion of the time-averaged radiation stresses" [33], an assumption that is often made in the calculation of radiation force exerted by standing waves [3, 29]. Forces due to progressive waves,

however, are expressed in terms of the intensity of the scattered wave [121, 177], as noted by Gor'kov [3]:

> The magnitude of the average force in a standing wave is larger than in a plane running wave. In the former case, in the quadratic expression for the force there are also important contributions from the interference terms between the incident and scattered waves, whereas for a running wave the magnitude of the momentum imparted to the particle by the waves is determined only by the momentum carried away by the scattered wave.

A comparison of the present formulation with that of Sepehrirahnama et al. is discussed further in Sec. C.7.

2.4 Examples

Westervelt's integral given by Eq. (2.1) is now evaluated in terms of Eqs. (2.26)–(2.29) for homogeneous and inhomogeneous spheres and cubes. Comparison of the results with previous works [3, 122, 144, 178] is facilitated by employing Gor'kov's contrast factors defined by Eqs. (2.4), which are related to γ_β and γ_ρ used in Secs. 2.2 and 2.3 through Eqs. (2.5). The radiation force is normalized by

$$F_0 = \frac{p_0^2 A_\parallel}{2\rho_0 c_0^2}, \tag{2.34}$$

where $A_\parallel$ is the cross-sectional area of the scatterer encountered by the incident wave. The incident wave is chosen to be oriented in the z direction, so $F_\parallel = F_z$, and the dot product $\mathbf{e}_\mathrm{i} \cdot \mathbf{e}_r$ appearing in Eqs. (2.1), (2.26), and (2.29) equals $\mathbf{e}_z \cdot \mathbf{e}_r = \cos\theta$, where θ is the spherical polar angle.

Homogeneous sphere

Considered first is the radiation force on a homogeneous compressible sphere of radius a with material properties given by $f_\beta = f_1$ and $f_\rho = f_2$, as defined by Eq. (2.4). According

to Eqs. (2.27)–(2.29), the polarizabilities are

$$\alpha_{\mathrm{m}} = -\tfrac{4}{3}\pi a^3 f_1\,, \qquad \alpha_{\mathrm{d}} = \tfrac{4}{3}\pi a^3 \frac{3f_2/2}{1+f_2/2}\,, \tag{2.35}$$

and $\boldsymbol{\alpha}_{\mathrm{c}} = \mathbf{0}$, where the coupled polarizability is calculated in spherical coordinates (r,θ,ϕ) by noting that $\mathbf{r}_{\mathrm{s}}$ in Eq. (2.29) equals $r_{\mathrm{s}}(\mathbf{e}_x \sin\theta_{\mathrm{s}}\cos\phi_{\mathrm{s}} + \mathbf{e}_y \sin\theta_{\mathrm{s}}\sin\phi_{\mathrm{s}} + \mathbf{e}_z\cos\theta_{\mathrm{s}})$ [8]. Inserting Eqs. (2.35) into $F_{\|}$ given by Eq. (2.31) yields the radiation force in the z direction,

$$\frac{F_z}{F_0} = \tfrac{4}{9}(ka)^4\left[f_1^2 + \frac{f_1 f_2}{1+f_2/2} + \frac{3f_2^2}{4(1+f_2^2/2)^2}\right], \tag{2.36}$$

where it has been noted that $A_{\|} = \pi a^2$.

The radiation force on a small sphere due to progressive waves was previously obtained by Gor'kov [3, Eq. (10)]. Gor'kov's result is recovered from Eq. (2.36) by noting that the Born approximation underlying Eq. (2.36) is satisfied if f_1 and f_2 are much less than unity [144], warranting the binomial expansion of the denominators of the terms in square brackets of Eq. (2.36):

$$\frac{f_1 f_2}{1+f_2/2} \simeq f_1 f_2(1-f_2/2)\,, \qquad \frac{3f_2^2}{4(1+f_2^2/2)^2} \simeq \tfrac{3}{4}f_2^2(1-f_2^2)\,.$$

The Born approximation therefore justifies retaining only the quadratic order of the contrast factors in Eq. (2.36), yielding

$$F_z = \frac{4\pi\langle I\rangle}{9c_0}a^2(ka)^4(f_1^2 + f_1 f_2 + \tfrac{3}{4}f_2^2), \tag{2.37}$$

where $\langle I\rangle = p_0^2/2\rho_0 c_0 = \rho_0 c_0 v_0^2/2$ is the time-averaged intensity of the incident wave [9]. Equation (2.37) recovers Gor'kov's Eq. (10) [3].

The validity of Eqs. (2.36) and (2.37) is assessed by comparison to the full expression for the radiation force on a homogeneous compressible sphere in terms of spherical wave expansions provided by Refs. 160, 179 and 144. The incident and scattered waves are expressed in terms of the eigenfunctions of the axisymmetric Helmholtz equation in spherical coordinates,

$$\tilde{p}_{\mathrm{i}} = \sum_{n=0}^{\infty} a_n j_n(kr)P_n(\cos\theta)\,, \qquad \tilde{p}_{\mathrm{s}} = \sum_{n=0}^{\infty} A_n a_n h_n^{(1)}(kr)P_n(\cos\theta)\,, \tag{2.38}$$

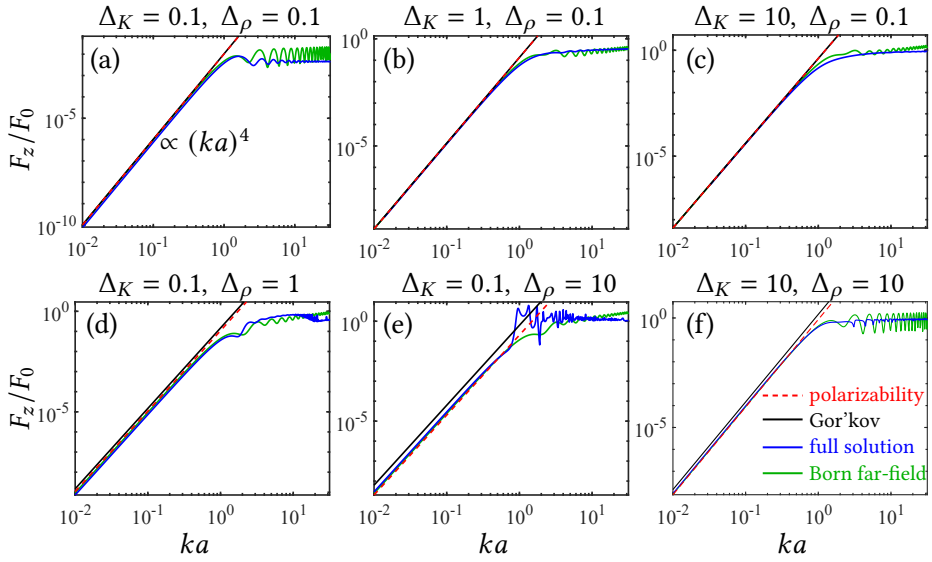

Figure 2.5: Comparison of the polarizability-based formulation given by Eq. (2.36) (dashed red lines), Gor'kov's result for the radiation force on a sphere given by Eq. (2.37) (solid black lines), the full expression for the radiation force on a sphere given by Eq. (2.39) (solid blue curves), and the radiation force on a cube having the same volume and material properties as the sphere given by Eq. (2.49) (solid green curves) as functions of ka. The contrasts $\Delta_K = (K_s - K_0)/K_0$ and $\Delta_\rho = (\rho_s - \rho_0)/\rho_0$ span two orders of magnitude, where plot (a) corresponds to a scatterer with weak material contrast and plot (f) approximates a rigid scatterer.

where j_n are the spherical Bessel functions, $h_n^{(1)}$ are the spherical Hankel functions of the first kind, and P_n are the Legendre polynomials. The coefficient $a_n = i^n(2n+1)$ corresponds to the incident plane wave [180, Item 10.60.7], and A_n corresponds to the scattered wave and is determined by satisfying the continuity of pressure and normal fluid velocity at $r = a$ [181, Eqs. (3.82) and (3.83)]. The normalized form of the radiation force is [144, Eq. (3)]

$$\frac{F_z}{F_0} = \mathrm{Re}\left[\frac{4i}{(ka)^2}\sum_{n=0}^{\infty}\frac{n+1}{(2n+1)(2n+3)}(A_n^* + A_{n+1} + 2A_n^*A_{n+1})a_n^*a_{n+1}\right]. \tag{2.39}$$

Equations (2.36), (2.37), and (2.39) are compared for six combinations of contrast factors in Fig. 2.5. The numerical evaluation of the summation in Eq. (2.39) is truncated to the first 70 terms, which is sufficient for convergence of the summation to $ka \simeq 90$. To

aid the characterization of the material properties, the dimensionless quantities

$$\Delta_K = (K_\mathrm{s} - K_0)/K_0\,, \qquad \Delta_\rho = (\rho_\mathrm{s} - \rho_0)/\rho_0 \tag{2.40}$$

originally introduced by Jerome et al. [144, Eq. (28)] are used, where $K_\mathrm{s} = 1/\beta_\mathrm{s}$ and $K_0 = 1/\beta_0$ are the bulk moduli of the sphere and the background medium, respectively. Equations (2.40) are related to f_1 and f_2 by

$$f_1 = \frac{\Delta_K}{1 + \Delta_K}\,, \qquad f_2 = \frac{\Delta_\rho}{1 + \frac{2}{3}\Delta_\rho}\,, \tag{2.41}$$

which show that the low-contrast condition $|f_1|, |f_2| \ll 1$ is equivalent to $|\Delta_K|, |\Delta_\rho| \ll 1$, for which Eqs. (2.41) become $f_1 \simeq \Delta_K$ and $f_2 \simeq \Delta_\rho$.

The solid black lines in Fig. 2.5 show that neglecting terms of cubic order and higher in the contrast factors leads to error for cases in which the contrast in density is much greater than the contrast in bulk modulus ($\Delta_\rho/\Delta_K \gg 1$). In such cases, Gor'kov's result given by Eq. (2.37) over-predicts the radiation force, e.g., Fig. 2.5(e). In contrast, the polarizability-based formulation given by Eq. (2.36), represented by the dashed red curves, recovers the subwavelength limit of the full solution given by Eq. (2.39) for all combinations of Δ_K and Δ_ρ considered.

The accuracy of the polarizability-based formulation for cases in which the material contrast is large reflects the fact that the Born approximation holds if the scatterer is sufficiently smaller than a wavelength. Similar observations were made by Jerome et al. regarding the Born approximation of radiation forces exerted by standing waves [144, Sec. III], as mentioned in Secs. 2.1 and 2.2. In the present work, the Born approximation holds for sufficiently low values of ka because in the absence of resonance, the smallness of the scatterer with respect to a wavelength guarantees that the magnitude of the scattered field is much weaker than that of the incident field, allowing $\tilde{p}_\mathrm{s}$ to be neglected in Eq. (2.7). Meanwhile, the Born approximation of Jerome et al. is satisfied for low ka because the volume of integration converges to a point as ka tends to zero, and the integral for the radiation force converges to the value of the integrand at that point [144, Sec. II].

Since the integrand given by Eq. (7) of Ref. 144 is derived from the small particle limit of the full solution given by Eq. (2.39), the Born approximation of the radiation force exerted by standing waves converges to the full expression for $ka \ll 1$ regardless of material contrast. More insight into scattering from small perfectly reflective spheres is provided by van de Hulst [23, pp. 158–161].

While the focus of the present work is the study of radiation force in the subwavelength regime, an explanation is owed as to why the high-frequency asymptote of the radiation force on a rigid sphere is $F_z = F_0$, as suggested by the solid blue curve in Fig. 2.5(f). The high-frequency asymptote of the force can be calculated by considering the limit $ka \gg 1$ of the time-averaged scattered intensity from a rigid sphere, given by the second of Morse and Ingard's Eqs. (8.2.3) [122]. From Eq. (B.115), the corresponding magnitude of the squared scattered directivity is

$$|\Phi|^2 = \tfrac{1}{4}a^2 \left[1 + \cot^2(\theta/2) J_1^2(ka\sin\theta)\right], \quad ka \gg 1, \tag{2.42}$$

where J_1 is the cylindrical Bessel function of order 1. Inserting Eq. (2.42) into Westervelt's integral yields

$$F_z = \frac{p_0^2}{2\rho_0 c_0^2}(2\pi a^2 - \pi a^2) = F_0, \quad ka \gg 1, \tag{2.43}$$

where $\oint |\Phi|^2 d\Omega$ is given Morse and Ingard [122, Eqs. (8.2.3)] and $-\oint |\Phi|^2 \mathbf{e}_\mathrm{i} \cdot \mathbf{e}_r \, d\Omega$ is calculated numerically. Equation (2.43) was obtained previously by Marston [182, Eq. (13)], and form functions for $ka = 15$ are shown in Fig. 2 of Ref. 183. An alternative calculation of the same result from the perspective of geometrical acoustics was obtained by Marston et al. [184, App. C] [185, Eq. (4)].

Homogeneous cube

Considered next is the radiation force on a homogeneous cube with volume and material properties that are equal to those of the homogeneous sphere considered above. The side

length of the cube is therefore $b = a(4\pi/3)^{1/3}$. The polarizabilities given by Eqs. (2.27)–(2.29) are evaluated in Cartesian coordinates, where the domain of integration is

$$|x_\mathrm{s}| \leq b/2\,, \qquad |y_\mathrm{s}| \leq b/2\,, \qquad |z_\mathrm{s}| \leq b/2\,, \tag{2.44}$$

yielding

$$\alpha_\mathrm{m} = -b^3 f_1\,, \qquad \alpha_\mathrm{d} = b^3 \frac{3f_2/2}{1 + f_2/2}\,, \tag{2.45}$$

and $\boldsymbol{\alpha}_\mathrm{c} = \mathbf{0}$. Inserting Eqs. (2.45) into $F_\parallel$ given by Eq. (2.31) and writing the result in terms of a again yields Eq. (2.36).

Assessing whether Eq. (2.36) accurately predicts the radiation force on a homogeneous subwavelength cube is challenging because no analytical expressions analogous to Eq. (2.39) are available for cubes [186]. While approximations for the field scattered by a homogeneous cube have been derived using the anomalous diffraction approximation [187, 188], such solutions are restricted to $ka \gg 1$, as described in Sec. 2.2. It is possible, however, to calculate the radiation force in the far field of the Born approximation by inserting Φ given by Eq. (2.11) (which holds for all ka) into Westervelt's integral. Comparing the result with Eq. (2.36) allows for the validity of the subwavelength approximation underlying Eq. (2.36) to be assessed, although the comparison does not account for the error associated with large material contrasts and resonances. Scattering from rigid cubes is discussed in a recent publication by Ospel [189].

Evaluating Eq. (2.11) over the domain given by Eq. (2.44) yields

$$\Phi(\mathbf{k}_\mathrm{s}) = \tfrac{1}{3} k^2 a^3 f(\mathbf{k}_\mathrm{s}) \left(-f_1 + \frac{3f_2/2}{1 + f_2/2} \cos\theta \right), \tag{2.46}$$

$$f(\mathbf{k}_\mathrm{s}) = \prod_{j=1}^{3} \frac{\sin[(k_{\mathrm{s}j} - k_{\mathrm{i}j})b/2]}{(k_{\mathrm{s}j} - k_{\mathrm{i}j})b/2}\,, \tag{2.47}$$

where $j = 1, 2$, and 3, represent x, y, and z, respectively, and where the 3D Fourier transform in Eq. (2.11) has been evaluated using the shifting property [190, Table 1-1, p. 65],

$$\mathcal{F}_\mathrm{3D}\{f(x,y,z)e^{i(\alpha x + \beta y + \gamma z)}\} = F(k_{\mathrm{s}x} - \alpha, k_{\mathrm{s}y} - \beta, k_{\mathrm{s}z} - \gamma)\,. \tag{2.48}$$

Westervelt's integral therefore equals

$$\frac{F_z}{F_0} = \int_0^{2\pi}\int_0^{\pi} |\Phi(\theta,\phi)/a|^2(1-\cos\theta)\sin\theta\, d\theta\, d\phi, \tag{2.49}$$

where Φ is given by Eq. (2.46). Equation (2.49) is evaluated numerically and is plotted as the solid green curves in Fig. 2.5, where it is compared with the polarizability-based force given by Eqs. (2.36) and the full expression of the force on a sphere having the same volume and material properties given by Eq. (2.39).

The coincidence of the dashed red curves representing Eq. (2.36) with the solid green curves representing Eq. (2.49) for $ka \ll 1$ in Fig. 2.5 demonstrates the validity of the subwavelength approximation leading to the polarizabilities given by Eqs. (2.26)–(2.29). The agreement of the solid green curves with the solid blue curves representing the full expression of the force on a sphere of equal volume and material properties shows that "geometric details that are much smaller than the wavelength are unimportant" [7, p. 494], i.e., the edges and corners of the cube that distinguish it from the sphere cannot be resolved for $ka \ll 1$. The agreement of the green and blue curves in Fig. 2.5 also shows that the Born approximation leading to Eq. (2.11) is satisfied if ka is sufficiently small regardless of material contrast, as discussed in Sec. 2.2.

Three-layered sphere

Attention is now turned to radiation forces exerted by plane progressive waves on inhomogeneous objects. A three-layered sphere is considered because such objects have previously been used to model radiation forces exerted by standing waves on eukaryotic cells [11, 178, 191, 192]. The inner, middle, and outer radii are denoted by a'', a', and a, respectively, as shown in Fig. 2.6. The contrast factors f_β and f_ρ are given by f_1'' and f_2'' for $r \le a''$, f_1' and f_2' for $a'' < r \le a'$, and f_1 and f_2 for $a' < r \le a$, respectively, where the numerical values of the parameters are provided in Tables I of Refs. 178 and 192. Evaluating

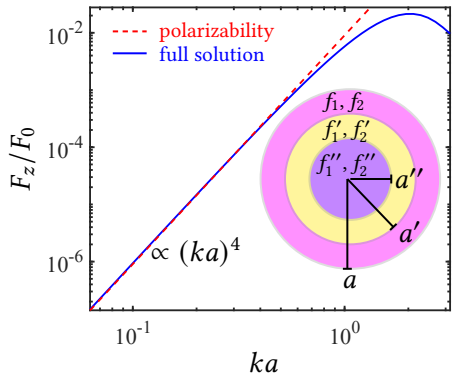

Figure 2.6: Comparison of the polarizability-based formulation given by Eqs. (2.31) in terms of Eqs. (2.50) and (2.51) (dashed red line) and the full expression based on spherical wave expansions [192] (solid blue curve) for the radiation force on a three-layered sphere as a function of ka, where the dimensions and material properties are provided in Table I of Wang et al. [178].

Eqs. (2.27)–(2.29) in this case yields

$$\alpha_{\mathrm{m}} = -\tfrac{4}{3}\pi a^3 \left[f_1'' \chi'' + f_1' (\chi' - \chi'') + f_1 (1 - \chi') \right], \tag{2.50}$$

$$\alpha_{\mathrm{d}} = \tfrac{4}{3}\pi a^3 \left[\frac{3 f_2''/2}{1 + f_2''/2} \chi'' + \frac{3 f_2'/2}{1 + f_2'/2} (\chi' - \chi'') + \frac{3 f_2/2}{1 + f_2/2} (1 - \chi') \right], \tag{2.51}$$

and $\boldsymbol{\alpha}_{\mathrm{c}} = \mathbf{0}$, where $\chi' = (a'/a)^3$ and $\chi'' = (a''/a)^3$ are the volume fractions of the regions enclosed by the middle and inner radii, respectively. Equations (2.50) and (2.51) in combination with Eq. (2.31) for $F_{\parallel}$ yields the Born approximation of the radiation force, which is compared with the full expression given by Eq. (10) of Ref. 192.

Equations (2.31) and the full expression are normalized by Eq. (2.34) for $A_{\parallel} = \pi a^2$ and are compared in Fig. 2.6. The agreement between the polarizability-based formulation and the full expression for $ka \ll 1$ shows that the present formulation accurately predicts forces exerted by progressive waves on subwavelength scatterers with segmented inhomogeneities that satisfy the Born approximation.

An analysis that includes resonance effects of concentric fluid spheres in standing wave fields was provided recently by Marston [170].

Inhomogeneous cube

Finally, an inhomogeneous cube of side length a with material properties given by $f_\beta = -2f_1 x_\mathrm{s}/a$ and $f_\rho = 4f_2(x_\mathrm{s}/a)/(3 - 2f_2 x_\mathrm{s}/a)$ is considered. The material properties are chosen such that Eqs. (2.27)–(2.29) yield $\alpha_\mathrm{m} = \alpha_\mathrm{d} = 0$ but $\boldsymbol{\alpha}_\mathrm{c} \neq \mathbf{0}$, as shown below, allowing for the effect of the coupled polarizability on the radiation force to be studied independently of the monopole and dipole polarizabilities. The radiation force in the direction of the incident wave is calculated for two incident-wave orientations: $\mathbf{e}_\mathrm{i} = \mathbf{e}_z$ and $\mathbf{e}_\mathrm{i} = \mathbf{e}_x$.

Incident wave in z direction The incident wave oriented in the z direction is described by setting $\mathbf{e}_\mathrm{i} = \mathbf{e}_z$, for which Eq. (2.29) in terms of the material properties defined above yields

$$\boldsymbol{\alpha}_\mathrm{c} = \tfrac{1}{6} k a^4 (f_1 + f_2 \cos\theta)\mathbf{e}_x \,, \tag{2.52}$$

Equation (2.52) is inserted into Φ given by Eq. (2.26), which is in turn inserted into Eq. (2.1) for the radiation force in the direction of the incident wave, yielding

$$\frac{F_z}{F_0} = \frac{(ka)^6}{432\pi}\left[f_1^2 + \tfrac{1}{5}(f_2^2 - 2f_1 f_2)\right]. \tag{2.53}$$

As anticipated in Sec. 2.3, $|\boldsymbol{\alpha}_\mathrm{c}|^2$ contributes to the radiation force at $O[(ka)^6]$. Equation (2.53) is compared in Fig. 2.7 with the force predicted in the far field of the Born approximation given by Eq. (2.49), where Φ given by Eq. (2.11) yields

$$\Phi(\mathbf{k}_\mathrm{s}) = \frac{k^2 a^3}{4\pi} f(\mathbf{k}_\mathrm{s})\,(f_1 + f_2\cos\theta)\,, \tag{2.54}$$

$$f(\mathbf{k}_\mathrm{s}) = \left\{\cos[(k_{\mathrm{s}x} - k_{\mathrm{i}x})a/2] - \frac{\sin[(k_{\mathrm{s}x} - k_{\mathrm{i}x})a/2]}{(k_{\mathrm{s}x} - k_{\mathrm{i}x})a/2}\right\} \times \frac{i}{(k_{\mathrm{s}x} - k_{\mathrm{i}x})a/2}\prod_{j=2}^{3}\frac{\sin[(k_{\mathrm{s}j} - k_{\mathrm{i}j})a/2]}{(k_{\mathrm{s}j} - k_{\mathrm{i}j})a/2}, \tag{2.55}$$

where $k_{\mathrm{i}z} = k$ and $k_{\mathrm{i}x} = k_{\mathrm{i}y} = 0$. The contrast factors $f_1 = 0.5$ ($\Delta_K = 1$) and $f_2 = 0.094$ ($\Delta_\rho = 0.1$) are used for the comparison. The agreement for $ka \ll 1$ between the dashed

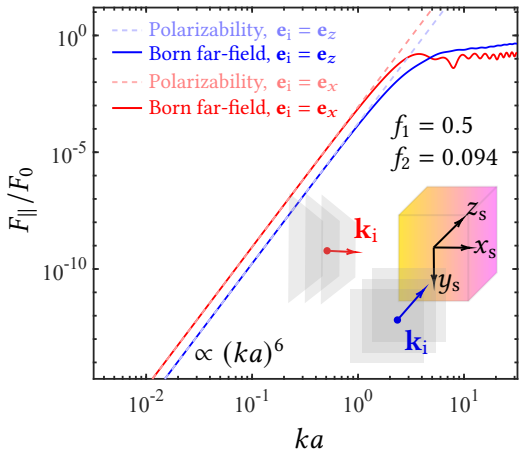

Figure 2.7: Radiation force in the direction of the incident wave as a function of ka on an inhomogeneous cube. The blue and red curves denote the force exerted by an incident wave traveling along the z and x directions, respectively. For incidence along the z axis, the force given by Eq. (2.53) (dashed light blue line) is compared with Eq. (2.49) in terms of Eq. (2.54) (solid dark blue line). For incidence along the x axis, the force given by Eq. (2.57) (dashed light red line) is compared with Eq. (2.58) in terms of Eq. (2.59) (solid dark red line).

light blue lines representing Eq. (2.53) and the solid blue curves representing the numerical evaluation of Eq. (2.49) in terms of Eq. (2.54) demonstrates that the present formulation accurately predicts the radiation force due to progressive waves on a subwavelength object with a continuous and asymmetric distribution of material inhomogeneity.

The fact that $\boldsymbol{\alpha}_c$ given by Eq. (2.52) breaks axisymmetry raises the question of whether the incident wave oriented in the z direction exerts a radiation force on the inhomogeneous cube in either of the transverse directions. To calculate the force in the x direction to dipole order, the directivity Φ given by Eq. (2.26) in terms of (2.52) is inserted into Westervelt's integral for $F_\perp$ given by Eq. (2.32) for $\mathbf{e}_m = \mathbf{e}_x$. Noting that $\mathbf{e}_x \cdot \mathbf{e}_r = \sin\theta \cos\phi$ and evaluating the integral results in zero force. Meanwhile, in the far field of the Born approximation, Φ given by Eq. (2.54) is inserted into Eq. (2.32), yielding a force that is proportional to $(ka)^6$ but is five orders of magnitude weaker than Eq. (2.53) for $ka \ll 1$. Evidently, at the order of the present approximation, radiation forces in transverse directions are due to effects higher than dipole order, which are accounted for in Φ given by Eq. (2.54) but not in Eq. (2.26). The force in the y direction, which is calculated by setting

$\mathbf{e}_y \cdot \mathbf{e}_r = \sin\theta \sin\phi$, vanishes both in the far field of the Born approximation and in its subwavelength limit due to symmetry about the x-z plane.

The prediction by the present formulation of zero transverse radiation forces on asymmetric objects is not surprising given the similar limitation on the Born approximation made by Jerome et al. that the transverse components "are simply not predicted by the model for the prescribed standing wave field" [144]. The fact that the force in the x direction calculated by Eq. (2.32) in terms of Eq. (2.54) is five orders of magnitude weaker than F_z given by Eq. (2.53) is reminiscent of the finding for standing waves that "when the conditions for the validity of the Born approximation are satisfied, the magnitudes of the transverse forces may be presumed small in relation to that of F_z" [144]. Examples beyond the Born approximation of subwavelength spheroids that experience sizable transverse forces are presented in Sec. C.6. The use of "large objects (> 20 wavelengths)" by Zhang and Ma to experimentally generate transverse radiation forces exerted by progressive waves [150] suggests that transverse forces also become more significant beyond the subwavelength limit.

Incident wave in x direction The incident wave is now chosen to be oriented in the direction of $\mathbf{e}_x$, while the orientation of the cube is left unchanged. The coupled polarizability given by Eq. (2.29) therefore becomes

$$\boldsymbol{\alpha}_{\mathrm{c}} = \tfrac{1}{6} ka^4 \left(f_1 + f_2 \sin\theta \cos\phi\right) \mathbf{e}_x \,, \tag{2.56}$$

and Westervelt's integral yields the force in the direction of the incident wave:

$$\frac{F_x}{F_0} = \frac{(ka)^6}{72\pi} \left(f_1^2 - \tfrac{6}{5} f_1 f_2 + \tfrac{7}{15} f_2^2\right) . \tag{2.57}$$

In Fig. 2.7, Eq. (2.57) is shown as the dashed light red line and is compared with the solid red curve, which represents the force predicted in the far field of the Born approximation given by

$$\frac{F_x}{F_0} = \int_0^{2\pi} \int_0^{\pi} |\Phi(\theta,\phi)/a|^2 (1 - \sin\theta\cos\phi) \sin\theta \, d\theta \, d\phi \,, \tag{2.58}$$

where from Eq. (2.11)

$$\Phi(\mathbf{k}_s) = \frac{k^2 a^3}{4\pi} f(\mathbf{k}_s)\,(f_1 + f_2 \sin\theta\cos\phi)\,, \tag{2.59}$$

and where $f(\mathbf{k}_s)$ is given by Eq. (2.55) with $k_{ix} = k$ and $k_{iy} = k_{iz} = 0$.

Comparison of Eqs. (2.53) and (2.57) in Fig. 2.7 reveals that the force aligned with the gradient of the material properties is greater than that perpendicular to the gradient of the material properties by an amount given by the ratio of Eq. (2.57) to Eq. (2.53), which in turn depends not on f_1 and f_2 but on $\Delta = f_1/f_2$:

$$\frac{F_x}{F_z} = 2\frac{\Delta^2 - 6\Delta/5 + 7/15}{\Delta^2/3 + (1 - 2\Delta)/15}\,. \tag{2.60}$$

For the material properties considered in Fig. 2.7, $\Delta = 5.3$ and Eq. (2.60) equals $F_x/F_z = 5.1$. If the cube differs from the background medium only by its density, $\Delta = 0$ and $F_x/F_z = 14$; if the cube differs from the background medium only by its compressibility, then $\Delta = \infty$ and $F_x/F_z = 6$.

Equation (2.60) raises the question of how the ratio depends on the material distribution. For example, consider an inhomogeneous cube of side length a consisting of two halves with material properties $f_\beta = f_1$ and $f_\rho = -2f_2/(3 + f_2)$ for $-a/2 \le x < 0$ and $f_\beta = -f_1$ and $f_\rho = 2f_2/(3 - f_2)$ for $0 \le x \le a/2$. Following the analysis above shows that F_z/F_0 and F_x/F_0 in this case are 9/4 times Eqs. (2.53) and (2.57), respectively. The values of F_z/F_0 and F_x/F_0 are in agreement with the numerical evaluation of Eqs. (2.49) and (2.58) for Φ given by Eqs. (2.54) and (2.59), respectively, where

$$\begin{aligned} f(\mathbf{k}_s) = {} & \{1 - \cos[(k_{sx} - k_{ix})a/2]\} \\ & \times \frac{i}{(k_{sx} - k_{ix})a/2} \prod_{j=2}^{3} \frac{\sin[(k_{sj} - k_{ij})a/2]}{(k_{sj} - k_{ij})a/2}\,. \end{aligned} \tag{2.61}$$

Thus F_x/F_z again results in Eq. (2.60) in the subwavelength limit, showing that such ratios are generally not unique to a given material distribution of a scatterer. A more complete exploration of how F_x/F_z depends on different material distributions may be pursued in the future.

2.5 Summary

Radiation forces exerted by plane progressive acoustic waves on subwavelength scatterers were calculated in terms of acoustic polarizabilities. The Born approximation allowed the monopole and dipole polarizabilities to be expressed as volume integrals over the material contrast factors. For homogeneous objects, the force is on the order of $(ka)^4$, as predicted by Gor'kov for a homogeneous sphere. It was found by comparison with the full expression of radiation force in terms of spherical wave expansions that Gor'kov's result is inaccurate for cases in which the contrast in density is much larger than the contrast in compressibility, whereas the present formulation more accurately predicts the radiation force for all material contrasts considered. For $ka \ll 1$, an identical radiation force is exerted on a homogeneous cube with the same material properties and volume as a homogeneous sphere. Inhomogeneous scatterers with compressibility and density contrast factors that are even functions of position also experience an $O[(ka)^4]$ force.

Material asymmetry was taken into account by extending Rayleigh scattering to $O[(ka)^3]$, leading to a volume integral for the coupled polarizability over the moment of the contrast factors. The coupled polarizability, which depends on both the frequency and direction of the incident wave, vanishes in the static limit and/or in the absence of material asymmetry, in which case the present formulation recovers Rayleigh scattering. Scatterers with odd compressibility and density contrast factors experience a radiation force on the order of $(ka)^6$. By considering an inhomogeneous cube with an asymmetric distribution of material properties, it was shown that material asymmetry leads to anisotropic radiation forces, i.e., forces that depend on the direction of the incident wave (see Sec. 1.1). The preferential direction in which the inhomogeneous cube is forced may find application in particle manipulation for advanced manufacturing [193].

The error associated with the far-field, Born, and subwavelength approximations leading to the integral expressions for the acoustic polarizabilities was also discussed. While the far-field approximation is consistent with Westervelt's integral and introduces no error in the calculation of radiation force, the Born and subwavelength approximations

introduce error when material contrasts are large and when the scatterer is larger than $ka \sim 0.8$. It was demonstrated by comparison with full expression of forces that the Born approximation can be satisfied for $ka \ll 1$ even when material contrasts are large. The interdependence of the Born and subwavelength approximations was discussed in the context of previous works.

The primary advantage of the formulation developed is its simplicity in solving a problem that would be intractable using partial-wave expansions. Potential applications and directions of future study are discussed in Sec. 5.1.

Chapter 3: Electromomentum coupling with magnetism

3.1 Introduction

Metamaterials utilize microscale subwavelength dynamics and mesoscale interactions to achieve macroscale properties that extend beyond those of conventional materials [41]. Figure 3.1 illustrates the relationship between the microscale, mesoscale, and macroscale. Although acoustic metamaterials became a popular research topic in the early 2000s [195], the concept of using subwavelength dynamics to achieve a desired macroscopic effect can be found in ancient and medieval architecture, as described by Atay et al. [196]. Reviews of acoustic metamaterials are provided by Hussein et al. [197], Cummer et al. [198], and Haberman and Guild [21].

The exotic properties of conventional acoustic metamaterials are characterized by the effective compressibility β and density ρ, while those of electromagnetic metama-

A summary of the results obtained in this chapter were published in Ref. 194. The author's contributions include generalizing the homogenization theory of Alù [12] and Sieck et al. [13] to account for piezoelectric heterogeneities, and generalizing the results of Kong et al. [69], Muhlestein et al. [70], and Pernas-Salomón and Shmuel [123] to a medium in which the elastic and electromagnetic constitutive relations are fully coupled.

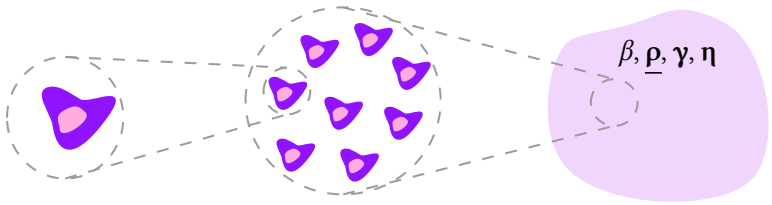

(a) Microscale (b) Mesoscale (c) Macroscale

Figure 3.1: (a) The microscale can be represented by a single representative volume element consisting of a single subwavelength scatterer. (b) The mesoscale considers the interactions of multiple scatterers, where scatterer separation distance is taken into consideration. These interactions yield (c) a macroscopically observable dynamic effective properties, which may differ from those of the constituents.

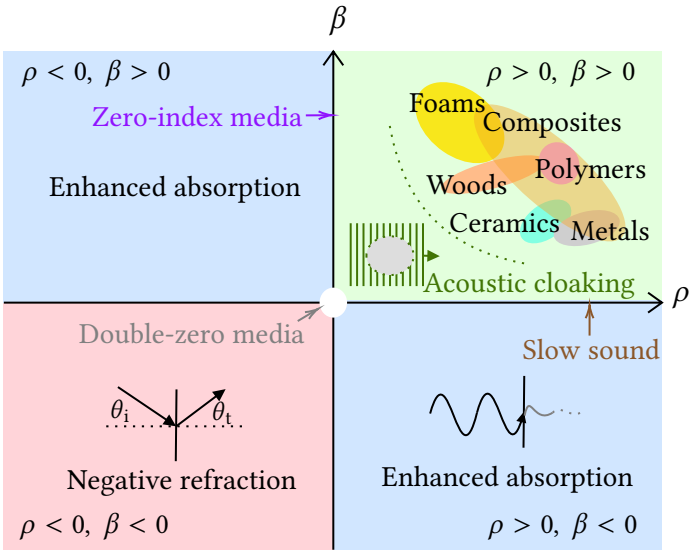

Figure 3.2: Parameter space of acoustic materials, where the density ρ is represented by the horizontal axis and the compressibility β is represented by the vertical axis. Conventional media and acoustic metamaterial cloaks lie in the first quadrant. The other three quadrants are accessible only by metamaterials. Adapted from Refs. 21 and 41.

terials are characterized by the effective permittivity ϵ and permeability μ [199]. The parameter space of acoustic metamaterials is shown graphically in Fig. 3.2; a similar parameter space exists for electromagnetics, for which β and ρ would be replaced by ϵ and μ, respectively. Conventional acoustic materials occupy the first quadrant of the figure, for which β and ρ are both positive. The second and fourth quadrants describe metamaterials in which acoustic waves are evanescent, since the speed of sound $c = 1/\sqrt{\beta\rho}$ is imaginary if β and ρ have different signs. The third quadrant, in which β and ρ are both negative, describes metamaterials in which sound waves propagate, but for which the points of constant phase travel in the opposite direction as the energy [200]. The macroscopic properties in the second, third, and fourth quadrants of Fig. 3.2 can be achieved by exploiting the microscopic dynamics and mesoscale interactions of scatterers that constitute metamaterials [201, 202].

The microscopic properties and structure are related to the dynamic effective macroscale through the process of homogenization, which determines the properties of a metamate-

Isotropic	Anisotropic	Biisotropic	Bianisotropic
$\mathbf{D} = \epsilon\mathbf{E}$ $\mathbf{B} = \mu\mathbf{H}$	$\mathbf{D} = \underline{\boldsymbol{\epsilon}} \cdot \mathbf{E}$ $\mathbf{B} = \underline{\boldsymbol{\mu}} \cdot \mathbf{H}$	$\mathbf{D} = \epsilon\mathbf{E} + \xi\mathbf{H}$ $\mathbf{B} = \zeta\mathbf{E} + \mu\mathbf{H}$	$\mathbf{D} = \underline{\boldsymbol{\epsilon}} \cdot \mathbf{E} + \underline{\boldsymbol{\xi}} \cdot \mathbf{H}$ $\mathbf{B} = \underline{\boldsymbol{\zeta}} \cdot \mathbf{E} + \underline{\boldsymbol{\mu}} \cdot \mathbf{H}$
(a)	(b)	(c)	(d)

Figure 3.3: Electromagnetic constitutive relations, which relate electric displacement $\mathbf{D}$ and magnetic flux density $\mathbf{B}$ to the electric field $\mathbf{E}$ and magnetic field $\mathbf{H}$. (a) Isotropic constitutive relations, (b) anisotropic relations, which give rise to birefringence, (c) biisotropic relations [204], and (d) bianisotropic relations.

rial. Homogenization entails more than a static average of the fields in a medium. Instead, respecting reciprocity and passivity requires that the dynamic macroscale properties be consistent with the effects of microscale dynamics. The dynamic homogenization scheme of Sieck et al. [13] revealed that the effective constitutive relations—the relationships between fields and effective material properties—become coupled and anisotropic at the macroscale due to asymmetries at the microscale and lattice effects at the mesoscale. Such constitutive relations are *bianisotropic* [203], where "bi-" refers to the coupling of two constitutive equations, and "an-" refers to the fact that the material properties are not the same in different directions. The corresponding electromagnetic constitutive relations are shown in Fig. 3.3(d).

The bianisotropic acoustic constitutive relations can be written in the form [13, Eq. (4)]

$$\varepsilon = -\beta p + \boldsymbol{\gamma} \cdot \mathbf{v}, \tag{3.1a}$$

$$\boldsymbol{\mu} = -\eta p + \underline{\boldsymbol{\rho}} \cdot \mathbf{v}, \tag{3.1b}$$

where ε is the volume strain, p is the acoustic pressure, $\boldsymbol{\mu}$ is the linearized momentum density vector, $\underline{\boldsymbol{\rho}}$ is the rank-2 dynamic density tensor, and $\mathbf{v}$ is the velocity. The quantities $\boldsymbol{\eta}$ and $\boldsymbol{\gamma}$ known as the Willis coupling vectors, which are nonzero due to microscale asymmetry and mesoscale lattice effects [13]. The coupling vectors are reductions of the third-order dynamic coupling tensor $\underset{\sim}{\mathbf{S}}$ originally introduced by J. R. Willis in 1981 [42].

Equations (3.1) can be written in the compact form

$$\begin{pmatrix} \varepsilon \\ \boldsymbol{\mu} \end{pmatrix} = \begin{pmatrix} -\beta & \boldsymbol{\gamma} \\ -\boldsymbol{\eta} & \underline{\underline{\rho}} \end{pmatrix} \begin{pmatrix} p \\ \mathbf{v} \end{pmatrix}, \tag{3.2}$$

where the inner products between quantities on the right-hand side are suppressed.[1] For discussions of how Eq. (3.2) is relevant to wave manipulation, see Refs. 45 and 205. The constitutive relations of elastodynamics analogous to Eq. (3.2) are [70, Eqs. (2)]

$$\begin{pmatrix} \underline{\boldsymbol{\varepsilon}} \\ \boldsymbol{\mu} \end{pmatrix} = \begin{pmatrix} \mathbb{M} & \underset{\sim}{\boldsymbol{\gamma}} \\ \underset{\sim}{\boldsymbol{\eta}} & \underline{\underline{\rho}} \end{pmatrix} \begin{pmatrix} \underline{\boldsymbol{\sigma}} \\ \mathbf{v} \end{pmatrix}, \tag{3.3}$$

where $\underline{\boldsymbol{\varepsilon}}$ is the strain tensor, $\underline{\boldsymbol{\sigma}}$ is the stress tensor, and $\mathbb{M}$ is the rank-4 compliance tensor. The Willis coupling quantities in Eq. (3.3) are rank-3 tensors [42, 206, 207],[2] which are related to Willis's tensor $\underline{\underline{\mathbf{S}}}$ by Eqs. (3.60c) and (3.60d). The two minus signs that appear in Eq. (3.2) but not in Eq. (3.3) arise because pressure is positive in terms of the inward normal vector while stress is positive in terms of the outward normal vector.[3] The relationship between Eqs. (3.2) and (3.3) is discussed further in Secs. 3.3 and 3.4.

The electromagnetic bianisotropic constitutive equations relating the electric displacement $\mathbf{D}$ and magnetic flux density $\mathbf{B}$ to the electric field $\mathbf{E}$ and magnetic field $\mathbf{H}$ are [69, Eq. (5)]

$$\begin{pmatrix} \mathbf{D} \\ \mathbf{B} \end{pmatrix} = \begin{pmatrix} \underline{\underline{\boldsymbol{\epsilon}}} & \underline{\underline{\boldsymbol{\xi}}} \\ \underline{\underline{\boldsymbol{\zeta}}} & \underline{\underline{\boldsymbol{\mu}}} \end{pmatrix} \begin{pmatrix} \mathbf{E} \\ \mathbf{H} \end{pmatrix}, \tag{3.4}$$

[1] The use of block matrices to express the bianisotropic constitutive relations is found in earlier literature [203]. The order of the inner product between each quantity on the right-hand side can be deduced by noting that the dth inner product [written $\cdot_{(d)}$] of two quantities of rank n and m (where $n+m \geq 2d$) results in an object of rank $n+m-2d$, i.e., $a_{(n)} \cdot_{(d)} b_{(m)} = c_{(n+m-2d)}$. In a particular basis, the dth inner product denotes summation over d indices of the matrix components.

[2] The inner product rule described in footnote 1 can be used to determine the order d of the inner products in Eq. (3.3). For example, the product relating $\underline{\boldsymbol{\varepsilon}}$ and $\underline{\boldsymbol{\sigma}}$ (both rank-2 tensors) through $\mathbb{M}$ (a rank-4 tensor) corresponds to $n=4$, $m=2$, and $n+m-2d=2$, i.e., $d=2$. Similarly, the equation relating $\underline{\boldsymbol{\varepsilon}}$ and $\mathbf{v}$ through $\underset{\sim}{\boldsymbol{\gamma}}$ corresponds to $n=3$, $m=1$, and $n+m-2d=2$, i.e., $d=1$. The first row of Eq. (3.3) is therefore written as $\underline{\boldsymbol{\varepsilon}} = \mathbb{M} : \underline{\boldsymbol{\sigma}} + \underset{\sim}{\boldsymbol{\gamma}} \cdot \mathbf{v}$.

[3] The pressure field p is used in Sec. 3.2 for ease of recovering the results of Ref. 13, but it is more natural to express the results of Sec. 3.4 in terms of the hydrostatic stress $\sigma_{\text{h}} = -p$; see Eqs. (3.163)–(3.165).

where $\underline{\boldsymbol{\epsilon}}$ and $\underline{\boldsymbol{\mu}}$ are the permittivity and permeability tensors, respectively, and $\underline{\boldsymbol{\zeta}}$ and $\underline{\boldsymbol{\xi}}$ are the electromagnetic bianisotropic tensors. The off-diagonal terms in Eq. (3.4) are analyzed in the context of metamaterials by Alù [12], and a review of bianisotropic metasurfaces is provided by Asadchy [208].

The bianisotropic terms in Eqs. (3.2)–(3.4) are relevant to acoustic, elastodynamic, and electromagnetic metamaterials because all periodic metamaterials experience lattice effects, and because subwavelength heterogeneities are often asymmetric. While acoustic and electromagnetic and metamaterials have been studied as separate entities, the proposition of Pernas-Salomón and Shmuel to design a piezoelectric bianisotropic material conceptualizes a more general class of materials that couples the mechanical and electrical domains [60]. Using an elastodynamic homogenization theory of heterogeneous piezoelectric media, Pernas-Salomón and Shmuel showed in the electrostatic approximation that the momentum-velocity constitutive relation couples to the electric constitutive relation by way of piezoelectricity and elastodynamic bianisotropy [60], as illustrated in Fig. 3.4(a). The coupling of the elastodynamic and electrostatic constitutive equations has been termed *electromomentum coupling*. For acoustic media with electromomentum coupling, Eq. (3.2) generalizes to

$$\begin{pmatrix} \varepsilon \\ \boldsymbol{\mu} \\ \mathbf{D} \end{pmatrix} = \begin{pmatrix} -\beta & \boldsymbol{\gamma} & \mathbf{e} \\ -\boldsymbol{\eta} & \underline{\boldsymbol{\rho}} & \underline{\mathbf{w}} \\ -\mathbf{d} & \underline{\mathbf{v}} & \underline{\boldsymbol{\epsilon}} \end{pmatrix} \begin{pmatrix} p \\ \mathbf{v} \\ \mathbf{E} \end{pmatrix}, \tag{3.5}$$

while Eq. (3.3) for elastodynamic media generalizes to [60]

$$\begin{pmatrix} \underline{\boldsymbol{\varepsilon}} \\ \boldsymbol{\mu} \\ \mathbf{D} \end{pmatrix} = \begin{pmatrix} \mathbb{M} & \underline{\boldsymbol{\gamma}} & \underline{\mathbf{e}} \\ \boldsymbol{\eta} & \underline{\boldsymbol{\rho}} & \underline{\mathbf{w}} \\ \underset{\sim}{\mathbf{d}} & \underline{\mathbf{v}} & \underline{\boldsymbol{\epsilon}} \end{pmatrix} \begin{pmatrix} \underline{\boldsymbol{\sigma}} \\ \mathbf{v} \\ \mathbf{E} \end{pmatrix}. \tag{3.6}$$

In both cases, electromomentum coupling requires an additional five constitutive parameters, where $\underline{\mathbf{v}}$ and $\underline{\mathbf{w}}$ are the rank-2 electromomentum coupling tensors. The conventional symbol $\underline{\mathbf{d}}$ for the rank-3 piezoelectric coupling tensor of the strain-charge form is used in the upper diagonal of Eqs. (3.5) and (3.6) [209, 210], while the symbol $\underline{\mathbf{e}}$ is used in the lower diagonal to maintain generality; physical constraints are invoked in Sec. 3.3

to relate the pairs of constitutive parameters across the main diagonal. Electromomentum coupling has since been studied analytically and numerically for plane elastic waves [62, 64], antiplanar shear waves [65], discrete 1D mass-spring-charge systems [66], and in non-periodic finite media [63]. The bounds due to reciprocity, passivity, and causality on the electromomentum-coupled constitutive relations have also been derived on Eq. (3.6) in the stress-charge form [123], in which $\underline{\boldsymbol{\sigma}}$, $\boldsymbol{\mu}$, and $\mathbf{D}$ appear on the left-hand side of the constitutive relations [210]. Preliminary experiments attempting to measure the electromomentum effect have also been conducted using a water-filled impedance tube with limited success [61]. An accessible introduction to electromomentum coupling is provided by Shmuel [211].

References 60–62, 64, 65, 123 and 66 describe the coupling of mechanical waves and electric fields in the electrostatic regime. The electrostatic approximation is appropriate because the ratio of the electromagnetic and mechanical wavelengths is normally very large, e.g., $O(10^6)$ in air and $O(10^5)$ in water. For a given frequency of electromechanical oscillation, the electric field therefore varies negligibly over the wavelength of the mechanical wave. The electromagnetic wave equation therefore reduces to Laplace's equation of electrostatics in a similar way that the acoustic wave equation reduces in the limit $ka \to 0$ to the Laplace equation of linearized incompressible flow (see Sec. A.1). However, a more precise treatment of electromomentum coupling accounts for the variation in time of the electric field, implicating the magnetic field by Ampère's law [8, Eq. (7.36)]. Consideration of the magnetic field describes piezoelectric and/or piezomagnetic asymmetric heterogeneities simultaneously interacting with acoustic (or elastic) and electromagnetic waves [212], as explored in the microscale analyses of Wallen et al. [67] and Lee et al. [68]. For acoustic waves, including electromagnetic bianisotropy, piezomagnetism, and magnetomomentum coupling generalizes Eq. (3.5) to

$$\begin{pmatrix} \varepsilon \\ \boldsymbol{\mu} \\ \mathbf{D} \\ \mathbf{B} \end{pmatrix} = \begin{pmatrix} -\beta & \boldsymbol{\gamma} & \mathbf{e} & \mathbf{c} \\ -\boldsymbol{\eta} & \underline{\boldsymbol{\rho}} & \underline{\mathbf{w}} & \underline{\mathbf{n}} \\ -\mathbf{d} & \underline{\mathbf{v}} & \underline{\boldsymbol{\epsilon}} & \underline{\boldsymbol{\xi}} \\ -\mathbf{b} & \underline{\mathbf{m}} & \underline{\boldsymbol{\zeta}} & \underline{\boldsymbol{\mu}} \end{pmatrix} \begin{pmatrix} p \\ \mathbf{v} \\ \mathbf{E} \\ \mathbf{H} \end{pmatrix}, \tag{3.7}$$

while for elastic waves, Eq. (3.6) generalizes to

$$\begin{pmatrix} \underline{\boldsymbol{\varepsilon}} \\ \boldsymbol{\mu} \\ \mathbf{D} \\ \mathbf{B} \end{pmatrix} = \begin{pmatrix} \mathbb{M} & \underset{\sim}{\boldsymbol{\gamma}} & \underline{\mathbf{e}} & \underset{\sim}{\mathbf{c}} \\ \underset{\sim}{\boldsymbol{\eta}} & \underline{\boldsymbol{\rho}} & \underline{\mathbf{w}} & \underline{\mathbf{n}} \\ \underset{\sim}{\mathbf{d}} & \underline{\mathbf{v}} & \underline{\boldsymbol{\epsilon}} & \underline{\boldsymbol{\xi}} \\ \underset{\sim}{\mathbf{b}} & \underline{\mathbf{m}} & \underline{\boldsymbol{\zeta}} & \underline{\boldsymbol{\mu}} \end{pmatrix} \begin{pmatrix} \underline{\boldsymbol{\sigma}} \\ \mathbf{v} \\ \mathbf{E} \\ \mathbf{H} \end{pmatrix}, \tag{3.8}$$

where $\mathbf{b}$ and $\mathbf{c}$ are the acoustic piezomagnetic coupling vectors and $\underset{\sim}{\mathbf{b}}$ and $\underset{\sim}{\mathbf{c}}$ are their elastic counterparts. Likewise, $\mathbf{m}$ and $\mathbf{n}$ ($\underset{\sim}{\mathbf{m}}$ and $\underline{\mathbf{n}}$) are the acoustic (elastic) magnetomomentum coupling vectors (tensors). The consideration of the magnetic field is motivated in part by Asadchy et al., who note in the context of metasurfaces that [208]

> ...the results obtained for manipulations of electromagnetic waves can be extended and generalized for finding means to manipulate waves of different nature such as acoustic or elastic waves. Even further, one can think about metasurfaces simultaneously controlling and transforming waves of different nature, which can lead to the creation of multiphysics bianisotropic metasurfaces.

While the observation above was written specifically in regards to metasurfaces, it applies equally to the bulk, i.e. metamaterials. Figure 3.4(b) shows the constitutive couplings when the magnetic field is considered.[4]

The present work explains the origins of electro- and magnetomomentum coupling using a dynamic homogenization theory that extends the work of Alù [12] and Sieck et al. [13] to piezoelectric media. In Sec. 3.2, the fields scattered by a periodic array of piezoelectric heterogeneities are shown to yield macroscopic constitutive relations of the form of Eq. (3.7). In Sec. 3.3, the constraints due to reciprocity and passivity on the macroscopic elasto-electromagnetic constitutive relations given by Eq. (3.8) are derived. The results of Sec. 3.3 are reduced to the acousto-electromagnetic limit in Sec. 3.4 to show that the results of Sec. 3.2 satisfy reciprocity and passivity.

[4]The constitutive relations given by Eqs. (3.5), (3.6), and Fig. 3.4(a) are called *trianisotropic* [120, p. 6], and those given by Eqs. (3.7), (3.8), and Figure 3.4(b) are called *quadranisotropic*.

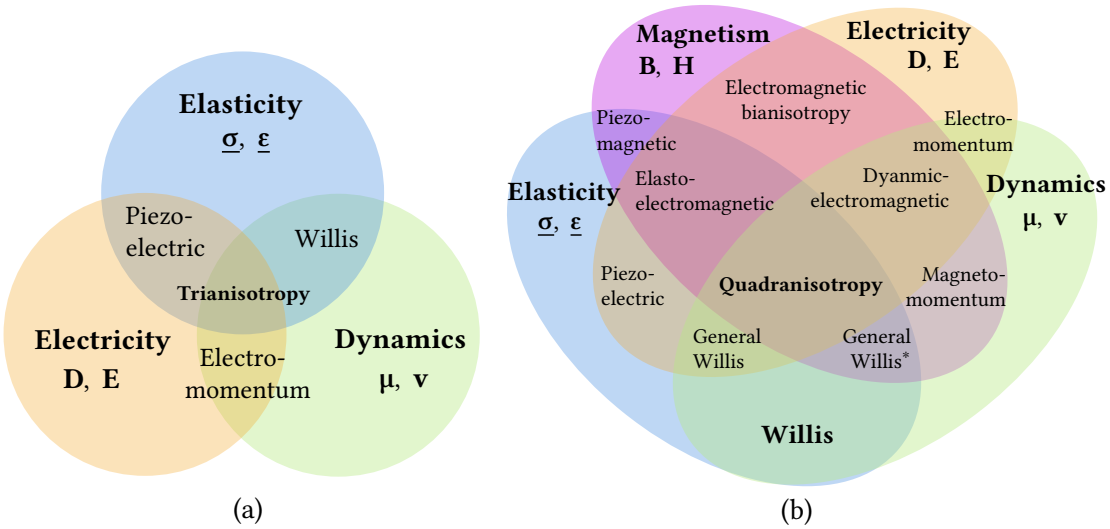

Figure 3.4: (a) Trianisotropic constitutive relations involving piezoelectric, Willis, and electromomentum coupling, as discussed in Refs. 60, 123 and 62. (b) Quadranisotropy involving the magnetic field, as implied by Refs. 67 and 68. *Reference 123 also theorizes the existence of magnetomomentum coupling, in which the electricity in (a) is replaced by magnetism, **D** and **E** are replaced by **B** and **H**, respectively, and piezoelectricity is replaced by piezomagnetism [213, p. 106].

3.2 Homogenization theory

Piezoelectric metamaterials are elastic composites [60], but it is instructive to consider their behavior for one-dimensional compressional wave motion, which is mathematically identical to one-dimensional acoustic wave motion, i.e., zero shear modulus. The reduction of elastodynamics to acoustics simplifies the analysis while retaining insights provided through investigation of the underlying physics [65, 214]. To demonstrate how microscopic asymmetric scattering leads to macroscopic coupling between the mechanical and electromagnetic fields, a dynamic homogenization is performed on a periodic array of identical, passive, and reciprocal piezoelectric scatterers suspended in a fluid. The present section results in constitutive relations of the form of Eqs. (3.7).

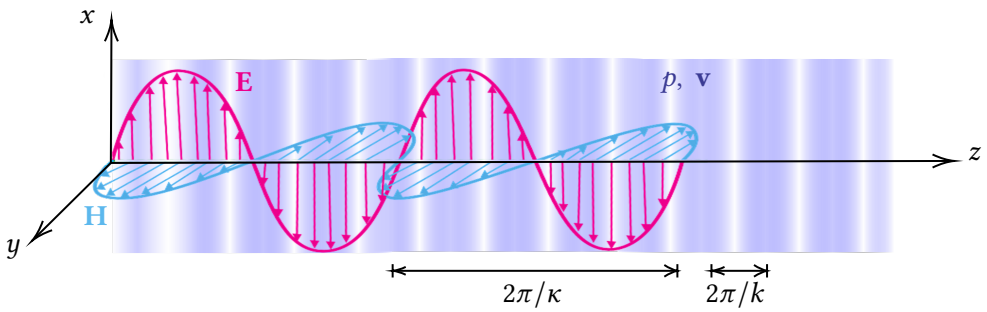

Figure 3.5: The incident acoustic and electromagnetic progressive wave fields given by Eqs. (3.9) displayed at an instant in time. The fields propagate in an isotropic background medium with properties β_0, ρ_0, ϵ_0, and μ_0 and obey the governing Eq. (3.10).

External fields

Begin by considering plane progressive acoustic and electromagnetic waves propagating in the z direction in a homogeneous fluid, depicted schematically in Fig. 3.5. The acoustic pressure and fluid velocity are given by the real parts of

$$p(z,t) = p_{\text{ext}} e^{i(kz-\omega t)}\,, \tag{3.9a}$$

$$\mathbf{v}(z,t) = v_{\text{ext}} e^{i(kz-\omega t)} \mathbf{e}_z\,, \tag{3.9b}$$

respectively, where k is the acoustic wavenumber and ω is the frequency of oscillation. The electric and magnetic fields are given by the real parts of

$$\mathbf{E}(z,t) = E_{\text{ext}} e^{i(\kappa z-\omega t)} \mathbf{e}_x\,, \tag{3.9c}$$

$$\mathbf{H}(z,t) = H_{\text{ext}} e^{i(\kappa z-\omega t)} \mathbf{e}_y\,, \tag{3.9d}$$

respectively, where κ is the electromagnetic wavenumber and $\mathbf{e}_x$, $\mathbf{e}_y$, and $\mathbf{e}_z$ are the Cartesian unit vectors.[5]

[5]Since the present work focuses on coupled linear fields, it is most convenient to consider the case in which the electromagnetic and acoustic frequencies are equal. Suppose the acoustic wave oscillates at angular frequency ω and the electromagnetic wave oscillates at $\omega' \neq \omega$. The acoustic and electromagnetic response will then occur at both ω and ω'. Since the system is linear, the total response is simply the superposition of the responses at ω and ω'. It therefore suffices to consider the dynamics at a single angular frequency ω.

The acoustic waves are governed by the conservation of momentum and conservation of mass [13, Eqs. (10)], given by

$$\boldsymbol{\nabla} p + \rho_0 \frac{\partial \mathbf{v}}{\partial t} = \mathbf{f}_{\text{ext}}\,, \tag{3.10a}$$

$$\boldsymbol{\nabla} \cdot \mathbf{v} + \beta_0 \frac{\partial p}{\partial t} = q_{\text{ext}}\,, \tag{3.10b}$$

respectively, where ρ_0 is the ambient density and β_0 is the background compressibility, as in Chap. 2. The force density $\mathbf{f}_{\text{ext}}$ in Eq. (3.10a) corresponds to a dipole source defined by Eq. (C.45), and the volume velocity density q_{ext} in Eq. (3.10b) corresponds to a monopole source defined by Eq. (C.44). Meanwhile, the electromagnetic waves are governed by Faraday's law and Ampère's law, given by

$$\boldsymbol{\nabla} \times \mathbf{E} + \mu_0 \frac{\partial \mathbf{H}}{\partial t} = -\mathbf{K}_{\text{ext}}\,, \tag{3.10c}$$

$$\boldsymbol{\nabla} \times \mathbf{H} - \epsilon_0 \frac{\partial \mathbf{E}}{\partial t} = \mathbf{J}_{\text{ext}}\,, \tag{3.10d}$$

respectively, where μ_0 is the permeability and ϵ_0 is the permittivity of the background medium. The source term $\mathbf{K}_{\text{ext}}$ in Eq. (3.10c) corresponds to an electric current density, and $\mathbf{J}_{\text{ext}}$ in Eqs. (3.10d) corresponds to a magnetic current density [12, Eqs. (1)]. Inserting Eqs. (3.9a) and (3.9b) into Eqs. (3.10a) and (3.10b) yields [13, Eqs. (10)]

$$ikp_{\text{ext}} = i\omega\rho_0 v_{\text{ext}} + f_{\text{ext}}\,, \tag{3.11a}$$

$$ikv_{\text{ext}} = i\omega\beta_0 p_{\text{ext}} + q_{\text{ext}}\,, \tag{3.11b}$$

where the vector notation and common factor of $e^{i(kz-\omega t)}$ have been suppressed in Eqs. (3.11a) and (3.11b). Similarly, inserting and Eqs. (3.9c) and (3.9d) into Eqs. (3.10c) and (3.10d) yields [12, Eqs. (2)]

$$i\kappa E_{\text{ext}} = i\omega\mu_0 H_{\text{ext}} - K_{\text{ext}}\,, \tag{3.11c}$$

$$i\kappa H_{\text{ext}} = i\omega\epsilon_0 E_{\text{ext}} - J_{\text{ext}}\,. \tag{3.11d}$$

The external fields described by Eqs. (3.11) will be combined with the effective fields derived below to describe the electroacoustic response of the effective medium.

Total and effective fields

In the presence of scatterers, the total acoustic fields equal the sum of the external and scattered acoustic fields [13, Fig. 3]:[6]

$$p(z) = p_{\text{ext}} e^{ikz} + p_{\text{s}}(z)\,, \tag{3.12a}$$

$$v(z) = v_{\text{ext}} e^{ikz} + v_{\text{s}}(z)\,. \tag{3.12b}$$

Similarly, the total electromagnetic fields equal

$$E(z) = E_{\text{ext}} e^{i\kappa z} + E_{\text{s}}(z)\,, \tag{3.12c}$$

$$H(z) = H_{\text{ext}} e^{i\kappa z} + H_{\text{s}}(z)\,. \tag{3.12d}$$

The notation introduced in Eq. (A.3), which is used in Chaps. 2 and 4 to distinguish real-valued solutions of the wave equation from complex-valued solutions of the Helmholtz equation, is suppressed in Eqs. (3.12) to conform to the notation of Refs. 12 and 13.

In the subwavelength limit, the scattered fields are described in terms of the lowest-order terms of the multipole expansion, as described for acoustic fields in Sec. C.5. The scattered acoustic monopole and dipole per unit volume are

$$\bar{m}(z) = -[\beta(z) - \beta_0] p(z)\,, \tag{3.13a}$$

$$\bar{d}(z) = [\rho(z) - \rho_0] u(z)\,, \tag{3.13b}$$

and the scattered electric and magnetic dipoles per unit volume are

$$\bar{P}(z) = -[\epsilon(z) - \epsilon_0] E(z)\,, \tag{3.13c}$$

$$\bar{M}(z) = [\mu(z) - \mu_0] H(z)\,, \tag{3.13d}$$

respectively. Combining Eqs. (3.10a) and (3.10b) with Eqs. (3.13a) and (3.13b) shows that the total acoustic fields satisfy [13, Eq. (11)]

$$\frac{dp(z)}{dz} = i\omega\rho_0 v(z) + i\omega\bar{d}(z) + f_{\text{ext}} e^{ikz}\,, \tag{3.14a}$$

$$\frac{dv(z)}{dz} = i\omega\beta_0 p(z) - i\omega\bar{m}(z) + q_{\text{ext}} e^{ikz}\,, \tag{3.14b}$$

[6] Equation (3.12a) is simply the one-dimensional version of Eq. (2.6) for an incident plane wave.

while combining Eqs. (3.10c) and (3.10d) with Eqs. (3.13c) and (3.13d) shows that the total electromagnetic fields satisfy [12, Eq. (3)]

$$\frac{dE(z)}{dz} = i\omega\mu_0 H(z) + i\omega\bar{M}(z) - K_{\text{ext}} e^{i\kappa z}\,, \tag{3.14c}$$

$$\frac{dH(z)}{dz} = i\omega\epsilon_0 E(z) + i\omega\bar{P}(z) - J_{\text{ext}} e^{i\kappa z}\,. \tag{3.14d}$$

Sieck et al. [13, Eq. (11)] note that continuous source distributions allow the macroscopic acoustic field amplitudes of a representative volume element to be determined uniquely by

$$ikp_{\text{eff}} = i\omega(\rho_0 v_{\text{eff}} + d_{\text{eff}}) + f_{\text{ext}}\,, \tag{3.15a}$$

$$ikv_{\text{eff}} = i\omega(\beta_0 p_{\text{eff}} - m_{\text{eff}}) + q_{\text{ext}}\,, \tag{3.15b}$$

where m_{eff} and d_{eff} are the effective acoustic monopole strength and dipole moment per volume, respectively. The electromagnetic counterparts of Eqs. (3.15a) and (3.15b) are

$$i\kappa E_{\text{eff}} = i\omega(\mu_0 H_{\text{eff}} + M_{\text{eff}}) - K_{\text{ext}}\,, \tag{3.15c}$$

$$i\kappa H_{\text{eff}} = i\omega(\epsilon_0 E_{\text{eff}} + P_{\text{eff}}) - J_{\text{ext}}\,, \tag{3.15d}$$

where P_{eff} and M_{eff} are the effective electric and magnetic dipole moments per volume, respectively. Meanwhile, the conventional governing equations for space- and time-harmonic acoustic fields are given by Eqs. (8) and (9) of Ref. 13:[7]

$$ikp = i\omega\mu_z + f\,, \tag{3.16a}$$

$$ikv = -i\omega\varepsilon + q\,. \tag{3.16b}$$

The analogous electromagnetic governing equations are given by Eqs. (10) of Ref. 12:

$$i\kappa E = i\omega B - K\,, \tag{3.16c}$$

$$i\kappa H = i\omega D - J\,. \tag{3.16d}$$

[7] The z component of the momentum density vector $\boldsymbol{\mu}$ is denoted μ_z to distinguish the quantity from the permeability.

Comparing Eqs. (3.15a) and (3.15b) to Eqs. (3.16a) and (3.16b) identifies the effective volume strain and momentum density [13, Eqs. (13)]:

$$\varepsilon_{\text{eff}} = -\beta_0 p_{\text{eff}} + m_{\text{eff}}\,, \tag{3.17a}$$

$$\mu_{z,\text{eff}} = \rho_0 v_{\text{eff}} + d_{\text{eff}}\,. \tag{3.17b}$$

Similarly, comparing Eqs. (3.15c) and (3.15d) to Eqs. (3.16c) and (3.16d) identifies the effective electric displacement and magnetic displacement [12, Eqs. (12)]:

$$D_{\text{eff}} = \epsilon_0 E_{\text{eff}} + P_{\text{eff}}\,, \tag{3.17c}$$

$$B_{\text{eff}} = \mu_0 H_{\text{eff}} + M_{\text{eff}}\,. \tag{3.17d}$$

The effective monopole strength and dipole moments in Eqs. (3.19) function as "sources" that arise due to the existence of acoustic and electromagnetic scatterers in the medium. Equations (3.17) are used in the final step of the homogenization procedure.

In order to describe the response of an effective medium, the effective fields must be expressed in terms of the external fields and the effective monopole and dipole terms. Denoting the sound speed $c_0 = 1/\sqrt{\beta_0\rho_0} = \omega/k_0$ and combining the external acoustic fields given by Eqs. (3.11a) and (3.11b) with the effective acoustic fields given by Eqs. (3.15a) and (3.15b) yields [13, Eqs. (14) and (15)]

$$p_{\text{eff}} = p_{\text{ext}} + \frac{1}{1-k_0^2/k^2}\left(-\frac{k_0^2}{k^2}\beta_0^{-1} m_{\text{eff}} + \frac{k_0}{k} c_0 d_{\text{eff}}\right), \tag{3.18a}$$

$$v_{\text{eff}} = v_{\text{ext}} + \frac{1}{1-k_0^2/k^2}\left(-\frac{k_0}{k} c_0 m_{\text{eff}} + \frac{k_0^2}{k^2}\rho_0^{-1} d_{\text{eff}}\right). \tag{3.18b}$$

Similarly, denoting the electromagnetic wave speed $C_0 = 1/\sqrt{\epsilon_0\mu_0} = \omega/\kappa_0$ and combining the external electromagnetic fields given by Eqs. (3.11c) and (3.11d) with the effective electromagnetic fields given by Eqs. (3.15c) and (3.15d) yields

$$E_{\text{eff}} = E_{\text{ext}} + \frac{1}{1-\kappa_0^2/\kappa^2}\left(\frac{\kappa_0^2}{\kappa^2}\epsilon_0^{-1} P_{\text{eff}} + \frac{\kappa_0}{\kappa} C_0 M_{\text{eff}}\right), \tag{3.18c}$$

$$H_{\text{eff}} = H_{\text{ext}} + \frac{1}{1-\kappa_0^2/\kappa^2}\left(\frac{\kappa_0}{\kappa} C_0 P_{\text{eff}} + \frac{\kappa_0^2}{\kappa^2}\mu_0^{-1} M_{\text{eff}}\right). \tag{3.18d}$$

The dipole and monopole terms in Eqs. (3.18a) and (3.18b), respectively, are odd in k, while the magnetic and electric dipole terms in Eqs. (3.18c) and (3.18d), respectively, are odd in κ, the significance of which is explained on p. 67. In the static limit $k \to 0$ and $\kappa \to 0$, Eqs. (3.18) reduce to [12, Eq. (11)]

$$p_{\text{eff}} \to p_{\text{ext}} + \frac{1}{\beta_0} m_{\text{eff}}\,, \qquad v_{\text{eff}} \to v_{\text{ext}} - \frac{1}{\rho_0} d_{\text{eff}}\,, \tag{3.19a}$$

$$E_{\text{eff}} \to E_{\text{ext}} - \frac{1}{\epsilon_0} P_{\text{eff}}\,, \qquad H_{\text{eff}} \to H_{\text{ext}} - \frac{1}{\mu_0} M_{\text{eff}}\,. \tag{3.19b}$$

Equations (3.19) show that only in the static limit (represented by the left-hand side of Fig. 1.1) are p_{eff}, v_{eff}, E_{eff}, and H_{eff} purely functions of the acoustic monopole strength density, acoustic dipole moment density, electric dipole moment density, and magnetic dipole moment density, respectively. Equations (3.18) reflect the fact that "an inherent form of [bianisotropy] at the unit cell level[8] stems from weak spatial dispersion effects when $[k, \kappa \neq 0]$, associated with finite phase velocity across each unit cell" [12].

Single scattering

In order to calculate the effective monopole strength and effective dipole moments that appear in Eq. (3.18) for the entire heterogeneous medium, the scattering due to a single asymmetric piezoelectric heterogeneity of length l is first considered. The heterogeneity is assumed to be inhomogeneous in the direction of wave propagation (the z direction) but homogeneous in the transverse (x-y) plane, as illustrated in Fig. 3.6. It is assumed that the heterogeneity is reciprocal, passive, and much smaller than a wavelength, i.e., $k_0 l \ll 1$ and $\kappa_0 l \ll 1$, where $k_0 = \omega\sqrt{\rho_0 \beta_0}$ and $\kappa_0 = \omega\sqrt{\mu_0 \epsilon_0}$. The subwavelength approximation allows the scattered field to be described by the leading order multipole scattering moments, namely the monopole and dipole moments m_n, d_n, P_n, and M_n, where n is an index that specifies the heterogeneity. The index $n = 0$ corresponds to the position $z = 0$, where the monopole strength m_0 and the dipole moments d_0, P_0, and M_0 are linearly related to the local fields by a generalized polarizability equation discussed below.

[8] i.e., dependence of the pressure on the dipole, velocity on the monopole, electric field on the magnetic

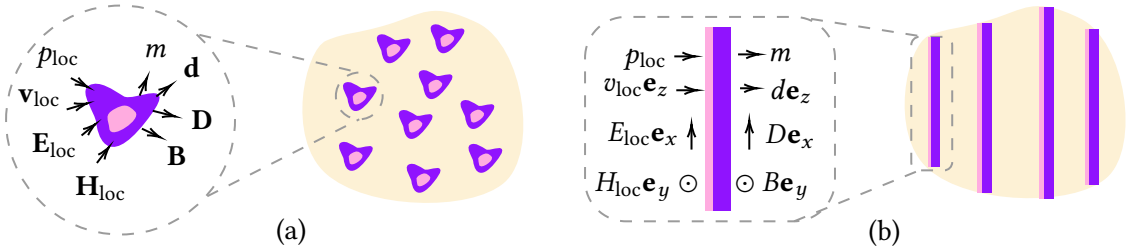

Figure 3.6: (a) The general scattering problem described by Refs. 67 and 68. (b) The reduction to plane acoustic and electromagnetic waves in Cartesian coordinates.

Several conventions for polarizability are used in the literature [56, 67, 68, 214], as discussed in the context of acoustics in Sec. C.7. In the present work, the polarizability equation is expressed such that each polarizability has units of volume, consistent with the polarizabilities used in Chap. 2 and Ref. 13.[9] In particular, the system of equations formed by Eqs. (2.20) and (2.21) is reduced to one-dimensional wave propagation and is expanded to include coupling terms associated with electromagnetism, piezoelectricity, and electromomentum coupling:[10]

$$\begin{bmatrix} m_0 \\ d_0 \\ P_0 \\ M_0 \end{bmatrix} = \begin{bmatrix} -\beta_0\alpha_{pp} & -i(\rho_0\beta_0)^{1/2}\alpha_{pv} & (\beta_0\epsilon_0)^{1/2}\alpha_{pE} & 0 \\ -i(\rho_0\beta_0)^{1/2}\alpha_{pv} & \rho_0\alpha_{vv} & -i(\rho_0\epsilon_0)^{1/2}\alpha_{vE} & 0 \\ -(\beta_0\epsilon_0)^{1/2}\alpha_{pE} & i(\rho_0\epsilon_0)^{1/2}\alpha_{vE} & \epsilon_0\alpha_{EE} & 0 \\ 0 & 0 & 0 & \mu_0\alpha_{HH} \end{bmatrix} \begin{bmatrix} p_{\text{loc}} \\ v_{\text{loc}} \\ E_{\text{loc}} \\ H_{\text{loc}} \end{bmatrix}. \tag{3.20}$$

The minus signs in Eq. (3.20) are due to the local pressure field p_{loc} being positive for compressions, and factors of i are included to account for effects that are related to local acceleration.[11] The combined factors of β_0, ρ_0, ϵ_0, and μ_0 are included so that the polarizabilities have units of volume and were determined using dimensional analysis. While Eq. (3.20) describes piezoelectric scatterers that are asymmetric with respect to their acoustic and piezoelectric properties, it is assumed that the scatterers are not piezomagnetic ($\alpha_{pH} = 0$), precluding the existence of local magnetomomentum coupling ($\alpha_{vH} = 0$).

dipole moment, and magnetic field on the electric dipole moment

[9] The electromagnetic polarizabilities of Ref. 12 also have units of volume. It is incorrectly stated below Eq. (16) of Ref. 12 that the polarizabilities have units of inverse volume.

[10] The polarizabilities of the present chapter are not restricted by the Born approximation, like those of Chap. 2.

[11] See the discussion on p. 31 for more discussion of the physical significance of the factor of i.

It is also assumed that the scatterers are electromagnetically symmetric ($\alpha_{EH} = 0$). The simplifications $\alpha_{pH} = \alpha_{vH} = \alpha_{EH} = 0$ are made to restrict attention to the types of scatterers introduced in Ref. 60. The simplifications also illustrate that the effective dynamic properties on the macroscale demonstrate full coupling of the form of Eq. (3.7) despite the fact that magnetic field coupling is absent in the scatterers. While nonzero values of α_{pH}, α_{vH}, and α_{EH} could be introduced to the present formulation, the chosen form of Eq. (3.20) has the additional benefit of simplifying the following algebra while retaining the physical effects relevant to describing electromomentum coupling and emergent magnetomomentum coupling.

In order to describe the fields scattered by a collection of heterogeneities, it is first necessary to invert Eq. (3.20) so that the local fields can be expressed in terms of the acoustic monopole strength and acoustic and electromagnetic dipole moments. The inverse of Eq. (3.20) can be written in the compact form

$$\begin{bmatrix} p_{\mathrm{loc}} \\ v_{\mathrm{loc}} \\ E_{\mathrm{loc}} \\ H_{\mathrm{loc}} \end{bmatrix} = \begin{bmatrix} -\beta_0^{-1}\tilde{\alpha}_{pp} & -i(\rho_0\beta_0)^{-1/2}\tilde{\alpha}_{pv} & (\beta_0\epsilon_0)^{-1/2}\tilde{\alpha}_{pE} & 0 \\ -i(\rho_0\beta_0)^{-1/2}\tilde{\alpha}_{pv} & \rho_0^{-1}\tilde{\alpha}_{vv} & -i(\rho_0\epsilon_0)^{-1/2}\tilde{\alpha}_{vE} & 0 \\ -(\beta_0\epsilon_0)^{-1/2}\tilde{\alpha}_{pE} & i(\rho_0\epsilon_0)^{-1/2}\tilde{\alpha}_{vE} & \epsilon_0^{-1}\tilde{\alpha}_{EE} & 0 \\ 0 & 0 & 0 & \mu_0^{-1}\tilde{\alpha}_{HH} \end{bmatrix} \begin{bmatrix} m_0 \\ d_0 \\ P_0 \\ M_0 \end{bmatrix}, \tag{3.21}$$

where the newly-defined *complementary polarizabilities* have dimensions of inverse volume. The complementary polarizabilities along the main diagonal of Eq. (3.21) are

$$\tilde{\alpha}_{pp} = -\Delta(\alpha_{EE}\alpha_{vv} - \alpha_{vE}^2), \quad \tilde{\alpha}_{vv} = \Delta(\alpha_{pE}^2 - \alpha_{EE}\alpha_{pp}), \quad \tilde{\alpha}_{EE} = \Delta(\alpha_{pv}^2 - \alpha_{pp}\alpha_{vv}), \tag{3.22a}$$

$$\tilde{\alpha}_{HH} = \Delta\alpha_{HH}^{-1}(\alpha_{EE}\alpha_{pv}^2 + 2\alpha_{pE}\alpha_{pv}\alpha_{vE} + \alpha_{pp}\alpha_{vE}^2 + \alpha_{pE}^2\alpha_{vv} - \alpha_{EE}\alpha_{pp}\alpha_{vv}), \tag{3.22b}$$

and the off-diagonal complementary polarizabilities are

$$\tilde{\alpha}_{pv} = -\Delta(\alpha_{pE}\alpha_{vE} + \alpha_{EE}\alpha_{pv}), \quad \tilde{\alpha}_{pE} = -\Delta(\alpha_{pv}\alpha_{vE} + \alpha_{pE}\alpha_{vv}), \quad \tilde{\alpha}_{vE} = \Delta(\alpha_{pE}\alpha_{pv} + \alpha_{pp}\alpha_{vE}), \tag{3.22c}$$

where

$$\Delta = (\alpha_{EE}\alpha_{pv}^2 + 2\alpha_{pE}\alpha_{pv}\alpha_{vE} + \alpha_{pp}\alpha_{vE}^2 + \alpha_{pE}^2\alpha_{vv} - \alpha_{EE}\alpha_{pp}\alpha_{vv})^{-1}. \tag{3.22d}$$

The 4×4 matrix in Eq. (3.21) relates the fields incident on a single heterogeneity to the scattered monopole strength and dipole moments, facilitating the calculation of the fields scattered by multiple heterogeneities.

Multiple scattering

The fields scattered by a collection of identically oriented and equally spaced heterogeneities are described using the one-dimensional Green's function of the Helmholtz equation derived in Sec. C.1 [see Eq. (C.12)],

$$g_{\mathrm{ac}}(z|z_n) = \frac{i}{2k_0 A} e^{ik_0|z-z_n|}, \qquad g_{\mathrm{em}}(z|z_n) = \frac{i}{2\kappa_0 A} e^{i\kappa_0|z-z_n|}, \tag{3.23}$$

where the factors of cross-sectional area A in the denominators of Eqs. (3.23) arise from applying the one-dimensional Green's function to three-dimensional plane waves. The acoustic fields at point z_m scattered by a heterogeneity at point z_n are then related to the monopole and dipole fields at the scatterer via the expressions

$$p_{\mathrm{s}}(z_m) = -\beta_0^{-1} G_{\mathrm{ac}}^{mn} m_n + c_0 G_{\mathrm{ac}}^{mn} d_n, \tag{3.24a}$$

$$v_{\mathrm{s}}(z_m) = -c_0 G_{\mathrm{ac}}^{mn} m_n + \rho_0^{-1} G_{\mathrm{ac}}^{mn} d_n, \tag{3.24b}$$

where it is noted that Eq. (3.24a) [which follows from Eq. (C.47)] is the reduction of Eq. (2.19) to one-dimensional acoustic wave propagation. The scattered electromagnetic fields are

$$E_{\mathrm{s}}(z_m) = \epsilon_0^{-1} G_{\mathrm{em}}^{mn} P_n + C_0 G_{\mathrm{em}}^{mn} M_n, \tag{3.24c}$$

$$H_{\mathrm{s}}(z_m) = C_0 G_{\mathrm{em}}^{mn} P_n + \mu_0^{-1} G_{\mathrm{em}}^{mn} M_n, \tag{3.24d}$$

where the use of scalar diffraction theory is justified because the components of the electric and magnetic fields satisfy scalar-valued Helmholtz equations for one-dimensional wave motion. The modified acoustic and electromagnetic Green's functions in Eqs. (3.24) are [13, Eq. (20)]

$$G_{\mathrm{ac}}^{mn} = k_0^2 g_{\mathrm{ac}}(z_m|z_n) = G_{\mathrm{ac}}^{nm}, \qquad G_{\mathrm{em}}^{mn} = \kappa_0^2 g_{\mathrm{em}}(z_m|z_n) = G_{\mathrm{em}}^{nm}. \tag{3.25}$$

The acoustic pressure and velocity local to each heterogeneity [see Eq. (3.21)] can then be expressed as the summation of the incident acoustic fields p_{ext} and v_{ext} and the fields

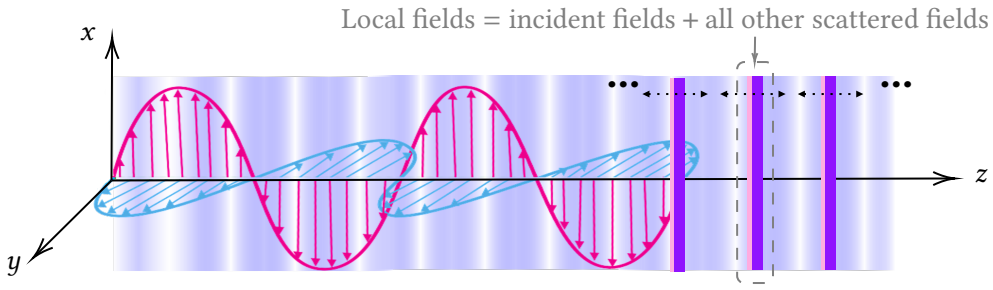

Figure 3.7: The fields that are local to each heterogeneity are the sum of the incident fields and the scattered fields.

p_s and v_s, which represent the acoustic fields scattered by all other heterogeneities, as depicted in Fig. 3.7 [13, Eq. (21)]:

$$p_{\text{loc}} = p_{\text{ext}} + \sum_{n\neq 0} \left(-\beta_0^{-1} G_{\text{ac}}^{0n} m_n + c_0 G_{\text{ac}}^{0n} d_n \right), \tag{3.26a}$$

$$v_{\text{loc}} = v_{\text{ext}} + \sum_{n\neq 0} \left(-c_0 G_{\text{ac}}^{0n} m_n + \rho_0^{-1} G_{\text{ac}}^{0n} d_n \right). \tag{3.26b}$$

Likewise, the local electromagnetic fields equal the sum of the incident electric and magnetic fields E_{ext} and H_{ext} and the scattered electric and magnetic fields E_s and H_s:

$$E_{\text{loc}} = E_{\text{ext}} + \sum_{n\neq 0} \left(\epsilon_0^{-1} G_{\text{em}}^{0n} P_n + C_0 G_{\text{em}}^{0n} M_n \right), \tag{3.26c}$$

$$H_{\text{loc}} = H_{\text{ext}} + \sum_{n\neq 0} \left(C_0 G_{\text{em}}^{0n} P_n + \mu_0^{-1} G_{\text{em}}^{0n} M_n \right). \tag{3.26d}$$

Equations (3.26) represents a form of the multiple scattering problem that can be used for arbitrary arrangements of scatterers, including random placement and finite collections of scatterers, as considered elsewhere [14, 215]. Assuming that the heterogeneities are spaced periodically facilitates the evaluation of the summations in Eqs. (3.26) using lattice sums representing the convergent infinite series of the Green's functions [216, 217]. Periodicity is introduced by the Floquet condition $m_n = m_0 e^{ikz_n}$, $d_n = d_0 e^{ikz_n}$, $P_n = P_0 e^{ikz_n}$, and $M_n = M_0 e^{ikz_n}$, for which Eqs. (3.26a) and (3.26b) become [13, Eq. (22)]

$$p_{\text{loc}} = p_{\text{ext}} - \beta_0^{-1} S_{\text{ac}} m_0 + c_0 S_{\text{ac}} d_0, \tag{3.27a}$$

$$u_{\text{loc}} = u_{\text{ext}} - c_0 S_{\text{ac}} m_0 + \rho_0^{-1} S_{\text{ac}} d_0 \tag{3.27b}$$

and Eqs. (3.26c) and (3.26d) become

$$E_{\mathrm{loc}} = E_{\mathrm{ext}} + \epsilon_0^{-1} S_{\mathrm{em}} P_0 + C_0 S_{\mathrm{em}} M_0 \,, \tag{3.27c}$$

$$H_{\mathrm{loc}} = H_{\mathrm{ext}} + C_0 S_{\mathrm{em}} P_0 + \mu_0^{-1} S_{\mathrm{em}} M_0 \,, \tag{3.27d}$$

where

$$S_{\mathrm{ac}} = \sum_{n\neq 0} e^{ikz_n} G_{\mathrm{ac}}^{0n} \,, \qquad S_{\mathrm{em}} = \sum_{n\neq 0} e^{i\kappa z_n} G_{\mathrm{em}}^{0n} \tag{3.28}$$

are the *interaction coefficients*, which have units of inverse volume.

Macroscopic fields

The local fields are now eliminated by combining Eqs. (3.21) and (3.27). The incident field amplitudes can then be expressed in terms of the background material properties, the complementary polarizabilities, the lattice sums, and the single-scatterer monopole strength and dipole moments:

$$p_{\mathrm{ext}} = -\beta_0^{-1}(\tilde{\alpha}_{pp} - S_{\mathrm{ac}}) m_0 + c_0(-i\tilde{\alpha}_{pv} - S_{\mathrm{ac}}) d_0 + (\beta_0\epsilon_0)^{-1/2}\tilde{\alpha}_{pE} P_0 \,, \tag{3.29a}$$

$$v_{\mathrm{ext}} = -c_0(i\tilde{\alpha}_{pv} - S_{\mathrm{ac}}) m_0 + \rho_0^{-1}(\tilde{\alpha}_{vv} - S_{\mathrm{ac}}) d_0 - i(\rho_0\epsilon_0)^{-1/2}\tilde{\alpha}_{vE} P_0 \,, \tag{3.29b}$$

$$E_{\mathrm{ext}} = -(\beta_0\epsilon_0)^{-1/2}\tilde{\alpha}_{pE} m_0 + i(\rho_0\epsilon_0)^{-1/2}\tilde{\alpha}_{vE} d_0 + \epsilon_0^{-1}(\tilde{\alpha}_{EE} - S_{\mathrm{em}}) P_0 - C_0 S_{\mathrm{em}} M_0 \,, \tag{3.29c}$$

$$H_{\mathrm{ext}} = -C_0 S_{\mathrm{em}} P_0 - \mu_0^{-1}(S_{\mathrm{em}} - \tilde{\alpha}_{HH}) M_0 \,. \tag{3.29d}$$

Interpreting the macroscopic monopole strength m_{eff} and dipole moments d_{eff}, P_{eff}, and M_{eff} as the density of the local monopole strength and dipole moments implies that $m_{\mathrm{eff}} = m_0/V$, $d_{\mathrm{eff}} = d_0/V$, $P_{\mathrm{eff}} = P_0/V$, and $M_{\mathrm{eff}} = M_0/V$, where V is the unit cell volume. Equations (3.29) in combination with Eqs. (3.18) therefore yield the macroscopic fields p_{eff}, v_{eff}, E_{eff}, and H_{eff} in terms of the effective displacements $\varepsilon_{\mathrm{eff}}$, $\mu_{z,\mathrm{eff}}$, D_{eff}, and B_{eff}, inversion of which results in the effective constitutive relations in terms of the macroscopic fields:

$$\begin{bmatrix} \varepsilon_{\mathrm{eff}} \\ \mu_{z,\mathrm{eff}} \\ D_{\mathrm{eff}} \\ B_{\mathrm{eff}} \end{bmatrix} = \begin{bmatrix} -\beta_{\mathrm{eff}} & \chi_{pv}^{\mathrm{o}} - i\chi_{pv}^{\mathrm{e}} & i\chi_{pE}^{\mathrm{o}} - \chi_{pE}^{\mathrm{e}} & -(\chi_{pH}^{\mathrm{o}} - i\chi_{pH}^{\mathrm{e}}) \\ -(\chi_{pv}^{\mathrm{o}} + i\chi_{pv}^{\mathrm{e}}) & \rho_{\mathrm{eff}} & \chi_{vE}^{\mathrm{o}} - i\chi_{vE}^{\mathrm{e}} & -i\chi_{vH}^{\mathrm{o}} + \chi_{vH}^{\mathrm{e}} \\ i\chi_{pE}^{\mathrm{o}} + \chi_{pE}^{\mathrm{e}} & \chi_{vE}^{\mathrm{o}} + i\chi_{vE}^{\mathrm{e}} & \epsilon_{\mathrm{eff}} & \chi_{EH}^{\mathrm{o}} \\ \chi_{pH}^{\mathrm{o}} + i\chi_{pH}^{\mathrm{e}} & i\chi_{vH}^{\mathrm{o}} + \chi_{vH}^{\mathrm{e}} & \chi_{EH}^{\mathrm{o}} & \mu_{\mathrm{eff}} \end{bmatrix} \begin{bmatrix} p_{\mathrm{eff}} \\ v_{\mathrm{eff}} \\ E_{\mathrm{eff}} \\ H_{\mathrm{eff}} \end{bmatrix} . \tag{3.30}$$

The diagonal elements of the 4×4 matrix in Eq. (3.30) are defined by

$$\frac{\beta_{\rm eff}}{\beta_0} = 1 + \Lambda_{pp}\,, \qquad \frac{\rho_{\rm eff}}{\rho_0} = 1 + \Lambda_{vv}\,, \tag{3.31a}$$

$$\frac{\epsilon_{\rm eff}}{\epsilon_0} = 1 + \Lambda_{EE}\,, \qquad \frac{\mu_{\rm eff}}{\mu_0} = 1 + \Lambda_{HH} \tag{3.31b}$$

and the quantities appearing in the off-diagonal elements are defined by

$$\chi^{\rm e}_{pv} = (\rho_0\beta_0)^{1/2}\Lambda^{\rm e}_{pv}\,, \qquad \chi^{\rm o}_{pv} = (\rho_0\beta_0)^{1/2}\Lambda^{\rm o}_{pv}\,, \tag{3.31c}$$

$$\chi^{\rm e}_{pE} = (\beta_0\epsilon_0)^{1/2}\Lambda^{\rm e}_{pE}\,, \qquad \chi^{\rm o}_{pE} = (\beta_0\epsilon_0)^{1/2}\Lambda^{\rm o}_{pE}\,, \tag{3.31d}$$

$$\chi^{\rm e}_{pH} = (\beta_0\mu_0)^{1/2}\Lambda^{\rm e}_{pH}\,, \qquad \chi^{\rm o}_{pH} = (\beta_0\mu_0)^{1/2}\Lambda^{\rm o}_{pH}\,, \tag{3.31e}$$

$$\chi^{\rm e}_{vE} = (\rho_0\epsilon_0)^{1/2}\Lambda^{\rm e}_{vE}\,, \qquad \chi^{\rm o}_{vE} = (\rho_0\epsilon_0)^{1/2}\Lambda^{\rm o}_{vE}\,, \tag{3.31f}$$

$$\chi^{\rm e}_{vH} = (\rho_0\mu_0)^{1/2}\Lambda^{\rm e}_{vH}, \qquad \chi^{\rm o}_{vH} = (\rho_0\mu_0)^{1/2}\Lambda^{\rm o}_{vH}\,, \tag{3.31g}$$

$$\chi^{\rm o}_{EH} = (\mu_0\epsilon_0)^{1/2}\Lambda^{\rm o}_{EH}\,, \tag{3.31h}$$

where the Λs in Eqs. (3.31) associated with the diagonal elements of Eq. (3.30) are

$$\begin{aligned}
\Lambda_{pp} &= \tilde\Delta^{-1}[(\tilde\Lambda^{\rm o}_{EH})^2\tilde\Lambda_{vv} + (\tilde\Lambda^{\rm e}_{vE})^2\tilde\Lambda_{HH} - \tilde\Lambda_{EE}\tilde\Lambda_{vv}\tilde\Lambda_{HH}],\\
\Lambda_{vv} &= \tilde\Delta^{-1}[(\tilde\Lambda^{\rm o}_{EH})^2\tilde\Lambda_{pp} + (\tilde\Lambda^{\rm e}_{pE})^2\tilde\Lambda_{HH} - \tilde\Lambda_{EE}\tilde\Lambda_{pp}\tilde\Lambda_{HH}],\\
\Lambda_{EE} &= \tilde\Delta^{-1}[(\tilde\Lambda^{\rm e}_{pv})^2\tilde\Lambda_{HH} + (\tilde\Lambda^{\rm o}_{pv})^2\tilde\Lambda_{HH} - \tilde\Lambda_{pp}\tilde\Lambda_{vv}\tilde\Lambda_{HH}],\\
\Lambda_{HH} &= \tilde\Delta^{-1}[\tilde\Lambda_{EE}(\tilde\Lambda^{\rm e}_{pv})^2 + \tilde\Lambda_{EE}(\tilde\Lambda^{\rm o}_{pv})^2 + 2\tilde\Lambda^{\rm e}_{pE}\tilde\Lambda^{\rm e}_{pv}\tilde\Lambda^{\rm e}_{vE}\\
&\qquad + \tilde\Lambda_{pp}(\tilde\Lambda^{\rm e}_{vE})^2 + (\tilde\Lambda^{\rm e}_{pE})^2\tilde\Lambda_{vv} - \tilde\Lambda_{EE}\tilde\Lambda_{pp}\tilde\Lambda_{vv}],
\end{aligned}$$

and where the Λs associated with the off-diagonal elements of Eq. (3.30) are

$$\Lambda^{\rm e}_{pv} = \tilde\Delta^{-1}[(\tilde\Lambda^{\rm o}_{EH})^2\tilde\Lambda^{\rm e}_{pv} - \tilde\Lambda_{EE}\tilde\Lambda^{\rm e}_{pv}\tilde\Lambda_{HH} - \tilde\Lambda^{\rm e}_{pE}\tilde\Lambda^{\rm e}_{vE}\tilde\Lambda_{HH}], \tag{3.32}$$

$$\Lambda^{\rm o}_{pv} = \tilde\Delta^{-1}[(\tilde\Lambda^{\rm o}_{EH})^2\tilde\Lambda^{\rm o}_{pv} - \tilde\Lambda_{EE}\tilde\Lambda^{\rm o}_{pv}\tilde\Lambda_{HH}], \tag{3.33}$$

$$\Lambda^{\rm e}_{pE} = \tilde\Delta^{-1}(\tilde\Lambda^{\rm e}_{pv}\tilde\Lambda^{\rm e}_{vE}\tilde\Lambda_{HH} + \tilde\Lambda^{\rm e}_{pE}\tilde\Lambda_{vv}\tilde\Lambda_{HH}), \quad \Lambda^{\rm o}_{pE} = -\tilde\Delta^{-1}\tilde\Lambda^{\rm o}_{pv}\tilde\Lambda^{\rm e}_{vE}\tilde\Lambda_{HH}, \tag{3.34}$$

$$\Lambda^{\rm e}_{pH} = -\tilde\Delta^{-1}\tilde\Lambda^{\rm o}_{EH}\tilde\Lambda^{\rm o}_{pv}\tilde\Lambda^{\rm e}_{vE}, \quad \Lambda^{\rm o}_{pH} = -\tilde\Delta^{-1}(\tilde\Lambda^{\rm o}_{EH}\tilde\Lambda^{\rm e}_{pv}\tilde\Lambda^{\rm e}_{vE} + \tilde\Lambda^{\rm o}_{EH}\tilde\Lambda^{\rm e}_{pE}\tilde\Lambda_{vv}), \tag{3.35}$$

$$\Lambda^{\rm e}_{vE} = \tilde\Delta^{-1}(\tilde\Lambda^{\rm e}_{pE}\tilde\Lambda^{\rm e}_{pv}\tilde\Lambda_{HH} + \tilde\Lambda_{pp}\tilde\Lambda^{\rm e}_{vE}\tilde\Lambda_{HH}), \quad \Lambda^{\rm o}_{vE} = -\tilde\Delta^{-1}\tilde\Lambda^{\rm e}_{pE}\tilde\Lambda^{\rm o}_{pv}\tilde\Lambda_{HH}, \tag{3.36}$$

$$\Lambda^{\rm e}_{vH} = \tilde\Delta^{-1}\tilde\Lambda^{\rm o}_{EH}\tilde\Lambda^{\rm e}_{pE}\tilde\Lambda^{\rm o}_{pv}, \quad \Lambda^{\rm o}_{vH} = -\tilde\Delta^{-1}(\tilde\Lambda^{\rm o}_{EH}\tilde\Lambda^{\rm e}_{pE}\tilde\Lambda^{\rm e}_{pv} + \tilde\Lambda^{\rm o}_{EH}\tilde\Lambda_{pp}\tilde\Lambda^{\rm e}_{vE}), \tag{3.37}$$

$$\Lambda^{\rm o}_{EH} = \tilde\Delta^{-1}\tilde\Lambda^{\rm o}_{EH}[-\tilde\Lambda^{\rm o}_{EH}(\tilde\Lambda^{\rm e}_{pv})^2 - \tilde\Lambda^{\rm o}_{EH}(\tilde\Lambda^{\rm o}_{pv})^2 + \tilde\Lambda^{\rm o}_{EH}\tilde\Lambda_{pp}\tilde\Lambda_{vv}]\,, \tag{3.38}$$

where

$$\begin{aligned}\tilde{\Delta} = &-(\tilde{\Lambda}^{\mathrm{o}}_{EH})^2(\tilde{\Lambda}^{\mathrm{e}}_{pv})^2 - (\tilde{\Lambda}^{\mathrm{o}}_{EH})^2(\tilde{\Lambda}^{\mathrm{o}}_{pv})^2 + (\tilde{\Lambda}^{\mathrm{o}}_{EH})^2\tilde{\Lambda}_{pp}\tilde{\Lambda}_{vv} + \tilde{\Lambda}_{EE}(\tilde{\Lambda}^{\mathrm{e}}_{pv})^2\tilde{\Lambda}_{HH} \\ &+ \tilde{\Lambda}_{EE}(\tilde{\Lambda}^{\mathrm{o}}_{pv})^2\tilde{\Lambda}_{HH} + 2\tilde{\Lambda}^{\mathrm{e}}_{pE}\tilde{\Lambda}^{\mathrm{e}}_{pv}\tilde{\Lambda}^{\mathrm{e}}_{vE}\tilde{\Lambda}_{HH} + \tilde{\Lambda}_{pp}(\tilde{\Lambda}^{\mathrm{e}}_{vE})^2\tilde{\Lambda}_{HH} + (\tilde{\Lambda}^{\mathrm{e}}_{pE})^2\tilde{\Lambda}_{vv}\tilde{\Lambda}_{HH} \\ &- \tilde{\Lambda}_{pp}\tilde{\Lambda}_{vv}\tilde{\Lambda}_{EE}\tilde{\Lambda}_{HH}.\end{aligned}$$

The $\tilde{\Lambda}$s in the above equations are in turn defined by

$$\tilde{\Lambda}_{pp} = V\tilde{\alpha}_{pp} - VS_{\mathrm{ac}} + \frac{(k_0/k)^2}{1-k_0^2/k^2}, \qquad \tilde{\Lambda}_{vv} = V\tilde{\alpha}_{vv} - VS_{\mathrm{ac}} + \frac{(k_0/k)^2}{1-k_0^2/k^2}, \tag{3.39a}$$

$$\tilde{\Lambda}_{EE} = V\tilde{\alpha}_{EE} - VS_{\mathrm{em}} + \frac{(\kappa_0/\kappa)^2}{1-\kappa_0^2/\kappa^2}, \qquad \tilde{\Lambda}_{HH} = V\tilde{\alpha}_{HH} - VS_{\mathrm{em}} + \frac{(\kappa_0/\kappa)^2}{1-\kappa_0^2/\kappa^2}, \tag{3.39b}$$

and

$$\tilde{\Lambda}^{\mathrm{e}}_{pv} = V\tilde{\alpha}_{pv}, \qquad \tilde{\Lambda}^{\mathrm{o}}_{pv} = -VS_{\mathrm{ac}} + \frac{k_0/k}{1-k_0^2/k^2}, \tag{3.40a}$$

$$\tilde{\Lambda}^{\mathrm{e}}_{vE} = V\tilde{\alpha}_{vE}, \qquad \tilde{\Lambda}^{\mathrm{o}}_{EH} = -VS_{\mathrm{em}} + \frac{\kappa_0/\kappa}{1-\kappa_0^2/\kappa^2}, \tag{3.40b}$$

$$\tilde{\Lambda}^{\mathrm{e}}_{pE} = V\tilde{\alpha}_{pE}. \tag{3.40c}$$

The superscripts "e" and "o" in Eqs. (3.30), (3.31), and (3.40) denote whether each term is even or odd in k and κ. The top-left 2×2 block of Eq. (3.30) recovers Eq. (35) of Ref. 13, and the bottom-right 2×2 block recovers Eq. (22) of Ref. 12, where the fact that $\chi^{\mathrm{e}}_{EH} = 0$ is consistent with the assumption in Eq. (3.20) that the scatterers are magnetically symmetric. The fact that $\chi^{\mathrm{o}}_{EH} \neq 0$ in Eq. (3.30) reflects that "even when inclusions are perfectly centersymmetric and with no inherent bianisotropy, a form of magnetoelectric coupling is still expected…due to lattice effects and the nonzero value of $[\kappa]$" [12]. Equation (3.30) corroborates the finding of Ref. 60 that asymmetric piezoelectric scatterers lead to electromomentum coupling, subscripted "vE." Figure 3.8 shows a schematic of the homogenized medium. Equation (3.30) also predicts emergent piezomagnetic and magnetomomentum effects, which are subscripted "pH" and "vH," respectively. While the magnitude of the magnetomomentum effect remains to be investigated in detail, the emergence of these effective dynamic couplings are consistent with the understanding that time-varying scat-

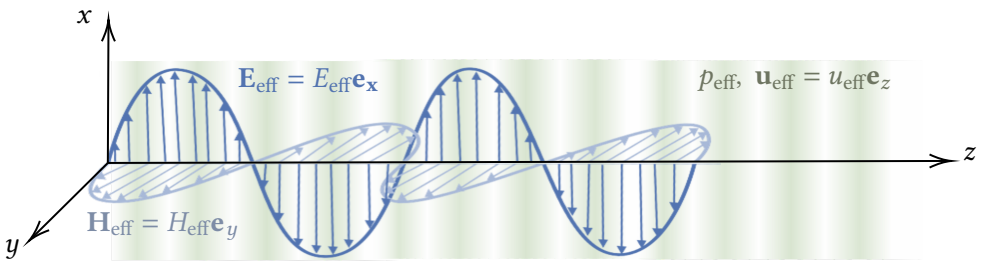

Figure 3.8: The macroscopic fields are the result of the homogenization theory.

tering of electric fields generated through local acoustical fields and piezoelectric scatterers. The primary contribution of this dynamic homogenization is to show that a formulation that considers electrodynamic effects must necessarily include coupling to magnetic fields, which may be of interest in future applications.

3.3 Constraints due to reciprocity and passivity

Since the piezoelectric scatterers described by Eq. (3.20) are reciprocal and passive at the microscale, the homogenized medium described by Eq. (3.30) should also obey reciprocity and passivity. In the present section, the constraints due to reciprocity and passivity are derived for the elasto-electrodynamic constitutive relations given by Eq. (3.8). The acoustic limit of the results are obtained in Sec. 3.4.

Constraints on the electromagnetic bianisotropic constitutive relations were originally obtained by Kong [69]. Alù discussed reciprocity and passivity in the context of electromagnetic metamaterials [12, 218, 219], which inspired subsequent studies in elastodynamics and acoustics by Muhlestein et al. [70] and Sieck et al. [13], respectively. More recently, constraints due to reciprocity and passivity on generalized Willis media were derived in the electrostatic and magnetostatic limits by Pernas-Salomón et al. [123]. However, the static approximations made in Ref. 123 are insufficient to describe the effective constitutive relations that arise from the polarizabilities considered in Refs. 67, 68, and Sec. 3.2. The contribution of the present section is the consideration of electrodynamics, which must consider the magnetic field, and the determination of constraints on the

piezomagnetic and magnetomomentum coupling tensors.

Stress-charge form vs. strain-charge form

The elastodynamic constitutive relations are often written with stress $\underline{\boldsymbol{\sigma}}$ on the left-hand side [70, 207, 214, 220], which defines the *stress form* of the constitutive relations. The stress form of Eq. (3.8) is[12]

$$\begin{pmatrix} \underline{\boldsymbol{\sigma}} \\ \boldsymbol{\mu} \\ \mathbf{D} \\ \mathbf{B} \end{pmatrix} = \begin{pmatrix} \mathbb{C} & \tilde{\underset{\sim}{\boldsymbol{\gamma}}} & -\tilde{\underset{\sim}{\mathbf{e}}} & -\tilde{\underset{\sim}{\mathbf{c}}} \\ \tilde{\boldsymbol{\eta}} & \tilde{\underline{\boldsymbol{\rho}}} & -\tilde{\underline{\mathbf{w}}} & -\tilde{\underline{\mathbf{n}}} \\ \tilde{\underset{\sim}{\mathbf{d}}} & \tilde{\underline{\mathbf{v}}} & \tilde{\epsilon} & \tilde{\xi} \\ \tilde{\underset{\sim}{\mathbf{b}}} & \tilde{\underline{\mathbf{m}}} & \tilde{\zeta} & \tilde{\underline{\boldsymbol{\mu}}} \end{pmatrix} \begin{pmatrix} \underline{\boldsymbol{\varepsilon}} \\ \mathbf{v} \\ \mathbf{E} \\ \mathbf{H} \end{pmatrix}, \tag{3.41}$$

where the minus sign preceding the magnetomomentum coupling tensor $\tilde{\underline{\mathbf{n}}}$ parallels the convention established in Refs. 60 and 123 for the electromomentum coupling tensor $\tilde{\underline{\mathbf{w}}}$. However, the *strain form* given by Eq. (3.8) (in which stress appears on the right-hand side) is more conducive to reducing the results for elastodynamics to acoustics [67, 68, 221]. Identifying stress as a dependent variable also parallels the electromagnetic constitutive relations: the compliance (rather than the stiffness) and density are the mechanical constitutive parameters that are analogous to the electromagnetic permittivity and permeability [13]. It is therefore desired to relate the constitutive parameters of the strain-charge form to the stress-charge form so that the present work can be compared with the results of Refs. 60, 62–66 and 123. These relations are determined by comparing Eqs. (3.8) and (3.41) row by row.

The first row of Eq. (3.41) is

$$\underline{\boldsymbol{\sigma}} = \mathbb{C} : \underline{\boldsymbol{\varepsilon}} + \tilde{\underset{\sim}{\boldsymbol{\gamma}}} \cdot \mathbf{v} - \tilde{\underset{\sim}{\mathbf{e}}} \cdot \mathbf{E} - \tilde{\underset{\sim}{\mathbf{c}}} \cdot \mathbf{H} \,. \tag{3.42}$$

[12] Equation (3.41) generalizes Eq. (7) of Ref. 123, where $\mathbf{E} = -\boldsymbol{\nabla}\phi$ and ϕ is the electric potential. The minus sign preceding the piezoelectric coupling tensor $\tilde{\underset{\sim}{\mathbf{e}}}$ is conventional [209, Table I]. The minus sign preceding $\tilde{\underset{\sim}{\mathbf{c}}}$ extends this convention to the piezomagnetic domain. The tildes in Eq. (3.41) distinguish the constitutive properties of the stress form from those of the strain form given by Eq. (3.8).

Solving Eq. (3.42) for $\underline{\boldsymbol{\varepsilon}}$ yields

$$\underline{\boldsymbol{\varepsilon}} = \mathbb{C}^{-1} : \underline{\boldsymbol{\sigma}} - (\mathbb{C}^{-1} : \underset{\sim}{\tilde{\boldsymbol{\gamma}}}) \cdot \mathbf{v} + (\mathbb{C}^{-1} : \underline{\tilde{\mathbf{e}}}) \cdot \mathbf{E} + (\mathbb{C}^{-1} : \underline{\tilde{\mathbf{c}}}) \cdot \mathbf{H} \,. \tag{3.43}$$

Meanwhile, the first row of Eq. (3.8) equals

$$\underline{\boldsymbol{\varepsilon}} = \mathbb{M} : \underline{\boldsymbol{\sigma}} + \underset{\sim}{\boldsymbol{\gamma}} \cdot \mathbf{v} + \underline{\mathbf{e}} \cdot \mathbf{E} + \underline{\mathbf{c}} \cdot \mathbf{H} \,. \tag{3.44}$$

Comparing Eq. (3.43) to Eq. (3.44) term by term identifies[13]

$$\mathbb{M} = \mathbb{C}^{-1} \,, \tag{3.45a}$$

$$\underset{\sim}{\boldsymbol{\gamma}} = -\mathbb{C}^{-1} : \underset{\sim}{\tilde{\boldsymbol{\gamma}}} \,, \tag{3.45b}$$

$$\underline{\mathbf{e}} = \mathbb{C}^{-1} : \underline{\tilde{\mathbf{e}}} \,, \tag{3.45c}$$

$$\underline{\mathbf{c}} = \mathbb{C}^{-1} : \underline{\tilde{\mathbf{c}}} \,. \tag{3.45d}$$

Equations (3.45) show that the Willis, piezoelectric, and piezomagnetic constitutive parameters of the stress form are related to the parameters of the strain form through the compliance tensor.

Attention is turned next to the second row of Eq. (3.41):

$$\boldsymbol{\mu} = \underset{\sim}{\tilde{\boldsymbol{\eta}}} : \underline{\boldsymbol{\varepsilon}} + \underline{\tilde{\boldsymbol{\rho}}} \cdot \mathbf{v} - \underline{\tilde{\mathbf{w}}} \cdot \mathbf{E} - \underline{\tilde{\mathbf{n}}} \cdot \mathbf{H} \,. \tag{3.46}$$

Inserting Eq. (3.43) into Eq. (3.46) yields

$$\begin{aligned} \boldsymbol{\mu} = {} & \underset{\sim}{\tilde{\boldsymbol{\eta}}} : (\mathbb{C}^{-1} : \underline{\boldsymbol{\sigma}}) - \underset{\sim}{\tilde{\boldsymbol{\eta}}} : (\mathbb{C}^{-1} : \underset{\sim}{\tilde{\boldsymbol{\gamma}}}) \cdot \mathbf{v} + \underset{\sim}{\tilde{\boldsymbol{\eta}}} : (\mathbb{C}^{-1} : \underline{\tilde{\mathbf{e}}}) \cdot \mathbf{E} \\ & + \underset{\sim}{\tilde{\boldsymbol{\eta}}} : (\mathbb{C}^{-1} : \underline{\tilde{\mathbf{c}}}) \cdot \mathbf{H} + \underline{\tilde{\boldsymbol{\rho}}} \cdot \mathbf{v} - \underline{\tilde{\mathbf{w}}} \cdot \mathbf{E} - \underline{\tilde{\mathbf{n}}} \cdot \mathbf{H} \,. \end{aligned}$$

Regrouping terms yields

$$\begin{aligned} \boldsymbol{\mu} = {} & (\underset{\sim}{\tilde{\boldsymbol{\eta}}} : \mathbb{C}^{-1}) : \underline{\boldsymbol{\sigma}} + (\underline{\tilde{\boldsymbol{\rho}}} - \underset{\sim}{\tilde{\boldsymbol{\eta}}} : \mathbb{C}^{-1} : \underset{\sim}{\tilde{\boldsymbol{\gamma}}}) \cdot \mathbf{v} - (\underline{\tilde{\mathbf{w}}} - \underset{\sim}{\tilde{\boldsymbol{\eta}}} : \mathbb{C}^{-1} : \underline{\tilde{\mathbf{e}}}) \cdot \mathbf{E} \\ & - (\underline{\tilde{\mathbf{n}}} - \underset{\sim}{\tilde{\boldsymbol{\eta}}} : \mathbb{C}^{-1} : \underline{\tilde{\mathbf{c}}}) \cdot \mathbf{H} \,. \end{aligned} \tag{3.47}$$

[13] The stiffness tensor as provided in Eq. (3.41) is often referred to in the literature of piezoelectricity as the stiffness at constant electric field, usually denotes as $\mathbb{C}_{\mathrm{E}}$. For the present case, the stiffness tensor refers to the case of constant (ideally zero) velocity, electric, and magnetic fields. Subscripts denoting constant fields have not been included in this work to minimize notational clutter.

Meanwhile, the second row of Eq. (3.8) equals

$$\boldsymbol{\mu} = \underset{\sim}{\boldsymbol{\eta}} : \underline{\boldsymbol{\sigma}} + \underline{\boldsymbol{\rho}} \cdot \mathbf{v} + \underline{\mathbf{w}} \cdot \mathbf{E} + \underline{\mathbf{n}} \cdot \mathbf{H} . \tag{3.48}$$

Comparing Eq. (3.47) to Eq. (3.48) identifies

$$\underset{\sim}{\boldsymbol{\eta}} = \underset{\sim}{\tilde{\boldsymbol{\eta}}} : \mathbb{C}^{-1} , \tag{3.49a}$$

$$\underline{\boldsymbol{\rho}} = \underline{\tilde{\boldsymbol{\rho}}} - \underset{\sim}{\tilde{\boldsymbol{\eta}}} : \mathbb{C}^{-1} : \underset{\sim}{\tilde{\boldsymbol{\gamma}}} , \tag{3.49b}$$

$$\underline{\mathbf{w}} = -\underline{\tilde{\mathbf{w}}} + \underset{\sim}{\tilde{\boldsymbol{\eta}}} : \mathbb{C}^{-1} : \underline{\tilde{\mathbf{e}}} , \tag{3.49c}$$

$$\underline{\mathbf{n}} = -\underline{\tilde{\mathbf{n}}} + \underset{\sim}{\tilde{\boldsymbol{\eta}}} : \mathbb{C}^{-1} : \underset{\sim}{\tilde{\mathbf{c}}} . \tag{3.49d}$$

Equation (3.49a) shows that the Willis coupling tensor of the strain form is related to that of the stress form through the compliance (i.e. the inverse of the stiffness tensor), similar to Eq. (3.45b). Meanwhile, Eqs. (3.49b)–(3.49d) show that the dynamic density, electromomentum, and magnetomomentum tensors of the strain form are related to those of the stress form through the Willis, piezoelectric, and piezomagnetic tensors.

The third row of Eq. (3.41) is

$$\mathbf{D} = \underline{\tilde{\mathbf{d}}} : \underline{\boldsymbol{\varepsilon}} + \underline{\tilde{\mathbf{v}}} \cdot \mathbf{v} + \underline{\tilde{\boldsymbol{\epsilon}}} \cdot \mathbf{E} + \underline{\tilde{\boldsymbol{\xi}}} \cdot \mathbf{H} . \tag{3.50}$$

Inserting Eq. (3.43) into Eq. (3.46) yields

$$\begin{aligned} \mathbf{D} = {} & \underline{\tilde{\mathbf{d}}} : (\mathbb{C}^{-1} : \underline{\boldsymbol{\sigma}}) - \underline{\tilde{\mathbf{d}}} : (\mathbb{C}^{-1} : \underset{\sim}{\tilde{\boldsymbol{\gamma}}}) \cdot \mathbf{v} + \underline{\tilde{\mathbf{d}}} : (\mathbb{C}^{-1} : \underline{\tilde{\mathbf{e}}}) \cdot \mathbf{E} + \underline{\tilde{\mathbf{d}}} : (\mathbb{C}^{-1} : \underset{\sim}{\tilde{\mathbf{c}}}) \cdot \mathbf{H} \\ & + \underline{\tilde{\mathbf{v}}} \cdot \mathbf{v} + \underline{\tilde{\boldsymbol{\epsilon}}} \cdot \mathbf{E} + \underline{\tilde{\boldsymbol{\xi}}} \cdot \mathbf{H} . \end{aligned}$$

Regrouping terms yields

$$\begin{aligned} \mathbf{D} = {} & (\underline{\tilde{\mathbf{d}}} : \mathbb{C}^{-1}) : \underline{\boldsymbol{\sigma}} + (\underline{\tilde{\mathbf{v}}} - \underline{\tilde{\mathbf{d}}} : \mathbb{C}^{-1} : \underset{\sim}{\tilde{\boldsymbol{\gamma}}}) \cdot \mathbf{v} \\ & + (\underline{\tilde{\boldsymbol{\epsilon}}} + \underline{\tilde{\mathbf{d}}} : \mathbb{C}^{-1} : \underline{\tilde{\mathbf{e}}}) \cdot \mathbf{E} + (\underline{\tilde{\boldsymbol{\xi}}} + \underline{\tilde{\mathbf{d}}} : \mathbb{C}^{-1} : \underset{\sim}{\tilde{\mathbf{c}}}) \cdot \mathbf{H} . \end{aligned} \tag{3.51}$$

Meanwhile, the third row of Eq. (3.8) equals

$$\mathbf{D} = \underline{\mathbf{d}} : \underline{\boldsymbol{\sigma}} + \underline{\mathbf{v}} \cdot \mathbf{v} + \underline{\boldsymbol{\epsilon}} \cdot \mathbf{E} + \underline{\boldsymbol{\xi}} \cdot \mathbf{H} . \tag{3.52}$$

Comparing Eq. (3.51) to Eq. (3.52) identifies

$$\underline{\mathbf{d}} = \tilde{\underline{\mathbf{d}}} : \mathbb{C}^{-1}, \tag{3.53a}$$

$$\underline{\mathbf{v}} = \tilde{\underline{\mathbf{v}}} - \tilde{\underline{\mathbf{d}}} : \mathbb{C}^{-1} : \tilde{\underset{\sim}{\boldsymbol{\gamma}}}, \tag{3.53b}$$

$$\underline{\boldsymbol{\epsilon}} = \tilde{\underline{\boldsymbol{\epsilon}}} + \tilde{\underline{\mathbf{d}}} : \mathbb{C}^{-1} : \tilde{\underline{\mathbf{e}}}, \tag{3.53c}$$

$$\underline{\boldsymbol{\xi}} = \tilde{\underline{\boldsymbol{\xi}}} + \tilde{\underline{\mathbf{d}}} : \mathbb{C}^{-1} : \tilde{\underline{\mathbf{c}}}. \tag{3.53d}$$

Conversions between the stress-charge and strain-charge forms of the four piezoelectric constitutive parameters are provided by Eqs. (3.45a), (3.45c), (3.53a), and (3.53c). To determine the inverse relations, these equations are solved for the parameters of the stress-charge form. The inversion of Eq. (3.45a) is trivial:

$$\mathbb{C} = \mathbb{M}^{-1}. \tag{3.54a}$$

Taking the double inner product of Eq. (3.53a) with $\mathbb{C}$ on the right and invoking Eq. (3.54a) yields

$$\tilde{\underline{\mathbf{d}}} = \underline{\mathbf{d}} : \mathbb{M}^{-1}. \tag{3.54b}$$

Similar manipulation of Eq. (3.45c) yields

$$\tilde{\underline{\mathbf{e}}} = \mathbb{M}^{-1} : \underline{\mathbf{e}}. \tag{3.54c}$$

Meanwhile, solving Eq. (3.53c) for $\tilde{\underline{\boldsymbol{\epsilon}}}$ yields $\tilde{\underline{\boldsymbol{\epsilon}}} = \underline{\boldsymbol{\epsilon}} - \tilde{\underline{\mathbf{d}}} : \mathbb{C}^{-1} : \tilde{\underline{\mathbf{e}}}$. Invoking Eqs. (3.54a), (3.54b), and (3.54c) yields

$$\tilde{\underline{\boldsymbol{\epsilon}}} = \underline{\boldsymbol{\epsilon}} - \underline{\mathbf{d}} : \mathbb{C} : \mathbb{C}^{-1} : (\mathbb{M}^{-1} : \underline{\mathbf{e}}) = \underline{\boldsymbol{\epsilon}} - \underline{\mathbf{d}} : \mathbb{I} : \mathbb{M}^{-1} : \underline{\mathbf{e}},$$

where the second equality follows from the associative property. Since $\mathbb{I} : \mathbb{M}^{-1} = \mathbb{M}^{-1}$, where $\mathbb{I}$ is the rank-4 identity tensor, it is determined that

$$\tilde{\underline{\boldsymbol{\epsilon}}} = \underline{\boldsymbol{\epsilon}} - \underline{\mathbf{d}} : \mathbb{M}^{-1} : \underline{\mathbf{e}}. \tag{3.54d}$$

Equations (3.54) recover the conversions between the strain-charge and stress-charge forms presented in Ref. 210.

Finally, the fourth row of Eq. (3.41) is

$$\mathbf{B} = \underline{\tilde{\mathbf{b}}} : \underline{\boldsymbol{\varepsilon}} + \underline{\tilde{\mathbf{m}}} \cdot \mathbf{v} + \underline{\tilde{\boldsymbol{\zeta}}} \cdot \mathbf{E} + \underline{\tilde{\boldsymbol{\mu}}} \cdot \mathbf{H} \,. \tag{3.55}$$

Insertion of Eq. (3.43) into Eq. (3.55) yields

$$\begin{aligned} \mathbf{B} = \underline{\tilde{\mathbf{b}}} : (\mathbb{C}^{-1} : \underline{\boldsymbol{\sigma}}) - \underline{\tilde{\mathbf{b}}} : (\mathbb{C}^{-1} : \underline{\tilde{\boldsymbol{\gamma}}}) \cdot \mathbf{v} + \underline{\tilde{\mathbf{b}}} : (\mathbb{C}^{-1} : \underline{\tilde{\mathbf{e}}}) \cdot \mathbf{E} \\ + \underline{\tilde{\mathbf{b}}} : (\mathbb{C}^{-1} : \underline{\tilde{\mathbf{c}}}) \cdot \mathbf{H} + \underline{\tilde{\mathbf{m}}} \cdot \mathbf{v} + \underline{\tilde{\boldsymbol{\zeta}}} \cdot \mathbf{E} + \underline{\tilde{\boldsymbol{\mu}}} \cdot \mathbf{H} , \end{aligned}$$

rearrangement of which results in

$$\begin{aligned} \mathbf{B} = (\underline{\tilde{\mathbf{b}}} : \mathbb{C}^{-1}) : \underline{\boldsymbol{\sigma}} + (\underline{\tilde{\mathbf{m}}} - \underline{\tilde{\mathbf{b}}} : \mathbb{C}^{-1} : \underline{\tilde{\boldsymbol{\gamma}}}) \cdot \mathbf{v} + (\underline{\tilde{\boldsymbol{\zeta}}} + \underline{\tilde{\mathbf{b}}} : \mathbb{C}^{-1} : \underline{\tilde{\mathbf{e}}}) \cdot \mathbf{E} \\ + (\underline{\tilde{\boldsymbol{\mu}}} + \underline{\tilde{\mathbf{b}}} : \mathbb{C}^{-1} : \underline{\tilde{\mathbf{c}}}) \cdot \mathbf{H} \,. \end{aligned} \tag{3.56}$$

Meanwhile, the fourth row of Eq. (3.8) equals

$$\mathbf{B} = \underline{\mathbf{b}} : \underline{\boldsymbol{\sigma}} + \underline{\mathbf{m}} \cdot \mathbf{v} + \underline{\boldsymbol{\zeta}} \cdot \mathbf{E} + \underline{\boldsymbol{\mu}} \cdot \mathbf{H} \,. \tag{3.57}$$

Comparing Eq. (3.56) with Eq. (3.57) identifies

$$\underline{\mathbf{b}} = \underline{\tilde{\mathbf{b}}} : \mathbb{C}^{-1} , \tag{3.58a}$$

$$\underline{\mathbf{m}} = \underline{\tilde{\mathbf{m}}} - \underline{\tilde{\mathbf{b}}} : \mathbb{C}^{-1} : \underline{\tilde{\boldsymbol{\gamma}}} , \tag{3.58b}$$

$$\underline{\boldsymbol{\zeta}} = \underline{\tilde{\boldsymbol{\zeta}}} + \underline{\tilde{\mathbf{b}}} : \mathbb{C}^{-1} : \underline{\tilde{\mathbf{e}}} , \tag{3.58c}$$

$$\underline{\boldsymbol{\mu}} = \underline{\tilde{\boldsymbol{\mu}}} + \underline{\tilde{\mathbf{b}}} : \mathbb{C}^{-1} : \underline{\tilde{\mathbf{c}}} . \tag{3.58d}$$

While the elastodynamic tensors $\underline{\boldsymbol{\rho}}$, $\underline{\boldsymbol{\gamma}}$, and $\underline{\boldsymbol{\eta}}$ of the strain form are related to their counterparts of the stress form through the Willis coupling tensors [Eqs. (3.49b), (3.45b), and (3.49a)], the mappings for the electromagnetic constitutive parameters given by Eqs. (3.53c), (3.53d), (3.58c), and (3.58d) are unrelated to the electromagnetic bianisotropy tensors of the stress form and are instead related through the piezoelectric and piezoelectric coupling tensors of the stress form. Therefore, in the absence of elastodynamics, $\underline{\tilde{\boldsymbol{\epsilon}}} = \underline{\boldsymbol{\epsilon}}$, $\underline{\tilde{\boldsymbol{\mu}}} = \underline{\boldsymbol{\mu}}$, $\underline{\tilde{\boldsymbol{\xi}}} = \underline{\boldsymbol{\xi}}$, and $\underline{\tilde{\boldsymbol{\zeta}}} = \underline{\boldsymbol{\zeta}}$, and the following discussion becomes purely electromagnetic. Conversely, in

the absence of electromagnetics, the discussion reduces to pure elastodynamics, although the difference between stress and strain forms is still maintained in that limit.

Equations (3.45), (3.49), (3.53), and (3.58) relating the constitutive parameters of the stress form [Eq. (3.41)] to those of the strain form [Eq. (3.8)] will be used when converting the results derived in Refs. 70 and 123 to the forms used in the present work. To relate the results of Ref. 123 to the present work, $\tilde{\underline{\mathbf{c}}}$, $\tilde{\underline{\mathbf{b}}}$, $\tilde{\underline{\mathbf{n}}}$, $\tilde{\underline{\mathbf{m}}}$, $\tilde{\underline{\boldsymbol{\xi}}}$, and $\tilde{\underline{\boldsymbol{\zeta}}}$ are set to zero and $\tilde{\underline{\boldsymbol{\mu}}} \to \mu_0$. Equations (3.45), (3.49), (3.53), and (3.58) reduce to

$$\mathbb{M} = \mathbb{C}^{-1}, \qquad \underline{\boldsymbol{\rho}} = \tilde{\underline{\boldsymbol{\rho}}} - \tilde{\underline{\boldsymbol{\eta}}} : \mathbb{C}^{-1} : \tilde{\underline{\boldsymbol{\gamma}}}, \qquad \underline{\boldsymbol{\gamma}} = -\mathbb{C}^{-1} : \tilde{\underline{\boldsymbol{\gamma}}}, \tag{3.59a}$$

$$\underline{\boldsymbol{\eta}} = \tilde{\underline{\boldsymbol{\eta}}} : \mathbb{C}^{-1}, \qquad \underline{\boldsymbol{\epsilon}} = \tilde{\underline{\boldsymbol{\epsilon}}} + \tilde{\underline{\mathbf{d}}} : \mathbb{C}^{-1} : \tilde{\underline{\mathbf{e}}}, \qquad \underline{\mathbf{e}} = \mathbb{C}^{-1} : \tilde{\underline{\mathbf{e}}}, \tag{3.59b}$$

$$\underline{\mathbf{d}} = \tilde{\underline{\mathbf{d}}} : \mathbb{C}^{-1}, \qquad \underline{\mathbf{w}} = -\tilde{\underline{\mathbf{w}}} + \tilde{\underline{\boldsymbol{\eta}}} : \mathbb{C}^{-1} : \tilde{\underline{\mathbf{e}}}, \qquad \underline{\mathbf{v}} = \tilde{\underline{\mathbf{v}}} - \tilde{\underline{\mathbf{d}}} : \mathbb{C}^{-1} : \tilde{\underline{\boldsymbol{\gamma}}}. \tag{3.59c}$$

To relate the constitutive parameters used in Ref. 70 to those used in the present work, the parameters $\tilde{\underline{\mathbf{e}}}$, $\tilde{\underline{\mathbf{d}}}$, $\tilde{\underline{\mathbf{w}}}$, $\underline{\mathbf{v}}$, and $\tilde{\underline{\boldsymbol{\epsilon}}}$ are set to zero, since Ref. 70 does not consider electric fields, leaving the first four of Eqs. (3.59). Meanwhile, if it is desired to instead convert the results derived in the present work to the forms used in Refs. 70 and 123, the inverses of Eqs. (3.59) are more useful. The relations converting the strain-charge parameters to stress-charge parameters given by Eqs. (3.45a), (3.45c), and (3.53c) were inverted in Eqs. (3.54); similar algebra leads to the inverse of Eqs. (3.59):

$$\mathbb{C} = \mathbb{M}^{-1}, \tag{3.60a}$$

$$\tilde{\underline{\boldsymbol{\rho}}} = \underline{\boldsymbol{\rho}} - \underline{\boldsymbol{\eta}} : \mathbb{M}^{-1} : \underline{\boldsymbol{\gamma}}, \tag{3.60b}$$

$$\tilde{\underline{\boldsymbol{\gamma}}} = -\mathbb{M}^{-1} : \underline{\boldsymbol{\gamma}}, \tag{3.60c}$$

$$\tilde{\underline{\boldsymbol{\eta}}} = \underline{\boldsymbol{\eta}} : \mathbb{M}^{-1}, \tag{3.60d}$$

$$\tilde{\underline{\boldsymbol{\epsilon}}} = \underline{\boldsymbol{\epsilon}} - \underline{\mathbf{d}} : \mathbb{M}^{-1} : \underline{\mathbf{e}}. \tag{3.60e}$$

$$\tilde{\underline{\mathbf{e}}} = \mathbb{M}^{-1} : \underline{\mathbf{e}}, \tag{3.60f}$$

$$\tilde{\underline{\mathbf{d}}} = \underline{\mathbf{d}} : \mathbb{M}^{-1}, \tag{3.60g}$$

$$\tilde{\underline{\mathbf{w}}} = -\underline{\mathbf{w}} + \underline{\boldsymbol{\eta}} : \mathbb{M}^{-1} : \underline{\mathbf{e}}, \tag{3.60h}$$

$$\tilde{\underline{\mathbf{v}}} = \underline{\mathbf{v}} - \underline{\mathbf{d}} : \mathbb{M}^{-1} : \underline{\boldsymbol{\gamma}}. \tag{3.60i}$$

To relate constitutive parameters used in this work to those used in Ref. 70, the parameters $\underset{\sim}{\mathbf{e}}$, $\underset{\sim}{\mathbf{d}}$, $\underline{\mathbf{w}}$, $\underline{\mathbf{v}}$, and $\underline{\boldsymbol{\epsilon}}$ are set to zero, leaving the first four of Eqs. (3.60).

Symmetries due to $\underline{\boldsymbol{\varepsilon}} = \underline{\boldsymbol{\varepsilon}}^{\mathrm{T}}$ and $\underline{\boldsymbol{\sigma}} = \underline{\boldsymbol{\sigma}}^{\mathrm{T}}$

Before discussing symmetries due to reciprocity and passivity, it is helpful to derive symmetries that arise due to the symmetries of the strain and stress tensors. The assumption of an irrotational medium $\boldsymbol{\nabla} \times \mathbf{u} = \mathbf{0}$ requires that

$$\underline{\boldsymbol{\varepsilon}} = \underline{\boldsymbol{\varepsilon}}^{\mathrm{T}}, \tag{3.61}$$

where $\mathbf{u}$ is the displacement vector [222, Eq. (1.19)]. Meanwhile, angular momentum conservation requires that the stress tensor be symmetric [222, p. 24]:

$$\underline{\boldsymbol{\sigma}} = \underline{\boldsymbol{\sigma}}^{\mathrm{T}}. \tag{3.62}$$

Equation (3.61) therefore permits Eq. (3.44) to be equated to its transpose, yielding

$$\mathbb{M} : \underline{\boldsymbol{\sigma}} + \underset{\sim}{\boldsymbol{\gamma}} \cdot \mathbf{v} + \underset{\sim}{\mathbf{e}} \cdot \mathbf{E} + \underset{\sim}{\mathbf{c}} \cdot \mathbf{H} = (\mathbb{M} : \underline{\boldsymbol{\sigma}})^{\mathrm{T}} + (\underset{\sim}{\boldsymbol{\gamma}} \cdot \mathbf{v})^{\mathrm{T}} + (\underset{\sim}{\mathbf{e}} \cdot \mathbf{E})^{\mathrm{T}} + (\underset{\sim}{\mathbf{c}} \cdot \mathbf{H})^{\mathrm{T}}.$$

Since the elastic and electromagnetic fields are arbitrary, the stress, velocity, electric and magnetic fields must be considered to be independent [70]. The equality is therefore satisfied if each term is symmetric:

$$\mathbb{M} : \underline{\boldsymbol{\sigma}} = (\mathbb{M} : \underline{\boldsymbol{\sigma}})^{\mathrm{T}}, \tag{3.63a}$$

$$\underset{\sim}{\boldsymbol{\gamma}} \cdot \mathbf{v} = (\underset{\sim}{\boldsymbol{\gamma}} \cdot \mathbf{v})^{\mathrm{T}}, \tag{3.63b}$$

$$\underset{\sim}{\mathbf{e}} \cdot \mathbf{E} = (\underset{\sim}{\mathbf{e}} \cdot \mathbf{E})^{\mathrm{T}}, \tag{3.63c}$$

$$\underset{\sim}{\mathbf{c}} \cdot \mathbf{H} = (\underset{\sim}{\mathbf{c}} \cdot \mathbf{H})^{\mathrm{T}}. \tag{3.63d}$$

Noting from Eq. (D.25) that a rank-4 tensor possessing first minor symmetry satisfies $\mathbb{A} : \underline{\mathbf{e}} = (\mathbb{A} : \underline{\mathbf{e}})^{\mathrm{T}}$, it is concluded from Eq. (3.63a) that

$$\mathbb{M} = \mathbb{M}^{\mathrm{t1}}. \tag{3.64a}$$

Meanwhile, since a rank-3 tensor possessing second minor symmetry satisfies $\underset{\sim}{\mathbf{a}} \cdot \mathbf{u} = (\underset{\sim}{\mathbf{a}} \cdot \mathbf{u})^{\mathrm{T}}$ [see Eq. (D.9)], it is concluded from Eqs. (3.63b), (3.63c), and (3.63d) that

$$\underset{\sim}{\boldsymbol{\gamma}} = \underset{\sim}{\boldsymbol{\gamma}}^{\mathrm{t1}}\,, \tag{3.64b}$$

$$\underset{\sim}{\mathbf{e}} = \underset{\sim}{\mathbf{e}}^{\mathrm{t1}}\,, \tag{3.64c}$$

$$\underset{\sim}{\mathbf{c}} = \underset{\sim}{\mathbf{c}}^{\mathrm{t1}}\,. \tag{3.64d}$$

When reduced to index notation as described by Eq. (D.26), Eq. (3.64a) equals

$$M_{ijkl} = M_{jikl}\,. \tag{3.65a}$$

Similarly, in view of Eq. (D.10), Eqs. (3.64b), (3.64c), and (3.64d) reduce to

$$\gamma_{ijk} = \gamma_{jik}\,, \tag{3.65b}$$

$$e_{ijk} = e_{jik}\,, \tag{3.65c}$$

$$c_{ijk} = c_{jik}\,, \tag{3.65d}$$

respectively.

Meanwhile, Eq. (3.62) allows Eq. (3.44) to be equated to

$$\mathbb{M} : \underline{\boldsymbol{\sigma}} + \underset{\sim}{\boldsymbol{\gamma}} \cdot \mathbf{v} + \underset{\sim}{\mathbf{e}} \cdot \mathbf{E} + \underset{\sim}{\mathbf{c}} \cdot \mathbf{H} = \mathbb{M} : \underline{\boldsymbol{\sigma}}^{\mathrm{T}} + \underset{\sim}{\boldsymbol{\gamma}} \cdot \mathbf{v} + \underset{\sim}{\mathbf{e}} \cdot \mathbf{E} + \underset{\sim}{\mathbf{c}} \cdot \mathbf{H}\,.$$

Canceling the common terms results in

$$\mathbb{M} : \underline{\boldsymbol{\sigma}} = \mathbb{M} : \underline{\boldsymbol{\sigma}}^{\mathrm{T}}\,.$$

In view of Eq. (D.27), it is concluded that the compliance tensor possesses second minor symmetry:

$$\mathbb{M} = \mathbb{M}^{\mathrm{t2}}\,. \tag{3.66a}$$

Equation (3.62) also allows Eqs. (3.48), (3.52), and (3.57) to be equated to

$$\begin{aligned}
\underset{\sim}{\boldsymbol{\eta}} : \underline{\boldsymbol{\sigma}}^{\mathrm{T}} + \underline{\boldsymbol{\rho}} \cdot \mathbf{v} + \underline{\mathbf{w}} \cdot \mathbf{E} + \underline{\mathbf{n}} \cdot \mathbf{H} &= \underset{\sim}{\boldsymbol{\eta}} : \underline{\boldsymbol{\sigma}} + \underline{\boldsymbol{\rho}} \cdot \mathbf{v} + \underline{\mathbf{w}} \cdot \mathbf{E} + \underline{\mathbf{n}} \cdot \mathbf{H}\,,\\
\underset{\sim}{\mathbf{d}} : \underline{\boldsymbol{\sigma}}^{\mathrm{T}} + \underline{\mathbf{v}} \cdot \mathbf{v} + \underline{\boldsymbol{\epsilon}} \cdot \mathbf{E} + \underline{\boldsymbol{\xi}} \cdot \mathbf{H} &= \underset{\sim}{\mathbf{d}} : \underline{\boldsymbol{\sigma}} + \underline{\mathbf{v}} \cdot \mathbf{v} + \underline{\boldsymbol{\epsilon}} \cdot \mathbf{E} + \underline{\boldsymbol{\xi}} \cdot \mathbf{H}\,,\\
\underset{\sim}{\mathbf{b}} : \underline{\boldsymbol{\sigma}}^{\mathrm{T}} + \underline{\mathbf{m}} \cdot \mathbf{v} + \underline{\boldsymbol{\zeta}} \cdot \mathbf{E} + \underline{\boldsymbol{\mu}} \cdot \mathbf{H} &= \underset{\sim}{\mathbf{b}} : \underline{\boldsymbol{\sigma}} + \underline{\mathbf{m}} \cdot \mathbf{v} + \underline{\boldsymbol{\zeta}} \cdot \mathbf{E} + \underline{\boldsymbol{\mu}} \cdot \mathbf{H}\,,
\end{aligned}$$

respectively. Canceling the common terms in the above equations yields

$$\underset{\sim}{\boldsymbol{\eta}} : \underline{\boldsymbol{\sigma}} = \underset{\sim}{\boldsymbol{\eta}} : \underline{\boldsymbol{\sigma}}^{\mathrm{T}},$$
$$\underset{\sim}{\mathbf{d}} : \underline{\boldsymbol{\sigma}} = \underset{\sim}{\mathbf{d}} : \underline{\boldsymbol{\sigma}}^{\mathrm{T}},$$
$$\underset{\sim}{\mathbf{b}} : \underline{\boldsymbol{\sigma}} = \underset{\sim}{\mathbf{b}} : \underline{\boldsymbol{\sigma}}^{\mathrm{T}}.$$

In view of Eq. (D.11), it is concluded that $\underset{\sim}{\boldsymbol{\eta}}$, $\underset{\sim}{\mathbf{d}}$, and $\underset{\sim}{\mathbf{b}}$ possess second minor symmetry:

$$\underset{\sim}{\boldsymbol{\eta}} = \underset{\sim}{\boldsymbol{\eta}}^{\mathrm{t2}}, \tag{3.66b}$$
$$\underset{\sim}{\mathbf{d}} = \underset{\sim}{\mathbf{d}}^{\mathrm{t2}}, \tag{3.66c}$$
$$\underset{\sim}{\mathbf{b}} = \underset{\sim}{\mathbf{b}}^{\mathrm{t2}}. \tag{3.66d}$$

When reduced to index notation as described by Eq. (D.28), Eq. (3.66a) becomes

$$M_{ijkl} = M_{ijlk}. \tag{3.67a}$$

Similarly, Eqs. (3.66b), (3.66c), and (3.66d) in view of Eq. (D.12) become

$$\eta_{ijk} = \eta_{ikj}, \tag{3.67b}$$
$$d_{ijk} = d_{ikj}, \tag{3.67c}$$
$$b_{ijk} = b_{ikj}, \tag{3.67d}$$

respectively. Equations (3.65a), (3.65b), (3.67a), and (3.67b) bear the same symmetries as Eqs. (2.2a)–(2.2d) of Ref. 70, although the material parameters used in Ref. 70 are not equal to those in the present work but are instead related through Eqs. (3.45) and (3.49).

Having derived the symmetries of the compliance tensor, the Willis coupling tensors, and the piezoelectric and piezomagnetic coupling tensors due to Eqs. (3.61) and (3.62), attention is now turned to the symmetries and constraints that arise due to reciprocity and passivity.

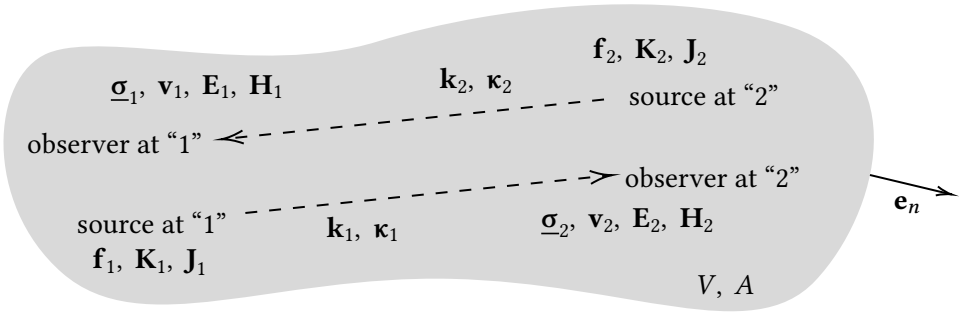

Figure 3.9: Elastodynamic and electromagnetic reciprocity in a piezoelectric and/or piezomagnetic medium. Suppose the stress $\underline{\boldsymbol{\sigma}}_1$, velocity $\mathbf{v}_1$, electric field $\mathbf{E}_1$, and magnetic field $\mathbf{H}_1$ are observed at location "1" due to a force $\mathbf{f}_2$, electric current density $\mathbf{J}_2$, and magnetic current density $\mathbf{K}_2$ at location "2." In a medium supporting reciprocal elastic and electromagnetic wave propagation, exchanging the position of the source and observer has no effect on the measured elastodynamic and electromagnetic fields.

Reciprocity

Auld presents two reciprocity theorems for piezoelectric media [223]. The first theorem applies in the electrostatic limit and was first derived by Havlice et al. [224]. The second theorem considers the electromagnetic nature of the piezoelectric medium. Pernas-Salomón and Shmuel [123] apply the first theorem to derive constraints on the stress-charge form of Eq. (3.6). In the present work, the second theorem is used to obtain constraints due to reciprocity on Eqs. (3.8). For completeness, the theorem is re-derived by considering elastic and electromagnetic wave motion with respect to two positions "1" and "2," as illustrated in Fig. 3.9.

The laws of Newton, Faraday, and Ampère dictate that at position "1,"

$$\boldsymbol{\nabla} \cdot \underline{\boldsymbol{\sigma}}_1 = \dot{\boldsymbol{\mu}}_1 - \mathbf{f}_1 \,, \tag{3.68a}$$

$$\boldsymbol{\nabla} \times \mathbf{E}_1 = -\dot{\mathbf{B}}_1 - \mathbf{K}_1 \,, \tag{3.68b}$$

$$\boldsymbol{\nabla} \times \mathbf{H}_1 = \dot{\mathbf{D}}_1 + \mathbf{J}_1 \,, \tag{3.68c}$$

respectively, while at position "2,"

$$\boldsymbol{\nabla} \cdot \underline{\boldsymbol{\sigma}}_2 = \dot{\boldsymbol{\mu}}_2 - \mathbf{f}_2 \,, \tag{3.69a}$$

$$\boldsymbol{\nabla} \times \mathbf{E}_2 = -\dot{\mathbf{B}}_2 - \mathbf{K}_2 \,, \tag{3.69b}$$

$$\boldsymbol{\nabla} \times \mathbf{H}_2 = \dot{\mathbf{D}}_2 + \mathbf{J}_2 \,, \tag{3.69c}$$

where the over-dot denotes a partial derivative with respect to time. Quadratic quantities are formed by taking the inner products of Eqs. (3.68a), (3.68b), and (3.68c) with $-\mathbf{v}_2$, $\mathbf{H}_2$, and $\mathbf{E}_2$, respectively, where the factor of -1 preceding $\mathbf{v}_2$ is motivated by the definition of the instantaneous elastodynamic intensity vector $-\underline{\boldsymbol{\sigma}} \cdot \mathbf{v}$:

$$-\mathbf{v}_2 \cdot (\boldsymbol{\nabla} \cdot \underline{\boldsymbol{\sigma}}_1) = -\mathbf{v}_2 \cdot \dot{\boldsymbol{\mu}}_1 + \mathbf{v}_2 \cdot \mathbf{f}_1 \,, \tag{3.70a}$$

$$\mathbf{H}_2 \cdot (\boldsymbol{\nabla} \times \mathbf{E}_1) = -\mathbf{H}_2 \cdot \dot{\mathbf{B}}_1 - \mathbf{H}_2 \cdot \mathbf{K}_1 \,, \tag{3.70b}$$

$$\mathbf{E}_2 \cdot (\boldsymbol{\nabla} \times \mathbf{H}_1) = \mathbf{E}_2 \cdot \dot{\mathbf{D}}_1 + \mathbf{E}_2 \cdot \mathbf{J}_1 \,. \tag{3.70c}$$

Similarly, Eqs. (3.69a), (3.69b), and (3.69c) are dotted with $-\mathbf{v}_1$, $\mathbf{H}_1$, and $\mathbf{E}_1$, respectively:

$$-\mathbf{v}_1 \cdot (\boldsymbol{\nabla} \cdot \underline{\boldsymbol{\sigma}}_2) = -\mathbf{v}_1 \cdot \dot{\boldsymbol{\mu}}_2 + \mathbf{v}_1 \cdot \mathbf{f}_2 \,, \tag{3.71a}$$

$$\mathbf{H}_1 \cdot (\boldsymbol{\nabla} \times \mathbf{E}_2) = -\mathbf{H}_1 \cdot \dot{\mathbf{B}}_2 - \mathbf{H}_1 \cdot \mathbf{K}_2 \,, \tag{3.71b}$$

$$\mathbf{E}_1 \cdot (\boldsymbol{\nabla} \times \mathbf{H}_2) = \mathbf{E}_1 \cdot \dot{\mathbf{D}}_2 + \mathbf{E}_1 \cdot \mathbf{J}_2 \,. \tag{3.71c}$$

Subtracting Eq. (3.71a) from Eq. (3.70a), Eq. (3.71c) from Eq. (3.70b), and Eq. (3.70c) from (3.71b) yields

$$\mathbf{v}_1 \cdot (\boldsymbol{\nabla} \cdot \underline{\boldsymbol{\sigma}}_2) - \mathbf{v}_2 \cdot (\boldsymbol{\nabla} \cdot \underline{\boldsymbol{\sigma}}_1) = \mathbf{v}_1 \cdot \dot{\boldsymbol{\mu}}_2 - \mathbf{v}_2 \cdot \dot{\boldsymbol{\mu}}_1 - \mathbf{v}_1 \cdot \mathbf{f}_2 + \mathbf{v}_2 \cdot \mathbf{f}_1 \,, \tag{3.72a}$$

$$\mathbf{H}_2 \cdot (\boldsymbol{\nabla} \times \mathbf{E}_1) - \mathbf{E}_1 \cdot (\boldsymbol{\nabla} \times \mathbf{H}_2) = -(\mathbf{H}_2 \cdot \dot{\mathbf{B}}_1 + \mathbf{E}_1 \cdot \dot{\mathbf{D}}_2) - \mathbf{E}_1 \cdot \mathbf{J}_2 - \mathbf{H}_2 \cdot \mathbf{K}_1 \,, \tag{3.72b}$$

$$\mathbf{H}_1 \cdot (\boldsymbol{\nabla} \times \mathbf{E}_2) - \mathbf{E}_2 \cdot (\boldsymbol{\nabla} \times \mathbf{H}_1) = -(\mathbf{H}_1 \cdot \dot{\mathbf{B}}_2 + \mathbf{E}_2 \cdot \dot{\mathbf{D}}_1) - \mathbf{E}_2 \cdot \mathbf{J}_1 - \mathbf{H}_1 \cdot \mathbf{K}_2 \,, \tag{3.72c}$$

respectively. Equation (3.72a) is simplified by noting from tensor analysis that

$$\boldsymbol{\nabla} \cdot (\underline{\boldsymbol{\sigma}}^{\mathrm{T}} \cdot \mathbf{v}) = (\boldsymbol{\nabla} \cdot \underline{\boldsymbol{\sigma}}) \cdot \mathbf{v} + \underline{\boldsymbol{\sigma}} : \boldsymbol{\nabla} \mathbf{v} \,.$$

Combining this relation with Eqs. (3.61) and (3.62) yields[14]

$$\mathbf{v} \cdot (\boldsymbol{\nabla} \cdot \underline{\boldsymbol{\sigma}}) = \boldsymbol{\nabla} \cdot (\underline{\boldsymbol{\sigma}} \cdot \mathbf{v}) - \underline{\boldsymbol{\sigma}} : \underline{\dot{\boldsymbol{\varepsilon}}},$$

insertion of which into the left-hand side of Eq. (3.72a) yields

$$\boldsymbol{\nabla} \cdot (\underline{\boldsymbol{\sigma}}_2 \cdot \mathbf{v}_1 - \underline{\boldsymbol{\sigma}}_1 \cdot \mathbf{v}_2) = \underline{\boldsymbol{\sigma}}_2 : \underline{\dot{\boldsymbol{\varepsilon}}}_1 - \underline{\boldsymbol{\sigma}}_1 : \underline{\dot{\boldsymbol{\varepsilon}}}_2 + \mathbf{v}_1 \cdot \dot{\boldsymbol{\mu}}_2 - \mathbf{v}_2 \cdot \dot{\boldsymbol{\mu}}_1 - \mathbf{v}_1 \cdot \mathbf{f}_2 + \mathbf{v}_2 \cdot \mathbf{f}_1. \tag{3.73}$$

Meanwhile, noting from vector analysis that

$$\mathbf{H} \cdot (\boldsymbol{\nabla} \times \mathbf{E}) = \mathbf{E} \cdot (\boldsymbol{\nabla} \times \mathbf{H}) + \boldsymbol{\nabla} \cdot (\mathbf{E} \times \mathbf{H})$$

allows the left-hand sides of Eqs. (3.72b) and (3.72c) to be written as $\boldsymbol{\nabla} \cdot (\mathbf{E}_1 \times \mathbf{H}_2)$ and $\boldsymbol{\nabla} \cdot (\mathbf{E}_2 \times \mathbf{H}_1)$, respectively:

$$\boldsymbol{\nabla} \cdot (\mathbf{E}_1 \times \mathbf{H}_2) = -(\mathbf{H}_2 \cdot \dot{\mathbf{B}}_1 + \mathbf{E}_1 \cdot \dot{\mathbf{D}}_2) - \mathbf{E}_1 \cdot \mathbf{J}_2 - \mathbf{H}_2 \cdot \mathbf{K}_1\,, \tag{3.74}$$

$$\boldsymbol{\nabla} \cdot (\mathbf{E}_2 \times \mathbf{H}_1) = -(\mathbf{H}_1 \cdot \dot{\mathbf{B}}_2 + \mathbf{E}_2 \cdot \dot{\mathbf{D}}_1) - \mathbf{E}_2 \cdot \mathbf{J}_1 - \mathbf{H}_1 \cdot \mathbf{K}_2\,. \tag{3.75}$$

Subtracting Eq. (3.75) from Eq. (3.74) yields

$$\begin{aligned}\boldsymbol{\nabla} \cdot (\mathbf{E}_1 \times \mathbf{H}_2 - \mathbf{E}_2 \times \mathbf{H}_1) = &-(\mathbf{H}_2 \cdot \dot{\mathbf{B}}_1 - \mathbf{H}_1 \cdot \dot{\mathbf{B}}_2 + \mathbf{E}_1 \cdot \dot{\mathbf{D}}_2 - \mathbf{E}_2 \cdot \dot{\mathbf{D}}_1) \\ &+ \mathbf{E}_2 \cdot \mathbf{J}_1 - \mathbf{E}_1 \cdot \mathbf{J}_2 + \mathbf{H}_1 \cdot \mathbf{K}_2 - \mathbf{H}_2 \cdot \mathbf{K}_1\,.\end{aligned} \tag{3.76}$$

Adding Eqs. (3.73) and (3.76), integrating over a volume V that contains points "1" and "2" enclosed by a surface A with outward unit normal $\mathbf{e}_n$, and applying the divergence theorem results in

$$\begin{aligned}&\oint_A (\underline{\boldsymbol{\sigma}}_2 \cdot \mathbf{v}_1 - \underline{\boldsymbol{\sigma}}_1 \cdot \mathbf{v}_2 + \mathbf{E}_1 \times \mathbf{H}_2 - \mathbf{E}_2 \times \mathbf{H}_1) \cdot \mathbf{e}_n \, dA \\ &\quad = \int_V (\mathbf{v}_2 \cdot \mathbf{f}_1 - \mathbf{v}_1 \cdot \mathbf{f}_2 + \mathbf{E}_2 \cdot \mathbf{J}_1 - \mathbf{E}_1 \cdot \mathbf{J}_2 + \mathbf{H}_1 \cdot \mathbf{K}_2 - \mathbf{H}_2 \cdot \mathbf{K}_1)\, dV \\ &\qquad + \int_V (\underline{\boldsymbol{\sigma}}_2 : \underline{\dot{\boldsymbol{\varepsilon}}}_1 - \underline{\boldsymbol{\sigma}}_1 : \underline{\dot{\boldsymbol{\varepsilon}}}_2 + \mathbf{v}_1 \cdot \dot{\boldsymbol{\mu}}_2 - \mathbf{v}_2 \cdot \dot{\boldsymbol{\mu}}_1 - \mathbf{E}_1 \cdot \dot{\mathbf{D}}_2 + \mathbf{E}_2 \cdot \dot{\mathbf{D}}_1 + \mathbf{H}_1 \cdot \dot{\mathbf{B}}_2 - \mathbf{H}_2 \cdot \dot{\mathbf{B}}_1) dV.\end{aligned} \tag{3.77}$$

[14] See Eq. (3.123); $\boldsymbol{\nabla}\mathbf{v} = \underline{\dot{\boldsymbol{\varepsilon}}}$ for an irrotational medium.

It is noted in passing that Eq. (3.77) equals Eq. (8.183) of Ref. 223 with $\dot{\underline{\boldsymbol{\varepsilon}}}$, $\mathbf{v}$, $\mathbf{H}$, and $\mathbf{D}$ evaluated at position "1" and $\underline{\boldsymbol{\sigma}}$, $\mathbf{f}$, $\dot{\boldsymbol{\mu}}$, $\mathbf{E}$, $\dot{\mathbf{B}}$, $\mathbf{J}$, and $\mathbf{K}$ evaluated at position "2,"

$$\oint_A (-\underline{\boldsymbol{\sigma}}_2 \cdot \mathbf{v}_1 + \mathbf{E}_2 \times \mathbf{H}_1) \cdot \mathbf{e}_n \, dA = -\int_V (\underline{\boldsymbol{\sigma}}_2 : \dot{\underline{\boldsymbol{\varepsilon}}}_1 + \mathbf{v}_1 \cdot \dot{\boldsymbol{\mu}}_2 + \mathbf{E}_2 \cdot \dot{\mathbf{D}}_1 + \mathbf{H}_1 \cdot \dot{\mathbf{B}}_2) \, dV - \int_V \mathbf{H}_1 \cdot \mathbf{K}_2 \, dV + \int_V (\mathbf{v}_1 \cdot \mathbf{f}_2 - \mathbf{E}_2 \cdot \mathbf{J}_1) \, dV,$$

subtracted from the same equation with the positions interchanged:

$$\oint_A (-\underline{\boldsymbol{\sigma}}_1 \cdot \mathbf{v}_2 + \mathbf{E}_1 \times \mathbf{H}_2) \cdot \mathbf{e}_n \, dA = -\int_V (\underline{\boldsymbol{\sigma}}_1 : \dot{\underline{\boldsymbol{\varepsilon}}}_2 + \mathbf{v}_2 \cdot \dot{\boldsymbol{\mu}}_1 + \mathbf{E}_1 \cdot \dot{\mathbf{D}}_2 + \mathbf{H}_2 \cdot \dot{\mathbf{B}}_1) \, dV - \int_V \mathbf{H}_2 \cdot \mathbf{K}_1 \, dV + \int_V (\mathbf{v}_2 \cdot \mathbf{f}_1 - \mathbf{E}_1 \cdot \mathbf{J}_2) \, dV.$$

The region of integration in Eq. (3.77) is now extended infinitely far, from where there are no incoming elastic and electromagnetic waves. This limit corresponds to the radius R of the surface tending to infinity, whereas the fields $\underline{\boldsymbol{\sigma}}$, $\mathbf{v}$, $\mathbf{E}$, and $\mathbf{H}$ emanating from points "1" and "2" are all proportional to $1/R$. The magnitude of the products $\underline{\boldsymbol{\sigma}} \cdot \mathbf{v}$ and $\mathbf{E} \times \mathbf{H}$ in this limit is therefore proportional to $1/R^2$. When taking the differences $\underline{\boldsymbol{\sigma}}_1 \cdot \mathbf{v}_2 - \underline{\boldsymbol{\sigma}}_2 \cdot \mathbf{v}_1$ and $\mathbf{E}_1 \cdot \mathbf{H}_2 - \mathbf{E}_2 \cdot \mathbf{H}_1$, the terms proportional to $1/R^2$ cancel, and the leading-order term is proportional to $1/R^3$. Since the area A is proportional to R^2, the integral on the left-hand of the above equation is proportional to $1/R$, which vanishes as $R \to \infty$ [225, p. 58]. Thus the left-hand side of Eq. (3.77) vanishes. Meanwhile, the reciprocity theorem states that the first integral on the right-hand side of Eq. (3.77) vanishes [70, 122, 221, 225]. The second integral on the right-hand side must therefore also vanish. Since the region of integration can be made arbitrarily small, the integrand itself equals zero:

$$\underline{\boldsymbol{\sigma}}_2 : \dot{\underline{\boldsymbol{\varepsilon}}}_1 - \underline{\boldsymbol{\sigma}}_1 : \dot{\underline{\boldsymbol{\varepsilon}}}_2 + \mathbf{v}_1 \cdot \dot{\boldsymbol{\mu}}_2 - \mathbf{v}_2 \cdot \dot{\boldsymbol{\mu}}_1 - \mathbf{E}_1 \cdot \dot{\mathbf{D}}_2 + \mathbf{E}_2 \cdot \dot{\mathbf{D}}_1 - \mathbf{H}_2 \cdot \dot{\mathbf{B}}_1 + \mathbf{H}_1 \cdot \dot{\mathbf{B}}_2 = 0 \,. \tag{3.78}$$

Note the presence of a time derivative in each term of Eq. (3.78). Assuming the fields are time-harmonic reduces the time derivatives to factors of $-i\omega$, which is common to all terms and can therefore be eliminated without lack of generality:

$$\underline{\boldsymbol{\sigma}}_2 : \underline{\boldsymbol{\varepsilon}}_1 - \underline{\boldsymbol{\sigma}}_1 : \underline{\boldsymbol{\varepsilon}}_2 + \mathbf{v}_1 \cdot \boldsymbol{\mu}_2 - \mathbf{v}_2 \cdot \boldsymbol{\mu}_1 - \mathbf{E}_1 \cdot \mathbf{D}_2 + \mathbf{E}_2 \cdot \mathbf{D}_1 - \mathbf{H}_2 \cdot \mathbf{B}_1 + \mathbf{H}_1 \cdot \mathbf{B}_2 = 0 \,. \tag{3.79}$$

Equations (3.44), (3.48), (3.52), and (3.57) are substituted into Eq. (3.79), and the inner products are expanded. Rearranging terms and invoking Eqs. (D.3), (D.16), (D.18), and (D.29) yields

$$
\begin{aligned}
&\underline{\underline{\sigma}}_2 : [(\mathbb{M} - \mathbb{M}^{\mathrm{T}}) : \underline{\underline{\sigma}}_1 + (\underset{\sim}{\gamma} + \underset{\sim}{\eta}^{\mathrm{T2}}) \cdot \mathbf{v}_1 + (\underline{\underline{e}} - \underline{\underline{d}}^{\mathrm{T2}}) \cdot \mathbf{E}_1 + (\underline{\underline{c}} + \underline{\underline{b}}^{\mathrm{T2}}) \cdot \mathbf{H}_1] \\
&\quad + \mathbf{v}_1 \cdot [(\underline{\underline{\rho}} - \underline{\underline{\rho}}^{\mathrm{T}}) \cdot \mathbf{v}_2 + (\underline{\mathbf{w}} + \underline{\mathbf{v}})^{\mathrm{T}} \cdot \mathbf{E}_2 + (\underline{\underline{n}} - \underline{\underline{m}}^{\mathrm{T}}) \cdot \mathbf{H}_2] - \mathbf{v}_2 \cdot [(\underset{\sim}{\eta} + \underset{\sim}{\gamma}^{\mathrm{T1}}) : \underline{\underline{\sigma}}_1] \\
&\quad - \mathbf{E}_1 \cdot [(\underline{\mathbf{v}} + \underline{\mathbf{w}}^{\mathrm{T}}) \cdot \mathbf{v}_2 + (\underline{\underline{\xi}} + \underline{\underline{\zeta}}^{\mathrm{T}}) \cdot \mathbf{H}_2] + \mathbf{E}_2 \cdot [(\underline{\underline{d}} - \underline{\underline{e}}^{\mathrm{T1}}) : \underline{\underline{\sigma}}_1 + (\underline{\underline{\epsilon}} - \underline{\underline{\epsilon}}^{\mathrm{T}}) \cdot \mathbf{E}_1] \\
&\quad + \mathbf{H}_2 \cdot [(-\underline{\underline{b}} - \underline{\underline{c}}^{\mathrm{T1}}) : \underline{\underline{\sigma}}_1] + \mathbf{H}_1 \cdot [(\underline{\underline{m}} - \underline{\underline{n}}^{\mathrm{T}}) \cdot \mathbf{v}_2 + (\underline{\underline{\zeta}} + \underline{\underline{\xi}}^{\mathrm{T}}) \cdot \mathbf{E}_2 + (\underline{\underline{\mu}} - \underline{\underline{\mu}}^{\mathrm{T}}) \cdot \mathbf{H}_2] = 0 \,.
\end{aligned}
$$

Since the force density, electric current density, and magnetic current density sources are arbitrary, the stress, velocity, electric, and magnetic fields are independent [70, 123]. Each term in the above equation must therefore vanish individually to satisfy the equality, yielding

$$\mathbb{M} = \mathbb{M}^{\mathrm{T}} \,, \tag{3.80a}$$

$$\underline{\underline{\rho}} = \underline{\underline{\rho}}^{\mathrm{T}} \,, \tag{3.80b}$$

$$\underline{\underline{\epsilon}} = \underline{\underline{\epsilon}}^{\mathrm{T}} \,, \tag{3.80c}$$

$$\underline{\underline{\mu}} = \underline{\underline{\mu}}^{\mathrm{T}} \tag{3.80d}$$

for the diagonal elements of the block tensor provided in Eq. (3.8),

$$\underset{\sim}{\eta} = -\underset{\sim}{\gamma}^{\mathrm{T1}} \,, \tag{3.80e}$$

$$\underline{\underline{\zeta}} = -\underline{\underline{\xi}}^{\mathrm{T}} \tag{3.80f}$$

for the bianisotropic coupling tensors,

$$\underline{\underline{e}} = \underline{\underline{d}}^{\mathrm{T2}} \,, \tag{3.80g}$$

$$\underline{\underline{c}} = -\underline{\underline{b}}^{\mathrm{T2}} \tag{3.80h}$$

for the piezoelectric and piezomagnetic coupling tensors, and

$$\underline{\mathbf{w}} = -\underline{\mathbf{v}}^{\mathrm{T}} \,, \tag{3.80i}$$

$$\underline{\underline{n}} = \underline{\underline{m}}^{\mathrm{T}} \tag{3.80j}$$

for the electro- and magnetomomentum coupling tensors. In view of Eqs. (D.20), the symmetries

$$\underset{\sim}{\boldsymbol{\gamma}} = -\underset{\sim}{\boldsymbol{\eta}}^{\mathrm{T2}}, \tag{3.80k}$$

$$\underset{\sim}{\mathbf{d}} = \underset{\sim}{\mathbf{e}}^{\mathrm{T1}}, \tag{3.80l}$$

$$\underset{\sim}{\mathbf{b}} = -\underset{\sim}{\mathbf{c}}^{\mathrm{T1}} \tag{3.80m}$$

are redundant with Eqs. (3.80e), (3.80g), and (3.80h), respectively, but they are listed because Muhlestein et al. [70] writes major symmetries of rank-3 tensors in terms of the T1 transposition while Pernas-Salomón and Shmuel [123] write these symmetries in terms of the T2 transposition. The novel results of the present section are given by Eqs. (3.80h) and (3.80j) for piezomagnetic and magnetomomentum coupling, respectively.

The minus signs in Eqs. (3.80) reflect how the fields and displacements in Eq. (3.8) transform under time reversal, $t \longrightarrow -t$. Minus signs do not appear for constitutive parameters that relate field variables [the right-hand column of Eq. (3.8)] to displacement variables [the left-hand side of Eq. (3.8)] that are either both even or both odd under time reversal. Minus signs appear in Eqs. (3.80) for cases in which the field variable is even and the displacement variable is odd, or in which the field variable is odd and the displacement variable is even. The transformation properties of the displacement and field variables in Eqs. (3.8) are summarized in Table 3.1, and more discussion of the transformation properties of mechanical and electromagnetic quantities is provided by Jackson [226, Sec. 6.10]. Constitutive parameters that relate two quantities that transform *similarly* under time reversal are displayed in red in Eq. (3.81), and parameters that relate two quantities that transform *differently* under time reversal are displayed in blue:

$$\begin{pmatrix} \underline{\boldsymbol{\varepsilon}} \\ \underline{\boldsymbol{\mu}} \\ \mathbf{D} \\ \mathbf{B} \end{pmatrix} = \begin{pmatrix} \mathbb{M} & \underset{\sim}{\boldsymbol{\gamma}} & \underline{\mathbf{e}} & \underline{\mathbf{c}} \\ \underset{\sim}{\boldsymbol{\eta}} & \underline{\boldsymbol{\rho}} & \underline{\mathbf{w}} & \underline{\mathbf{n}} \\ \underline{\mathbf{d}} & \underline{\mathbf{v}} & \underline{\boldsymbol{\epsilon}} & \underline{\boldsymbol{\xi}} \\ \underline{\mathbf{b}} & \underline{\mathbf{m}} & \underline{\boldsymbol{\zeta}} & \underline{\boldsymbol{\mu}} \end{pmatrix} \begin{pmatrix} \underline{\boldsymbol{\sigma}} \\ \mathbf{v} \\ \mathbf{E} \\ \mathbf{H} \end{pmatrix}. \tag{3.81}$$

The color-coded Eq. (3.81) and Table 3.1 will also be used to interpret the results of Sec. 3.4.

Quantity	Symbol	Rank	Spatial inversion	Time reversal
Strain	$\underline{\boldsymbol{\varepsilon}}$	2	odd	even
Momentum density	$\boldsymbol{\mu}$	1	odd	odd
Electric displacement	$\mathbf{D}$	1	odd	even
Magnetic flux density	$\mathbf{B}$	1	even	odd
Stress	$\underline{\boldsymbol{\sigma}}$	2	odd	even
Velocity	$\mathbf{v}$	1	odd	odd
Electric field	$\mathbf{E}$	1	odd	even
Magnetic field	$\mathbf{H}$	1	even	odd

Table 3.1: Transformation properties of the displacements and fields in Eqs. (3.8) under rotation (rank), spatial inversion, and time reversal. Based partially on Table 6.1 of Ref. 226.

Equations (3.80) can be reduced to index notation by way of Eqs. (D.4), (D.17), (D.19), and (D.30). The diagonal elements of the indicial form of Eq. (3.8) satisfy

$$M_{ijkl} = M_{klij}\,, \tag{3.82a}$$

$$\rho_{ij} = \rho_{ji}\,, \tag{3.82b}$$

$$\epsilon_{ij} = \epsilon_{ji}\,, \tag{3.82c}$$

$$\mu_{ij} = \mu_{ji}\,, \tag{3.82d}$$

while the bianisotropic, piezoelectric, piezomagnetic, and electro- and magneto-momentum matrix elements satisfy

$$\eta_{ijk} = -\gamma_{jki}\,, \tag{3.82e}$$

$$\zeta_{ij} = -\xi_{ji}\,, \tag{3.82f}$$

$$e_{ijk} = d_{kij}\,, \tag{3.82g}$$

$$c_{ijk} = -b_{kij}\,, \tag{3.82h}$$

$$w_{ij} = -v_{ji}\,, \tag{3.82i}$$

$$n_{ij} = m_{ji}\,, \tag{3.82j}$$

where Eqs. (3.80k)–(3.80m) reduce to

$$\gamma_{ijk} = -\eta_{kij}\,, \tag{3.82k}$$

$$d_{ijk} = e_{jki}\,, \tag{3.82l}$$

$$b_{ijk} = -c_{jki}\,. \tag{3.82m}$$

Equations (3.82), along with the indicial versions of Eqs. (3.45) and (3.49), allow for more immediate comparison to the results of Refs. 69, 70, and 123, as shown below.

Recovering the results of Muhlestein et al. For simple cases, symbolic notation can be used to recover the results of Ref. 70. For example, the major symmetry of the compliance tensor $\mathbb{M}$ given by Eq. (3.80a) can recover the major symmetry of the stiffness tensor $\mathbb{C}$ used in Ref. 70 as follows. In view of Eq. (3.45a), Eq. (3.80a) implies that $(\mathbb{C}^{-1})^{\mathrm{T}} = \mathbb{C}^{-1}$. Invoking Eq. (D.37) yields $(\mathbb{C}^{\mathrm{T}})^{-1} = \mathbb{C}^{-1}$. Taking the inverse of this relation and invoking the fact that the inverse of the inverse of a rank four tensor is the rank-four tensor itself [Eq. (D.36)] shows that $\mathbb{C} = \mathbb{C}^{\mathrm{T}}$, recovering Eqs. (3.10a) of Ref. 70 when expressed in the index notation provided by Eq. (D.30).

For other cases, index notation simplifies the algebraic manipulation required to recover the results of Ref. 70. For example, the symmetry of the dynamic density tensor of the strain form when written in index notation is provided by Eq. (3.82b). To obtain the corresponding relation of the stress form, Eq. (3.60b) is reduced to index notation, where $(\mathbb{M}^{-1})_{kmlp}$ denotes the component of the basis representation of $\mathbb{M}^{-1}$:

$$\tilde{\rho}_{ij} = \rho_{ij} - \eta_{ikm}(\mathbb{M}^{-1})_{kmlp}\gamma_{lpj}\,. \tag{3.83}$$

Transposition of Eq. (3.83) is achieved by interchanging the indices i and j:

$$\tilde{\rho}_{ji} = \rho_{ji} - \eta_{jkm}(\mathbb{M}^{-1})_{kmlp}\gamma_{lpi}\,. \tag{3.84}$$

Subtracting Eq. (3.84) from Eq. (3.83) and noting from Eq. (3.82b) that $\rho_{ij} - \rho_{ji} = 0$ yields

$$\tilde{\rho}_{ij} - \tilde{\rho}_{ji} = -\eta_{ikm}(\mathbb{M}^{-1})_{kmlp}\gamma_{lpj} + \eta_{jmk}(\mathbb{M}^{-1})_{kmlp}\gamma_{lpi}\,. \tag{3.85}$$

The first term on the right-hand side of Eq. (3.85) is manipulated by invoking Eqs. (3.82e) and (3.82k):

$$-\eta_{ikm}(\mathbb{M}^{-1})_{kmlp}\gamma_{lpj} = -(-\gamma_{kmi})(\mathbb{M}^{-1})_{kmlp}(-\eta_{jlp})\,.$$

Invoking Eq. (3.82a) yields

$$-\eta_{ikm}(\mathbb{M}^{-1})_{kmlp}\gamma_{lpj} = -\eta_{jlp}(\mathbb{M}^{-1})_{lpkm}\gamma_{kmi}\,. \tag{3.86}$$

Since l, k, m, and p are summing indices, they can be renamed for one another ($p \leftrightarrow m$ and $l \leftrightarrow k$) on the right-hand side of Eq. (3.86):

$$-\eta_{ikm}(\mathbb{M}^{-1})_{kmlp}\gamma_{lpj} = -\eta_{jkm}(\mathbb{M}^{-1})_{kmlp}\gamma_{lpi}\,. \tag{3.87}$$

Inserting Eq. (3.87) into Eq. (3.85) yields

$$\tilde{\rho}_{ij} - \tilde{\rho}_{ji} = -\eta_{jkm}(\mathbb{M}^{-1})_{kmlp}\gamma_{lpi} + \eta_{jkm}(\mathbb{M}^{-1})_{kmlp}\gamma_{lpi} = 0\,, \tag{3.88}$$

resulting in

$$\tilde{\rho}_{ij} = \tilde{\rho}_{ji}\,,$$

which recovers Eq. (3.10b) of Ref. 70.

Indicial notation can be used to also recover the relationship between the Willis coupling tensors of the stress form from that of the strain form. The mapping between $\underset{\sim}{\tilde{\boldsymbol{\eta}}}$ and $\underset{\sim}{\boldsymbol{\eta}}$ provided by Eq. (3.49a) is first represented wiht index notation:

$$\tilde{\eta}_{ijk} = \eta_{imn}(\mathbb{M}^{-1})_{mnjk}\,.$$

Invoking Eq. (3.82e) results in

$$\tilde{\eta}_{ijk} = -\gamma_{mni}(\mathbb{M}^{-1})_{mnjk}\,. \tag{3.89}$$

Next, it is noted that Eq. (3.45b) in index notation can be expressed as

$$\gamma_{mni} = -M_{mnpq}\tilde{\gamma}_{pqi}\,. \tag{3.90}$$

Insertion of Eq. (3.90) into Eq. (3.89) yields

$$\tilde{\eta}_{ijk} = M_{mnpq}\tilde{\gamma}_{pqi}(\mathbb{M}^{-1})_{mnjk} \, .$$

The major symmetry of the compliance given indicially by Eq. (3.82a) is invoked, where it is noted that the major transpose of the inverse of a rank-4 tensor equals the inverse of the major transpose [Eq. (D.37)], giving

$$\tilde{\eta}_{ijk} = \tilde{\gamma}_{pqi}M_{pqmn}(\mathbb{M}^{-1})_{mnjk} \, . \tag{3.91}$$

Since $M_{pqmn}(\mathbb{M}^{-1})_{mnjk}$ are the components I_{pqjk} of the rank-4 identity tensor $\mathbb{I}$, Eq. (3.91) becomes

$$\tilde{\eta}_{ijk} = \tilde{\gamma}_{pqi}I_{pqjk} \, . \tag{3.92}$$

Since $I_{pqjk} = I_{jkpq}$ [227, Sec. 5.5], Eq. (3.92) becomes

$$\tilde{\eta}_{ijk} = \tilde{\gamma}_{pqi}I_{jkpq} = \tilde{\gamma}_{ijk} \, ,$$

recovering Eq. (3.10c) of Ref. 70.

Recovering the results of Pernas-Salomón and Shmuel The results of Pernas-Salomón and Shmuel [123] recover those of Muhlestein et al. [70] in the absence of the electric field. It is now demonstrated that the results of the present section recover the constraints derived in Ref. 123 due to reciprocity on the permittivity tensor and the piezoelectric and electromomentum coupling tensors of the stress-charge form. The constraint on the permittivity tensor of the stress form is recovered first by reducing Eq. (3.60e) to index notation,

$$\tilde{\epsilon}_{ij} = \epsilon_{ij} - d_{ikm}(\mathbb{M}^{-1})_{kmlp}e_{lpj} \, , \tag{3.93}$$

the transpose of which is

$$\tilde{\epsilon}_{ji} = \epsilon_{ji} - d_{jkm}(\mathbb{M}^{-1})_{kmlp}e_{lpi} \, . \tag{3.94}$$

Subtracting Eq. (3.94) from Eq. (3.93) and invoking Eq. (3.82c) yields

$$\tilde{\epsilon}_{ij} - \tilde{\epsilon}_{ji} = -d_{ikm}(\mathbb{M}^{-1})_{kmlp}e_{lpj} + d_{jkm}(\mathbb{M}^{-1})_{kmlp}e_{lpi} \,. \tag{3.95}$$

The first term on the right-hand side of Eq. (3.95) is manipulated by invoking Eqs. (3.82l) and (3.82g):

$$-d_{ikm}(\mathbb{M}^{-1})_{kmlp}e_{lpj} = -e_{kmi}(\mathbb{M}^{-1})_{kmlp}d_{jlp} \,.$$

Invoking Eq. (3.82a) yields

$$-d_{ikm}(\mathbb{M}^{-1})_{kmlp}e_{lpj} = -d_{jlp}(\mathbb{M}^{-1})_{lpkm}e_{kmi} \,. \tag{3.96}$$

Since l, k, m, and p are summing indices, they can be renamed for one another ($p \leftrightarrow m$ and $l \leftrightarrow k$) on the right-hand side of Eq. (3.96), resulting in

$$-d_{ikm}(\mathbb{M}^{-1})_{kmlp}e_{lpj} = -d_{jkm}(\mathbb{M}^{-1})_{kmlp}e_{lpi} \,. \tag{3.97}$$

Inserting Eq. (3.97) into Eq. (3.95) yields

$$\tilde{\epsilon}_{ij} - \tilde{\epsilon}_{ji} = -d_{jkm}(\mathbb{M}^{-1})_{kmlp}e_{lpi} + d_{jkm}(\mathbb{M}^{-1})_{kmlp}e_{lpi} = 0 \,, \tag{3.98}$$

resulting in

$$\tilde{\epsilon}_{ij} = \tilde{\epsilon}_{ji} \,.$$

The first of Eqs. (42) of Ref. 123 is therefore recovered.

Attention is next turned to the piezoelectric coupling tensors. Renaming indices $i \mapsto m$, $j \mapsto n$, and $k \mapsto i$ in Eq. (3.82g) yields

$$d_{imn} = e_{mni} \,. \tag{3.99}$$

Multiplying Eq. (3.99) by $(\mathbb{M}^{-1})_{jkmn}$ yields

$$d_{imn}(\mathbb{M}^{-1})_{jkmn} = e_{mni}(\mathbb{M}^{-1})_{jkmn} \,.$$

Invoking Eq. (3.82a) results in

$$d_{imn}(\mathbb{M}^{-1})_{mnjk} = (\mathbb{M}^{-1})_{jkmn}e_{mni}\,. \tag{3.100}$$

Since the indicial forms of Eqs. (3.60g) and (3.60f) are

$$\tilde{d}_{ijk} = d_{imn}(\mathbb{M}^{-1})_{mnjk} \quad \text{and} \quad \tilde{e}_{jki} = (\mathbb{M}^{-1})_{jkmn}e_{mni}\,, \tag{3.101}$$

respectively, Eq. (3.100) becomes

$$\tilde{d}_{ijk} = \tilde{e}_{jki}\,.$$

Renaming indices $i \mapsto k$, $j \mapsto i$, and $k \mapsto j$ yields

$$\tilde{e}_{ijk} = \tilde{d}_{kij}\,, \tag{3.102}$$

which recovers the second of Eqs. (42) of Ref. 123. Equation (3.102) is well known in the piezoelectricity literature [209, Table 1].

Finally, the relationship between the electromomentum coupling tensors of the strain form is converted to that of the stress form. Equations (3.60h) and (3.60i) in index notation are expressed as

$$\tilde{w}_{ij} = -w_{ij} + \eta_{imn}(\mathbb{M}^{-1})_{mnkl}e_{klj}\,, \tag{3.103a}$$

$$\tilde{v}_{ij} = v_{ij} - d_{imn}(\mathbb{M}^{-1})_{mnkl}\gamma_{klj}\,. \tag{3.103b}$$

Invoking Eqs. (3.82e) and (3.99) yields

$$\tilde{w}_{ij} = -w_{ij} + e_{klj}(\mathbb{M}^{-1})_{mnkl}\gamma_{mni}\,, \tag{3.104a}$$

$$\tilde{v}_{ij} = v_{ij} - e_{mni}(\mathbb{M}^{-1})_{mnkl}\gamma_{klj}\,. \tag{3.104b}$$

Transposing Eq. (3.104b) amounts to interchanging $i \leftrightarrow j$, yielding

$$\tilde{v}_{ji} = v_{ji} - e_{mnj}(\mathbb{M}^{-1})_{mnkl}\gamma_{kli}\,,$$

By Eq. (3.82i), the above equation becomes

$$\tilde{v}_{ji} = -w_{ij} - e_{mnj}(\mathbb{M}^{-1})_{mnkl}\gamma_{kli} \,. \tag{3.105}$$

Subtracting Eq. (3.104a) from Eq. (3.105) yields

$$\tilde{v}_{ji} - \tilde{w}_{ij} = e_{klj}(\mathbb{M}^{-1})_{mnkl}\gamma_{mni} - e_{mnj}(\mathbb{M}^{-1})_{mnkl}\gamma_{kli} \,. \tag{3.106}$$

The summing indices in the second term are interchanged, e.g., $m \leftrightarrow k$ and $n \leftrightarrow l$, and Eqs. (3.82a) and (D.37) are invoked, resulting in

$$\tilde{v}_{ji} - \tilde{w}_{ij} = e_{klj}(\mathbb{M}^{-1})_{mnkl}\gamma_{mni} - e_{klj}(\mathbb{M}^{-1})_{mnkl}\gamma_{mni} = 0 \,,$$

showing that $\tilde{v}_{ji} = \tilde{w}_{ij}$. The third of Eqs. (42) of Ref. 123 is therefore recovered.

Recovering the results of Kong Setting the elastodynamic parameters to zero reduces the present formulation to pure electrodynamics, in which case there is no distinction between the stress-charge and strain-charge forms of the constitutive equations.[15] However, an alternative convention is sometimes used in electromagnetism in which **D** and **H** (rather than **D** and **B**) appear on the left-hand side of the constitutive equations:

$$\begin{pmatrix} c\mathbf{D} \\ \mathbf{H} \end{pmatrix} = \begin{pmatrix} \underline{\mathbf{P}} & \underline{\mathbf{L}} \\ \underline{\mathbf{M}} & \underline{\mathbf{Q}} \end{pmatrix} \begin{pmatrix} \mathbf{E} \\ c\mathbf{B} \end{pmatrix} . \tag{3.107}$$

Kong uses the Eq. (3.107) to show that reciprocity enforces [69, Eqs. (23)]

$$\underline{\mathbf{P}} = \underline{\mathbf{P}}^{\mathrm{T}} \,, \tag{3.108a}$$

$$\underline{\mathbf{Q}} = \underline{\mathbf{Q}}^{\mathrm{T}} \,, \tag{3.108b}$$

$$\underline{\mathbf{M}} = \underline{\mathbf{L}}^{\mathrm{T}} \,. \tag{3.108c}$$

[15] Since there is no ambiguity here between elastic and electromagnetic waves, C_0 from Sec. 3.2 is denoted by c in this section to match the notation of Kong [69].

To determine whether Eqs. (3.108) are consistent with Eqs. (3.80c), (3.80d), and (3.80f), the mappings between the **D**-**H** and **D**-**B** forms given by Eq. (5) of Ref. 69 are used:

$$\underline{\boldsymbol{\epsilon}} = \frac{1}{c}(\underline{\mathbf{P}} - \underline{\mathbf{L}} \cdot \underline{\mathbf{Q}}^{-1} \cdot \underline{\mathbf{M}}) \,, \tag{3.109a}$$

$$\underline{\boldsymbol{\mu}} = \frac{1}{c}\underline{\mathbf{Q}}^{-1} \,, \tag{3.109b}$$

$$\underline{\boldsymbol{\xi}} = \frac{1}{c}\underline{\mathbf{L}} \cdot \underline{\mathbf{Q}}^{-1} \,, \tag{3.109c}$$

$$\underline{\boldsymbol{\zeta}} = -\frac{1}{c}\underline{\mathbf{Q}}^{-1} \cdot \underline{\mathbf{M}} \,. \tag{3.109d}$$

Symbolic notation can be used to recover Eq. (3.80d) from Eq. (3.108b). Transposing Eq. (3.109b) yields

$$\underline{\boldsymbol{\mu}}^{\mathrm{T}} = \frac{1}{c}(\underline{\mathbf{Q}}^{-1})^{\mathrm{T}} = \frac{1}{c}(\underline{\mathbf{Q}}^{\mathrm{T}})^{-1} \,, \tag{3.110}$$

where the second equality holds because the inverse of the transpose of a rank-2 tensor equals the transpose of the inverse.[16] Subtracting Eq. (3.110) from Eq. (3.109b) yields

$$\underline{\boldsymbol{\mu}}^{\mathrm{T}} - \underline{\boldsymbol{\mu}} = \frac{1}{c}(\underline{\mathbf{Q}}^{\mathrm{T}})^{-1} - \frac{1}{c}\underline{\mathbf{Q}}^{-1} = \underline{\mathbf{0}} \,,$$

where the second equality holds by Eq. (3.108b). It is therefore concluded that $\underline{\boldsymbol{\mu}} = \underline{\boldsymbol{\mu}}^{\mathrm{T}}$, recovering Eq. (3.80d).

Index notation is used to recover Eqs. (3.82c) and (3.82f) from Eqs. (3.108). Equations (3.109) in index notation become

$$\epsilon_{ij} = \frac{1}{c}[P_{ij} - L_{ik}(\underline{\mathbf{Q}}^{-1})_{km}]M_{mj} \,, \tag{3.111a}$$

$$\mu_{ij} = \frac{1}{c}(\underline{\mathbf{Q}}^{-1})_{ij} \,, \tag{3.111b}$$

$$\xi_{ij} = \frac{1}{c}L_{ik}(\underline{\mathbf{Q}}^{-1})_{kj} \,, \tag{3.111c}$$

$$\zeta_{ij} = -\frac{1}{c}(\underline{\mathbf{Q}}^{-1})_{ik}M_{kj} \,. \tag{3.111d}$$

[16] The proof of this fact is identical to the rank-4 case [see Eq. (D.37)] upon replacing the rank-4 tensor with a rank-2 tensor, and replacing the rank-2 tensor with vectors.

Equation (3.82c) is first recovered by transposing Eq. (3.111a):

$$\epsilon_{ji} = \frac{1}{c}[P_{ji} - L_{jk}(\underline{\mathbf{Q}}^{-1})_{km}]M_{mi}\,. \tag{3.112}$$

Subtracting Eq. (3.112) from Eq. (3.111a) and invoking the indicial form of Eq. (3.108a) yields

$$\epsilon_{ij} - \epsilon_{ji} = \frac{1}{c}[L_{jk}(\underline{\mathbf{Q}}^{-1})_{km}M_{mi} - L_{ik}(\underline{\mathbf{Q}}^{-1})_{km}M_{mj}]\,. \tag{3.113}$$

In view of the indicial forms of Eqs. (3.108c) and (3.108b), Eq. (3.113) becomes

$$\epsilon_{ij} - \epsilon_{ji} = \frac{1}{c}[L_{im}(\underline{\mathbf{Q}}^{-1})_{mk}M_{kj} - L_{ik}(\underline{\mathbf{Q}}^{-1})_{km}M_{mj}]\,. \tag{3.114}$$

Exchanging the summing indices $k \leftrightarrow m$ in the second term yields

$$\epsilon_{ij} - \epsilon_{ji} = \frac{1}{c}[L_{im}(\underline{\mathbf{Q}}^{-1})_{mk}M_{kj} - L_{im}(\underline{\mathbf{Q}}^{-1})_{mk}M_{kj}] = 0\,, \tag{3.115}$$

recovering $\epsilon_{ij} = \epsilon_{ji}$ given by Eq. (3.82c).

Finally, to recover Eq. (3.82f), the transpose of Eq. (3.111c) is taken:

$$\xi_{ji} = \frac{1}{c}L_{jk}(\underline{\mathbf{Q}}^{-1})_{ki}\,. \tag{3.116}$$

Meanwhile, combining the indicial forms of Eqs. (3.108b) and (3.108c) with Eq. (3.111d) yields

$$\zeta_{ij} = -\frac{1}{c}L_{jk}(\underline{\mathbf{Q}}^{-1})_{ki}\,. \tag{3.117}$$

Adding Eq. (3.116) from Eq. (3.117) results in

$$\zeta_{ij} + \xi_{ji} = -\frac{1}{c}L_{jk}(\underline{\mathbf{Q}}^{-1})_{ki} + \frac{1}{c}L_{jk}(\underline{\mathbf{Q}}^{-1})_{ki} = 0\,.$$

It is therefore concluded that $\zeta_{ij} = -\xi_{ji}$, recovering Eq. (3.82f).

Passivity

The constraints due to passivity on the bianisotropic electrodynamic constitutive equations are provided by Ref. 69, while the constraints on the bianisotropic elastodynamic equations are provided in Refs. 228, 229, and 70. The following derivation of the constraints due to passivity on Eq. (3.8) recovers the results of Refs. 70, 123, and 69 in limiting cases.

The time-averaged elastodynamic intensity is [223, p. 145]

$$\langle \mathbf{i} \rangle = -\tfrac{1}{2} \operatorname{Re}(\underline{\boldsymbol{\sigma}} \cdot \mathbf{v}^*) \,, \tag{3.118}$$

while the time-averaged electromagnetic intensity is [226, Eq. (6.132)]

$$\langle \mathbf{I} \rangle = \tfrac{1}{2} \operatorname{Re}(\mathbf{E} \times \mathbf{H}^*) \,. \tag{3.119}$$

Since the present formulation admits both elastic and electromagnetic fields, the total time-averaged intensity is given by the sum of Eqs. (3.118) and (3.119):

$$\langle \mathbf{i} + \mathbf{I} \rangle = -\tfrac{1}{2} \operatorname{Re}(\underline{\boldsymbol{\sigma}} \cdot \mathbf{v}^*) + \tfrac{1}{2} \operatorname{Re}(\mathbf{E} \times \mathbf{H}^*) \,. \tag{3.120}$$

Passive media satisfy

$$\boldsymbol{\nabla} \cdot \langle \mathbf{i} + \mathbf{I} \rangle \leq 0 \,, \tag{3.121}$$

and passive and lossless media satisfy the equality in Eq. (3.121). Combination of Eq. (3.120) and (3.121) results in

$$-\tfrac{1}{2} \operatorname{Re}[\boldsymbol{\nabla} \cdot (\underline{\boldsymbol{\sigma}} \cdot \mathbf{v}^*)] + \tfrac{1}{2} \operatorname{Re}[\boldsymbol{\nabla} \cdot (\mathbf{E} \times \mathbf{H}^*)] \leq 0 \,.$$

Using tensor[17] and vector[18] calculus identities along with Eq. (3.62) results in

$$-\tfrac{1}{2} \operatorname{Re}(\underline{\boldsymbol{\sigma}} : \boldsymbol{\nabla} \mathbf{v}^* + \mathbf{v}^* \cdot \boldsymbol{\nabla} \cdot \underline{\boldsymbol{\sigma}}) + \tfrac{1}{2} \operatorname{Re}[(\boldsymbol{\nabla} \times \mathbf{E}) \cdot \mathbf{H}^* - \mathbf{E} \cdot (\boldsymbol{\nabla} \times \mathbf{H}^*)] \leq 0 \,. \tag{3.122}$$

[17] $\boldsymbol{\nabla} \cdot (\underline{\boldsymbol{\sigma}}^{\mathrm{T}} \cdot \mathbf{v}) = \underline{\boldsymbol{\sigma}} : \boldsymbol{\nabla} \mathbf{v} + (\boldsymbol{\nabla} \cdot \underline{\boldsymbol{\sigma}}) \cdot \mathbf{v}$
[18] $\boldsymbol{\nabla} \cdot (\mathbf{E} \times \mathbf{H}) = \mathbf{H} \cdot (\boldsymbol{\nabla} \times \mathbf{E}) - \mathbf{E} \cdot (\boldsymbol{\nabla} \times \mathbf{H})$

The first term of Eq. (3.122) is simplified by noting that for a time-harmonic irrotational medium,[19]

$$\boldsymbol{\nabla}\mathbf{v}^* = i\omega\boldsymbol{\nabla}\mathbf{u}^* = i\omega\underline{\boldsymbol{\varepsilon}}^* \,. \tag{3.123}$$

The second term of Eq. (3.122) can be written in terms of the equation of motion,

$$\boldsymbol{\nabla}\cdot\underline{\boldsymbol{\sigma}} = \dot{\boldsymbol{\mu}} = -i\omega\boldsymbol{\mu}\,, \tag{3.124}$$

where the second equality holds because $\boldsymbol{\mu}$ is also time-harmonic. Meanwhile, the third term of Eq. (3.122) can be written in terms of the time-harmonic and source-free laws of Faraday and Ampère:

$$\boldsymbol{\nabla}\times\mathbf{E} = i\omega\mathbf{B}\,, \tag{3.125}$$

$$\boldsymbol{\nabla}\times\mathbf{H}^* = i\omega\mathbf{D}^* \,. \tag{3.126}$$

Inserting Eqs. (3.123)– (3.126) into Eq. (3.122) and multiplying by -1 on both sides yields

$$\tfrac{1}{2}\operatorname{Re}[\underline{\boldsymbol{\sigma}} : (i\omega\underline{\boldsymbol{\varepsilon}}^*) - i\omega\boldsymbol{\mu}\cdot\mathbf{v}^*] + \tfrac{1}{2}\operatorname{Re}[i\omega\mathbf{D}^*\cdot\mathbf{E} - i\omega\mathbf{B}\cdot\mathbf{H}^*] \geq 0\,. \tag{3.127}$$

The property $\operatorname{Re}(iz) = i(z - z^*)/2$ for a complex quantity z is used to take the real part of Eq. (3.127):

$$\begin{aligned}\frac{i\omega}{4}(&\underline{\boldsymbol{\sigma}} : \underline{\boldsymbol{\varepsilon}}^* - \underline{\boldsymbol{\sigma}}^* : \underline{\boldsymbol{\varepsilon}} - \boldsymbol{\mu}\cdot\mathbf{v}^* + \boldsymbol{\mu}^*\cdot\mathbf{v} \\ &+ \mathbf{E}\cdot\mathbf{D}^* - \mathbf{E}^*\cdot\mathbf{D} - \mathbf{H}^*\cdot\mathbf{B} + \mathbf{H}\cdot\mathbf{B}^*) \geq 0\,.\end{aligned} \tag{3.128}$$

To determine how passivity constrains the elasto-electrodynamic constitutive equations, Eq. (3.8) is substituted into Eq. (3.128). Expanding the inner products, rearranging terms, invoking Eqs. (D.38), (D.39c), (D.39d), and (D.40a), and applying Eqs. (D.5), (D.20), and

[19] Note that $\underline{\boldsymbol{\varepsilon}} = \boldsymbol{\nabla}\mathbf{u}$ for $\boldsymbol{\nabla}\times\mathbf{u} = \mathbf{0}$. Taking the time derivative of this result yields Eq. (3.123).

(D.31) yields

$$\begin{aligned}\frac{i\omega}{4}\Big\{&[(\mathbb{M}-\mathbb{M}^{\mathrm{T}*}):\underline{\boldsymbol{\sigma}}^*]:\underline{\boldsymbol{\sigma}}-[(\underline{\boldsymbol{\rho}}-\underline{\boldsymbol{\rho}}^{\mathrm{T}*})\cdot\mathbf{v}^*]\cdot\mathbf{v}\\&+[(\underset{\sim}{\boldsymbol{\gamma}}^*-\underset{\sim}{\boldsymbol{\eta}}^{\mathrm{T}2})\cdot\mathbf{v}^*]:\underline{\boldsymbol{\sigma}}+[(\underset{\sim}{\boldsymbol{\eta}}^{\mathrm{T}2*}-\underset{\sim}{\boldsymbol{\gamma}})\cdot\mathbf{v}]:\underline{\boldsymbol{\sigma}}^*\\&+[(\underline{\mathbf{e}}^*-\underline{\mathbf{d}}^{\mathrm{T}2})\cdot\mathbf{E}^*]:\underline{\boldsymbol{\sigma}}+[(\underline{\mathbf{d}}^{\mathrm{T}2*}-\underline{\mathbf{e}})\cdot\mathbf{E}]:\underline{\boldsymbol{\sigma}}^*\\&+[(\underline{\mathbf{c}}^*-\underline{\mathbf{b}}^{\mathrm{T}2})\cdot\mathbf{H}^*]:\underline{\boldsymbol{\sigma}}+[(\underline{\mathbf{b}}^{\mathrm{T}2*}-\underline{\mathbf{c}})\cdot\mathbf{H}]:\underline{\boldsymbol{\sigma}}^*\\&+[(\underline{\mathbf{v}}^*-\underline{\mathbf{w}}^{\mathrm{T}})\cdot\mathbf{v}^*]\cdot\mathbf{E}+[(\underline{\mathbf{w}}^{\mathrm{T}*}-\underline{\mathbf{v}})\cdot\mathbf{v}]\cdot\mathbf{E}^*\\&+[(\underline{\mathbf{m}}^*-\underline{\mathbf{n}}^{\mathrm{T}})\cdot\mathbf{v}^*]\cdot\mathbf{H}+[(\underline{\mathbf{n}}^{\mathrm{T}*}-\underline{\mathbf{m}})\cdot\mathbf{v}]\cdot\mathbf{H}^*\\&+[(\underline{\boldsymbol{\xi}}^*-\underline{\boldsymbol{\zeta}}^{\mathrm{T}})\cdot\mathbf{H}^*]\cdot\mathbf{E}+[(\underline{\boldsymbol{\zeta}}^{\mathrm{T}*}-\underline{\boldsymbol{\xi}})\cdot\mathbf{H}]\cdot\mathbf{E}^*\\&-[(\underline{\boldsymbol{\epsilon}}-\underline{\boldsymbol{\epsilon}}^{\mathrm{T}*})\cdot\mathbf{E}]\cdot\mathbf{E}^*-[(\underline{\boldsymbol{\mu}}-\underline{\boldsymbol{\mu}}^{\mathrm{T}*})\cdot\mathbf{H}]\cdot\mathbf{H}^*\Big\}\geq 0\,.\end{aligned}\tag{3.129}$$

Since the stress, velocity, electric, and magnetic fields can be imposed independently in the low-frequency limit [70, 123], the individual terms of Eq. (3.129) must be greater than or equal to 0. Since the factor of $-i\omega$ corresponds to the time derivative of a quantity, and since the factor of $i\omega$ corresponds to the time derivative of its complex conjugate, the first term on the left-hand side of Eq. (3.129) yields $i\omega[(\mathbb{M}-\mathbb{M}^{\mathrm{T}*}):\underline{\boldsymbol{\sigma}}^*]:\underline{\boldsymbol{\sigma}}/4\geq 0$, which can be written as

$$\tfrac{1}{4}[(\mathbb{M}:\dot{\underline{\boldsymbol{\sigma}}}^*):\underline{\boldsymbol{\sigma}}+(\mathbb{M}^*:\dot{\underline{\boldsymbol{\sigma}}}):\underline{\boldsymbol{\sigma}}^*]=\tfrac{1}{2}\operatorname{Re}[(\mathbb{M}:\dot{\underline{\boldsymbol{\sigma}}}^*):\underline{\boldsymbol{\sigma}}]\geq 0\,.$$

The second and last two terms on the left-hand side of Eq. (3.129) can be manipulated similarly, yielding the inequalities

$$\tfrac{1}{2}\operatorname{Re}[(\mathbb{M}:\dot{\underline{\boldsymbol{\sigma}}}^*):\underline{\boldsymbol{\sigma}}]=\frac{i\omega}{4}[(\mathbb{M}-\mathbb{M}^{\mathrm{T}*}):\underline{\boldsymbol{\sigma}}^*]:\underline{\boldsymbol{\sigma}}\geq 0\,,\tag{3.130a}$$

$$\tfrac{1}{2}\operatorname{Re}[(\underline{\boldsymbol{\rho}}\cdot\mathbf{v}^*)\cdot\dot{\mathbf{v}}]=-\frac{i\omega}{4}[(\underline{\boldsymbol{\rho}}-\underline{\boldsymbol{\rho}}^{\mathrm{T}*})\cdot\mathbf{v}^*]\cdot\mathbf{v}\quad\geq 0\,,\tag{3.130b}$$

$$\tfrac{1}{2}\operatorname{Re}[(\underline{\boldsymbol{\epsilon}}\cdot\mathbf{E}^*)\cdot\dot{\mathbf{E}}]=-\frac{i\omega}{4}[(\underline{\boldsymbol{\epsilon}}-\underline{\boldsymbol{\epsilon}}^{\mathrm{T}*})\cdot\mathbf{E}^*]\cdot\mathbf{E}\quad\geq 0\,,\tag{3.130c}$$

$$\tfrac{1}{2}\operatorname{Re}[(\underline{\boldsymbol{\mu}}\cdot\mathbf{H}^*)\cdot\dot{\mathbf{H}}]=-\frac{i\omega}{4}[(\underline{\boldsymbol{\mu}}-\underline{\boldsymbol{\mu}}^{\mathrm{T}*})\cdot\mathbf{H}^*]\cdot\mathbf{H}\geq 0\,.\tag{3.130d}$$

The remaining terms of Eq. (3.129) can be manipulated similarly, resulting in the inequal-

ity

$$\begin{aligned}
&\mathrm{Re}[(\underset{\sim}{\boldsymbol{\eta}}^{\mathrm{T}2}\cdot\mathbf{v}^{*}):\dot{\underline{\boldsymbol{\sigma}}}-(\underset{\sim}{\boldsymbol{\gamma}}\cdot\mathbf{v}):\dot{\underline{\boldsymbol{\sigma}}}^{*}]+\mathrm{Re}[(\underset{\sim}{\mathbf{d}}^{\mathrm{T}2}\cdot\mathbf{E}^{*}):\dot{\underline{\boldsymbol{\sigma}}}-(\underset{\sim}{\mathbf{e}}\cdot\mathbf{E}):\dot{\underline{\boldsymbol{\sigma}}}^{*}]\\
&\quad+\mathrm{Re}[(\underset{\sim}{\mathbf{b}}^{\mathrm{T}2}\cdot\mathbf{H}^{*}):\dot{\underline{\boldsymbol{\sigma}}}-(\underset{\sim}{\mathbf{c}}\cdot\mathbf{H}):\dot{\underline{\boldsymbol{\sigma}}}^{*}]+\mathrm{Re}[(\underline{\mathbf{w}}^{\mathrm{T}}\cdot\mathbf{v}^{*})\cdot\dot{\mathbf{E}}-(\underline{\mathbf{v}}\cdot\mathbf{v})\cdot\dot{\mathbf{E}}^{*}]\\
&\quad+\mathrm{Re}[(\underline{\mathbf{n}}^{\mathrm{T}}\cdot\mathbf{v}^{*})\cdot\dot{\mathbf{H}}-(\underline{\mathbf{m}}\cdot\mathbf{v})\cdot\dot{\mathbf{H}}^{*}]+\mathrm{Re}[(\underline{\boldsymbol{\zeta}}^{\mathrm{T}}\cdot\mathbf{H}^{*})\cdot\dot{\mathbf{E}}-(\underline{\boldsymbol{\xi}}\cdot\mathbf{H})\cdot\dot{\mathbf{E}}^{*}]\\
&\quad\geq-\mathrm{Re}[(\mathbb{M}:\dot{\underline{\boldsymbol{\sigma}}}^{*}):\underline{\boldsymbol{\sigma}}]-\mathrm{Re}[(\underline{\boldsymbol{\rho}}\cdot\mathbf{v}^{*})\cdot\dot{\mathbf{v}}]-\mathrm{Re}[(\underline{\boldsymbol{\epsilon}}\cdot\mathbf{E}^{*})\cdot\dot{\mathbf{E}}]-\mathrm{Re}[(\underline{\boldsymbol{\mu}}\cdot\mathbf{H}^{*})\cdot\dot{\mathbf{H}}]\,.
\end{aligned}\tag{3.130e}$$

Neglecting electric and magnetic fields shows that Eqs. (3.130) have the same form as Eqs. (3.13) and (3.14) of Ref. 70. For lossless media, the equality in Eq. (3.129) is satisfied, requiring that the diagonal elements of Eq. (3.8) satisfy

$$\mathbb{M}=\mathbb{M}^{\mathrm{T}*}\,,\tag{3.131a}$$

$$\underline{\boldsymbol{\rho}}=\underline{\boldsymbol{\rho}}^{\mathrm{T}*}\,,\tag{3.131b}$$

$$\underline{\boldsymbol{\epsilon}}=\underline{\boldsymbol{\epsilon}}^{\mathrm{T}*}\,,\tag{3.131c}$$

$$\underline{\boldsymbol{\mu}}=\underline{\boldsymbol{\mu}}^{\mathrm{T}*}\,,\tag{3.131d}$$

while the off-diagonal elements satisfy

$$\underset{\sim}{\boldsymbol{\gamma}}=\underset{\sim}{\boldsymbol{\eta}}^{\mathrm{T}2*}\,,\tag{3.131e}$$

$$\underset{\sim}{\mathbf{e}}=\underset{\sim}{\mathbf{d}}^{\mathrm{T}2*}\,,\tag{3.131f}$$

$$\underset{\sim}{\mathbf{c}}=\underset{\sim}{\mathbf{b}}^{\mathrm{T}2*}\,,\tag{3.131g}$$

$$\underline{\mathbf{w}}=\underline{\mathbf{v}}^{\mathrm{T}*}\,,\tag{3.131h}$$

$$\underline{\mathbf{n}}=\underline{\mathbf{m}}^{\mathrm{T}*}\,,\tag{3.131i}$$

$$\underline{\boldsymbol{\xi}}=\underline{\boldsymbol{\zeta}}^{\mathrm{T}*}\,,\tag{3.131j}$$

where the definitions of the Hermitian conjugates are provided in Sec. D.5. Equations (3.131c), (3.131d), and (3.131j) recover Eqs. (8) of Ref. 69. Conversions similar to those presented previously may be performed to show that Eqs. (3.131) recover the results of Refs. 70 and 123 in the absence of electrodynamics and magnetism, respectively.

Reciprocity and passivity

A medium described by Eqs. (3.8) that is both passive and reciprocal medium must satisfy Eqs. (3.80) and (3.130), yielding the inequalities

$$\begin{aligned}
\frac{i\omega}{4}[(\mathbb{M}-\mathbb{M}^*) : \underline{\boldsymbol{\sigma}}^*] : \underline{\boldsymbol{\sigma}} \geq 0\,,\\
-\frac{i\omega}{4}[(\underline{\boldsymbol{\rho}}-\underline{\boldsymbol{\rho}}^*)\cdot\mathbf{v}^*]\cdot\mathbf{v} \geq 0\,,\\
-\frac{i\omega}{4}[(\underline{\boldsymbol{\epsilon}}-\underline{\boldsymbol{\epsilon}}^*)\cdot\mathbf{E}^*]\cdot\mathbf{E} \geq 0\,,\\
-\frac{i\omega}{4}[(\underline{\boldsymbol{\mu}}-\underline{\boldsymbol{\mu}}^*)\cdot\mathbf{H}^*]\cdot\mathbf{H} \geq 0\,.
\end{aligned}$$

The relation $z - z^* = 2i\,\mathrm{Im}(z)$ is used to identify the imaginary parts of the quantities:

$$[\mathrm{Im}(\mathbb{M}) : \underline{\boldsymbol{\sigma}}^*] : \underline{\boldsymbol{\sigma}} \leq 0\,, \tag{3.132a}$$

$$[\mathrm{Im}(\underline{\boldsymbol{\rho}})\cdot\mathbf{v}^*]\cdot\mathbf{v} \geq 0\,, \tag{3.132b}$$

$$[\mathrm{Im}(\underline{\boldsymbol{\epsilon}})\cdot\mathbf{E}^*]\cdot\mathbf{E} \geq 0\,, \tag{3.132c}$$

$$[\mathrm{Im}(\underline{\boldsymbol{\mu}})\cdot\mathbf{H}^*]\cdot\mathbf{H} \geq 0\,. \tag{3.132d}$$

Equations (3.132a) and (3.132b) are the strain form of Eqs. (3.15) of Ref. 70. For a lossless, passive, and reciprocal medium, Eqs. (3.80) and (3.131) are combined by noting that a tensor that is simultaneously symmetric and Hermitian must be purely real-valued. To prove this, write $\mathbb{M}$ in terms of its real and imaginary parts:

$$\mathbb{M} = \mathrm{Re}(\mathbb{M}) + i\,\mathrm{Im}(\mathbb{M})\,. \tag{3.133}$$

Since the transpose operation is linear, the major transpose of Eq. (3.133) is

$$\mathbb{M}^{\mathrm{T}} = \mathrm{Re}(\mathbb{M}^{\mathrm{T}}) + i\,\mathrm{Im}(\mathbb{M}^{\mathrm{T}})\,. \tag{3.134}$$

Similarly, the Hermitian conjugate of $\mathbb{M}$ is

$$\mathbb{M}^{\mathrm{T}*} = \mathrm{Re}(\mathbb{M}^{\mathrm{T}}) - i\,\mathrm{Im}(\mathbb{M}^{\mathrm{T}})\,. \tag{3.135}$$

Combining Eqs. (3.80a) and (3.131a) with Eqs. (3.134) and (3.135) yields

$$\mathbb{M} = \mathbb{M}^{\mathrm{T}} = \mathrm{Re}(\mathbb{M}^{\mathrm{T}}) + i\,\mathrm{Im}(\mathbb{M}^{\mathrm{T}})\,, \tag{3.136}$$

$$\mathbb{M} = \mathbb{M}^{\mathrm{T}*} = \mathrm{Re}(\mathbb{M}^{\mathrm{T}}) - i\,\mathrm{Im}(\mathbb{M}^{\mathrm{T}})\,. \tag{3.137}$$

Adding Eqs. (3.136) and (3.137) and dividing by 2 yields

$$\mathbb{M} = \mathrm{Re}(\mathbb{M}^{\mathrm{T}})\,. \tag{3.138}$$

But since $\mathbb{M} = \mathbb{M}^{\mathrm{T}}$, it is concluded from Eq. (3.138) that

$$\mathbb{M} = \mathrm{Re}(\mathbb{M})\,. \tag{3.139a}$$

A similar argument can be made for rank-2 tensors that are both symmetric [see Eqs. (3.80b), (3.80c), and (3.80d)] and Hermitian [see Eqs. (3.131b), (3.131c), and (3.131d)], resulting in

$$\underline{\boldsymbol{\rho}} = \mathrm{Re}(\underline{\boldsymbol{\rho}})\,, \tag{3.139b}$$

$$\underline{\boldsymbol{\epsilon}} = \mathrm{Re}(\underline{\boldsymbol{\epsilon}})\,, \tag{3.139c}$$

$$\underline{\boldsymbol{\mu}} = \mathrm{Re}(\underline{\boldsymbol{\mu}})\,. \tag{3.139d}$$

Equations (3.139) are equivalent to stating that the imaginary parts of the compliance, dynamic density, permittivity, and permeability tensors vanish in reciprocal, passive, and lossless media:

$$\mathrm{Im}(\mathbb{M}) = \mathbb{O}\,, \quad \mathrm{Im}(\underline{\boldsymbol{\rho}}) = \underline{\mathbf{0}}\,, \quad \mathrm{Im}(\underline{\boldsymbol{\epsilon}}) = \underline{\mathbf{0}}\,, \quad \mathrm{Im}(\underline{\boldsymbol{\mu}}) = \underline{\mathbf{0}}\,. \tag{3.140}$$

The first two of Eqs. (3.140) in combination with Eqs. (3.60c) and (3.60d) recover Eqs. (3.17) of Ref. 70.

Considered next are the Willis coupling tensors $\underset{\sim}{\boldsymbol{\eta}}$ and $\underset{\sim}{\boldsymbol{\gamma}}$ expressed in terms of their real and imaginary parts:

$$\underset{\sim}{\boldsymbol{\eta}} = \mathrm{Re}(\underset{\sim}{\boldsymbol{\eta}}) + i\,\mathrm{Im}(\underset{\sim}{\boldsymbol{\eta}})\,, \tag{3.141a}$$

$$\underset{\sim}{\boldsymbol{\gamma}} = \mathrm{Re}(\underset{\sim}{\boldsymbol{\gamma}}) + i\,\mathrm{Im}(\underset{\sim}{\boldsymbol{\gamma}})\,. \tag{3.141b}$$

The first major transpose of Eq. (3.141b) is

$$\underset{\sim}{\boldsymbol{\gamma}}^{\mathrm{T1}} = \mathrm{Re}(\underset{\sim}{\boldsymbol{\gamma}}^{\mathrm{T1}}) + i\,\mathrm{Im}(\underset{\sim}{\boldsymbol{\gamma}}^{\mathrm{T1}})\,, \tag{3.142}$$

while the Hermitian conjugate of Eq. (3.141b) is

$$\underset{\sim}{\boldsymbol{\gamma}}^{\mathrm{T1}*} = \mathrm{Re}(\underset{\sim}{\boldsymbol{\gamma}}^{\mathrm{T1}}) - i\,\mathrm{Im}(\underset{\sim}{\boldsymbol{\gamma}}^{\mathrm{T1}})\,. \tag{3.143}$$

It was found that for reciprocal media, $\underset{\sim}{\boldsymbol{\eta}} = -\underset{\sim}{\boldsymbol{\gamma}}^{\mathrm{T1}}$ [Eq. (3.80e)], while in lossless media, $\underset{\sim}{\boldsymbol{\eta}} = \underset{\sim}{\boldsymbol{\gamma}}^{\mathrm{T1}*}$ [which follows from taking the first major transpose of Eq. (3.131e) and invoking Eq. (D.20a)]. Combining these relations yields

$$\underset{\sim}{\boldsymbol{\gamma}}^{\mathrm{T1}} + \underset{\sim}{\boldsymbol{\gamma}}^{\mathrm{T1}*} = \underline{\mathbf{0}}\,. \tag{3.144}$$

Inserting Eqs. (3.142) and (3.143) into Eq. (3.144) yields

$$\underset{\sim}{\boldsymbol{\gamma}}^{\mathrm{T1}} + \underset{\sim}{\boldsymbol{\gamma}}^{\mathrm{T1}*} = 2\,\mathrm{Re}(\underset{\sim}{\boldsymbol{\gamma}}^{\mathrm{T1}}) = \underline{\mathbf{0}} \implies \mathrm{Re}(\underset{\sim}{\boldsymbol{\gamma}}^{\mathrm{T1}}) = \underline{\mathbf{0}}\,. \tag{3.145}$$

Since from Eq. (3.143) $\underset{\sim}{\boldsymbol{\eta}} = \underset{\sim}{\boldsymbol{\gamma}}^{\mathrm{T1}*} = \mathrm{Re}(\underset{\sim}{\boldsymbol{\gamma}}^{\mathrm{T1}}) - i\,\mathrm{Im}(\underset{\sim}{\boldsymbol{\gamma}}^{\mathrm{T1}})$, it is concluded that

$$\underset{\sim}{\boldsymbol{\eta}} = -i\,\mathrm{Im}(\underset{\sim}{\boldsymbol{\gamma}}^{\mathrm{T1}})\,,$$

which is to say that $\underset{\sim}{\boldsymbol{\eta}}$ is purely imaginary. Since $\underline{\mathbf{b}} = -\underline{\mathbf{c}}^{\mathrm{T1}}$ and $\underline{\mathbf{b}} = \underline{\mathbf{c}}^{\mathrm{T1}*}$ from Eqs. (D.20a), (3.80m), and (3.131g), $\underline{\mathbf{w}} = -\underline{\mathbf{v}}^{\mathrm{T}}$ and $\underline{\mathbf{w}} = \underline{\mathbf{v}}^{\mathrm{T}*}$ from Eqs. (3.80i) and (3.131h), and $\underline{\boldsymbol{\zeta}} = -\underline{\boldsymbol{\xi}}^{\mathrm{T}}$ and $\underline{\boldsymbol{\zeta}}^{\mathrm{T}*} = \underline{\boldsymbol{\xi}}$ from Eqs. (3.80f) and (3.131j), the same argument can be applied to show that the real parts of these tensors vanish for reciprocal, passive, and lossless media:

$$\mathrm{Re}(\underset{\sim}{\boldsymbol{\gamma}}) = \underline{\mathbf{0}}, \qquad \mathrm{Re}(\underset{\sim}{\boldsymbol{\eta}}) = \underline{\mathbf{0}}, \tag{3.146a}$$

$$\mathrm{Re}(\underline{\mathbf{c}}) = \underline{\mathbf{0}}, \qquad \mathrm{Re}(\underline{\mathbf{b}}) = \underline{\mathbf{0}}, \tag{3.146b}$$

$$\mathrm{Re}(\underline{\mathbf{w}}) = \underline{\mathbf{0}}, \qquad \mathrm{Re}(\underline{\mathbf{v}}) = \underline{\mathbf{0}}, \tag{3.146c}$$

$$\mathrm{Re}(\underline{\boldsymbol{\zeta}}) = \underline{\mathbf{0}}, \qquad \mathrm{Re}(\underline{\boldsymbol{\xi}}) = \underline{\mathbf{0}}\,. \tag{3.146d}$$

Equation (3.146) shows that constitutive parameters relating field and displacement variables that transform *differently* under time reversal [displayed in blue in Eq. (3.81)] are

purely imaginary in reciprocal, passive, and lossless media. The conclusions made about Eqs. (3.146a) in Ref. [70] therefore also apply to the piezomagnetic, electromomentum, and electromagnetic bianisotropic tensors.

Finally, the piezoelectric coupling tensors $\underset{\sim}{\mathbf{d}}$ and $\underset{\sim}{\mathbf{e}}$ are expressed in terms of their real and imaginary parts by

$$\underset{\sim}{\mathbf{d}} = \mathrm{Re}(\underset{\sim}{\mathbf{d}}) + i\,\mathrm{Im}(\underset{\sim}{\mathbf{d}})\,, \tag{3.147a}$$

$$\underset{\sim}{\mathbf{e}} = \mathrm{Re}(\underset{\sim}{\mathbf{e}}) + i\,\mathrm{Im}(\underset{\sim}{\mathbf{e}})\,. \tag{3.147b}$$

The first major transpose of Eq. (3.147a) is

$$\underset{\sim}{\mathbf{e}}^{\mathrm{T}1} = \mathrm{Re}(\underset{\sim}{\mathbf{e}}^{\mathrm{T}1}) + i\,\mathrm{Im}(\underset{\sim}{\mathbf{e}}^{\mathrm{T}1})\,, \tag{3.148}$$

while the Hermitian conjugate of Eq. (3.147a) is

$$\underset{\sim}{\mathbf{e}}^{\mathrm{T}1*} = \mathrm{Re}(\underset{\sim}{\mathbf{e}}^{\mathrm{T}1}) - i\,\mathrm{Im}(\underset{\sim}{\mathbf{e}}^{\mathrm{T}1})\,. \tag{3.149}$$

It was found that for reciprocal media, $\underset{\sim}{\mathbf{d}} = \underset{\sim}{\mathbf{e}}^{\mathrm{T}1}$ [Eq. (3.80e) in combination with Eq. (D.20a)], while in lossless media, $\underset{\sim}{\mathbf{d}} = \underset{\sim}{\mathbf{e}}^{\mathrm{T}1*}$ [which follows from taking the first major transpose of Eq. (3.131f) and invoking Eq. (D.20a)]. Combining these relations yields

$$\underset{\sim}{\mathbf{e}}^{\mathrm{T}1} - \underset{\sim}{\mathbf{e}}^{\mathrm{T}1*} = \underset{\sim}{\mathbf{0}}\,. \tag{3.150}$$

Inserting Eqs. (3.148) and (3.149) into Eq. (3.150) yields

$$\underset{\sim}{\mathbf{e}}^{\mathrm{T}1} - \underset{\sim}{\mathbf{e}}^{\mathrm{T}1*} = 2i\,\mathrm{Im}(\underset{\sim}{\mathbf{e}}^{\mathrm{T}1}) = \underset{\sim}{\mathbf{0}} \implies \mathrm{Im}(\underset{\sim}{\mathbf{e}}^{\mathrm{T}1}) = \underset{\sim}{\mathbf{0}}\,. \tag{3.151}$$

Since from Eq. (3.149) $\underset{\sim}{\mathbf{d}} = \underset{\sim}{\mathbf{e}}^{\mathrm{T}1*} = \mathrm{Re}(\underset{\sim}{\mathbf{e}}^{\mathrm{T}1}) - i\,\mathrm{Im}(\underset{\sim}{\mathbf{e}}^{\mathrm{T}1})$, it is concluded that

$$\underset{\sim}{\mathbf{d}} = \mathrm{Re}(\underset{\sim}{\mathbf{e}}^{\mathrm{T}1})\,,$$

which is to say that $\underset{\sim}{\mathbf{d}}$ is purely real. Since $\underline{\mathbf{n}} = \underline{\underline{\mathbf{m}}}^{\mathrm{T}}$ and $\underline{\mathbf{n}} = \underline{\underline{\mathbf{m}}}^{\mathrm{T}*}$ from Eqs. (3.80j) and (3.131i), the same argument can be applied to show that the imaginary parts of these tensors vanish for reciprocal, passive, and lossless media:

$$\mathrm{Im}(\underset{\sim}{\mathbf{d}}) = \underset{\sim}{\mathbf{0}}\,, \qquad \mathrm{Im}(\underset{\sim}{\mathbf{e}}) = \underset{\sim}{\mathbf{0}}\,, \tag{3.152a}$$

$$\mathrm{Im}(\underline{\mathbf{n}}) = \underline{\mathbf{0}}\,, \qquad \mathrm{Im}(\underline{\underline{\mathbf{m}}}) = \underline{\underline{\mathbf{0}}}\,. \tag{3.152b}$$

Equations (3.140) and (3.152) show that constitutive parameters relating field and displacement variables that transform *similarly* under time reversal [displayed in red in Eq. (3.81)] are purely real in reciprocal, passive, and lossless media.

3.4 Reduction to acousto-electromagnetic relations

The analysis of Sec. 3.3 is now reduced to acousto-electromagnetic media, for which the effective constitutive relations are given by Eq. (3.7). The reduction shows that the constraints due to reciprocity and passivity are consistent with Eq. (3.30).

Reciprocity

The constraints due to reciprocity can be obtained from Eq. (3.79) by noting that the rank-3 tensors $\underset{\sim}{\boldsymbol{\eta}}$, $\underset{\sim}{\boldsymbol{\gamma}}$, $\underline{\mathbf{d}}$, $\underline{\mathbf{e}}$, $\underline{\mathbf{b}}$, and $\underline{\mathbf{c}}$ reduce to vectors, and that [70, Eqs. (5.4)]

$$p = -\tfrac{1}{3}\mathrm{Tr}\,\underline{\boldsymbol{\sigma}}\,, \qquad \varepsilon = \mathrm{Tr}\,\underline{\boldsymbol{\varepsilon}}\,, \qquad \beta = M_{iijj}/9\,, \tag{3.153}$$

where "Tr " denotes the trace of a rank-2 tensor [230, Eq. (1.2.7)]. Equation (3.79) therefore reduces to

$$p_1\varepsilon_2 - p_2\varepsilon_1 + \mathbf{v}_1\cdot\boldsymbol{\mu}_2 - \mathbf{v}_2\cdot\boldsymbol{\mu}_1 - \mathbf{E}_1\cdot\mathbf{D}_2 + \mathbf{E}_2\cdot\mathbf{D}_1 + \mathbf{H}_1\cdot\mathbf{B}_2 - \mathbf{H}_2\cdot\mathbf{B}_1 = 0\,. \tag{3.154}$$

Equation (3.154) can alternatively be derived by following the procedure outlined in Sec. 3.3, i.e., starting with the time-harmonic form of the governing equations at location "1" and taking inner products with the fields $\mathbf{v}_2$, p_2, $\mathbf{H}_2$, and $\mathbf{E}_2$ at location "2":

$$\mathbf{v}_2\cdot\boldsymbol{\nabla}p_1 = i\omega\mathbf{v}_2\cdot\boldsymbol{\mu}_1 + \mathbf{v}_2\cdot\mathbf{f}_1\,, \tag{3.155a}$$

$$p_2\boldsymbol{\nabla}\cdot\mathbf{v}_1 = -i\omega p_2\varepsilon_1 + p_2 q_1\,, \tag{3.155b}$$

$$\mathbf{H}_2\cdot(\boldsymbol{\nabla}\times\mathbf{E}_1) = i\omega\mathbf{H}_2\cdot\mathbf{B}_1 - \mathbf{H}_2\cdot\mathbf{K}_1\,, \tag{3.155c}$$

$$\mathbf{E}_2\cdot(\boldsymbol{\nabla}\times\mathbf{H}_1) = -i\omega\mathbf{E}_2\cdot\mathbf{D}_1 + \mathbf{E}_2\cdot\mathbf{J}_1\,. \tag{3.155d}$$

A similar set of equations can be formed with the locations interchanged. The resulting equations can be combined in the manner outlined in Sec. 3.3 [221, Sec. 3.3.1] and integrated over a volume V enclosed by a surface A, with outward unit normal $\mathbf{e}_n$. Application

of the divergence theorem yields

$$\begin{aligned}\int_A &(p_1\mathbf{v}_2 - p_2\mathbf{v}_1 \;+\; \mathbf{E}_1\times\mathbf{H}_2 - \mathbf{E}_2\times\mathbf{H}_1)\cdot\mathbf{e}_n dA \\ &= \int_V (\mathbf{v}_2\cdot\mathbf{f}_1 - \mathbf{v}_1\cdot\mathbf{f}_2 + p_1 q_2 - p_2 q_1 + \mathbf{E}_2\cdot\mathbf{J}_1 - \mathbf{E}_1\cdot\mathbf{J}_2 + \mathbf{H}_1\cdot\mathbf{K}_2 - \mathbf{H}_2\cdot\mathbf{K}_1)dV \\ &\quad - i\omega\int_V (p_1\varepsilon_2 - p_2\varepsilon_1 + \mathbf{v}_1\cdot\boldsymbol{\mu}_2 - \mathbf{v}_2\cdot\boldsymbol{\mu}_1 - \mathbf{E}_1\cdot\mathbf{D}_2 + \mathbf{E}_2\cdot\mathbf{D}_1 + \mathbf{H}_1\cdot\mathbf{B}_2 - \mathbf{H}_2\cdot\mathbf{B}_1)dV.\end{aligned}$$

Following the argument made in Sec. 3.3 in reference to Eq. (3.77) yields Eq. (3.154).

To derive constraints due to reciprocity, the acousto-electromagnetic constitutive relations given by Eq. (3.7) are substituted into Eq. (3.154), noting from Sec. 3.2 and Refs. 12 and 13 that the coupling parameters can be grouped into even and odd factors of $\mathbf{k}$ and $\boldsymbol{\kappa}$ [221, Sec. 3.3.1]:

$$\boldsymbol{\gamma} = \boldsymbol{\gamma}^{\mathrm{e}} + \boldsymbol{\gamma}^{\mathrm{o}}, \quad \boldsymbol{\eta} = \boldsymbol{\eta}^{\mathrm{e}} + \boldsymbol{\eta}^{\mathrm{o}}, \quad \underline{\zeta} = \underline{\zeta}^{\mathrm{e}} + \underline{\zeta}^{\mathrm{o}}, \quad \text{etc.}$$

Therefore, for constitutive parameters associated with fields at position "1,"

$$\boldsymbol{\gamma}_1 = \boldsymbol{\gamma}^{\mathrm{e}} + \boldsymbol{\gamma}^{\mathrm{o}}, \quad \boldsymbol{\eta}_1 = \boldsymbol{\eta}^{\mathrm{e}} + \boldsymbol{\eta}^{\mathrm{o}}, \quad \underline{\zeta}_1 = \underline{\zeta}^{\mathrm{e}} + \underline{\zeta}^{\mathrm{o}}, \quad \text{etc.},$$

while for constitutive parameters associated with fields at position "2,"

$$\boldsymbol{\gamma}_2 = \boldsymbol{\gamma}^{\mathrm{e}} - \boldsymbol{\gamma}^{\mathrm{o}}, \quad \boldsymbol{\eta}_2 = \boldsymbol{\eta}^{\mathrm{e}} - \boldsymbol{\eta}^{\mathrm{o}}, \quad \underline{\zeta}_2 = \underline{\zeta}^{\mathrm{e}} - \underline{\zeta}^{\mathrm{o}}, \quad \text{etc.}$$

Rearranging the resulting terms of Eq. (3.154) results in the following identifications:

$$\underline{\rho} = \underline{\rho}^{\mathrm{T}}, \tag{3.156a}$$

$$\boldsymbol{\eta}^{\mathrm{e}} = -\boldsymbol{\gamma}^{\mathrm{e}}, \tag{3.156b}$$

$$\boldsymbol{\eta}^{\mathrm{o}} = \boldsymbol{\gamma}^{\mathrm{o}}, \tag{3.156c}$$

$$\underline{\mu} = \underline{\mu}^{\mathrm{T}}, \tag{3.156d}$$

$$\underline{\epsilon} = \underline{\epsilon}^{\mathrm{T}}, \tag{3.156e}$$

$$\underline{\zeta}^{\mathrm{e}} = -(\underline{\xi}^{\mathrm{e}})^{\mathrm{T}}, \tag{3.156f}$$

$$\underline{\zeta}^{\mathrm{o}} = (\underline{\xi}^{\mathrm{o}})^{\mathrm{T}}. \tag{3.156g}$$

Equations (3.156a), (3.156b), and (3.156c) recover the relations listed below Eq. (3.14) of Ref. 221. Substitution of Eqs. (3.156) into $\boldsymbol{\gamma} = \boldsymbol{\gamma}^{\mathrm{e}} + \boldsymbol{\gamma}^{\mathrm{o}}$ and $\underline{\xi} = \underline{\xi}^{\mathrm{e}} + \underline{\xi}^{\mathrm{o}}$ shows that

$$\boldsymbol{\gamma} = \boldsymbol{\eta}^{\mathrm{o}} - \boldsymbol{\eta}^{\mathrm{e}}\,, \tag{3.157a}$$

$$\underline{\xi} = (\underline{\zeta}^{\mathrm{o}})^{\mathrm{T}} - (\underline{\zeta}^{\mathrm{e}})^{\mathrm{T}}\,. \tag{3.157b}$$

Relations corresponding to the piezoelectric, piezomagnetic, electromomentum, and magnetomomentum constitutive tensors also emerge:

$$\underline{\mathbf{w}}^{\mathrm{e}} = -(\underline{\mathbf{v}}^{\mathrm{e}})^{\mathrm{T}}\,, \qquad \underline{\mathbf{w}}^{\mathrm{o}} = (\underline{\mathbf{v}}^{\mathrm{o}})^{\mathrm{T}}\,, \qquad \underline{\mathbf{n}}^{\mathrm{e}} = (\underline{\mathbf{m}}^{\mathrm{e}})^{\mathrm{T}}\,, \tag{3.158a}$$

$$\underline{\mathbf{n}}^{\mathrm{o}} = -(\underline{\mathbf{m}}^{\mathrm{o}})^{\mathrm{T}}\,, \qquad \mathbf{e}^{\mathrm{e}} = \mathbf{d}^{\mathrm{e}}\,, \qquad \mathbf{e}^{\mathrm{o}} = -\mathbf{d}^{\mathrm{o}}\,, \tag{3.158b}$$

$$\mathbf{c}^{\mathrm{e}} = -\mathbf{b}^{\mathrm{e}}\,, \qquad \mathbf{c}^{\mathrm{o}} = \mathbf{b}^{\mathrm{o}}\,. \tag{3.158c}$$

From Eqs. (3.158), it can be seen that

$$\underline{\mathbf{w}} = (\underline{\mathbf{v}}^{\mathrm{o}})^{\mathrm{T}} - (\underline{\mathbf{v}}^{\mathrm{e}})^{\mathrm{T}}\,, \qquad \underline{\mathbf{n}} = (\underline{\mathbf{m}}^{\mathrm{e}})^{\mathrm{T}} - (\underline{\mathbf{m}}^{\mathrm{o}})^{\mathrm{T}}\,, \tag{3.159a}$$

$$\mathbf{e} = \mathbf{d}^{\mathrm{e}} - \mathbf{d}^{\mathrm{o}}\,, \qquad \mathbf{c} = \mathbf{b}^{\mathrm{o}} - \mathbf{b}^{\mathrm{e}}\,. \tag{3.159b}$$

Combining Eqs. (3.157) and (3.159) with the decompositions[20]

$$\boldsymbol{\eta} = \chi^{\mathrm{o}}_{pv} + i\chi^{\mathrm{e}}_{pv}\,, \qquad \mathbf{d} = -i\chi^{\mathrm{o}}_{pE} - \chi^{\mathrm{e}}_{pE}\,, \qquad \mathbf{b} = -\chi^{\mathrm{o}}_{pH} - i\chi^{\mathrm{e}}_{pH}\,, \tag{3.160a}$$

$$\underline{\mathbf{v}} = \underline{\chi}^{\mathrm{o}}_{vE} + i\underline{\chi}^{\mathrm{e}}_{vE}\,, \qquad \underline{\mathbf{m}} = i\underline{\chi}^{\mathrm{o}}_{vH} + \underline{\chi}^{\mathrm{e}}_{vH}\,, \qquad \underline{\zeta} = \underline{\chi}^{\mathrm{o}}_{EH} + i\underline{\chi}^{\mathrm{e}}_{EH} \tag{3.160b}$$

recovers the form of the 4×4 matrix in Eq. (3.30), showing that the homogenized medium in Sec. 3.2 obeys reciprocity.

Passivity

Reducing Eq. (3.128) to the acoustic limit described by Eqs. (3.153) yields

$$\frac{i\omega}{4}(\boldsymbol{\mu}\cdot\mathbf{v}^{*} - \boldsymbol{\mu}^{*}\cdot\mathbf{v} + \varepsilon^{*}p - \varepsilon p^{*} + \mathbf{B}\cdot\mathbf{H}^{*} - \mathbf{B}^{*}\cdot\mathbf{H} - \mathbf{D}^{*}\cdot\mathbf{E} + \mathbf{D}\cdot\mathbf{E}^{*}) = 0\,. \tag{3.161}$$

[20] The placement of the factors of i in Eq. (3.160) is motivated by Refs. 12 and 13 and can be determined from Table 3.1. Constitutive parameters relating fields and displacements that transform similarly under time reversal have odd parts multiplied by factors of i, while parameters relating fields and displacements that transform differently under time reversal have even parts multiplied by factors of i. The subscripts uE and uH in Eq. (11b) of Ref. 194 should be vE and vH, respectively, as shown in Eqs. (3.160b).

Substitution of Eq. (3.7) into Eq. (3.161) and rearrangement of terms eventually yields

$$\operatorname{Im}(\beta) = 0\,, \tag{3.162a}$$

$$\underline{\boldsymbol{\rho}}^{\mathrm{T}*} = \underline{\boldsymbol{\rho}}\,, \tag{3.162b}$$

$$\boldsymbol{\eta} = \boldsymbol{\gamma}^{*}\,, \tag{3.162c}$$

$$\underline{\boldsymbol{\mu}} = \underline{\boldsymbol{\mu}}^{\mathrm{T}*}\,, \tag{3.162d}$$

$$\underline{\boldsymbol{\epsilon}} = \underline{\boldsymbol{\epsilon}}^{\mathrm{T}*}\,, \tag{3.162e}$$

$$\underline{\boldsymbol{\zeta}} = \underline{\boldsymbol{\xi}}^{\mathrm{T}*}\,, \tag{3.162f}$$

recovering previous results for acoustics [221, Sec. 3.3.2] and electromagnetics [69, Eqs. (8)]. The novel results due to passivity are

$$\underline{\mathbf{v}}^{\mathrm{T}*} = \underline{\mathbf{w}}\,, \tag{3.162g}$$

$$\underline{\mathbf{m}}^{\mathrm{T}*} = \underline{\mathbf{n}}\,, \tag{3.162h}$$

$$\mathbf{d} = \mathbf{e}^{*}\,, \tag{3.162i}$$

$$\mathbf{b} = \mathbf{c}^{*}\,. \tag{3.162j}$$

In view of Eqs. (3.162), Eq. (3.7) reduces from sixteen to ten constitutive parameters,

$$\begin{bmatrix} \varepsilon \\ \boldsymbol{\mu} \\ \mathbf{D} \\ \mathbf{B} \end{bmatrix} = \begin{bmatrix} \operatorname{Re}(\beta) & \boldsymbol{\gamma} & \mathbf{e} & \mathbf{c} \\ \boldsymbol{\gamma}^{*} & \underline{\boldsymbol{\rho}} & \underline{\mathbf{w}} & \underline{\mathbf{n}} \\ \mathbf{e}^{*} & \underline{\mathbf{w}}^{\mathrm{T}*} & \underline{\boldsymbol{\epsilon}} & \underline{\boldsymbol{\xi}} \\ \mathbf{c}^{*} & \underline{\mathbf{n}}^{\mathrm{T}*} & \underline{\boldsymbol{\xi}}^{\mathrm{T}*} & \underline{\boldsymbol{\mu}} \end{bmatrix} \begin{bmatrix} \sigma_{\mathrm{h}} \\ \mathbf{v} \\ \mathbf{E} \\ \mathbf{H} \end{bmatrix}, \tag{3.163}$$

where $\sigma_{\mathrm{h}} = -p$ is the hydrostatic stress. According to Eqs. (3.162b), (3.162e), and (3.162d), the three tensors on the main diagonal are Hermitian. Equation (3.163) can be written in the form

$$\begin{pmatrix} \varepsilon \\ \boldsymbol{\mu} \\ \mathbf{D} \\ \mathbf{B} \end{pmatrix} = [Y] \begin{pmatrix} \sigma_{\mathrm{h}} \\ \mathbf{v} \\ \mathbf{E} \\ \mathbf{H} \end{pmatrix}, \quad [Y] \equiv \begin{pmatrix} \beta & \boldsymbol{\gamma} & \mathbf{e} & \mathbf{c} \\ \boldsymbol{\eta} & \underline{\boldsymbol{\rho}} & \underline{\mathbf{w}} & \underline{\mathbf{n}} \\ \mathbf{d} & \underline{\mathbf{v}} & \underline{\boldsymbol{\epsilon}} & \underline{\boldsymbol{\xi}} \\ \mathbf{b} & \underline{\mathbf{m}} & \underline{\boldsymbol{\zeta}} & \underline{\boldsymbol{\mu}} \end{pmatrix} = [Y]^{\mathrm{T}*}, \tag{3.164}$$

which is consistent with Eq. (3.30) when expressed in terms of the hydrostatic pressure $\sigma_{\text{h,eff}} = -p_{\text{eff}}$:[21]

$$\begin{pmatrix} \varepsilon_{\text{eff}} \\ \mu_{z,\text{eff}} \\ D_{\text{eff}} \\ B_{\text{eff}} \end{pmatrix} = \begin{pmatrix} \beta_{\text{eff}} & \chi^{\text{o}}_{pv} - i\chi^{\text{e}}_{pv} & i\chi^{\text{o}}_{pE} - \chi^{\text{e}}_{pE} & -\chi^{\text{o}}_{pH} + i\chi^{\text{e}}_{pH} \\ \chi^{\text{o}}_{pv} + i\chi^{\text{e}}_{pv} & \rho_{\text{eff}} & \chi^{\text{o}}_{vE} - i\chi^{\text{e}}_{vE} & -i\chi^{\text{o}}_{vH} + \chi^{\text{e}}_{vH} \\ -i\chi^{\text{o}}_{pE} - \chi^{\text{e}}_{pE} & \chi^{\text{o}}_{vE} + i\chi^{\text{e}}_{vE} & \epsilon_{\text{eff}} & \chi^{\text{o}}_{EH} \\ -\chi^{\text{o}}_{pH} - i\chi^{\text{e}}_{pH} & i\chi^{\text{o}}_{vH} + \chi^{\text{e}}_{vH} & \chi^{\text{o}}_{EH} & \mu_{\text{eff}} \end{pmatrix} \begin{pmatrix} \sigma_{\text{h,eff}} \\ v_{\text{eff}} \\ E_{\text{eff}} \\ H_{\text{eff}} \end{pmatrix}. \tag{3.165}$$

The terms in the 4×4 matrix of Eq. (3.165) have been color-coded according to the discussion of Eq. (3.81).

3.5 Summary

The acoustic homogenization theory of Sieck et al. [13] was generalized to include the simultaneous scattering of electromagnetic waves. Sieck's definitions of the acoustic monopole strength and dipole moment in terms of acoustic polarizabilities were extended by the addition of piezoelectric, piezomagnetic, and electromomentum terms. The acoustic monopole strength and acousto-electromagnetic dipole moments were related to the incident fields through a 4×4 polarizability matrix, which characterizes a subwavelength, asymmetric, passive, and reciprocal piezoelectric heterogeneity. By homogenizing a one-dimensional periodic array of such heterogeneities, the scalar-valued effective constitutive relations were found to be given by Eq. (3.30). The off-diagonal terms in Eq. (3.30) were shown to be functions of lattice sums and complementary polarizabilities, which characterize meso- and microscale effects, respectively. The present work shows that magnetomomentum coupling (denoted by the subscripts "vH") arises even when piezomagnetic coupling does not exist at the microscale.

The constraints due to reciprocity and passivity on the elasto-electromagnetic form of the effective constitutive relations were determined. The results recovered those of Refs. 69, 70, and 123 in the absence of elastodynamics, electrodynamics, and magnetism, respectively. The novel results are provided by Eqs. (3.146b), (3.152b), (3.131g),

[21] The subscript pu in Eq. (5) (second row, first column) of Ref. 194 should be pv, shown correctly in Eq. (3.165).

and (3.131i). The acoustic limit of the elasto-electrodynamic results were shown to be consistent with Eq. (3.30), suggesting that the homogenization theory obeys reciprocity and passivity.

Future research directions related to electromomentum coupling are outlined in Sec. 5.2.

Chapter 4: Analysis of linear acoustic vortex beams

4.1 Introduction

Vortex beams have been studied in optics for over three decades, starting with the observation by Allen et al. [233] that eigenfunctions used in paraxial optics possess orbital angular momentum proportional to the orbital number ℓ, also known as the azimuthal index or topological charge. Optical vortices have since been studied intensely, leading to their application to particle manipulation using optical tweezers and communication devices with high data rates [234]. Interest in optical vortices began with the study by Coullet et al. [235], who demonstrated the existence of vortex states of light in a laser cavity through a numerical study of the Maxwell-Bloch equations. Coullet et al. were inspired by hydrodynamic vortex rings, which were first studied by Helmholtz [236]. The study of vortices returned to fluid mechanics, not as the traditional incompressible rotation of a fluid but as an acoustic wave phenomenon, with Hefner and Marston's [10] numerical and experimental demonstration of an underwater acoustic vortex beam. Analogous to their optical counterparts, acoustic vortex beams have since been applied to particle manipulation [73, 74, 76–81] and acoustic communication [85–91]. They have also been applied in biomedical ultrasound [82–84] and have even been used to create sound-diffusing surfaces [92]. An extensive review of the generation and application of acoustic vortex beams was published recently by Guo et al. [98].

The generation of acoustic vortex beams remains a central challenge to their use. A straightforward approach is to use arrays of acoustic transducers with the necessary phasing and amplitude shading with [237] or without [81, 238] focusing lenses. While the use of arrays of active elements has the advantage of being adaptable to different scenarios, they require multiple electroacoustic channels with their associated hardware

The contents of this chapter have been published in Refs. 107, 231, and 232. The author's contributions include deriving solutions, comparing the results to Fourier acoustics, generating figures, writing Refs. 231 and 232, and responding to reviewers.

and algorithms to generate the desired field [81]. Alternative single-channel approaches include the use of a wrapped transducer geometry as shown by Baudoin et al. [79], or a helicoidal transducer shape that introduces the necessary angle-dependent phase gradient at the radiating surface as first shown by Hefner and Marston [10]. The latter examples were precursors to more recent efforts to design conventional or metamaterial lenses to introduce the helicoidal and focusing phase so that one may use a single channel source that has a uniformly phased aperture [94, 101, 111, 239, 240]. Metamaterial examples include the use of side-branch Helmholtz resonators [98, 241] or labyrinthine structures to generate acoustic vortices in air [96, 242]. Other unique approaches include using arrays of helicoids [243], circular gratings to create a leaky wave antenna [244, 245], and the generation of vortices in reflected sound fields by designing grooves in a reflective surface [97]. Adaptation of metamaterial structures designed for airborne acoustics has been extended to underwater acoustics, with examples including two sets of Archimedian spirals, [94] porous rubber layers with spatially-graded subwavelength structure [239], and pentamode lattice structures [90] similar to previous work on planar underwater pentamode lenses [246, 247].

The design of conventional or metamaterial vortex sources requires accurate and efficient analytical or numerical models to calculate the field, similar to how the design of focused sources could be informed by the O'Neil model [248] prior to development of more computationally expensive numerical models. The development of analytical descriptions of sound beams often begins with the Rayleigh integral [9, Chap. 14], which is accurate for all ka. A simplified diffraction integral equivalent to the Rayleigh integral is developed in Sec. 4.2 for time-harmonic fields radiated by baffled circular pistons with a vortex phase dependence. The integral is obtained by solving the Helmholtz equation in an infinitely large cylindrical waveguide, demonstrating that diffraction in free space is a limiting case of modal analysis. While the Rayleigh integral is typically interpreted as a sum of simple sources, the derivation in Sec. 4.2 shows that the Rayleigh integral can also be cast as a sum of eigenfunctions of the Helmholtz equation. The alternative formulation is used to recover the axial pressure radiated by a baffled circular piston and solve the Helmholtz

equation numerically for a vortex beam.

Analytical solutions for acoustic vortex beams radiated by circular pistons are derived in Sec. 4.3 by appealing to the paraxial approximation. The solution of the paraxial approximation is given by the Fresnel approximation of the Rayleigh integral, evaluation of which yields analytical solutions in the far field of an unfocused source and in the focal plane of a focused source in terms of an infinite series of Bessel functions for orbital numbers $\ell > -2$. The solutions are reduced to closed forms for $0 \leq \ell \leq 4$, which correspond to orbital numbers commonly used in experiments [71]. Meanwhile, consideration of a Gaussian amplitude distribution in the source plane is leads to closed-form solutions for $\ell > -2$ in all space for both unfocused and focused sources.

The vortex ring radius is a useful measure in both optics [249, 250] and acoustics [112]. For unfocused vortex fields, the ring radius is defined as the distance from the beam axis to the first local maximum, whereas for focused vortex fields the definition of ring radius is normally restricted to the focal plane focal plane even though the vortex ring does not necessarily reside in the focal plane. The utility of the analytical solutions obtained in Sec. 4.3 is demonstrated in Sec. 4.4 by deriving the vortex ring radii associated with the circular piston sources and Gaussian sources. For both sources, the ring radii in the focal plane and far field are linear functions of the orbital number.

A simple criterion is obtained in Sec. 4.5 for the parameter space in which solutions based on the paraxial approximation for unfocused vortex beams are accurate, which is confirmed by comparisons with solutions of the Helmholtz equation. A similar comparison is performed for focused beams, but the additional complexity introduced by focusing precludes derivation of an analytical criterion. Instead, regions of the parameter space in which the paraxial approximation was found to be accurate for focused beams are presented as decision matrices.

As the orbital number increases in focused vortex beams, the vortex ring not only increases in radius but also moves out of the focal plane in the direction of the source. Under certain conditions, the vortex ring becomes redistributed along a surface that encloses

a shadow zone in the prefocal region. These features motivate the study of vortex beams in the infinite-frequency limit in Sec. 4.6, which yields an analytical expression for the coordinates of the caustic surfaces in vortex beams. In focused vortex beams, the caustic surface in the prefocal region is a spheroid that encloses the shadow zone predicted by diffraction theory. A related wave phenomenon, referred to as an autofocusing vortex beam, has been observed in optics and modeled with caustics predicted by geometrical acoustics [117]. Distinctions between autofocusing vortex beams and the vortex beams modeled in the present work are drawn following the discussion of Figs. 4.15 and 4.16 below.

4.2 Simplified diffraction integral for circular pistons

Studies of acoustic vortex beams often consider radiation from circular pistons [74, 76, 78, 83, 84, 101, 237, 240, 251–254]. A circular piston that radiates a time-harmonic acoustic vortex beam can be described in cylindrical coordinates (r, θ, z) by its velocity in the z direction,[1]

$$\tilde{v}_z(r, \theta, 0) = v_0 \operatorname{circ}(r/a) e^{i\ell\theta}, \tag{4.1}$$

where $\operatorname{circ}(r/a) = 1$ for $0 < r/a \leq 1$ and 0 elsewhere, a is the radius of the piston, and ℓ is the orbital number, which is nonzero for vortex beams [10, 103]. With zero amplitude assigned at $r = 0$, the ambiguity in phase at $r = 0$ for $\ell \neq 0$ is avoided without affecting the integrations in the following analysis.

The Rayleigh integral [22, Eq. (5.2.6)]

$$\tilde{p}(\mathbf{r}) = -\frac{ik\rho_0 c_0}{2\pi} \int_{S_0} \tilde{v}_z(\mathbf{r}_0) \frac{e^{ik|\mathbf{r}-\mathbf{r}_0|}}{|\mathbf{r}-\mathbf{r}_0|} \, dS_0 \tag{4.2}$$

is an exact solution of the Helmholtz equation given by Eq. (A.1) and is often the starting point for obtaining the time-harmonic pressure $\tilde{p}$ radiated in an infinite half-space, where

[1] As in Chap. 2, physical quantities are obtained by multiplying complex-valued quantities by $e^{-i\omega t}$ and taking the real part of the resulting expression. For example, the physical field corresponding to Eq. (4.1) is $v_z(r, \theta, 0) = v_0 \operatorname{circ}(r/a) \cos(\ell\theta - \omega t)$.

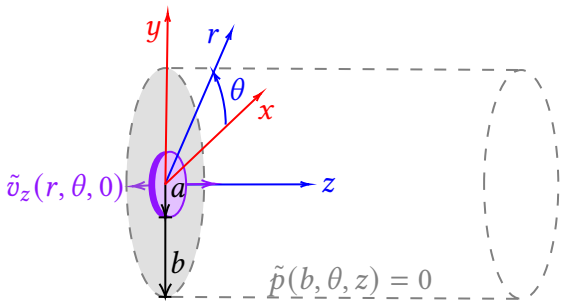

Figure 4.1: Baffled circular piston of radius a in the plane $z = 0$ with normal velocity amplitude v_0. The piston is concentric within a pressure-release cylindrical waveguide of radius b.

k is the wavenumber, ρ_0 is the ambient density of the fluid, c_0 is the sound speed, and S_0 is the radiating surface in the source plane $z = 0$. Equation (4.2) is traditionally derived from the Helmholtz-Kirchhoff integral given by Eq. (C.23) [22, Sec. 5.2.1]. In the present section, Eq. (4.2) is obtained for the case of a circular piston by considering a different problem: a piston described by Eq. (4.1) placed concentrically within a pressure-release waveguide of radius b as shown in Fig. 4.1. A piston in an infinite baffle is obtained in the limit as $b \to \infty$, whereupon the sum of modes in the waveguide becomes an integral in free space over the cylindrical eigenfunctions of the Helmholtz equation.

The recovery of Eq. (4.2) from the modal solution demonstrates that diffraction theory can be viewed as a limiting case of modal analysis. Starting with the modal solution draws a parallel with the solution of the paraxial equation in terms of Laguerre-Gaussian modes [10] and provides a natural way of describing diffraction in cylindrical coordinates. The representation of Eq. (4.2) in terms of the cylindrical eigenfunctions of the Helmholtz equation is amenable to problems with cylindrical features and rotational symmetry, including scattering [108, 255]. The results of this work also simplify the numerical evaluation of Eq. (4.2) for sources described by Eq. (4.1) by reducing the surface integral to an integral over a single variable.

The modal solution of the Helmholtz equation for the piston in the waveguide of finite radius b is obtained first. The limit $b \to \infty$ is then taken, and Eq. (4.2) is recovered. Two examples that demonstrate the utility of the present formulation follow.

Modal solution in waveguide

The general solution of the Helmholtz equation for the geometry depicted in Fig. 4.1 is [9, Chap. 11, Eq. (A–13)]

$$\tilde{p}(r,\theta,z) = \sum_{q=-\infty}^{\infty} \sum_{m=1}^{\infty} A_{qm} J_q(\alpha_{qm} r/b) e^{i(q\theta+\beta_{qm}z)}\,, \tag{4.3}$$

where α_{qm} is the mth root of the Bessel function J of order q, and where

$$\beta_{qm} = \sqrt{k^2 - (\alpha_{qm}/b)^2}$$

is the z component of the wave vector. For Eq. (4.3) to equal Eq. (4.1) in the source plane, set

$$q = \ell\,, \qquad \tilde{v}_z = \frac{1}{ik\rho_0 c_0} \left.\frac{\partial p}{\partial z}\right|_{z=0}\,,$$

resulting in

$$\sum_{m=1}^{\infty} A_{\ell m} \beta_{\ell m} J_\ell(\alpha_{\ell m} r/b) = k\rho_0 c_0 v_0 \,\mathrm{circ}(r/a)\,. \tag{4.4}$$

Multiplication of Eq. (4.4) by $r J_\ell(\alpha_{\ell n} r/b)$ and integration over r from 0 to b yields

$$\sum_{m=1}^{\infty} A_{\ell m} \beta_{\ell m} \int_0^b J_\ell(\alpha_{\ell m} r/b) J_\ell(\alpha_{\ell n} r/b) r\,dr = k\rho_0 c_0 v_0 \int_0^a J_\ell(\alpha_{\ell n} r/b) r\,dr\,. \tag{4.5}$$

The left-hand side of Eq. (4.5) is integrated using the orthogonality relation [256, Item 6.521-1]

$$\int_0^b J_\ell(\alpha_{\ell m} r/b) J_\ell(\alpha_{\ell n} r/b) r\,dr = \frac{b^2}{2} \delta_{mn} J_{\ell+1}^2(\alpha_{\ell n})\,,$$

yielding

$$A_{\ell n} \beta_{\ell n} J_{\ell+1}^2(\alpha_{\ell n}) = 2k\rho_0 c_0 v_0 \alpha_{\ell n}^{-2} F_\ell(\alpha_{\ell n} a/b) \tag{4.6}$$

for $\ell > -2$, where δ_{mn} is the Kronecker delta and [257, Item 11.1.1]

$$F_\ell(\xi) = \int_0^\xi J_\ell(t) t\,dt = \xi \frac{\Gamma(\ell/2+1)}{\Gamma(\ell/2)} \sum_{k=0}^{\infty} \frac{(\ell+2k+1)\Gamma(\ell/2+k)}{\Gamma(\ell/2+2+k)} J_{\ell+2k+1}(\xi)\,, \tag{4.7}$$

where Γ is the gamma function [256, Sec. 8.31]. Equation (4.7) is equivalent to the following closed-form expressions for $0 \leq \ell \leq 4$:

$$F_0(\xi) = \xi J_1(\xi)\,, \qquad \ell = 0\,, \tag{4.8}$$

$$F_1(\xi) = \tfrac{\pi}{2}\xi\left[\mathbf{H}_0(\xi)J_1(\xi) - \mathbf{H}_1(\xi)J_0(\xi)\right]\,, \qquad \ell = 1\,, \tag{4.9}$$

$$F_2(\xi) = 2 - 2J_0(\xi) - \xi J_1(\xi)\,, \qquad \ell = 2\,, \tag{4.10}$$

$$F_3(\xi) = \left[\tfrac{3\pi}{2}\xi\,\mathbf{H}_0(\xi) - 8\right]J_1(\xi) + \left[4\xi - \tfrac{3\pi}{2}\xi\,\mathbf{H}_1(\xi)\right]J_0(\xi)\,, \qquad \ell = 3\,, \tag{4.11}$$

$$F_4(\xi) = 4 - 8J_1(\xi)/\xi - 4J_2(\xi) - \xi J_3(\xi)\,, \qquad \ell = 4\,, \tag{4.12}$$

where $\mathbf{H}_0$ and $\mathbf{H}_1$ are the zeroth- and first-order Struve functions [256, Item 8.550.1]. Solving Eq. (4.6) for $A_{\ell n}$ yields the solution of the Helmholtz equation for the geometry shown in Fig. 4.1:

$$\tilde{p}(r,\theta,z) = \sum_{n=1}^{\infty} A_{\ell n} J_\ell(\alpha_{\ell n} r/b) e^{i(\ell\theta + \beta_{\ell n} z)}\,, \tag{4.13}$$

$$A_{\ell n} = 2\rho_0 c_0 v_0 \frac{k}{\alpha_{\ell n}^2 \beta_{\ell n}} \frac{F_\ell(\alpha_{\ell n} a/b)}{J_{\ell+1}^2(\alpha_{\ell n})}\,, \tag{4.14}$$

$$\beta_{\ell n} = \sqrt{k^2 - (\alpha_{\ell n}/b)^2}\,. \tag{4.15}$$

The restriction $\ell > -2$ on Eq. (4.7) is purely mathematical and does not restrict the magnitude of Eq. (4.13) (and the magnitudes of the following results) from being interpreted for $\ell \leq -2$. The magnitude of the pressure field is unaltered by changing the sign of ℓ, whereas the effect on the phase is only to reverse the helical polarity (sometimes referred to as handedness or chirality) of the wavefronts.

Limit of infinite waveguide radius

The limit $b \to \infty$ of Eq. (4.13) corresponds to the field radiated into an infinite half-space and is obtained by noting that the ratio $\alpha_{\ell n}/b$ appearing in Eqs. (4.13)–(4.15) is vanishingly small except for large n, for which [256, Item 8.547]

$$\alpha_{\ell n} \simeq \pi(n - 1/4 + \ell/2), \quad n \gg 1\,. \tag{4.16}$$

Introducing the dimensionless parameter

$$\zeta = \frac{a}{b}\pi(n - 1/4 + \ell/2) \tag{4.17}$$

permits Eqs. (4.14) and (4.15) to be written for large n as

$$A_{\ell n} \simeq \rho_0 c_0 v_0 \frac{\Delta\zeta}{\zeta} \frac{F_\ell(\zeta)}{\sqrt{1 - (\zeta/ka)^2}}, \tag{4.18}$$

$$\beta_{\ell n} \simeq k\sqrt{1 - (\zeta/ka)^2}, \quad n \gg 1, \tag{4.19}$$

respectively, where $\Delta\zeta = \pi a/b$, and where the relation [257, Item 9.2.1]

$$J_\nu(x) \simeq \sqrt{\frac{2}{\pi x}} \cos(x - \nu\pi/2 - \pi/4), \quad x \gg 1 \tag{4.20}$$

has been used to obtain the asymptotic form of $J_{\ell+1}(\alpha_{\ell n})$ appearing in Eq. (4.14):

$$\frac{1}{J^2_{\ell+1}(\alpha_{\ell n})} \simeq \frac{\pi^2}{2}(n - 1/4 + \ell/2), \quad n \gg 1. \tag{4.21}$$

Inserting Eqs. (4.17)–(4.19) into Eq. (4.13) yields

$$\tilde{p}(r, \theta, z) = \rho_0 c_0 v_0 e^{i\ell\theta} \sum_{n=1}^{\infty} \frac{\Delta\zeta}{\zeta} \frac{F_\ell(\zeta) J_\ell(\zeta r/a)}{\sqrt{1 - (\zeta/ka)^2}} e^{ikz\sqrt{1-(\zeta/ka)^2}}. \tag{4.22}$$

In the limit $b \to \infty$, $\Delta\zeta$ becomes $d\zeta$, and the summation becomes an integral:

$$\tilde{p}(r, \theta, z) = \rho_0 c_0 v_0 e^{i\ell\theta} \int_0^\infty \frac{F_\ell(\zeta) J_\ell(\zeta r/a)}{\zeta\sqrt{1 - (\zeta/ka)^2}} e^{ikz\sqrt{1-(\zeta/ka)^2}} d\zeta. \tag{4.23}$$

Noting from Eqs. (4.15), (4.17), and (4.19) that $\zeta = k_r a$ and $\sqrt{1 - (\zeta/ka)^2} = k_z/k$, where k_r and k_z are the r and z components of the wave vector, respectively, allows Eq. (4.23) to be expressed as

$$\tilde{p}(r, \theta, z) = \rho_0 c_0 v_0 e^{i\ell\theta} k \int_0^\infty F_\ell(k_r a) J_\ell(k_r r) \frac{e^{ik_z z}}{k_z} \frac{dk_r}{k_r}. \tag{4.24}$$

Equation (4.24) is equivalent to the Rayleigh integral, as will soon be shown. While the Rayleigh integral is traditionally interpreted as the "sum of the radiations from... individual simple sources" [9, p. 360], Eq. (4.24) shows that the Rayleigh integral can also be viewed

as a sum of the eigenfunctions $J_\ell(k_r r)e^{i(\ell\theta+k_z z)}$ of the Helmholtz equation. The eigenfunctions are also known as Bessel beams [108], which are convenient for analysis because they do not diffract [258]. Equation (4.24) can then be interpreted as the Bessel-beam decomposition of the field radiated by a source described by Eq. (4.1). Studies involving individual Bessel beams may be generalized using Eq. (4.24) to fields radiated by circular pistons, although the superposition principle underlying such a decomposition requires that the wave phenomenon of interest be linear [183].

The Bessel-beam decomposition of radiation from a circular pressure source for $\ell = 0$ was previously derived by King [259, Eq. (5)], Junger and Feit [260, Eqs. (5.4) and (5.16)], and Daniel et al. [255, Eqs. (3) and (B5)]. Setting $\ell = 0$ in Eq. (4.24) and identifying $k_r = \lambda$, $ik_z = \mu$, $\tilde{v}_z = -(\partial\phi/\partial z)|_{z=0}$, $p = ik\rho_0 c_0\phi$, and $v_0 = \dot{x}$ recovers Eq. (5) of Ref. 259, where the convention $i(\omega t - kz)$ used in Ref. 259 explains the minus sign in the exponential of Eq. (5). Similarly, identifying $k_r = \gamma$ and $-ikc_0 v_0 = \ddot{W}$ recovers Eq. (5.16) in combination with Eq. (5.4) of Ref. 260. Meanwhile, denoting $k_r = k\sin\beta$ and $k_z = k\cos\beta$ recovers Eq. (3) in combination with Eq. (B-5) of Ref. 255, where the additional factor of $\cos\beta$ in Eq. (B5) appears because a pressure source is considered in Ref. 255, whereas a velocity source is considered in Refs. 259, 260, and the present section.

Equation (4.24) is also obtained if the boundary at $r = b$ is rigid ($\partial p/\partial r|_{r=b} = 0$), in which case the modal solution of the Helmholtz equation is[2]

$$\tilde{p}(r,\theta,z) = \sum_{n=1}^{\infty} A'_{\ell n} J_\ell(\alpha'_{\ell n} r/b) e^{i(\ell\theta+\beta'_{\ell n} z)}, \tag{4.25}$$

$$A'_{\ell n} = \frac{2\rho_0 c_0 v_0}{1-(\ell/\alpha'_{\ell n})^2} \frac{k}{\alpha'^2_{\ell n}\beta'_{\ell n}} \frac{F_\ell(\alpha'_{\ell n} a/b)}{J^2_\ell(\alpha'_{\ell n})}, \tag{4.26}$$

$$\beta'_{\ell n} = \sqrt{k^2 - (\alpha'_{\ell n}/b)^2}, \tag{4.27}$$

where $\alpha'_{\ell n}$ is the nth root of the derivative of J_ℓ, and where the orthogonality integral leading to Eq. (4.26) is given by Prob. 3-8 of Ref. 261. The asymptotic form of Eq. (4.26) for

[2]Equations (4.25)–(4.27) for an axisymmetric circular piston ($\ell = 0$) in a rigid cylindrical waveguide were presented in spring 2022 by M. F. Hamilton in Acoustics II, an introductory graduate-level course in the Walker Department of Mechanical Engineering at the University of Texas at Austin.

$n \gg 1$ is obtained using the relation [180, Item 10.21.20]

$$\alpha'_{\ell n} \simeq \pi(n - 3/4 + \ell/2)\,, \quad n \gg 1\,, \tag{4.28}$$

which in combination with Eq. (4.20) yields

$$A'_{\ell n} \simeq \frac{\rho_0 c_0 v_0}{1 - (\ell \Delta\zeta'/\pi\zeta')^2} \frac{\Delta\zeta'}{\zeta'} \frac{F_\ell(\zeta')}{\sqrt{1 - (\zeta'/ka)^2}}\,, \quad n \gg 1\,, \tag{4.29}$$

where $\zeta' = \pi(n - 3/4 + \ell/2)a/b$ and $\Delta\zeta' = \pi a/b$. In the limit $b \to \infty$, $\Delta\zeta'$ in Eq. (4.29) becomes $d\zeta'$, $\Delta\zeta'^2$ becomes $d\zeta'^2 = 0$, and the sum in Eq. (4.25) becomes an integral. Equation (4.23) [and hence Eq. (4.24)] is recovered by noting that ζ' is an integration variable and can be renamed ζ.

Recovering the Rayleigh integral

To recover Eq. (4.2) from Eq. (4.24), note that [262, Sec. 2.2, Eq. (5)]

$$J_\ell(k_r r) = \frac{1}{2\pi} \int_0^{2\pi} e^{i\ell\phi} e^{-ik_r r \sin\phi} d\phi\,. \tag{4.30}$$

Changing variables to $\phi = \psi - \theta - \pi/2$ allows Eq. (4.24) to be expressed as

$$\tilde{p}(r, \theta, z) = \frac{k\rho_0 c_0}{2\pi} \int_0^{2\pi} \int_0^{\infty} v_0 F_\ell(k_r a) e^{i\ell(\psi - \pi/2)} e^{ik_r r \cos(\theta - \psi)} \frac{e^{ik_z z}}{k_z} \frac{dk_r}{k_r} d\psi\,. \tag{4.31}$$

Combining Eq. (4.1) with the integral representations of F_ℓ and J_ℓ shows that

$$v_0 F_\ell(k_r a) e^{i\ell(\psi - \pi/2)} = \frac{k_r^2}{2\pi} \mathcal{F}_{2D}\{\tilde{v}_z(r, \theta)\}\,,$$

where $\tilde{v}_z$ is given by Eq. (4.1), reducing Eq. (4.31) to

$$\tilde{p}(x, y, z) = \rho_0 c_0 k\, \mathcal{F}_{2D}^{-1}\{\mathcal{F}_{2D}[\tilde{v}_z(r, \theta)] e^{ik_z z}/k_z\}\,, \tag{4.32}$$

where $\mathcal{F}_{2D}$ and $\mathcal{F}_{2D}^{-1}$ are the polar forms of the spatial Fourier transform pair,

$$\mathcal{F}_{2D}\{f(r, \theta)\} = \hat{f}(k_r, \psi) = \int_0^{2\pi} \int_0^{\infty} f(r, \theta) e^{-ik_r r \cos(\theta - \psi)} r\, dr\, d\theta, \tag{4.33}$$

$$\mathcal{F}_{2D}^{-1}\{\hat{f}(r, \theta)\} = f(r, \theta) = \frac{1}{4\pi^2} \int_0^{2\pi} \int_0^{\infty} \hat{f}(k_r, \psi) e^{ik_r r \cos(\theta - \psi)} k_r\, dk_r\, d\psi. \tag{4.34}$$

The polar components of the wavenumber k_r and ψ in Eqs. (4.33) and (4.34) are related to the Cartesian components k_x and k_y by

$$k_x = k_r \cos\psi\,, \qquad k_y = k_r \sin\psi\,, \tag{4.35}$$

$$k_r = (k_x^2 + k_y^2)^{1/2}\,, \qquad \psi = \arctan(k_y/k_x)\,. \tag{4.36}$$

In terms of Eqs. (4.35), Eq. (4.32) can be expressed as

$$p = \rho_0 c_0 k\, \mathcal{F}_{xy}^{-1}\{\mathcal{F}_{xy}[\tilde{v}_z(x,y)]e^{ik_z z}/k_z\}\,, \tag{4.37}$$

where $\mathcal{F}_{xy}$ and $\mathcal{F}_{xy}^{-1}$ are given by Eqs. (E.2) and (E.3), respectively, and for which Eq. (4.1) becomes

$$\tilde{v}_z(x,y) = v_0 \,\mathrm{circ}\left(\sqrt{x^2+y^2}/a\right) e^{i\ell \arctan(y/x)}\,. \tag{4.38}$$

Equation (4.37) recovers Eq. (E.20), which describes the acoustic radiation from a velocity source using Fourier acoustics. Invoking the convolution theorem, Eq. (4.37) becomes

$$\tilde{p}(x,y,z) = \rho_0 c_0 k\, \mathcal{F}_{xy}^{-1}\{\mathcal{F}_{xy}[\tilde{v}_z(x,y)]\} ** \mathcal{F}_{xy}^{-1}\{e^{ik_z z}/k_z\}\,, \tag{4.39}$$

where the double asterisk in Eq. (4.39) denotes convolution over x and y. Equation (4.39) is simplified by noting that $\mathcal{F}_{xy}^{-1}\{\mathcal{F}_{xy}[\tilde{v}_z(x,y)]\} = \tilde{v}_z(x,y)$ and $\mathcal{F}_{xy}\{e^{ikr}/r\} = i2\pi e^{ik_z|z|}/k_z$ [263, pp. 227–234], where $r = \sqrt{x^2+y^2+z^2}$:

$$\tilde{p}(x,y,z) = -\frac{ik\rho_0 c_0}{2\pi}\, \tilde{v}_z(x,y) ** \frac{e^{ikr}}{r}\,. \tag{4.40}$$

By the definition of the convolution operation, Eq. (4.40) recovers Eq. (4.2) expressed in Cartesian coordinates, for which $\mathbf{r} = x\mathbf{e}_x + y\mathbf{e}_y + z\mathbf{e}_z$, $\mathbf{r}_0 = x_0\mathbf{e}_x + y_0\mathbf{e}_y$, and $dS_0 = dx_0\, dy_0$, where $\mathbf{e}_x$, $\mathbf{e}_y$, and $\mathbf{e}_z$ are the Cartesian unit vectors. The recovery of Eq. (4.2) from Eq. (4.3) shows that diffraction theory can be recovered from a modal solution in an infinitely large enclosure. While the traditional derivation of the Rayleigh integral requires knowledge of special functions, Green's functions, and the principle of reciprocity [22, 122], these concepts were not invoked above. The simplicity comes at the expense of the generality of the present derivation, which is restricted to circular sources.

Two examples

The utility of Eq. (4.24) is demonstrated by two examples. In terms of the dimensionless parameters $P = \tilde{p}/\rho_0 c_0 v_0$, $R = r/a$, $Z = z/z_\mathrm{R}$, and $K = ka$, where z_R is the Rayleigh distance $ka^2/2$, Eq. (4.23) becomes

$$P = e^{i\ell\theta} \int_0^\infty \frac{F_\ell(\zeta) J_\ell(\zeta R)}{\zeta \sqrt{1-(\zeta/K)^2}} \, e^{iK^2 Z \sqrt{1-(\zeta/K)^2}/2} \, d\zeta \,. \tag{4.41}$$

Considered first is the axial pressure radiated by a planar circular piston obtained by setting $R = \ell = 0$, yielding [256, Item 6.637-1]

$$\begin{aligned} P(Z) &= \int_0^\infty \frac{J_1(\zeta)}{\sqrt{1-(\zeta/K)^2}} \, e^{iK^2 Z \sqrt{1-(\zeta/K)^2}/2} d\zeta \\ &= -iK \, I_{1/2}[-i\chi_-(Z)] \, K_{1/2}[-i\chi_+(Z)] \,, \end{aligned} \tag{4.42}$$

where I_ν and K_ν are the νth-order modified Bessel functions of the first and second kind, respectively, and where

$$\chi_\pm(Z) = (K/2)\big[\sqrt{1+(KZ/2)^2} \pm KZ/2\big]. \tag{4.43}$$

The relations [256, Items 8.406-3 and 8.464-1] [257, Item 9.6.2]

$$I_\nu(x) = i^{-\nu} J_\nu(ix) \,, \qquad K_\nu(ix) = \frac{\pi}{2\sin(\nu\pi)} [I_{-\nu}(ix) - I_\nu(ix)] \,, \tag{4.44}$$

$$J_{1/2}(x) = \sqrt{\frac{2x}{\pi}} \, \frac{\sin x}{x} \,, \qquad J_{-1/2}(x) = \sqrt{\frac{2x}{\pi}} \, \frac{\cos x}{x} \tag{4.45}$$

reduce Eq. (4.42) to

$$P(Z) = -2i \sin[\chi_-(Z)] e^{i\chi_+(Z)} \,, \tag{4.46}$$

recovering the axial pressure radiated by a planar circular piston [22, Eq. (5.7.3)], which is traditionally derived by evaluating Eq. (4.2) for $|\mathbf{r} - \mathbf{r}_0| = \sqrt{r_0^2 + z^2}$ and $\tilde{v}_z = v_0 \, \mathrm{circ}(r_0/a)$.

Considered next is the numerical evaluation of Eq. (4.41), which is compared with the angular spectrum method given by Eq. (E.20) in Fig. 4.2. The comparison is performed for $\ell = 1$, the orbital number most commonly used in vortex beam experiments [71].

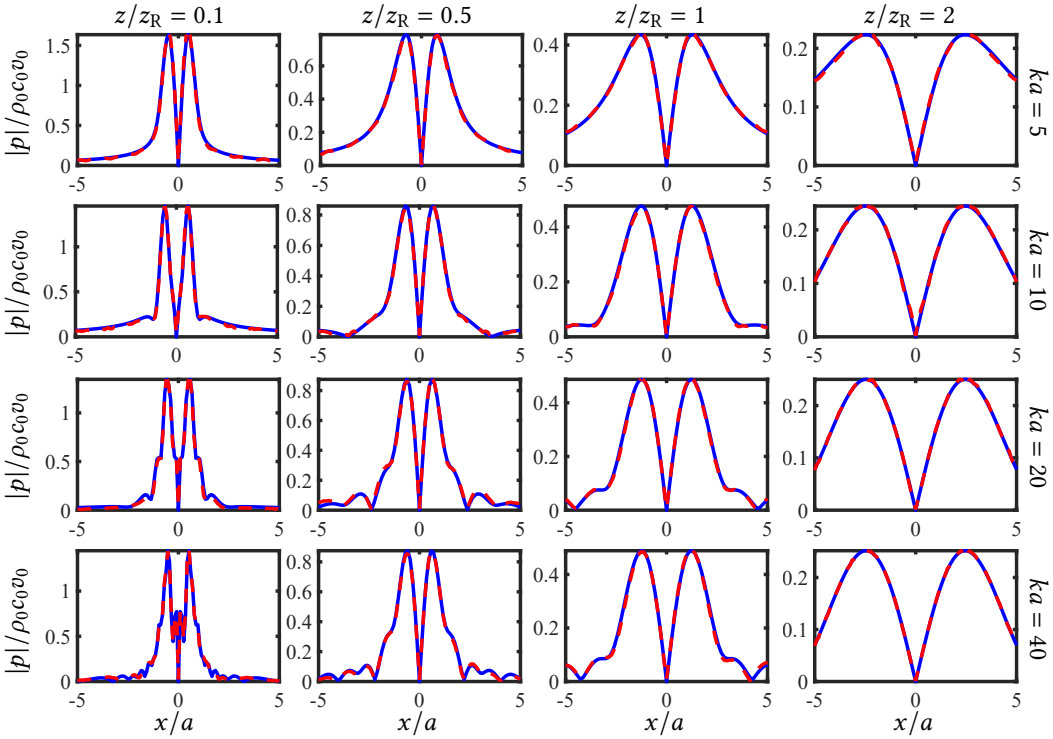

Figure 4.2: Equation (4.24) (solid blue curves) compared with Eq. (E.20) (dashed red curves) for the source condition given by Eq. (4.1) with $\ell = 1$.

The dashed red curves representing Eq. (E.20) were generated by carefully adjusting the domain and number of transverse discretization points to avoid errors due to aliasing [255, 264–266]. Numerical integration of Eq. (4.41), represented by the blue curves in Fig. 4.2, avoids the artifacts associated with simulation based on Fourier acoustics and is relatively easy to implement, making it advantageous over, but less general than, the evaluation of Eq. (E.20).

While analytical solutions of the paraxial equation are available in the far field $z \gtrsim ka^2$ for sources described by Eq. (4.1), as shown in Sec. 4.3, such solutions satisfactorily match the solution of the Helmholtz equation for $ka \gtrsim 4\ell$, as discussed in Sec. 4.5. Studies involving near-field effects [72, 267], high orbital numbers [101], and/or vortex fields at low ka can therefore utilize the numerical evaluation of Eq. (4.41), which is an exact solution of the Helmholtz equation.

For sources described by Eq. (4.1), Eq. (4.41) can be obtained directly from Eq. (4.32) by replacing the Fourier transforms with ℓth-order Hankel transforms. The advantages of Eq. (4.41) over Eq. (E.20) described above arise because the forward transform of Eq. (4.1) is evaluated analytically in Eq. (4.41) rather than numerically in Eq. (E.20).

4.3 Paraxial approximation of vortex beams

Although Eq. (4.24) is an exact solution of the Helmholtz equation, it can be evaluated analytically only in limiting cases, e.g., $\ell = R = 0$. To obtain more general analytical results, it is necessary to make approximations that simplify the theory of diffraction. For sufficiently large ka, waves radiated in the z direction can be described by $\tilde{p} = qe^{ikz}$,[3] where q is a function that varies sufficiently slowly with z. If $|\partial^2 q/\partial z^2| \ll 2k|\partial q/\partial z|$, Eq. (A.1) may be replaced by the paraxial equation given by Eq. (A.25). The solution of Eq. (A.25) may be expressed in Cartesian coordinates as the Fresnel diffraction integral,

[3]The physical pressure field p is related to q by $p(\mathbf{r}, t) = \mathrm{Re}[\tilde{p}(\mathbf{r})e^{-i\omega t}] = \mathrm{Re}[q(\mathbf{r})e^{i(kz-\omega t)}]$.

as shown in Sec. E.2:

$$q(x,y,z) = -\frac{ik}{2\pi z}\iint_{-\infty}^{\infty} q(x_0,y_0,0)e^{i(k/2z)[(x-x_0)^2+(y-y_0)^2]}\,dx_0\,dy_0\,. \tag{4.47}$$

Consistent with the paraxial approximation, the pressure source condition $q(x,y,0)$ may be replaced by the z component of the particle velocity in the source plane multiplied by $\rho_0 c_0$ [268]. Since the source conditions for vortex beams are conveniently expressed in cylindrical coordinates [e.g., Eq. (4.1)], it is beneficial to convert Eq. (4.47) to cylindrical coordinates:

$$q(r,\theta,z) = -\frac{ik}{2\pi z}\int_0^{2\pi}\int_0^{\infty} q(r_0,\theta_0,0)e^{i(k/2z)[r^2+r_0^2-2rr_0\cos(\theta_0-\theta)]}\,r_0\,dr_0\,d\theta_0\,. \tag{4.48}$$

Uniform circular amplitude

Making the variable substitution $\theta_0 = \phi - \pi/2 + \theta$ in Eq. (4.48) in order to convert $\cos(\theta_0-\theta)$ to $\sin\phi$ and employing Watson's relation given by Eq. (4.30) yields

$$\int_0^{2\pi} e^{i\ell\theta_0}e^{-i(krr_0/z)\cos(\theta_0-\theta)}\,d\theta_0 = 2\pi e^{i\ell(\theta-\pi/2)}J_\ell(krr_0/z)\,. \tag{4.49}$$

Using $q(r,\theta,0) = \rho_0 c_0 \tilde{v}_z(r,\theta,0)$ to replace Eq. (4.1) with

$$q(r,\theta,0) = p_0\,\mathrm{circ}(r/a)e^{i\ell\theta} \tag{4.50}$$

in Eq. (4.48) and applying Eq. (4.49) yields

$$q(r,\theta,z) = -ikp_0\frac{e^{i(ka^2/2z)r^2/a^2}}{z}e^{i\ell(\theta-\pi/2)}\int_0^a e^{i(ka^2/2z)r_0^2/a^2}J_\ell(krr_0/z)\,r_0\,dr_0\,. \tag{4.51}$$

For $z \gg z_\mathrm{R}$, where $z_\mathrm{R} = ka^2/2$ is the Rayleigh distance, Eq. (4.51) reduces to

$$q(r,\theta,z) = -ikp_0\frac{1}{z}e^{i\ell(\theta-\pi/2)}\int_0^a J_\ell(krr_0/z)\,r_0\,dr_0\,, \quad z \gg z_\mathrm{R}\,, \tag{4.52}$$

resulting in the analytical solution

$$q_\ell(r,\theta,z) = -ip_0\frac{z}{kr^2}e^{i\ell(\theta-\pi/2)}F_\ell(kar/z)\,, \quad z \gg z_\mathrm{R}\,, \tag{4.53}$$

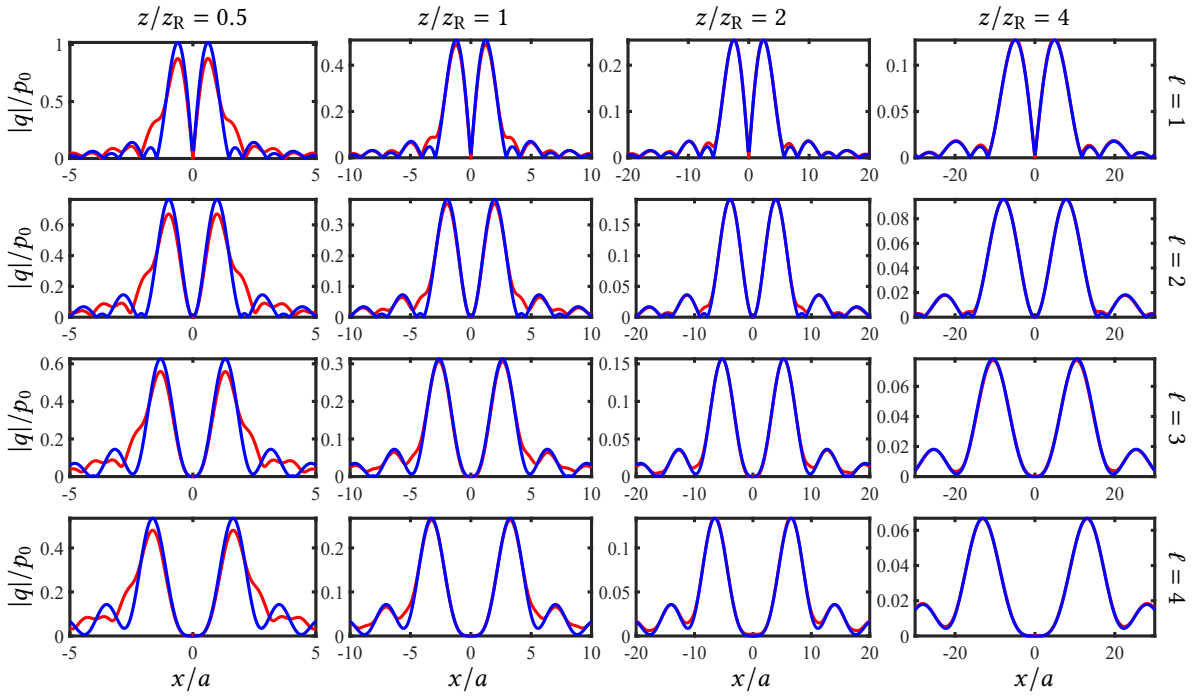

Figure 4.3: Comparison of the analytical solution of the paraxial equation in the far field given by Eq. (4.53) (blue lines) with the numerical solution of the paraxial equation calculated using Eq. (4.55) (red lines) for the source condition given by Eq. (4.56) with $0 \leq \ell \leq 4$ and $z/z_R = 0.5$, 1, 2, and 4.

where F_ℓ is given for $\ell > -2$ by Eq. (4.7). In the limiting case $\ell = 0$, Eq. (4.53) with relation (4.8) recovers the far-field paraxial pressure radiated by a circular piston:

$$q(r,\theta,z) = -ip_0 \frac{ka^2}{2z} \frac{2J_1(kar/z)}{kar/z}, \quad z \gg z_\mathrm{R}, \quad \ell = 0. \tag{4.54}$$

The validity of Eq. (4.53) is assessed by comparison with the field calculated using the paraxial approximation of Eq. (E.13), given by[4]

$$p(x,y,z) = \mathcal{F}_{xy}^{-1}\left\{\mathcal{F}_{xy}[q(x,y,0)]\, e^{ik_z z}\right\}, \quad k_z = k - \frac{k_x^2 + k_y^2}{2k}, \tag{4.55}$$

where the stated approximation for k_z makes Eq. (4.55) divided by e^{ikz} equivalent to Eq. (4.51), which is an exact solution of Eq. (A.25). Equation (4.50) is expressed in Cartesian coordinates as

$$q(x,y,0) = p_0 \,\mathrm{circ}(\sqrt{x^2+y^2}/a) e^{i\ell \arctan(y/x)} \tag{4.56}$$

for the source function used in Eq. (4.55), where $\arctan(y/x)$ is calculated using $\mathtt{atan2}(y,x)$. In Fig. 4.3, the validity of the far-field approximation $z \gg z_\mathrm{R}$ is assessed by comparing Eqs. (4.53) and (4.55) for $0.5 \le z/z_\mathrm{R} \le 4$ and $0 \le \ell \le 4$. The comparison reveals that Eq. (4.53) approximates the exact solution of Eq. (A.25) reasonably well for $z/z_\mathrm{R} \simeq 2$, and that convergence is achieved for $z/z_\mathrm{R} \gtrsim 4$.

Spherically focused vortex beams are often used for particle manipulation [101, 238, 269]. To describe a spherically focused vortex beam with a geometric focal length d, Eq. (4.50) is multiplied by the phase factor $\exp(-ikr^2/2d)$ derived in Sec. E.3:

$$q(r,\theta,0) = p_0 \,\mathrm{circ}(r/a)\, e^{-ikr^2/2d}\, e^{i\ell\theta}. \tag{4.57}$$

Combining Eqs. (4.48) and (4.57) and evaluating the integral over θ using Eq. (4.49) yields

$$q(r,\theta,z) = -ikp_0 \frac{e^{ikr^2/2z}}{z} e^{i\ell(\theta-\pi/2)} \int_0^a e^{i(ka^2/2z)(1-z/d)r_0^2/a^2} J_\ell(krr_0/z)\, r_0\, dr_0. \tag{4.58}$$

[4] Equation (4.55) is incorrectly written as q in Eq. (10) of Ref. 231.

The integral in Eq. (4.58) reduces to the form of Eq. (4.7) in the focal plane $z = d$, resulting in

$$q_\ell(r, \theta, d) = -ip_0 \frac{d}{kr^2} e^{ikr^2/2d} e^{i\ell(\theta - \pi/2)} F_\ell(kar/d)\,, \tag{4.59}$$

where F_ℓ is given by Eq. (4.7). In the limiting case $\ell = 0$, Eq. (4.59) reduces to

$$q(r, \theta, d) = -ip_0 \frac{ka^2}{2d} e^{ikr^2/2d} \frac{2J_1(kar/d)}{kar/d}\,, \quad \ell = 0\,, \tag{4.60}$$

recovering the paraxial pressure field in the focal plane of a spherically focused circular piston. A solution in the form of Eq. (4.59) in combination with Eq. (4.9) was obtained previously in optics by Sacks et al. [270, Eq. (15)] for $\ell = 1$. Comparison with numerical solutions based on Eq. (4.55) shown in Fig. 4.4 demonstrates that Eq. (4.59) satisfies Eq. (A.25), where the source condition in Eq. (4.55) is given by Eq. (4.57) in Cartesian coordinates:

$$q(x, y, 0) = p_0 \,\mathrm{circ}(\sqrt{x^2 + y^2}/a) e^{-ik(x^2+y^2)/2d} e^{i\ell \arctan(y/x)}\,. \tag{4.61}$$

Limitations on the accuracy of the paraxial approximation for a focused uniform circular piston as the ratio d/a is reduced are assessed as functions of ka and ℓ in the right column of Fig. 4.8.

Gaussian amplitude

While studies of vortex beams radiated by circular pistons can benefit from the above analysis, Eqs. (4.53) and (4.59) are restricted to $z \gtrsim z_\mathrm{R}$ and $z = d$, respectively. Theoretical studies of diffracting sound beams often rely on solutions that describe the full field. For example, studies of nonlinear acoustic propagation effects in vortex beams [271] require the entire linear field be determined in order to calculate the second harmonic [6, Sec. 8.3.1]. The desire to obtain solutions more general than Eqs. (4.53) and (4.59) motivates the consideration of an idealized source condition: a focused vortex source with a Gaussian amplitude distribution given by

$$q(r, \theta, 0) = p_0 e^{-r^2/a^2} e^{-ikr^2/2d} e^{i\ell\theta}\,. \tag{4.62}$$

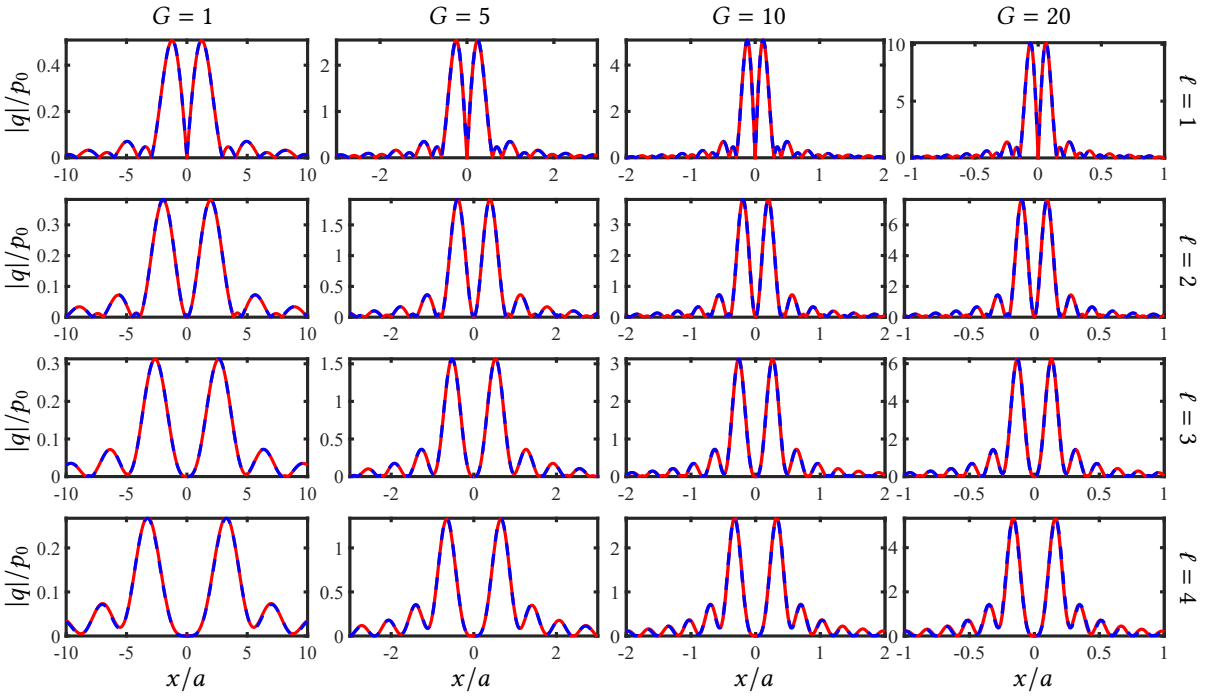

Figure 4.4: Comparison of the analytical solution of the paraxial equation in the focal plane given by Eqs. (4.59) (dashed blue lines) to the exact solution of the paraxial equation calculated given by Eq. (4.55) with the source condition given by Eq. (4.61) (red lines) for $1 \leq \ell \leq 4$ and $G = ka^2/2d = 1$, 5, 10, and 20.

The corresponding source condition for the unfocused vortex beam is obtained by setting $d = \infty$:

$$q(r, \theta, 0) = p_0 e^{-r^2/a^2} e^{i\ell\theta} . \tag{4.63}$$

The solution of Eq. (A.25) is obtained by inserting Eq. (4.62) into Eq. (4.48):

$$q(r, \theta, z) = -\frac{ikp_0}{2\pi z} e^{ikr^2/2z} \int_0^\infty e^{-r_0^2/a^2} e^{i(kr_0^2/2)(z^{-1}-d^{-1})} r_0 \, dr_0 \\ \times \int_0^{2\pi} e^{i\ell\theta_0} e^{-i(krr_0/z)\cos(\theta_0-\theta)} \, d\theta_0 . \tag{4.64}$$

In view of Eq. (4.49), Eq. (4.64) reduces to

$$q(r, \theta, z) = -ikp_0 \frac{e^{ikr^2/2z}}{z} e^{i\ell(\theta-\pi/2)} \int_0^\infty e^{-[1-i(ka^2/2z)(1-z/d)]r_0^2/a^2} J_\ell(krr_0/z) \, r_0 \, dr_0 , \tag{4.65}$$

in which the coefficients of r_0^2 have been grouped together in preparation for the remaining integration. The integral over r_0 is evaluated with the relation [256, Item 6.631-7]

$$\int_0^\infty x e^{-\alpha x^2} J_n(\beta x) \, dx = \frac{\sqrt{\pi}\beta}{8\alpha^{3/2}} \exp(-\beta^2/8\alpha) \left[I_{(n-1)/2}(\beta^2/8\alpha) - I_{(n+1)/2}(\beta^2/8\alpha) \right] , \tag{4.66}$$

where I_ν is the νth-order modified Bessel function of the first kind defined by the first of Eqs. (4.44). Equation (4.66), which is restricted to $\mathrm{Re}(\alpha) > 0$ and $n > -2$, is used to evaluate Eq. (4.65) by setting

$$\alpha = \frac{1}{a^2} - \frac{ik}{2}\left(\frac{1}{z} - \frac{1}{d}\right), \qquad \beta \equiv kr/z , \qquad n = \ell , \qquad r_0 = x ,$$

yielding

$$q_\ell(r, \theta, z) = \sqrt{8\pi} \frac{p_0 z}{kr^2} \chi^{3/2} e^{-\chi} \left[I_{(\ell-1)/2}(\chi) - I_{(\ell+1)/2}(\chi) \right] e^{i[\ell\theta - (\ell+1)\pi/2 + kr^2/2z]} , \tag{4.67}$$

$$\chi(r, z) = \frac{\frac{1}{8}(kar/z)^2}{1 - i(ka^2/2z)(1 - z/d)} . \tag{4.68}$$

Equation (4.67) is the solution in the paraxial approximation for a focused vortex beam radiated by a source with a Gaussian amplitude distribution described by Eq. (4.62); the solution for the unfocused source given by Eq. (4.63) is obtained by setting $d = \infty$ in Eq. (4.68).

Since Eq. (4.67) holds for $z \geq 0$, one way to assess its validity is to examine whether it obeys the conservation of energy. Since no absorption is included in Eq. (A.25), the power radiated by the source must be conserved by the beam. Given that the time-averaged intensity radiated by the source is $I = |q(r,\theta,0)|^2/2\rho_0 c_0$ in the paraxial approximation, the corresponding time-averaged power radiated by the source is

$$\mathcal{P}_0 = \frac{1}{2\rho_0 c_0} \int_0^{2\pi} \int_0^{\infty} |q(r,\theta,0)|^2 r \, dr \, d\theta = \frac{\pi a^2 p_0^2}{4\rho_0 c_0}, \tag{4.69}$$

which is independent of ℓ. Meanwhile, the magnitude of Eq. (4.67) is

$$|q_\ell(r,z)| = \sqrt{8\pi} \frac{p_0 z}{kr^2} \left| \chi^{3/2} e^{-\chi} \left[I_{(\ell-1)/2}(\chi) - I_{(\ell+1)/2}(\chi) \right] \right|. \tag{4.70}$$

Numerical integration of $|q(r,z)|^2$ over any plane for which z is constant shows that the source power $\mathcal{P}_0$ in Eq. (4.69) is recovered independently of ℓ.

A solution in the general form of Eq. (4.67) was obtained previously in optics by Kotlyar et al. [272, Eq. (22)] for an unfocused vortex beam ($d = \infty$), although their solution is expressed less compactly in terms of the notation employed in Sec. E.5. For the case of a focused vortex beam, evaluation of Eq. (4.67) in the focal plane ($z = d$) recovers the corresponding result obtained in optics by Sacks et al. [270, Eq. (14)].

Setting $\ell = 0$ in Eq. (4.67) restores axisymmetry and recovers the traditional solution for a focused Gaussian beam given by [6, Eq. (8.37)]

$$q(r,z) = \frac{p_0}{1 - (1 - iG^{-1})z/d} \exp\left[-\frac{(1+iG)r^2/a^2}{1 - (1 - iG^{-1})z/d} \right], \quad \ell = 0, \tag{4.71}$$

where $G = ka^2/2d$ is the gain at the geometric focus, $(r,z) = (0,d)$. The recovery of Eq. (4.71) from Eq. (4.67), which is detailed in Sec. E.4, follows from the relation[5]

$$I_{-1/2}(\chi) - I_{1/2}(\chi) = -\sqrt{2\chi/\pi}\, h_0^{(1)}(i\chi) = \sqrt{2/\pi}\, \frac{e^{-\chi}}{\sqrt{\chi}}, \tag{4.72}$$

[5]Equation (4.72) can be derived from Eqs. (4.44) and (4.45) by noting that $h_0^{(1)}(ix) = j_0(ix) + in_0(ix) = \sinh(x)/x - \cosh(x)/x$, where j_0 and n_0 are the zeroth-order spherical Bessel and Neumann functions.

where $h_0^{(1)}$ is the spherical Hankel function of the first kind of order zero. The beam profile of Eq. (4.71) perpendicular to the z axis is Gaussian at all distances. In the focal plane, one obtains $|q(r,d)| = Gp_0 e^{-r^2/(a/G)^2}$, indicating that the amplitude is increased, and the beamwidth is decreased, by the factor G. For an unfocused source ($d = \infty$), Eq. (4.71) reduces to

$$q(r,z) = \frac{p_0}{1 + iz/z_\mathrm{R}} \exp\left(-\frac{r^2/a^2}{1 + iz/z_\mathrm{R}}\right), \quad \ell = 0, \quad d = \infty, \tag{4.73}$$

where $z_\mathrm{R} = ka^2/2$ is the Rayleigh distance.

A common alternative approach to describing vortex beams in the paraxial approximation is the Laguerre-Gauss expansion [10]. The coefficients in this expansion are calculated analytically in Sec. E.5 for an unfocused beam, the source condition for which is Eq. (4.63). The resulting expansions are compared with the solution given by Eq. (4.67) with $d = \infty$. While the field radiated by a Gaussian vortex source consists of a closed-form analytical expression given by Eq. (4.67), it is shown in Sec. E.5 that an infinite series is required to describe the same beam using the Laguerre-Gauss expansion.

4.4 Vortex ring radii

The vortex ring radius—the distance from the beam axis to the first local maximum—is a useful measure in both optics [250, Eq. (5)] and acoustics [112, Eq. (19)]. For the vortex beam radiated by a circular piston described by Eqs. (4.50) and (4.57), the ring radius can be calculated by setting the r derivative of the magnitude of Eqs. (4.53) and (4.59) to zero, which is equivalent to solving[6]

$$\frac{d|\xi^{-2} F_\ell(\xi)|}{d\xi} = 0, \tag{4.74}$$

[6]Equation (4.74) is incorrectly printed in-line as $d|\xi^{-1}F_\ell(\xi)|/d\xi = 0$ in Sec. 4 of Ref. 231. The error did not affect the rest of the analysis of Ref. 231.

ℓ	1	2	3	4	5	6	7	8	9	10
ξ_ℓ	2.452	3.923	5.262	6.536	7.768	8.973	10.156	11.33	12.476	13.619

Table 4.1: Roots ξ_ℓ of Eq. (4.75) for $1 \le \ell \le 10$.

where $\xi = kar/z$ for Eq. (4.53) and $\xi = kar/d$ for Eq. (4.59). Equation (4.74) is evaluated using Eq. (4.7) for F_ℓ, resulting in [256, Item 8.471-2]

$$\sum_{k=0}^{\infty} \frac{(\ell+2k+1)\Gamma(\ell/2+k)}{\Gamma(\ell/2+2+k)} \left[\frac{J_{\ell+2k}(\xi) - J_{\ell+2k+2}(\xi)}{2\xi} - \frac{J_{\ell+2k+1}(\xi)}{\xi^2} \right] = 0\,. \tag{4.75}$$

The roots ξ_ℓ of Eq. (4.75) determined numerically are listed in Table 4.1 for $1 \le \ell \le 10$. A least-squares fit results in the linear relation

$$\xi_\ell = 1.23\ell + 1.49\,. \tag{4.76}$$

The relations $\xi_\ell = kar_\ell/z$ for Eq. (4.53) and $\xi_\ell = kar_\ell/d$ for Eq. (4.59) yield

$$r_\ell = \frac{\xi_\ell z}{ka}, \quad z \gg z_\mathrm{R} \tag{4.77}$$

for the ring radius in the far field of the unfocused vortex beam described by Eq. (4.53) and

$$r_\ell = \frac{\xi_\ell d}{ka}, \quad z = d \tag{4.78}$$

in the focal plane of the vortex beam described by Eq. (4.59). A linear dependence on ℓ was also obtained by Curtis and Grier [250, Eq. (5)] for the ring radius in the focal plane of an optical vortex beam with uniform amplitude in the source plane.

The ring radii of vortex beams radiated by Gaussian vortex sources are also calculated in the far field of an unfocused beam and in the focal plane of a focused beam. In both cases, χ given by Eq. (4.68) is a real-valued quantity:

$$\chi = \tfrac{1}{8}(kar/z)^2, \quad d = \infty, \quad z \gg z_\mathrm{R}, \tag{4.79}$$

$$= \tfrac{1}{8}(kar/d)^2, \quad z = d\,. \tag{4.80}$$

ℓ	1	2	3	4	5	6	7	8	9	10
χ_ℓ	0.356	0.897	1.618	2.536	3.672	5.044	6.661	8.529	10.649	13.020
η_ℓ	1.689	2.678	3.597	4.504	5.420	6.352	7.300	8.261	9.230	10.206

Table 4.2: The roots χ_ℓ of Eq. (4.82) and the corresponding coefficients $\eta_\ell = \sqrt{8\chi_\ell}$ for $1 \leq \ell \leq 10$.

The locations of the amplitude maxima described by Eq. (4.70) in the plane of interest perpendicular to the z axis are determined by setting $\partial|q|/\partial r = 0$ for $|q|$ given by Eq. (4.70), which for the cases defined by Eqs. (4.79) and (4.80) are equivalent to satisfying the relation

$$\frac{d}{d\chi}\left\{\chi^{1/2}e^{-\chi}\left[I_{(\ell-1)/2}(\chi) - I_{(\ell+1)/2}(\chi)\right]\right\} = 0\,. \tag{4.81}$$

Taking the derivative yields

$$(\ell - 4\chi)I_{(\ell-1)/2}(\chi) + (\ell + 4\chi)I_{(\ell+1)/2}(\chi) = 0\,, \tag{4.82}$$

which is the relation obtained by Kotlyar et al. [272, Eq. (29)] for the far-field case in Eq. (4.79), the root of which they present only for $\ell = 2$. Here, Eq. (4.82) is solved numerically for the single root χ_ℓ corresponding to each orbital number. In the axisymmetric case ($\ell = 0$), Eq. (4.82) yields $\chi_0 = 0$, as required for the fields described by Eqs. (4.71) and (4.73), whose amplitudes decrease monotonically with distance from the z axis. The roots χ_ℓ for $1 \leq \ell \leq 10$ are presented in Table 4.2. The ring radius in the far field of an unfocused vortex beam described by Eq. (4.67) in combination with Eq. (4.79) is

$$r_\ell = \eta_\ell z/ka\,, \quad d = \infty\,, \quad z \gg z_\mathrm{R}\,. \tag{4.83}$$

An alternative form of Eq. (4.83) is $\psi_\ell = \arctan(\eta_\ell/ka)$, where ψ_ℓ is the angle with respect to the z axis of the maximum in the far field, defined by $\tan\psi_\ell = r_\ell/z$. Meanwhile, the ring radius in the focal plane of the vortex beam described by Eq. (4.67) in combination with Eq. (4.80) is

$$r_\ell = \eta_\ell d/ka\,. \quad z = d\,. \tag{4.84}$$

The values of $\eta_\ell = \sqrt{8\chi_\ell}$ are also presented in Table 4.2. A least squares fit of the values in the bottom row of Table 4.2 over the range $1 \leq \ell \leq 10$ yields the linear relation

$$\eta_\ell = 0.94\ell + 0.75\,. \tag{4.85}$$

Equations (4.77) and (4.78) accurately provide the ring radius of the magnitudes of Eqs. (4.53) and (4.59), respectively. Equations (4.83) and (4.84) similarly provide the vortex ring radius corresponding to Eq. (4.70) for χ given by Eqs. (4.79) and (4.80), respectively. In all four cases, the radius of the first local maximum is predicted to be a linear function of ℓ. In practice, however, the position of the global maximum of the field is often of greater interest. Geometrical acoustics is used in Sec. 4.6 to show that the radial position of the global maximum is a nonlinear function of ℓ for both unfocused and focused vortex beams, which limits the utility of the results of the present section.

4.5 Validity of the paraxial approximation

Unfocused vortex beams

Limitations on Eqs. (4.53), (4.59), and (4.67) that arise from the paraxial approximation associated with Eq. (A.25) may be identified by comparison with solutions of the Helmholtz equation, Eq. (A.1), that satisfy the same source conditions. The solutions of Eq. (A.1) used for comparison in the present section are obtained numerically using Fourier acoustics, as was done in Fig. 4.2. For a source described by a pressure field in the plane $z = 0$, the solution of Eq. (A.1) is given by Eq. (E.13), notated in the present section by

$$\tilde{p}_{\mathrm{H}}(x, y, z) = \mathcal{F}_{xy}^{-1}\left\{\mathcal{F}_{xy}[\tilde{p}_{\mathrm{H}}(x, y, 0)]\, e^{ik_z z}\right\}, \tag{4.86}$$

where $k_z = (k^2 - k_x^2 - k_y^2)^{1/2}$. The subscript "H" is introduced to distinguish the solution of the Helmholtz equation from its paraxial approximation, with $\tilde{p}_{\mathrm{H}}(x, y, 0) = q(x, y, 0)$ in the source plane. Compared first with Eq. (4.86) is the field given by Eq. (4.67) for $d = \infty$, corresponding to radiation from an unfocused Gaussian vortex source described by Eq. (4.63). As mentioned in Sec. 4.3, the Gaussian vortex source is advantageous in comparison with the circular piston for its relative analytical simplicity. The validity of the paraxial approximation for vortex beams radiated by circular pistons is discussed after studying the Gaussian vortex source.

The paraxial approximation underlying the slow variation in q as a function of z which leads to Eq. (A.25) is based on the assumption that the radiated field is formed

by waves propagating in directions forming small angles with the z axis, as discussed in Sec. E.2. As ℓ increases, these angles increase, and the paraxial approximation becomes increasingly inaccurate. This feature of the field is characterized by its angular spectrum, which is obtained by taking the spatial Fourier transform of the source function. To obtain an analytical expression for the angular spectrum, the polar form of Eq. (E.2) given by Eq. (4.33) is used, where k_r of Sec. 4.2 is denoted here by κ for convenience. Substitution of Eq. (4.63) in (4.33) and making use of Eqs. (4.30) and (4.66) as before yields for the angular spectrum of the unfocused Gaussian vortex source

$$\hat{q}(\kappa,\psi,0) = a^2 p_0 \frac{\pi^{3/2}}{\sqrt{2}} \Omega^{1/2} e^{-\Omega} \left[I_{(\ell-1)/2}(\Omega) - I_{(\ell+1)/2}(\Omega) \right] e^{i\ell(\psi-\pi/2)}, \quad d = \infty, \tag{4.87}$$

where $\Omega = \frac{1}{8}(\kappa a)^2$.

Since Eq. (4.87) has the same form as Eq. (4.67), the location of the peak in the angular spectrum determined by setting $d|\hat{q}|/d\Omega = 0$ yields $\Omega = \chi_\ell$, where χ_ℓ is the root of Eq. (4.82). Making use of the relation $\chi_\ell = \frac{1}{8}\eta_\ell^2$ employed in Eqs. (4.83) and (4.84), one obtains $\kappa_\ell = \eta_\ell/a$ for the value of κ where the peak in the angular spectrum occurs, which increases linearly with ℓ according to Eq. (4.85). For ℓ sufficiently large that $\kappa_\ell > k$, in which case $k_z = (k^2 - \kappa^2)^{1/2}$ in Eq. (4.86) is imaginary for $\kappa \simeq \kappa_\ell$, the plane waves in the angular spectrum forming the vortex ring defined by Eq. (4.83) are evanescent. Evanescent waves are not described by the paraxial approximation, which corresponds to replacing k_z by $k - \kappa^2/2k$ in Eq. (4.86) [273], requiring $\kappa^2 \ll k^2$ for this approximation to be accurate. The paraxial approximation should therefore provide an accurate description of the ring that characterizes a vortex beam if

$$k^2 \gg \kappa_\ell^2, \tag{4.88}$$

which for Eq. (4.67) in the absence of focusing corresponds to $(ka)^2 \gg \eta_\ell^2$, or alternatively

$$(ka)^2 \gg \ell^2, \quad d = \infty, \tag{4.89}$$

based on the values of η_ℓ in the lower row of Table 4.2. This result is consistent with the statement preceding the paraxial approximation in Eq. (A.25) that q is a slowly varying function of z.

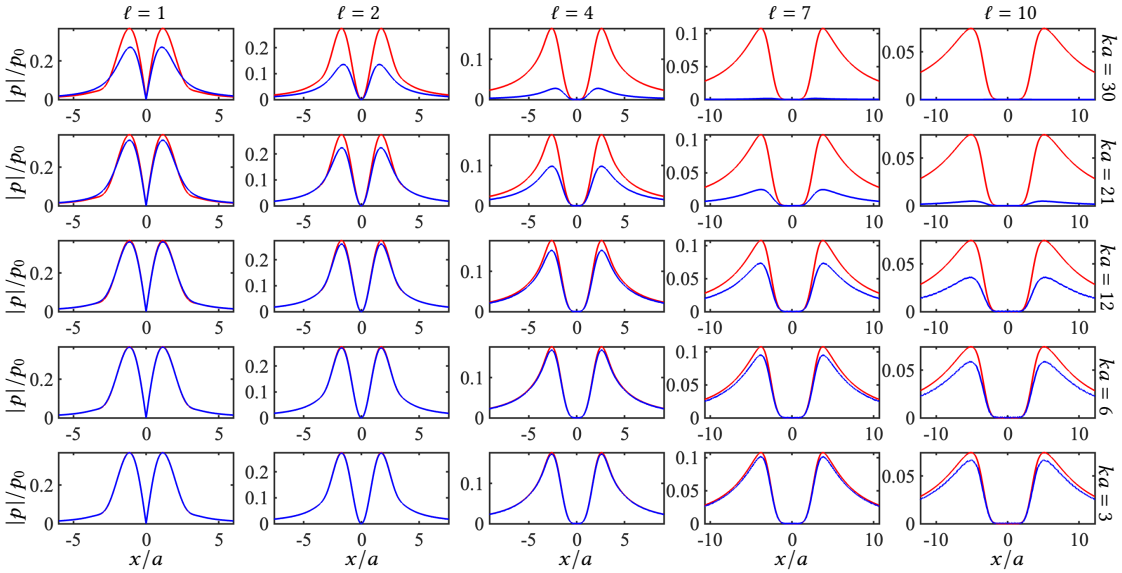

Figure 4.5: Comparison of Eq. (4.70) (red curves) for source condition (4.63) with solutions of the Helmholtz equation (blue curves) obtained numerically from Eq. (4.86) at $z = z_R$. The relation $ka = 3\ell$ applies to each plot that lies along the diagonal extending from the lower left to upper right corner, with $ka > 3\ell$ for each plot above the diagonal and $ka < 3\ell$ for each plot below the diagonal.

Graphical comparison is used to assess whether Eq. (4.89) accurately determines the parameter space in which the paraxial approximation correctly predicts the vortex ring radiated by the unfocused source defined by Eq. (4.63). Presented in Fig. 4.5 is a comparison of Eq. (4.70) (red curves) in the absence of focusing ($d = \infty$) with the magnitudes of the solutions of the Helmholtz equation (blue curves) obtained numerically from Eq. (4.86), in which Eq. (4.63) has been converted to Cartesian coordinates:[7]

$$\tilde{p}_H(x, y, 0) = p_0 e^{-(x^2+y^2)/a^2} e^{i\ell \arctan(x,y)} . \tag{4.90}$$

All beam profiles were calculated at the same distance from the source plane, $z/z_R = 1$, where $z_R = ka^2/2$ is the Rayleigh distance. The columns in Fig. 4.5 correspond to different values of ℓ increasing from 1 to 10, and the values of ka for the rows were chosen to be 3 times the values of ℓ used for the columns. In this way, the relation $ka = 3\ell$ applies to

[7] As in Sec. 4.3, the function arctan is evaluated numerically using $\texttt{atan2}(y, x)$ to determine the phase angle throughout the range $-\pi < \theta \leq \pi$.

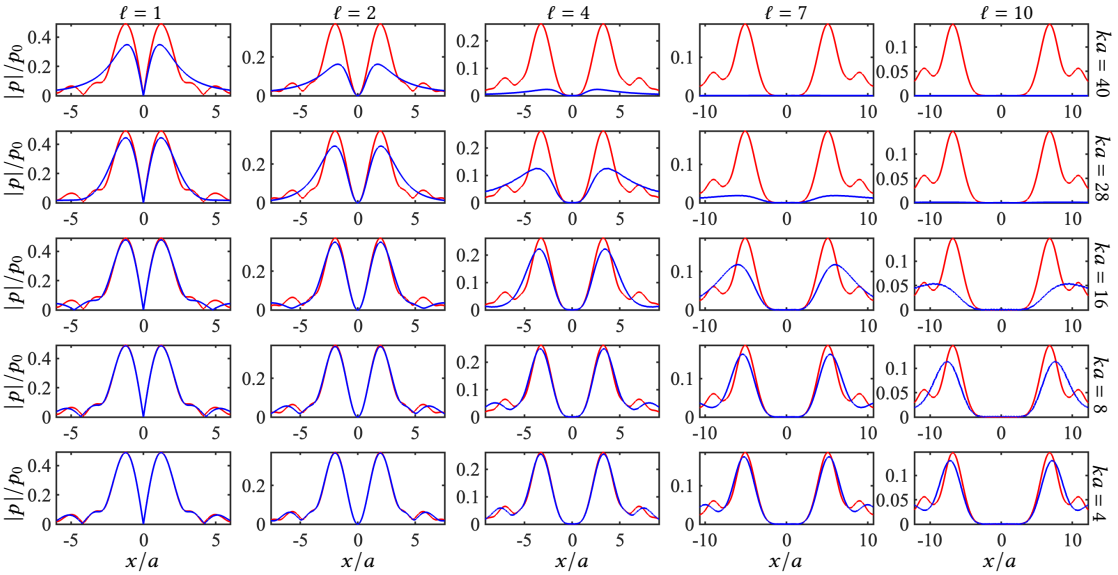

Figure 4.6: Comparison of the paraxial approximation (red curves) with the solution of the Helmholtz equation (blue curves) at $z = z_R$ as in Fig. 4.5 but for the unfocused uniform circular source condition in Eq. (4.50). The paraxial approximation in this case is obtained numerically from Eq. (4.86) with k_z replaced by $k - (k_x^2 + k_y^2)/2k$. The relation $ka = 4\ell$ applies to each plot along the diagonal, with $ka > 4\ell$ for each plot above the diagonal and $ka < 4\ell$ for each plot below the diagonal.

each plot that lies along the diagonal extending from the lower left to upper right corner of Fig. 4.5. It is observed that above the diagonal, where $ka > 3\ell$ for each plot, the paraxial approximation is in good agreement with the solution of the Helmholtz equation, and below the diagonal, where $ka < 3\ell$ for each plot, there is noticeable disagreement that increases with ℓ for any fixed value of ka. Comparisons at distances $z/z_R = 0.5$ and $z/z_R = 2$ look much the same. Since $(ka)^2 = 9\ell^2$ applies to all plots along the diagonal of Fig. 4.5, the relation

$$ka > 3\ell\,, \quad d = \infty\,, \tag{4.91}$$

is consistent with the criterion in Eq. (4.89) for the paraxial approximation to accurately describe an unfocused vortex beam with Gaussian amplitude distribution in the source plane for $\ell \lesssim 10$.

To check whether the criterion in Eq. (4.89) is suitable for vortex beams generated

by the unfocused circular source condition given by Eq. (4.50), Eq. (4.86) is used to solve the Helmholtz equation, Eq. (A.1), while Eq. (4.55) is used to solve its paraxial approximation, Eq. (A.25), as was done in Sec. 4.3. Solutions of Eqs. (A.1) and (A.25) for Eq. (4.50) are compared in Fig. 4.6, which has the same format as Fig. 4.5 except with $ka = 4\ell$ for the plots along the diagonal. The agreement above the diagonal, where $ka > 4\ell$ for each plot, is not quite as good as above the diagonal in Fig. 4.5, but the differences are mainly in the sidelobes outside the vortex ring. Equation (4.89) is thus observed to also be a reasonable criterion for use of the paraxial approximation to describe the vortex rings in fields corresponding to the unfocused source function in Eq. (4.50), at least for $\ell \lesssim 10$.

The reader is referred to Zhang and Marston [73] for discussion of modeling angular momentum flux in acoustic vortex beams with and without use of the paraxial approximation.

Focused vortex beams

The approach used above to assess the validity of the paraxial approximation applies to focused vortex beams as well. Inclusion of focusing in Eq. (4.87) for the angular spectrum is straightforward. Equation (4.62) is recovered by replacing a^2 in Eq. (4.63) with the complex quantity $\tilde{a}^2 = a^2/(1 + iG)$, where $G = ka^2/2d$. Focusing is therefore included in Eq. (4.87) by multiplying the expression by $(1 + iG)^{-1}$ and replacing the quantity Ω with $\tilde{\Omega} = \frac{1}{8}(\kappa a)^2/(1 + iG)$. Since $\hat{q}$ is then a function of the complex quantity $\tilde{\Omega}$, the roots of Eq. (4.82) no longer determine the values of κ_ℓ associated with the peaks in the angular spectra.

Presented in Fig. 4.7(a) are the values of $\kappa_\ell a$ corresponding to the maximum value in the magnitude of the angular spectrum $|\hat{q}(\kappa a)|$ calculated numerically for $1 \leq \ell \leq 10$ with values of G increasing in order from $G = 0$ (bottom curve) to $G = 80$ (top curve). In contrast with the unfocused vortex beam ($G = 0$), the dependence on ℓ is no longer linear for $G > 0$, and the departure from a linear dependence increases with G. Also, it follows from the relation $(\kappa a)^2 = 8(1 + iG)\tilde{\Omega}$ that $\kappa a \simeq (8iG\tilde{\Omega})^{1/2}$ for $G^2 \gg 1$, and it may be

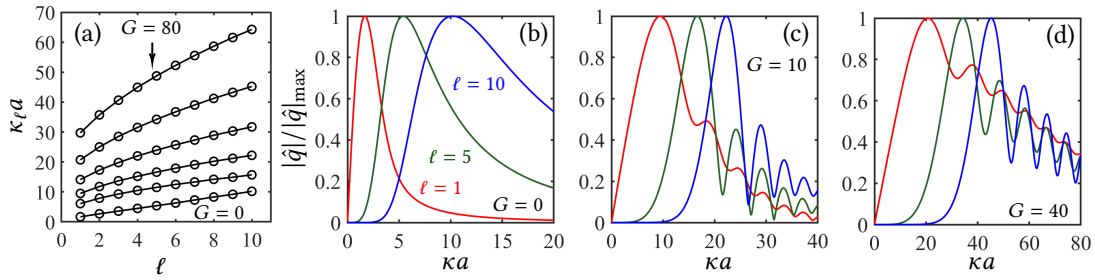

Figure 4.7: (a) Values of $\kappa_\ell a$ for selected values of ℓ and $G = ka^2/2d$, with the curves for $G = 0$, 5, 10, 20, 40 and 80 displayed with G increasing from bottom to top, corresponding to the maximum value in the magnitude of the angular spectrum described by Eq. (4.87) following modification for application to a focused vortex beam as described in the text. Magnitudes of the angular spectra for $\ell = 1$, 5, and 10 are shown for (b) $G = 0$, (c) $G = 10$, and (d) $G = 40$.

observed that for $G > 0$ the curves for different values of G in Fig. 4.7(a) increase relative to one another approximately in proportion to $G^{1/2}$. As for unfocused vortex beams, the criterion for the validity of the paraxial approximation in the case of focused vortex beams is given by Eq. (4.88), $k^2 \gg \kappa_\ell^2$. However, the dependence of $\kappa_\ell a$ on ℓ and G observed in Fig. 4.7(a) does not lend itself to formulation of a simple explicit criterion such as Eq. (4.89) for unfocused vortex beams.

Further insight into the difficulty with determining a simple criterion for the accuracy of the paraxial approximation used for focused vortex beams is provided by the magnitudes of the angular spectra presented in Fig. 4.7(b) through 4(d) for (b) $G = 0$, (c) $G = 10$, and (d) $G = 40$, with $\ell = 1$, 5, and 10 for each value of G. Whereas the spectra in Fig. 4.7(b) for unfocused beams ($G = 0$) possess no oscillations, the spectra in Fig. 4.7(c) and (d) not only reveal pronounced oscillations, but also increased spatial bandwidth, associated with focusing ($G > 0$).

A parametric study similar to those in Figs. 4.5 and 4.6, in which the fields radiated by unfocused sources calculated with solutions of the Helmholtz equation and their paraxial approximations are compared as functions of ka and ℓ, was performed for focused sources, which introduces the additional parameter d/a. For reference, it should be noted that ka and d/a are related to the quantity G in Fig. 4.7 by their ratio $ka/(d/a) = 2G$. The

Ref.	Authors	d/a	ka	Means of generation
74	Anhauser et al.	2	181	phase plate
76	Wunenburger et al.	2	206	phase plate
83	Jiménez-Gambín et al.	2.8	106	phase plate
237	Baresch et al.	1.4	102	transducer array
101	Terzi et al.	2	231.6	phase plate
274	Jimenez et al.	1.8	40	transducer array
275	Gspan et al.*	3.75	25.4	phase plate
252	Zhou et al.	1	212	transducer array
254	Zhao et al.	0.87	439	transducer array
253	Lo et al.	2	127.2	phase plate
276	Li et al.	8.6	29.6	transducer array
269	Marzo et al.*	< 2	80.6	transducer array

Table 4.3: Values of d/a and ka used in acoustic vortex beam experiments. *There is some uncertainty in the value of d/a in Refs. 275 and 269.

comparisons for focused beams employ the source conditions in Eqs. (4.62) and (4.57) for Gaussian and uniform amplitude distributions, respectively.

Due to the size of the parameter space for focused sources, the results are summarized in Fig. 4.8 as a color-coded decision matrix in which green indicates good agreement, blue indicates borderline agreement, and purple indicates poor agreement in the vicinity of the vortex ring, with the left column corresponding to a Gaussian source, and right column to a uniform source. The subjective determination of good versus poor agreement coincides nominally with the comparisons above and below the diagonals, respectively, in Fig. 4.5 and 4.6. The parameter space covered by Fig. 4.8 ($10 \leq ka \leq 200$, $1 \leq \ell \leq 10$, and $2 \leq d/a \leq 5$), with emphasis on the focal region ($z/d \sim 1$), coincides with experiments and applications reported in the literature [74, 76, 83, 101, 117, 252, 253, 274–276], as summarized in Table 4.3.

The largest discrepancies between results for focused Gaussian and uniform sources occur for $d/a = 2$ (first row in Fig. 4.8), indicating that for the Gaussian source the accuracy of the paraxial approximation is poor for all considered values of ka and ℓ due to the strong convergence of the field. In this case, the aperture half-angle $\arctan(a/d)$ is approximately 26°, which is usually considered as a nominal limit on the accuracy of the

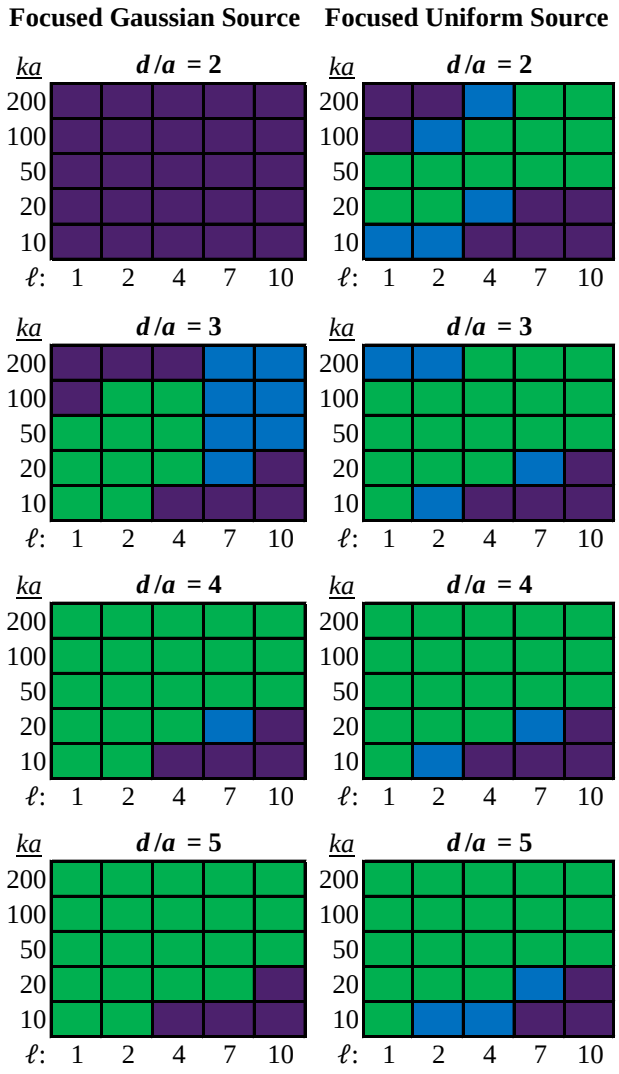

Figure 4.8: Color-coded decision matrix comparing solutions of the Helmholtz equation with solutions of its paraxial approximation for a focused Gaussian source (left column) and a focused uniform source (right column). Green indicates good agreement, blue indicates borderline agreement, and purple indicates poor agreement in the region occupied by the vortex ring near the focal plane ($z/d \sim 1$). The parameter space ($10 \leq ka \leq 200$, $1 \leq \ell \leq 10$, and $2 \leq d/a \leq 5$) coincides with experiments and applications reported in the literature [74, 76, 83, 101, 117, 252, 253, 274–276]. See Table 4.3.

paraxial approximation in the far field of an unfocused source, as discussed in Sec. E.2. In the focal region of the focused Gaussian source, significant contributions to the field arrive from angles greater than 26° with respect to the z axis due to the spatial extent of the source beyond $r = a$, whereas for the uniform circular source the contributions are confined to angles less than approximately 26°. Solutions based on the paraxial approximation are reasonably accurate for the uniform source along the diagonal indicated by the green cells corresponding to increase in both ka and ℓ.

For $d/a = 3$ (second row in Fig. 4.8), there exists a range of ka and ℓ for which the paraxial approximation for the Gaussian source is accurate due to reduction of the aperture half-angle to approximately 18°, and the paraxial approximation for the uniform source is observed to be accurate for a wider range of ka and ℓ than is the case for $d/a = 2$. The same trend continues for $d/a = 4$ (third row) and $d/a = 5$ (fourth row), for which the paraxial approximation is accurate for wider ranges of ka and ℓ.

Finally, of interest in a focused vortex beam is not only movement of the global maximum out of the focal plane as ℓ increases, which was noted at the end of Sec. 4.4, but also the corresponding spatial redistribution of the local maxima in the field. These phenomena are illustrated by the field plots in Fig. 4.9 calculated using Eq. (4.70) for $G = 10$ (upper row) and $G = 20$ (lower row). In each case, the vortex ring for $\ell = 1$ located in the plane $z/d \simeq 1$ is redistributed along a spheroidal surface that encloses the prefocal region as ℓ increases, with the coordinates of the spheroidal surface obtained from geometrical acoustics provided in Eq. (4.114). Since $G = 10$ corresponds to values of $(ka, d/a)$ equal to either $(80, 4)$ or $(100, 5)$, and $G = 20$ corresponds to either $(160, 4)$ or $(200, 5)$, the third and fourth rows of Fig. 4.8 indicate that the fields represented in Fig. 4.9 obtained with a solution based on the paraxial approximation are in good agreement with solutions of the Helmholtz equation for practical parameter values.

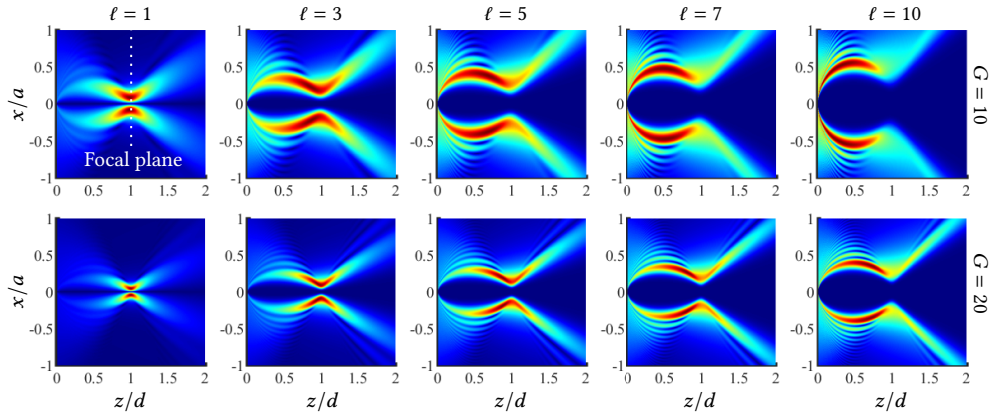

Figure 4.9: Plots of field amplitudes obtained from Eq. (4.70) for focused beams with $G = 10$ (upper row) and $G = 20$ (lower row) illustrating movement of the global maximum toward the source, and the corresponding spatial redistribution of local maxima, as ℓ is increased. The color maps range from dark blue for zero pressure amplitude to dark red for maximum pressure amplitude, with the maximum amplitude specific to each combination of parameters G and ℓ in order to best depict the dynamic range of the corresponding field structure.

4.6 Geometrical acoustics for vortex beams

Insight into movement of the vortex ring out of the focal plane and toward the source as ℓ increases is provided by geometrical acoustics, which is symbolized by the right-hand side of Fig. 1.1 and the top-left corner of Fig. A.2. In the immediate vicinity of the source plane, the pressure field $p = qe^{ikz}$ may be expressed as

$$\tilde{p}(r, \theta, z) \simeq p_0 f(r) e^{i\phi}, \quad z \simeq 0, \tag{4.92}$$

where $f(r)$ is the amplitude distribution in the source plane, assumed axisymmetric, and the phase

$$\phi(r, \theta, z) = -kr^2/2d + \ell\theta + kz \tag{4.93}$$

defines a wavefront in a focused vortex beam leaving the source plane in the paraxial approximation. For the focused Gaussian vortex source condition given by Eq. (4.62), the amplitude distribution is $f(r) = e^{-r^2/a^2}$, while $f(r) = \mathrm{circ}(r/a)$ for the focused circular vortex source condition given by Eq. (4.57). The wave normal at any point on the wavefront is defined by $\mathbf{n} = \boldsymbol{\nabla}\phi/|\boldsymbol{\nabla}\phi|$, which is evaluated for a point P in the source plane at

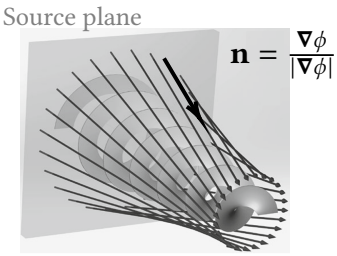

Figure 4.10: Schematic of the wave normal $\mathbf{n}$ (thick black arrow) in a vortex beam. The helical surface is described by Eq. (4.93) set equal to a constant, e.g., $-kr^2/2d + \ell\theta + kz = \text{constant}$. The thin black arrows are other rays emanating from the source plane. Adapted from Ref. 114 with permission from Springer Nature.

distance r_0 from the z axis to obtain

$$\mathbf{n} = \gamma^{-1}[-(r_0/d)\,\mathbf{e}_r + (\ell/kr_0)\,\mathbf{e}_\theta + \mathbf{e}_z]\,, \tag{4.94}$$

where $\gamma = [(r_0/d)^2 + (\ell/kr_0)^2 + 1]^{1/2}$ and $|\mathbf{n}| = 1$. A schematic of the wave normal is shown in Fig. 4.10.

Because the medium is homogeneous, any ray emanating from the source plane follows a straight line in direction $\mathbf{n}$ [22, Sec. 8.2]. Therefore, a ray starting at point P and traveling distance s arrives at a point Q whose position is given by the vector $\mathbf{R} = s\mathbf{n}$ relative to point P. This relation applies to a ray emanating from any point on a circle of radius r_0 in the plane $z = 0$ because $\mathbf{R}$ is the location relative to that point on the circle. Here and below, the word "circle" designates its perimeter and not the region enclosed by the perimeter. The family of rays emanating from the circle forms an axisymmetric surface surrounding the z axis. Thus in any plane perpendicular to the z axis, the locations where the rays pass through that plane form a circle. The first objective is to determine the radius $\Delta(r_0, z)$ of that circle as a function of distance z from the source plane.

The distance s along any ray path emanating from the circle of radius r_0 in the plane $z = 0$ is related to the coordinate z by $z = \mathbf{R} \cdot \mathbf{e}_z = \gamma^{-1}s$. Therefore $\mathbf{R} = \gamma z\mathbf{n}$, and from Eq. (4.94)

$$\mathbf{R} = -(r_0 z/d)\mathbf{e}_r + (\ell z/kr_0)\mathbf{e}_\theta + z\mathbf{e}_z\,. \tag{4.95}$$

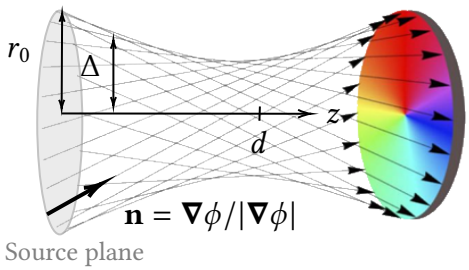

Figure 4.11: Illustration of rays with $\ell > 0$ emanating from a circle of radius r_0 in the source plane $z = 0$ pointing in direction given by Eq. (4.94). While the rays travel in straight lines, the path Δ given by Eq. (4.96) bends. Δ is the radius of the circle formed by the family of rays emanating from the circle of radius r_0 centered at the origin O in the source plane and intersecting a plane perpendicular to the z axis. Adapted from Fig. 1(b) of Ref. 277, licensed under CC BY 4.0. Source plane and annotations added by the author.

The r and θ components form the vector $\mathbf{r}_Q = -(r_0 z/d)\mathbf{e}_r + (\ell z/k r_0)\mathbf{e}_\theta$ for the location of point Q in the plane perpendicular to the z axis, with $\mathbf{r}_Q$ expressed in the polar coordinate system (r, θ) whose origin and orientation are defined by the location of point P on the circle of radius r_0 in the source plane. Since the location of the global origin O associated with the beam axis in this polar coordinate system is $\mathbf{r}_O = -r_0\mathbf{e}_r$, the distance between points Q and O in a plane perpendicular to the z axis is $\Delta = |\mathbf{r}_Q - \mathbf{r}_O|$, or

$$\frac{\Delta(r_0, z)}{r_0} = \left[(1 - z/d)^2 + (\ell d/k r_0^2)^2 (z/d)^2\right]^{1/2} . \tag{4.96}$$

More generally, Δ is the radius of the circle formed by the family of rays emanating from the circle of radius r_0 centered at the origin O in the source plane and intersecting a plane perpendicular to the z axis at an arbitrary distance from the source plane, as illustrated in Fig. 4.11.[8] As required, Eq. (4.96) reduces to $\Delta = r_0$ at $z = 0$.

The vortex rings discussed in Sec. 4.4 are formed by radiation from the entire source plane, not from just a circle of radius r_0. Before taking into account radiation

[8] Equation (4.96) can be rearranged into the form of a hyperboloid of one sheet, given in Cartesian coordinates by $\Delta^2/a_r^2 - (z - \beta/2\alpha)^2/b_r^2 = 1$, where $a_r = r_0\sqrt{2\alpha - \beta^2}/2\sqrt{\alpha}$, $b_r = \sqrt{2\alpha - \beta^2}/2\alpha$ with $\alpha = d^{-2} + (\ell/k r_0^2)^2$ and $\beta = 2/d$. Examples of hyperboloids in architecture, like the Corporation Street Bridge in Manchester and the Essarts-le-Roi water tower in France, may provide insight into the structure described by Eqs. (4.96).

from the entire source plane, it is useful to examine first the properties of Eq. (4.96) for a fixed value of r_0. The vertex where Δ is minimized is located at the value of z found by setting $\partial\Delta/\partial z = 0$ to obtain

$$\frac{z_{\text{ver}}(r_0)}{d} = \frac{1}{1 + (\ell d/kr_0^2)^2}, \tag{4.97}$$

and the corresponding minimum value of Δ is obtained by setting $z = z_{\text{ver}}$ in Eq. (4.96):

$$\frac{\Delta_{\min}(r_0)}{r_0} = \frac{\ell d/kr_0^2}{\sqrt{1 + (\ell d/kr_0^2)^2}}. \tag{4.98}$$

Equation (4.96) is symmetric about $z = z_{\text{ver}}$ in the region $0 \le z \le 2z_{\text{ver}}$. Equations (4.96)–(4.98) all depend on the dimensionless combination $\ell d/kr_0^2$.

Shown in Fig. 4.12 are plots of Δ/r_0 versus z/d obtained from Eq. (4.96) for $d/kr_0^2 = 0.1$ and $0 \le \ell \le 5$. The vertex moves toward the source as ℓ is increased according to Eq. (4.97), which is consistent with the direction of the shift in the location of the vortex ring observed in Fig. 4.9. The distance between the vertex and the z axis is observed to increase linearly with ℓ as long as $(\ell d/kr_0^2)^2$ remains small in the denominator of Eq. (4.98). This linear increase is consistent with the dependence of the vortex ring radius on ℓ predicted by Eqs. (4.84) and (4.85).

Limiting forms of Eq. (4.96) are now compared with the results obtained in Sec. 4.4. The radius of the circle in the focal plane predicted by geometrical acoustics is, with $z = d$ in Eq. (4.96), $\Delta = \ell d/kr_0$, which is observed to be similar to the expression for the ring radius given by Eq. (4.84). The result $\Delta = \ell d/kr_0$ differs from Eq. (4.98) because the latter does not correspond to the radius of the circle in the focal plane, but at the location z_{ver} of the vertex predicted by geometrical acoustics, which is less than d. For an unfocused beam, evaluating Eq. (4.96) with $d = \infty$ yields $\Delta = r_0[1 + (\ell z/kr_0^2)^2]^{1/2}$, and then evaluating this limit in the far field ($\ell z \gg kr_0^2$) yields $\Delta = \ell z/kr_0$, which is similar to Eq. (4.83). Considered next is the field structure predicted by geometrical acoustics for the more general case in which radiation from the entire source plane is taken into account, not from just source points confined to a circle.

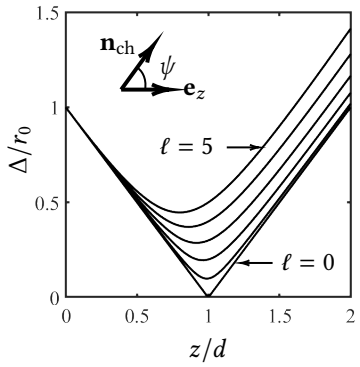

Figure 4.12: Plots of Δ/r_0 versus z/d obtained from Eq. (4.96) for $d/kr_0^2 = 0.1$ and $0 \le \ell \le 5$ displayed with ℓ increasing from bottom to top. The unit vector $\mathbf{n}_{\rm ch}$ and angle ψ correspond to Eq. (4.101), with the positive value of ψ chosen for illustration associated with the nominal directions of the annular channels following the curves in the region $z/d \gtrsim 1.5$.

Equation (4.96) is now used to determine the pressure amplitude in a plane at distance z from a source possessing the arbitrary axisymmetric amplitude distribution $p_0 f(r)$ in Eq. (4.92). The relation [22, Eq. (8.5.4)]

$$P(\Delta, z) = p_0 f(r_0) \sqrt{\frac{A(r_0, 0)}{A(r_0, z)}} \tag{4.99}$$

for the pressure amplitude P is used for this purpose, where $A(r_0, z)$ is the area of the annular channel corresponding to rays emanating from source points with amplitude $p_0 f(r_0)$ at distance r_0 from the z axis. Equation (4.99) is derived by taking the infinite-frequency limit of the Helmholtz equation in Sec. A.1 [see Eq. (A.42)]. The pressure $P(\Delta, z)$ is expressed as a function of Δ rather than r_0 because the coordinates (Δ, z) identify the location in the field where the pressure is desired. Source point locations identified by $r = r_0$ on the right-hand side of Eq. (4.99) map onto field points at $r = \Delta(r_0, z)$ according to Eq. (4.96), the inversion of which permits r_0 to be expressed in terms of (Δ, z),

$$r_0(\Delta, z) = \frac{2^{-1/2}}{|1 - z/d|} \left[\Delta^2 + \sqrt{\Delta^4 - \Delta_c^4(z)}\right]^{1/2}, \quad \Delta > \Delta_{\rm c}(z)\,, \tag{4.100}$$

where $\Delta_{\rm c}(z)$ is defined in Eqs. (4.111) and (4.112). The "+" sign is chosen when using the quadratic formula to obtain Eq. (4.100) to recover the fact that $\Delta = r_0$ at $z = 0$, where

it is noted that $\Delta_c(0) = 0$ from Eq. (4.111). Regions in which $\Delta < \Delta_c(z)$ are shadow zones ($P = 0$) predicted by geometrical acoustics, and Eq. (4.100) is not relevant in regions where there are no ray paths. Equation (4.100) can thus be used to evaluate the pressure amplitude in Eq. (4.99) as an explicit function of the field points $(r, z) = (\Delta, z)$. The only restriction is that the source must possess an axisymmetric amplitude distribution as described by $p_0 f(r)$ in Eq. (4.92), such that the amplitude of the field throughout the vortex beam is independent of θ, as is usually the case.

The area function $A(r_0, z)$ in Eq. (4.99) usually corresponds to the cross section of a ray tube encircling a particular ray path, e.g., emanating from a point (r_0, θ) in the source plane as defined by Eq. (4.94). However, of interest here is the amplitude and not the phase of the pressure, and due to the axisymmetric geometry of the annular channel formed by the family of rays radiated by a thin annulus of inner radius r_0 in the source plane, the amplitude does not depend on θ. It is therefore expedient to define A instead to be the cross-sectional area of the channel with unit normal in the r-z plane forming angle $\psi(r_0, z)$ with the z axis as defined in Fig. 4.12:

$$\mathbf{n}_{\text{ch}} = \sin\psi(r_0, z)\,\mathbf{e}_r + \cos\psi(r_0, z)\,\mathbf{e}_z\,. \tag{4.101}$$

The direction of the channel normal $\mathbf{n}_{\text{ch}}$ is thus everywhere tangent to the corresponding curves in Fig. 4.12.

The angle $\psi(r_0, z)$ may be expressed as $\tan\psi = \partial\Delta/\partial z$, which yields for the vector components in Eq. (4.101)

$$\sin\psi(r_0, z) = \frac{\partial\Delta/\partial z}{\sqrt{(\partial\Delta/\partial z)^2 + 1}}\,, \tag{4.102}$$

$$\cos\psi(r_0, z) = \frac{1}{\sqrt{(\partial\Delta/\partial z)^2 + 1}}\,, \tag{4.103}$$

and thus

$$\mathbf{n}_{\text{ch}} = \frac{(\partial\Delta/\partial z)\,\mathbf{e}_r + \mathbf{e}_z}{\sqrt{(\partial\Delta/\partial z)^2 + 1}}\,, \tag{4.104}$$

where

$$\frac{\partial \Delta}{\partial z} = -\frac{r_0}{d} \frac{1 - z/d - (\ell d/k r_0^2)^2 z/d}{[(1 - z/d)^2 + (\ell d/k r_0^2)^2 (z/d)^2]^{1/2}} \,. \tag{4.105}$$

The form of Eq. (4.104) facilitates comparison with the wave normal $\mathbf{n}$ defined by Eq. (4.94), which determines the directions of the ray paths within the annular channel.

Only for $\ell = 0$ is $\mathbf{n}_{\text{ch}}$ equivalent to $\mathbf{n}$:

$$\mathbf{n}_{\text{ch}} = \frac{-\text{sgn}(1 - z/d)(r_0/d)\, \mathbf{e}_r + \mathbf{e}_z}{\sqrt{(r_0/d)^2 + 1}} \,, \quad \ell = 0 \,. \tag{4.106}$$

In this case the component $\mathbf{e}_\theta$ in Eq. (4.94) vanishes, and all rays intersect the z axis at $z = d$. Equation (4.106) describes a conical structure for the annular channel that is symmetric about its vertex in the plane $z = d$ as illustrated in Fig. 4.12, and in the first column of Fig. 4.15. Since the expression for $\mathbf{n}$ in Eq. (4.94) is restricted to the source plane, unlike Eq. (4.106) it does not account for the sign change in the coefficient of $\mathbf{e}_r$ beyond the focal plane $z = d$, where the ray paths diverge from the z axis.

For $\ell \neq 0$, the nonzero component $\mathbf{e}_\theta$ in Eq. (4.94) prevents $\mathbf{n}_{\text{ch}}$ from being equivalent to $\mathbf{n}$. Although $\mathbf{n}_{\text{ch}}$ can be the projection of $\mathbf{n}$ onto the r-z plane, this occurs only for two values of z:

$$\mathbf{n}_{\text{ch}} = \frac{-\text{sgn}(1 - z/z_{\text{ver}})(r_0/d)\, \mathbf{e}_r + \mathbf{e}_z}{\sqrt{(r_0/d)^2 + 1}} \,, \quad \ell \neq 0 \,, \quad z = 0 \;\text{ or }\; 2z_{\text{ver}} \,, \tag{4.107}$$

where z_{ver} is the location of the minimum channel radius, as defined in Eq. (4.97). Equation (4.107) applies only in the plane $z = 0$ or $z = 2z_{\text{ver}}$, and nowhere else. Apart from the sign change for $z = 2z_{\text{ver}}$ associated with divergence of the rays in the region $z > z_{\text{ver}}$, Eq. (4.107) is observed to be equivalent to Eq. (4.94) if the component $\mathbf{e}_\theta$ is removed. More generally, as noted following Eq. (4.98), the annular channel radius $\Delta(r_0, z)$ is symmetric about the vertex at $z = z_{\text{ver}}$ in the region $0 \leq z \leq 2z_{\text{ver}}$, and therefore ψ is symmetric about this turning point, with $\psi < 0$ for $z < z_{\text{ver}}$, $\psi = 0$ at $z = z_{\text{ver}}$, and $\psi > 0$ for $z > z_{\text{ver}}$.

It also proves convenient to express the cross-sectional area A, the orientation of which is defined by Eqs. (4.101) and (4.104), in terms of the cross-sectional area A_z formed

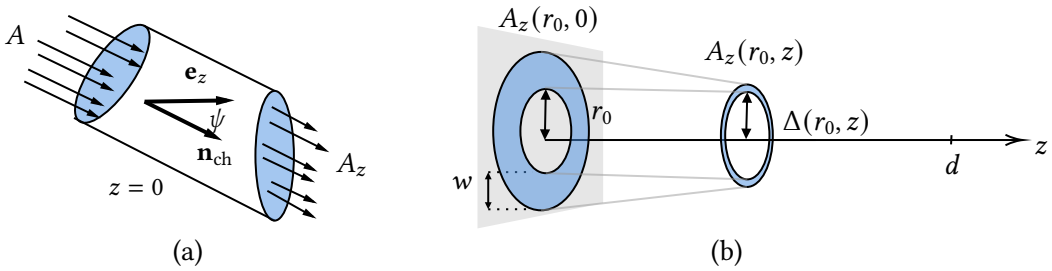

Figure 4.13: (a) Illustration of cross sectional area A of a local section of an annular ray channel and the cross-sectional area A_z formed by the intersection of the channel with any plane perpendicular to the z axis. The case illustrated is in the source plane $z = 0$, for which $\mathbf{n}_{\rm ch}$ and $\mathbf{n}$, the wave normal, are oriented in the same direction, as seen in Eq. (4.107). (b) Illustration of the evolution in z of the annular ray channel with an area given by Eq. (4.109).

by the intersection of the annular ray channel with any plane perpendicular to the z axis, such that A_z has unit normal $\mathbf{e}_z$, as illustrated in Fig. 4.13(a):

$$A(r_0, z) = A_z(r_0, z) \cos\psi(r_0, z) \,. \tag{4.108}$$

In Eq. (4.99), $p_0 f(r_0)$ is thus the pressure amplitude in a thin annulus of inner radius r_0 and area $A_z(r_0, 0)$ in the source plane $z = 0$, and $P(\Delta, z)$ is the pressure amplitude in the corresponding annular ray channel of inner radius $\Delta(r_0, z)$ and area $A_z(r_0, z)$ at $z \geq 0$. These quantities are illustrated in Fig. 4.13(b). The annulus of inner radius r_0 at $z = 0$ is assigned an infinitesimal width w such that its area is $A_z(r_0, 0) = 2\pi r_0 w$, with the area of the annular channel at distances $z \geq 0$ given by

$$\begin{aligned} A_z(r_0, z) &= 2\pi\Delta(r_0, z)|\Delta(r_0 + w, z) - \Delta(r_0, z)| \\ &\simeq 2\pi\Delta(r_0, z) w |\partial\Delta/\partial r_0| \\ &= 2\pi r_0 w \left|(1 - z/d)^2 - (\ell d/k r_0^2)^2 (z/d)^2\right| \,. \end{aligned} \tag{4.109}$$

Combining Eqs. (4.99), (4.108), and (4.109) yields

$$P(\Delta, z) = p_0 f(r_0) \left[\frac{\cos\psi(r_0, 0)/\cos\psi(r_0, z)}{\left|(1 - z/d)^2 - (\ell d/k r_0^2)^2 (z/d)^2\right|}\right]^{1/2} \tag{4.110}$$

for the pressure amplitude in the annulus of inner radius $r = \Delta(r_0, z)$ at distances $z \geq 0$ from the source plane and $r > \Delta_{\rm c}(z)$ from the z axis due to the family of rays emanating

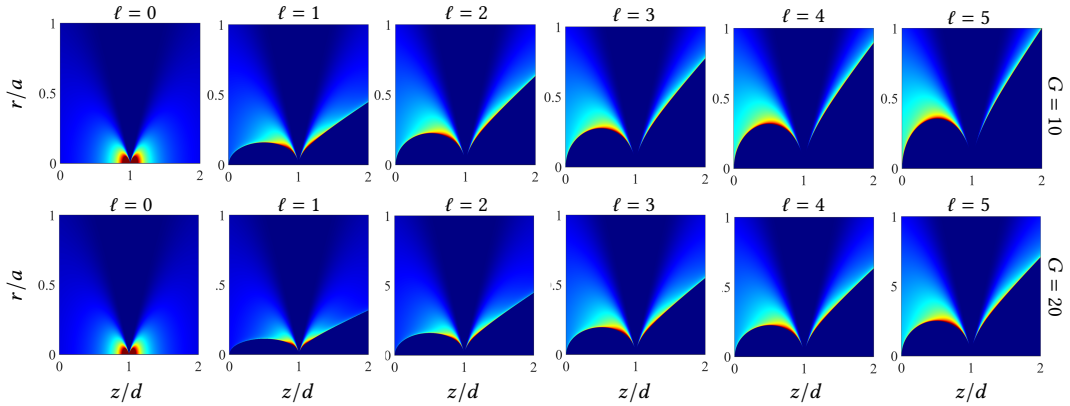

Figure 4.14: Plot of Eq. (4.110) with $f(r) = e^{-r^2/a^2}$ for $G = 10$ (first row) and $G = 20$ (second row), illustrating how geometrical acoustics captures the spatial transformation of the field as ℓ is increased in the range $0 \leq \ell \leq 5$. The field is plotted in only one hemisphere to emphasize the structure of the field. Comparison to the first two rows of Fig. 4.15 reveals that while geometrical acoustics recovers the basic structure of the field transformation, it does not predict the global maximum of the field or the existence of sidelobes. See caption of Fig. 4.9 for explanation of the color maps.

from the annulus of inner radius $r = r_0$ in the source plane. Equation (4.110) is plotted in Fig. 4.14 for a Gaussian amplitude shading $f(r) = e^{-r^2/a^2}$ in the source plane, revealing that geometrical acoustics successfully describes how the field transforms with changes in the orbital number but does not recover the effects of diffraction, e.g., the location of the global maximum of the field or the existence of sidelobes.

Of interest in the present section are the shift and distortion of the vortex ring depicted in Fig. 4.9 as ℓ increases. These spatial features are associated with the caustics created by the vorticity of the sound field. Caustics are paths along which cross-sectional areas of the annular ray channels vanish and the corresponding pressure amplitude predicted by geometrical acoustics is infinite. Setting $A_z(r_0, z) = 0$ in Eq. (4.109), which results in an equation that is quadratic in z, yields the two roots $z/d = (1 \pm \ell d/kr_0^2)^{-1}$. The roots are rewritten as $r_0^2 = \pm(\ell z/k)/(1 - z/d)$ and substituted into Eq. (4.96) to obtain the path of the caustic:

$$\Delta_c(z) = \sqrt{(2\ell d/k)(z/d)|1 - z/d|}\,. \tag{4.111}$$

For comparison with Eq. (4.70), and to facilitate interpretation, $\Delta_c(z)$ is normalized by the characteristic source radius a:

$$\frac{\Delta_c(z)}{a} = \sqrt{(\ell/G)(z/d)|1 - z/d|}, \tag{4.112}$$

where $G = ka^2/2d$ as before. It is observed that $\Delta_c(z)$ is zero at $z = 0$ and $z = d$, and in between it is symmetric about $z = \frac{1}{2}d$, at which point the caustic in the region $z < d$ is furthest from the z axis, with the distance from the z axis given by $\Delta_c/a = \frac{1}{2}\sqrt{\ell/G}$. For $z \gg d$, the distance between the caustic and the z axis increases linearly with z according to $\Delta_c/a \simeq \sqrt{\ell/G}(z/d)$. The normalized form of Eq. (4.96) for the path of each annular ray channel in the r-z plane is given by

$$\frac{\Delta(r_0, z)}{a} = \frac{r_0}{a}\left[(1 - z/d)^2 + \frac{(\ell/2G)^2(z/d)^2}{(r_0/a)^4}\right]^{1/2}, \tag{4.113}$$

with the coordinates for where the distance between each path and the z axis is minimized given by Eqs. (4.97) and (4.98). For $\ell = 0$, the result for the caustic reduces to $\Delta_c(z) = 0$, merely indicating that the caustic vanishes, and Eq. (4.113) reduces to the result for a converging spherical wave, $\Delta(r_0, z) = r_0|1 - z/d|$.

Shown in Fig. 4.15 are overlays of Eq. (4.112) for the caustics (thick lines) and Eq. (4.113) for the annular ray channels (thin lines) on top of color plots for the amplitude of the pressure field obtained from Eq. (4.70) for $G = 10$ (first row) and $G = 20$ (second and third rows), with $\ell = 0$, 1, 2, 3, 4, and 5 for the six columns in the first and second row, and $\ell = 0$, 2, 4, 6, 8, and 10 in the third row (i.e., double the corresponding values in the first two rows). The parameters match those in Fig. 4.9 in order to illustrate how, as ℓ is increased, geometrical acoustics can be used to interpret the movement of the global maximum toward the source and the corresponding spatial redistribution of local maxima. Figures 4.9 and 4.15 are somewhat different in appearance because in the latter only the upper half of the field is displayed, and with the vertical axes expanded in order to better resolve the features of the annular ray channels. For clarity, only channels emanating from the region $0 \le r/a \le 1$ in the source plane are displayed. One consequence of this

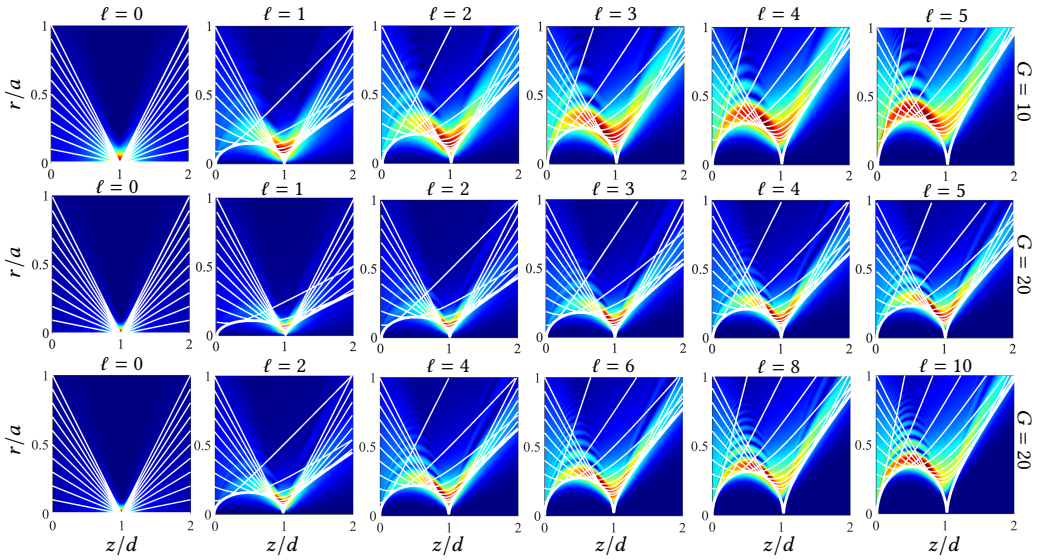

Figure 4.15: Overlays of Eq. (4.112) for the caustics (thick lines) and Eq. (4.113) for the annular ray channels (thin lines) on top of color plots for the amplitude of the pressure field obtained from Eq. (4.70) for $G = 10$ (first row) and $G = 20$ (second and third rows) illustrating movement of the global maximum toward the source, and the corresponding spatial redistribution of local maxima, as ℓ is increased in the range $0 \leq \ell \leq 5$ in the first and second rows and $0 \leq \ell \leq 10$ in the third row. For clarity, only annular ray channels emanating from the region $0 \leq r/a \leq 1$ in the source plane are displayed. See caption of Fig. 4.9 for explanation of the color maps.

truncation is that channels forming the bottom of the "V" in the caustic at $z/d = 1$ are absent, e.g., especially for $G = 10$ and $\ell = 5$.

It is observed in Fig. 4.15 that Eq. (4.112) for the caustic defines rather well the shadow zones in both the pre- and postfocal regions. It is also observed that the trajectory of the global maximum follows the caustic in the direction of the source as ℓ increases. Comparing the first and second rows as ℓ is increased from 0 to 5 reveals that the movement of the global maximum toward the source is less pronounced for $G = 20$ (second row) than for $G = 10$ (first row). However, comparing the first and third rows as ℓ is increased from 0 to 5 in the former ($G = 10$) but from 0 to 10 in the latter ($G = 20$), it is observed that the movement of the global maximum toward the source is very much the same even though the values of G differ by a factor of 2. This is due to the fact that the paths of the annular ray channels defined by Eq. (4.96), and the paths of the caustics defined by Eq. (4.111), do not vary with ℓ and k when the ratio ℓ/k is held constant, which corresponds to maintaining a constant ratio ℓ/G in Eqs. (4.112) and (4.113). The main difference in the field calculations based on Eq. (4.70) in the first and third rows is the higher spatial frequency in the third row, which corresponds to the value of k being doubled. Starting with Eq. (4.94), all subsequent equations in the present section depend on ℓ and k only in the ratio ℓ/k, including the equations in the discussion about unfocused vortex beams beginning on p. 154.

The above analysis is repeated for the focused focused circular vortex source in Eq. (4.57) by setting $f(r) = \mathrm{circ}(r/a)$. The geometry of the rays is identical to that for Eq. (4.62), with the exception that rays associated with Eq. (4.57) originate from the finite region $0 < r \leq a$. The ray features in Fig. 4.16 are therefore identical to those in Fig. 4.15, but the underying color plots represent the paraxial field corresponding to Eq. (4.57).

We now examine the geometry of the shadow zone in the prefocal region. Letting (x_c, y_c, z_c) be the coordinates of the surface defined by the caustic, one may write $\Delta_c^2 =$

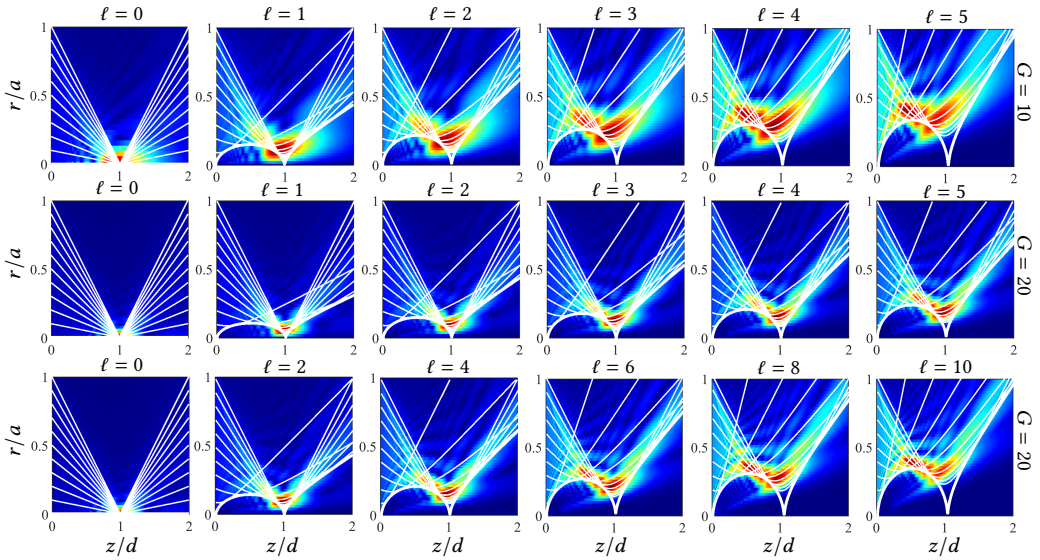

Figure 4.16: See caption of Fig. 4.15. The ray features displayed here are identical to those of Fig. 4.15, but the underlying pressure field is obtained from Eq. (4.55) with source condition (4.61). In contrast to Fig. 4.15, the annular ray channels for $f(r) = \mathrm{circ}(r/a)$ emanate only from the region $0 \le r/a \le 1$, whereas the ray channels extend infinitely in the source plane for $f(r) = e^{-r^2/a^2}$ but are suppressed for clarity in Fig. 4.15.

$x_c^2 + y_c^2$ and rearrange Eq. (4.112) to obtain

$$\frac{x_c^2 + y_c^2}{a_c^2} + \frac{(z_c - d/2)^2}{c_c^2} = 1\,, \quad 0 \le z_c \le d\,, \tag{4.114}$$

which describes a spheroid in the prefocal region centered at $z_c = d/2$ along its axis of symmetry with

$$a_c^2 = \ell a^2/4G\,, \quad c_c^2 = d^2/4\,. \tag{4.115}$$

Equation (4.114) corresponds to a prolate spheroid for $a_c < c_c$ and an oblate spheroid for $a_c > c_c$, or

$$(d/a)^2 G > \ell\,, \quad \text{prolate spheroid}\,, \tag{4.116}$$

$$(d/a)^2 G < \ell\,, \quad \text{oblate spheroid}\,. \tag{4.117}$$

One may also write $(d/a)^2 G = \pi d/\lambda$, where $\lambda = 2\pi/k$, and therefore whether the shape of the shadow zone predicted by geometrical acoustics in the prefocal region is prolate

or oblate depends only on the ratio of focal length to wavelength relative to the orbital number. Since the volume of the spheroid is $\frac{4}{3}\pi a_c^2 c_c$, the volume of the shadow zone enclosed by the caustic surface in the prefocal region may be expressed as $V_c = \frac{1}{6}\ell\lambda d^2$, in which the product $\ell\lambda$ is a consequence of the ratio ℓ/k that is discussed in connection with Fig. 4.15.

Figure 4.8 indicates that the paraxial approximation is accurate in the parameter space defined by $d/a \geq 4$, $ka \geq 50$, and $1 \leq \ell \leq 10$, in which case for $G \geq 5$ one obtains $(d/a)^2 G \geq 80$. Thus, the caustic surface in the prefocal region is a prolate spheroid for all cases considered in Figs. 4.9 and 4.15. The prefocal caustic surface for $G = 10$ and $\ell = 5$ in Fig. 4.15 (and for $G = 20$ and $\ell = 10$ as well) appears oblate rather than prolate only because of the aspect ratio employed to emphasize the field structure surrounding the caustic. Oblate spheroids may be encountered under other circumstances.

Prefocal shadow zones like those in Fig. 4.9 are not restricted to vortex beams with Gaussian and uniform circular amplitude shadings. For example, a source amplitude described by a raised cosine of finite extent defined by $f(r) = \frac{1}{2}[1 + \cos(\pi r/2a)]$ for $0 \leq r \leq 2a$ and zero otherwise in place of $f(r) = e^{-r^2/a^2}$ in Eq. (4.62) produces field patterns very similar to those in Fig. 4.9.[9] The spheroidal cavities surrounded by steep pressure gradients in Fig. 4.9 may prove useful for particle trapping in three dimensions, a subject of interest in recent studies [237, 278].

A wave phenomenon referred to in optics as an autofocusing vortex beam [117] bears resemblance to the field structures in the regions corresponding to $z > d/2$ in Fig. 4.15. The autofocusing effect is created by positioning the source plane at $z = d/2$. Instead of the phase term $-kr^2/2d$ at $z = 0$ in Eq. (4.93), a different phase term is used at $z = d/2$ to produce an abruptly converging vortex field in the region $z > d/2$ that follows a caustic similar to Eq. (4.111). In addition to the significantly different source conditions

[9] For the raised cosine source function mentioned two paragraphs above Eq. (62) in Ref. 107 as a practical approximation of an infinitely wide Gaussian source function, the raised cosine should have an upper limit of $2a$ instead of a.

used to create the autofocusing effect, the expressions for the caustics do not lend themselves to describing the field produced by the source condition in Eqs. (4.92) and (4.93) and exhibited throughout the regions $z > 0$ in Fig. 4.15. A number of other publications on autofocusing optical beams, dating back to 2010, may be found in Ref. 117.

Simplified forms of the results obtained with geometrical acoustics for focused vortex beams are now considered in the absence of focusing. With $d = \infty$, Eqs. (4.96) and (4.109) for the distance between the annular ray channel and the z axis, and the corresponding cross-sectional area of the channel perpendicular to the z axis, reduce to

$$\Delta(r_0, z) = r_0[1 + (\ell z/kr_0^2)^2]^{1/2}, \tag{4.118}$$

$$A_z(r_0, z) = 2\pi r_0 w|1 - (\ell z/kr_0^2)^2|, \tag{4.119}$$

respectively. The limiting forms of Eqs. (4.97) and (4.98), $z_{\text{ver}} = 0$ and $\Delta_{\min} = r_0$, merely reflect the fact that Δ increases continuously with distance from the source plane for $\ell > 0$, and it remains constant for $\ell = 0$. Equation (4.111) for the caustic becomes

$$\Delta_c(z) = \sqrt{2\ell z/k}, \tag{4.120}$$

which for $\ell > 0$ defines a paraboloid that increases in proportion to $z^{1/2}$ from the source plane to the far field. The amplitude of the pressure field outside the shadow zone enclosed by the paraboloidal caustic surface is, from Eq. (4.110),

$$P(\Delta, z) = p_0 f(r_0)\left[\frac{\cos\psi(r_0, 0)/\cos\psi(r_0, z)}{\left|1 - (\ell z/kr_0^2)^2\right|}\right]^{1/2}, \tag{4.121}$$

and Eq. (4.100), which is used to express r_0 as a function of (Δ, z), reduces to

$$r_0(\Delta, z) = 2^{-1/2}\left[\Delta^2 + \sqrt{\Delta^4 - \Delta_c^4(z)}\right]^{1/2}, \quad \Delta > \Delta_c(z). \tag{4.122}$$

Equations (4.102) and (4.103) defining the angle ψ of the annular ray channel in the r-z plane retain the same forms, but Eq. (4.105) reduces to

$$\frac{\partial\Delta}{\partial z} = \frac{\ell}{kr_0}\frac{\ell z/kr_0^2}{\sqrt{1 + (\ell z/kr_0^2)^2}}, \tag{4.123}$$

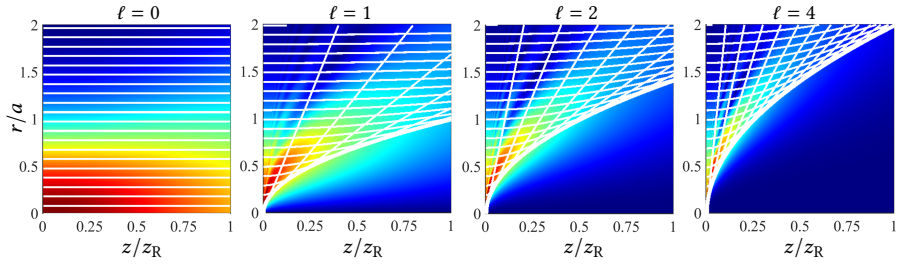

Figure 4.17: Overlays of Eq. (4.120) for the caustics (thick lines) and Eq. (4.118) for the annular ray channels (thin lines) on top of color plots for the amplitude of the pressure field obtained from Eq. (4.70) for $d = \infty$ (no focusing) and several values of ℓ. In terms of the Rayleigh distance $z_R = ka^2/2$ appearing in the figure, Eq. (4.120) may be expressed as $\Delta_c/a = (\ell z/z_R)^{1/2}$. See caption of Fig. 4.9 for explanation of the color maps.

which for $\ell > 0$ further reduces to ℓ/kr_0 in the far field ($\ell z \gg kr_0^2$). For $\ell = 0$ one obtains $\psi = 0$, and all ray channels are parallel to the z axis. In Fig. 4.17, Eqs. (4.118) and (4.120) are overlayed on the amplitude of the pressure field obtained from Eq. (4.70) for several values of ℓ. Figure 4.18 displays the same ray features over the domain $0 < r \leq 1$ for the pressure field obtained from Eq. (4.55) with source condition (4.56).

The paraxial solutions for $f(r) = \text{circ}(r/a)$ in Figs. 4.16 and 4.18 do not conform as well to the caustics as do the paraxial solutions for $f(r) = e^{-r^2/a^2}$ in Figs. 4.15 and 4.17. The discrepancies are due to the jump at $r = a$ in $f(r) = \text{circ}(r/a)$, which makes the effects of diffraction substantially more prominent than for $f(r) = e^{-r^2/a^2}$. Still, the diffraction patterns in Figs. 4.16 and 4.18 coincide reasonably well with the ray features. The caustics in Figs. 4.16 and 4.18 demarcate the borders of the global maxima and the shadow zones for $\ell > 0$ despite the complexity of the field. As G is increased in Fig. 4.16, the diffraction and ray features draw closer together because increasing ka tends toward the ray limit.

4.7 Summary

The history of vortex beams and the motivation for the development of analytical solutions was discussed in Sec. 4.1. A simplified diffraction integral equivalent to the Rayleigh

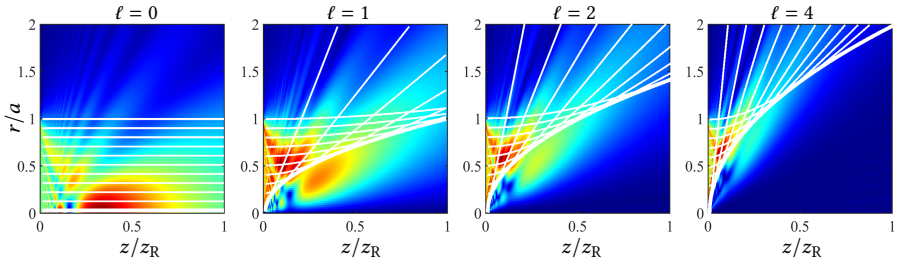

Figure 4.18: See caption of Fig. 4.17. The ray features displayed here are identical to those of Fig. 4.17, but the underlying pressure field is obtained from Eq. (4.86) with source condition (4.56).

integral for circular pistons was derived in Sec. 4.2 by considering a piston in an infinitely large cylindrical waveguide. While the diffraction integral must be evaluated numerically in most cases, it provides an exact solution for vortex beams radiated by circular pistons, making it relevant to source configurations determined in Sec. 4.5 in which the paraxial approximation is not accurate. The simplified diffraction integral was recast as a sum of Bessel beams, allowing for analyses involving individual Bessel beams to be generalized to radiation from sources described by Eq. (4.1). The formulation recovered the axial pressure due to a planar circular piston and was used to calculate the solution of the Helmholtz equation for a vortex beam with $\ell = 1$. Evaluation of the diffraction integral in terms of the eigenfunctions of the Helmholtz equation was shown to avoid the artifacts associated with the numerical implementation based on Fourier acoustics.

Analytical descriptions of vortex beams radiated by sources with circular and Gaussian amplitude distributions were obtained in the paraxial approximation in Sec. 4.3. The solutions for focused beams may describe acoustic tweezers that exploit the pressure minimum along the axis to trap particles [279, Sec. 4.1.2], while solutions for unfocused beams may find relevance to high-speed communication applications that employ multiplexing based on the orbital number [87]. The utility of the analytical solutions was demonstrated in Sec. 4.4 by calculating the vortex ring radii in the focal plane and far field of vortex beams generated by circular and Gaussian amplitude distributions. The vortex ring radii in all cases were found to be linear functions of the orbital number.

Section 4.5 assessed the accuracy of the paraxial approximation when applied to

vortex beams. Comparisons with solutions of the Helmholtz equation demonstrated that for the paraxial approximation of an unfocused beam to be accurate, the value of ka for the source should be several times larger than the value of the orbital number up to at least $\ell = 10$. Focusing introduces the ratio d/a of focal length to source radius, and it also significantly alters the structure of the angular spectra, the combination of which prevented determination of a simple analytical criterion for agreement with the Helmholtz equation. Values of d/a, ka, and ℓ for which the paraxial approximation of a focused vortex beam is reasonably accurate were presented using the decision matrix in Fig. 4.8.

It was found that as ℓ increases for a focused vortex beam, the vortex ring moves out of the focal plane in the direction of the source, and for $10 \lesssim G \lesssim 20$ ($G = ka^2/2d$) the maximum amplitude is redistributed along a spheroidal surface enclosing a shadow zone in the prefocal region. These observations motivated development in Sec. 4.6 of a model based on geometrical acoustics for a source with an axisymmetric amplitude distribution. The ray theory resulted in a simple expression for the coordinates of the caustic surfaces formed by focused and unfocused vortex beams. An explicit expression based on geometrical acoustics was also developed for the pressure amplitude in a vortex beam.

The exact, paraxial, and ray models presented here provide expressions and insights for features of acoustic vortex beams that have not previously been investigated in detail. The results may prove useful for applications in science and engineering. Future research directions related to vortex beams are outlined in Sec. 5.3.

Chapter 5: Conclusion and future directions

The assumption of symmetry simplifies the analysis of scattering and diffraction phenomena and conveys the underlying physics with minimal mathematical complication. Chapters 2–4 show that breaking symmetry results in interesting physical behaviors that contribute additional degrees of freedom across the frequency spectrum. Mathematical complication was avoided by appealing to the approximations outlined in Sec. 1.2 and App. A. The primary contributions of Chaps. 2–4 are summarized below, and future research directions are outlined.

5.1 Radiation force

In Chap. 2, the acoustic radiation force due to progressive waves on subwavelength scatterers was calculated in the Born approximation. Rayleigh scattering was generalized to order $(ka)^3$, allowing for material inhomogeneity to be considered. Simple formulas were obtained for acoustic polarizability, which represent the scattered field at dipole order. Gor'kov's $O[(ka)^4]$ force was recovered for scatterers with even distributions of material properties [3, Eq. (10)], while scatterers with odd contrast factors were shown to experience an $O[(ka)^6]$ force. The analytical formulation was found to be accurate for $ka \lesssim 0.8$, similar to Jerome and Hamilton's integral for the radiation force exerted by standing waves on inhomogeneous objects [144, Eq. (16)].

Many aspects of radiation force remain to be explored, and Poynting's comments from 1905 are still relevant [135, p. 406]:

> The Radiation Theory is only just starting on its journey. Its feet are not yet clogged by any certain data, and all directions are yet open to it. Any suggestion for its future course appears to be permissible, and it is only by trial that we shall find what ways are barred. At least we may be sure that it deals with real effects and that it must be taken into account.

Below are a few research directions related to Chap. 2.

Scatterer with nonzero values of α_m, α_d, and $\boldsymbol{\alpha}_\mathrm{c}$

A subwavelength Born scatterer characterized by nonzero values of α_m, α_d, and $\boldsymbol{\alpha}_\mathrm{c}$ experiences radiation forces of orders $(ka)^4$ [associated with the first three terms of Eq. (2.30)] and $(ka)^6$ [associated with the last term of Eq. (2.30)]. Such scatterers were not considered as examples in Chap. 2, but their application to engineering [162] may be explored in the future. The presence of all three polarizabilities may lead to additional dynamics that are absent when either $\boldsymbol{\alpha}_\mathrm{c} = \mathbf{0}$ or $\alpha_\mathrm{m} = \alpha_\mathrm{d} = 0$. To consider such a scatterer, the material properties

$$\gamma_\beta = \gamma_1 + 2\gamma_2 x_\mathrm{s}/a\,, \qquad \gamma_\rho = \gamma_3 + 2\gamma_4 x_\mathrm{s}/a \tag{5.1}$$

may be used, where γ_1, γ_2, γ_3, and γ_4 are constants. Setting $\gamma_2 = \gamma_4 = 0$ recovers the homogeneous cube described in Sec. 2.4, while $\gamma_1 = \gamma_3 = 0$ recovers the inhomogeneous cube considered at the end of Sec. 2.4.

Finite cylinder

The discussion of cubes and spheres in Sec. 2.4 leads naturally to the study of cylinders. The radiation force on a finite cylinder could be calculated using Eq. (2.1) in combination with Eqs. (2.26)–(2.29), and the validity of the result could be assessed by comparison to Eq. (2.1) in combination with Eq. (2.11). For a homogeneous cylinder having equal properties and volume as the homogeneous sphere and cube considered in Sec. 2.4, the radiation force should be given by Eq. (2.36). Material inhomogeneity could be considered along the axis of the cylinder, as previously considered by Jerome and Hamilton for forces exerted by standing waves [31, Fig. 4].

Radiation torque

Acoustic radiation torque can be calculated using the far-field directivity in the Born approximation given by Eq. (2.11) or its subwavelength limit given by (2.26) in combi-

nation with Maidanik's formulation for the torque exerted by plane progressive waves [280, Eq. (28)]. The inhomogeneous cube considered in Sec. 2.4 experiences zero radiation torque at dipole order for both configurations of the incident wave, but the inclusion of higher-order terms in the multipole expansion may lead to interesting dynamics related to the angular stability of the scatterer.

Scatterer in a paraxial beam

The expressions derived may model the radiation force exerted by paraxial beams to reasonable accuracy because the incident waves of high-frequency beams are quasiplanar, as discussed in Sec. 4.3. For example, the force on a subwavelength dielectric sphere suspended in an optical beam [281] has a functional form similar to the polarizability-based force given by Eq. (2.36), suggesting that the force in the direction of the primary direction of incident wave motion can be approximated locally by the results of Chap. 2. Meanwhile, transverse forces exerted by beams act as standing wave fields conducive to the Born approximation developed by Jerome et al. [144], as discussed by Fan and Zhang [282].

Future work may involve combining Eqs. (2.1) and Eqs. (2.26)–(2.29) with Eq. (16) of Ref. 11 to determine whether the total force vector exerted by a sound beam equals the vector sum of the forces predicted in Chap. 2 and Ref. 11. While the radiation forces exerted individually by two different wave fields cannot in general be added to calculate the radiation force exerted by the sum of the two fields, the superposition principle might be permissible in the Born approximation that underlies both Chap. 2 and Ref. 11. The validity of the solution may be assessed by comparison with results based on the finite element method.

Scatterer in an acoustofluidic device

Acoustofluidic devices like those described by Jo and Guldiken [283] similarly involve a combination of standing and progressive wave fields. The force exerted by the standing

wave component on biological media is conducive to the Born approximation developed by Jerome et al., as shown in Ref. 192. Future work may consider using Eqs. (2.1) and Eqs. (2.26)–(2.29) to calculate the radiation force exerted by the progressive wave component.

Scattering solution at quadrupolar order

The scattering solution developed in Sec. 2.3 was truncated at dipole order. The restriction to dipole order arose due to the Taylor expansions introduced in Eqs. (2.16) and (2.17). To more accurately describe scattered fields on the order of $ka = 1$, additional terms in Eqs. (2.16) and (2.17) could be retained, e.g.,

$$e^{i\mathbf{k}_\mathrm{i}\cdot\mathbf{r}_\mathrm{s}} \simeq 1 + i\mathbf{k}_\mathrm{i}\cdot\mathbf{r}_\mathrm{s} - (\mathbf{k}_\mathrm{i}\cdot\mathbf{r}_\mathrm{s})^2 \tag{5.2}$$

$$e^{-i\mathbf{k}_\mathrm{s}\cdot\mathbf{r}_\mathrm{s}} \simeq 1 - i\mathbf{k}_\mathrm{s}\cdot\mathbf{r}_\mathrm{s} - (\mathbf{k}_\mathrm{s}\cdot\mathbf{r}_\mathrm{s})^2\,. \tag{5.3}$$

Additional polarizabilities representing the second moment of the contrast factors γ_β and γ_ρ would result from following the procedure in Sec. 2.3. It is anticipated that the additional polarizabilities relate the incident fields to the scattered quadrupole, as may be shown by extending App. C.5 to quadrupole order.

Time-modulated scatterer

The formulation presented in Chap. 2 assume that the material properties of the scatterer are independent of time. However, interesting physics may arise from the consideration of a scatterer in motion. Future work may involve calculating the field scattered by a spinning asymmetric subwavelength object, as depicted in Fig. 5.1. For simplicity, a sphere consisting of two hemispheres of different compressibilities could be considered, while the density of both hemispheres equals that of the background medium. First, the scattering problem could be solved for the un-modulated case, for which the compressibility contrast factors are given by

$$\gamma_\beta = \begin{cases} \gamma_\mathrm{T}\,, & 0 \le \theta \le \pi/2 \\ \gamma_\mathrm{B}\,, & \pi/2 < \theta \le \pi\,, \end{cases} \tag{5.4}$$

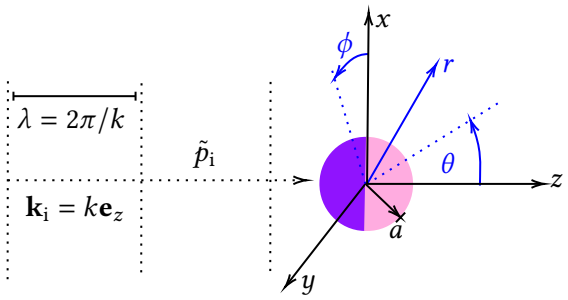

Figure 5.1: Spherical scatterer consisting of two hemispheres of varying compressibilities. The incident wave is oriented in the z direction. The integration for the polarizability are performed in spherical coordinates (r, θ, ϕ).

where "T" and "B" denote "top" and "bottom," respectively. Evaluation of Eqs. (2.27) and (2.29) yield

$$\alpha_\mathrm{m} = \tfrac{2}{3}\pi a^3(\gamma_\mathrm{T} + \gamma_\mathrm{B})\,, \tag{5.5}$$

$$\boldsymbol{\alpha}_\mathrm{c} = \tfrac{1}{4}\pi k a^4(\gamma_\mathrm{T} - \gamma_\mathrm{B})\mathbf{e}_z\,. \tag{5.6}$$

In terms of the Eqs. (5.5) and (5.6), the normalized scattered directivity is

$$\frac{\Phi(\theta)}{a} = \tfrac{1}{48}(ka)^2\left[8(\gamma_\mathrm{T} + \gamma_\mathrm{B}) + 3ika(\gamma_\mathrm{T} - \gamma_\mathrm{B})(1 - \cos\theta)\right]. \tag{5.7}$$

In the limiting case that γ_T equals γ_B, the coupled polarizability $\boldsymbol{\alpha}_\mathrm{c}$ vanishes, leading to an omnidirectional directivity given by the first term of Eq. (5.7). In the case that $\gamma_\mathrm{T} = -\gamma_\mathrm{B}$ the monopole polarizability α_m vanishes, leading to a cardioid directivity given by the second term of Eq. (5.7).

To study scatterers in motion, it is necessary to return from Eq. (2.2) to the inhomogeneous wave equation given by Eq. (C.28) for $\gamma_\rho = 0$ [122, Eq. (8.1.11)]:

$$\nabla^2 p - \frac{1}{c_0^2}\frac{\partial^2 p}{\partial t^2} = \frac{\gamma_\beta(\mathbf{r}, t)}{c_0^2}\frac{\partial^2 p}{\partial t^2}\,. \tag{5.8}$$

For example, assume that the asymmetric scatterer introduced above spins about the y axis with angular frequency $\nu\omega$, where ω is the angular frequency of the acoustic wave and ν is a real number. Positive values of ν correspond to rotation about the $+y$ axis, while negative values correspond to rotation about the $-y$ axis. Integer values of ν correspond

to rotations that are in phase with the acoustic wave. To describe the spinning motion, consider the material properties given by

$$\gamma_\beta = \begin{cases} \gamma_\mathrm{T}\,, & 0 \leq \nu\theta - \omega t \leq \pi/2 \\ \gamma_\mathrm{B}\,, & \pi/2 < \nu\theta - \omega t \leq \pi\,. \end{cases} \tag{5.9}$$

Although Eq. (5.8) is admittedly challenging to solve for the conditions given by Eq. (5.9), the physical implications of the anticipated scattered field are interesting: a time-harmonic rotating object is expected to generate a field that carries acoustic orbital angular momentum, like the fields described in Chap. 4. Rotating asymmetric scatterers may therefore offer a new way to generate acoustic vortex fields.

Waves on a string

The theory presented in Chap. 2 has been reduced to one dimension by considering waves on a string. The advantage of studying waves on a string is the reduction of vector- and tensor-valued quantities [Eqs. (B.42) and (B.43)] to scalars [Eqs. (B.78) and (B.82)]. While calculating acoustic radiation force involves evaluating the surface integral given by Eq. (B.47), calculating radiation force exerted by waves on a string amounts to taking the difference given by Eq. (B.84). Calculations of radiation forces exerted by progressive waves on a string on Born scatterers were presented at the 189th Meeting of the Acoustical Society of America in Honolulu, HI [284]. Future calculations may consider the radiation force exerted by standing waves in the Born approximation. Measurements of radiation forces exerted by progressive and standing waves on a string may also be pursued in the future.

Surface gravity waves

Radiation force can be studied in two dimensions by considering surface gravity waves. The advantage of the two-dimensional scenario is the simplification of both the scattering problem and calculation of the radiation force. The line integral given by Eq. (B.73) maybe used in the future to calculate radiation forces exerted by surface gravity waves in the infinite-frequency limit discussed below.

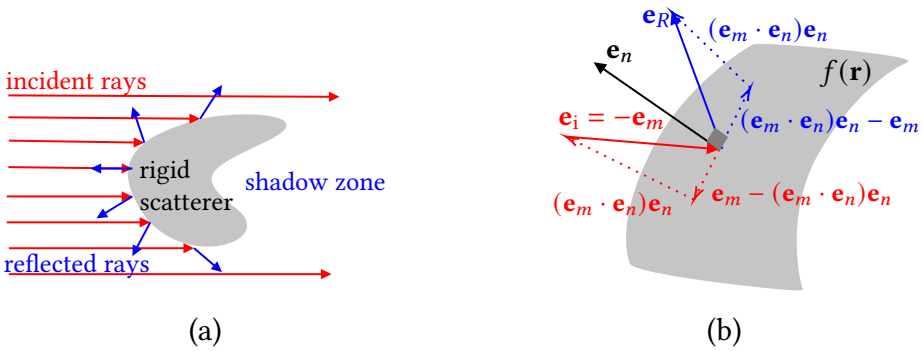

Figure 5.2: (a) Incident, reflected, and shadow fields. (b) Reflection of incident ray $\mathbf{e}_\mathrm{i}$ from rigid surface $f(\mathbf{r})$, where $\mathbf{e}_n = \boldsymbol{\nabla} f / |\boldsymbol{\nabla} f|$ and the reflected unit vector is $\mathbf{e}_R = \mathbf{e}_\mathrm{i} - 2(\mathbf{e}_\mathrm{i} \cdot \mathbf{e}_n)\mathbf{e}_n$.

Infinite-frequency limit

While Chap. 2 provides the low-ka asymptote of radiation force exerted by plane progressive waves, the asymptote $ka \to \infty$ may be pursued in the future. Figures 2.5–2.7 show that as ka becomes large, the radiation force converges to a constant as the effects of diffraction are suppressed. The infinite-frequency asymptote for a rigid sphere is given by Eq. (2.43), but analogous expressions for inhomogeneous and/or asymmetric objects remain unavailable. Although the limit $ka \gg 1$ has been considered previously [110, 184, 185, 285, 286], the limit $ka \to \infty$ has not been used to calculate radiation force. In fact, Westervelt's integral cannot be used in the infinite-frequency limit because the surface integral requires that the scattered intensity be proportional to r^{-2}. Scattered intensities in the infinite-frequency limit obey no such inverse square law, as illustrated by the fact that a perfectly reflecting or absorbing scatterer casts a shadow behind itself equal to the negative of the incident wave and proportional to r^0. An analog of Westervelt's far-field integral must therefore be derived for waves at infinite frequencies.

Following the development of the theory, pulling forces [162, 282] and radiation torques [73, 155] could be investigated. Reducing the three-dimensional acoustical theory to two dimensions describes radiation forces exerted by progressive surface gravity waves, as discussed above. One benefit of the two-dimensional problem in the limit $ka \to \infty$ is the simplified geometry of the scattering problem, which is confined to a plane.

5.2 Electromomentum coupling

In Chap. 3, a piezoelectric matamaterial giving rise to electromomentum coupling was studied at the micro-, meso-, and macroscale, and the bounds on the constitutive parameters of media that couple elastodynamics and electrodynamics were derived. The fields scattered by a one-dimensional lattice of asymmetric piezoelectric heterogeneities were calculated, leading to fully coupled acousto-electromagnetic constitutive relations. To demonstrate that the homogenization theory satisfied constraints on constitutive relations due to reciprocity and passivity, the analyses of Refs. 69, 70 and 221 were generalized to Eqs. (3.7) and (3.8) to include the magnetic field. The results of Refs. 12, 13, 69, 70, 218, 219 and 123 were recovered in limiting cases. The homogenization theory explained the microscale origins of electro- and magnetomomentum coupling in terms of multiple scattering, revealing two novel couplings between the acoustic and electromagnetic constitutive relations. The additional couplings to the magnetic field may guide the design of multiphysics metamaterials.

Future areas of research include the implementation of electromomentum-coupled behavior in FEM schemes [287] and the experimental demonstration of electromomentum coupling [61].

5.3 Vortex beams

In Chap. 4, the axisymmetry of sound beams was broken by considering a vortex phase dependence. An alternative diffraction integral over a single coordinate was derived to describe a vortex beam radiated by a circular piston. The diffraction integral was shown to be equivalent to the Rayleigh integral and was interpreted as an infinite sum of Bessel beams. The desire to obtain closed-form expressions for vortex beams motivated the introduction of the paraxial approximation, which holds for sufficiently large ka. Solutions of the paraxial equation were developed for vortex beams radiated by sources with circular and Gaussian amplitude shadings. The solutions were used to calculate the vortex ring radius. It was observed that the vortex ring radius of focused beams corresponded

to the global maximum of the field for low orbital numbers, but that the global maximum shifted out of the focal plane and towards the source as the orbital number increased. The geometrical acoustics limit $ka \to \infty$ was used to show that this behavior was due to spheroidal caustics that form in the prefocal region of focused vortex beams.

While vortex beams have found application in biological media [84], air [92], and the ocean [91], several aspects of vortex beam theory remain unsolved. Listed below are a few potential research directions.

Rectangular piston

A circular piston was used in Sec. 4.2 to obtain an alternative form of the Rayleigh integral. Similar derivations can be performed for sources of different shapes and/or phase dependencies. For example, consider a baffled rectangular piston of width w and height h described in the source plane $z = 0$ by

$$\tilde{v}_z(x, y, 0) = v_0 \operatorname{rect}(x/w) \operatorname{rect}(y/h)\,, \tag{5.10}$$

where $\operatorname{rect}(t) = 1$ for $|t| \leq 1/2$ and 0 for $|t| > 1/2$. Suppose the piston is placed within a pressure-release waveguide with a square cross section of side length b. The solution of the wave equation could be derived by setting Eq. (5.10) equal to zero at $x = y = b$ and equal to the general solution of the Helmholtz equation in Cartesian coordinates [9, Eq. (12.B-10)] at $z = 0$. The limit of the resulting expression as b tends to infinity would recover the field radiated by a baffled rectangular piston in free space. It may then be possible to reduce the resulting expression to the form of Eq. (4.2) in Cartesian coordinates.

Radiation pressure on a fluid interface

As discussed in App. B, acoustic waves exert a time-averaged force on scatterers due to momentum conservation at quadratic order. The radiation force on an arbitrary scatterer in any incident wave field is given by Eq. (B.88). Chapter 2 provides examples of forces exerted on objects much smaller than a wavelength. In contrast, a very large scatterer

can be approximated locally as an infinite planar interface, similar to those encountered in Chap. 3 of Ref. 9. For normal incidence, the surface integral for the radiation force given by Eq. (B.88) reduces to the difference between the time-averaged radiation stress ahead of and behind the interface, times the area of the interface. The radiation force divided by the area of the interface is the *radiation pressure* on the interface.

Wang and Lee consider the radiation pressure exerted by a sound beam on a fluid interface by considering Bessel beams of order zero [288, Sec. 6.2.2.3]. The analysis of Wang and Lee may be generalized in two ways. First, Eq. (4.24) for $\ell = 0$ may be used to calculate the radiation pressure exerted by a circular piston on an interface. Such a configuration is encountered in a *crystal fountain*, in which an ultrasonic transducer (typically composed of a piezoelectric crystal) is placed in shallow water and pointed upwards at the air-water interface. Second, Wang and Lee's derivation can be generalized for $\ell > 0$. The orbital angular momentum carried by the vortex beam will presumably cause fluid vorticity at the interface between two viscous fluids.

Propagation in inhomogeneous media

The study of acoustic vortex beam propagation in inhomogeneous media is motivated by application of vortex beams for underwater communication [91, 289, 290]. The ray theory for vortex beam propagation in a homogeneous medium developed in Sec. 4.6 may be generalized to an inhomogeneous medium by considering a linear sound speed profile [22, Sec. 8.3.2]. In the inhomogeneous medium, Eq. (4.94) for $\mathbf{n}$ still determines the direction in which the rays are launched. However, the following development of the vector $\mathbf{R}$ must be modified to account for the fact that rays in a medium with a linear sound speed profile travel in circular trajectories.

Nonlinear acoustic vortex beams

While nonlinear acoustic vortex beams have been studied numerically [271, 291] and experimentally [105, 292], analytical solutions for the second harmonic remain challenging

to obtain due to mathematical complications introduced by the dependence of the field on the azimuthal angle ϕ.[1] Perturbation solutions based on Green's function solutions [6, 293] lead to difficulties for vortex beams, and nonlinear acoustic ray theory cannot be applied due to the presence of caustics in both unfocused and focused vortex beams. A more rudimentary approach is suggested below for future consideration.

The far field of a spherical wave with directivity D in a fluid of density ρ_0 and sound speed c_0 is represented by the real part of

$$p_1 = -\frac{i\rho_0 c_0 v_0}{kr} D(\theta, \phi) e^{-i\omega\tau}, \tag{5.11}$$

where v_0 is the velocity amplitude at $r = a$, θ and ϕ are the spherical polar and azimuthal coordinates, ω is angular frequency, $k = \omega/c_0$ is the wavenumber, and $\tau = t - (r-a)/c_0$ is retarded time. For $kr \gg 1$ and $|\boldsymbol{\nabla} D| \ll k$, the second harmonic associated with Eq. (5.11) is given by

$$p_2 = \frac{i\beta\rho_0 v_0^2 ka}{2} \frac{\ln(r/a)}{r/a} D^2(\theta, \phi) e^{-2i\omega\tau}. \tag{5.12}$$

The real part of Eq. (5.12) for $D = 1$ recovers Eq. (4.285) of Ref. 294, where the minus sign appearing in that equation corresponds to diverging waves [294, p. 136]. A result similar to Eq. (5.12) was originally obtained by Westervelt and Radue [295], although their equation appears to be a factor of 2 larger.[2] Equation (5.12) does not account for harmonic generation associated with the near field of the beam. Near field effects are discussed in the Fresnel approximation by Hamilton [6, Eq. (8.33)], who notes that the integral required to account for these effects must be calculated numerically.

It is convenient to introduce the normalized quantities

$$P_1 = p_1/\rho_0 c_0 v_0, \qquad K = ka \tag{5.13a}$$

[1] Since spherical coordinates are used below, the symbol θ (used in Chap. 4 for the azimuthal angle) is now used for the polar angle, as in Chap. 2.

[2] The linearized state equations $p_1 = \rho_1 c_0^2$ and $p_2 = \rho_2 c_0^2$ have been used to convert Westervelt's result (originally written in terms of perturbation densities ρ_1 and ρ_2) to acoustic pressures p_1 and p_2. Also note that $B/A = \rho_0 c_0^{-2} (\partial^2 P/\partial\rho^2)_0$ and $\beta = 1 + B/2A$ [6, Eqs. (2.6) and (2.16)].

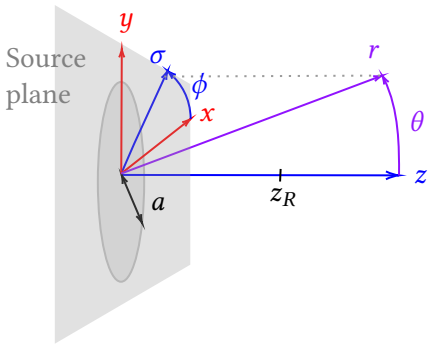

Figure 5.3: Cartesian coordinates (x, y, z), cylindrical coordinates (σ, ϕ, z), and spherical coordinates (r, θ, ϕ) shown with respect to the source plane $z = 0$, where a is the characteristic radius of the source and $z_R = ka^2/2$ is the Rayleigh distance. The vortex phase dependence considered is in the azimuthal angle ϕ.

and coordinates

$$S = \sigma/a\,, \qquad Z = z/z_R\,, \qquad R = r/a = \sqrt{\sigma^2 + z^2}/a = \sqrt{S^2 + (KZ/2)^2}, \tag{5.13b}$$

where $z_R = ka^2/2$, allowing the magnitude of Eq. (5.11) to be written as

$$P_1(S, Z) = \frac{|D|}{KR}\,. \tag{5.14}$$

To normalize Eq. (5.12), divide both sides by $\rho_0 c_0^2$, identify v_0/c_0 as the acoustic Mach number ϵ, denote $P_2 = p_2/\rho_0 c_0^2$, and note that $\beta = 2N/\epsilon K^2$, where $N = z_R/\bar{z}$ is the ratio of the diffraction length to the shock-formation distance $\bar{z} = 1/\beta\epsilon k$ [296]:

$$|P_2(S, Z)| = N\epsilon \frac{\ln R}{KR} |D|^2\,. \tag{5.15}$$

For example, consider a Gaussian velocity source of characteristic radius a with a vortex-phase dependence. In the source plane $z = 0$, the normal velocity field is given by the real part of

$$v_z(\sigma, \phi, t) = v_0 e^{-(\sigma/a)^2} e^{i(\ell\phi - \omega t)}, \tag{5.16}$$

where σ is cylindrical radial coordinate and ℓ is the orbital number. The cylindrical polar coordinate ϕ equals the spherical azimuthal coordinate, as shown in Fig. 5.3. In the

Fraunhofer approximation, the pressure field of the fundamental is given by the real part of

$$p_1 = -\frac{i\omega\rho_0}{2\pi}\frac{e^{i(kr-\omega t)}}{r}\int_0^{2\pi}\int_0^{\infty} v_z(\sigma_0,\phi_0)e^{-i\kappa\sigma_0\cos(\phi-\phi_0)}\sigma_0\,d\sigma_0\,d\phi_0\,, \tag{5.17}$$

where $\kappa = k\sin\theta$ is the component of the wavenumber in the x-y plane. Combining Eqs. (5.16) and (5.17) while recalling Eq. (4.49) yields

$$p_1 = -i\omega\rho_0\frac{e^{i(kr-\omega t)}}{r}v_0 e^{i\ell(\phi-\pi/2)}\int_0^{\infty} e^{-\sigma_0^2/a^2}J_\ell(\kappa\sigma_0)\,\sigma_0\,d\sigma_0\,. \tag{5.18}$$

Equation (5.18) reduces to Eq. (5.11), where the directivity is [256, Item 6.631-7]

$$D(\theta,\phi) = \tfrac{1}{8}\sqrt{\pi}(ka)^3\sin\theta e^{-\chi}\left[I_{(\ell-1)/2}(\chi) - I_{(\ell+1)/2}(\chi)\right]e^{i\ell(\phi-\pi/2)}\,, \quad \ell > -2\,, \tag{5.19}$$

and $\chi = \frac{1}{8}(ka\sin\theta)^2$. In terms of the normalized quantities introduced above, the magnitude of Eq. (5.19) is

$$|D| = \tfrac{1}{8}\sqrt{\pi}K^3\sin\theta e^{-\chi}\left|I_{(\ell-1)/2}(\chi) - I_{(\ell+1)/2}(\chi)\right|, \quad \chi = \tfrac{1}{8}(KS/R)^2\,. \tag{5.20}$$

In Fig. 5.4, Eqs. (5.14) and (5.15) in combination with Eq. (5.20) are compared to the fundamental and second harmonic predicted by the numerical solution of the Westervelt equation based on operator splitting [297] for $\ell = 1$. The parameters used in the plots are

$$ka = 180\,, \quad A = \alpha z_R = 0.01\,, \quad N = z_R/\bar{z} = 0.504, \quad \epsilon = 8.88\times10^{-6}\,, \tag{5.21}$$

which correspond to values used in recent experiments performed by R. P. Williams [298].

Consider as another example a circular piston of radius a with vortex-phase dependence, described in the source plane $z = 0$ by the real part of

$$v_z(\sigma,\phi,t) = v_0\,\mathrm{circ}(\sigma/a)e^{i(\ell\phi-\omega t)}. \tag{5.22}$$

Combining Eqs. (5.17), (4.49), and (5.22) yields

$$p_1 = -i\omega\rho_0\frac{e^{i(kr-\omega t)}}{r}v_0 e^{i\ell(\phi-\pi/2)}\int_0^{a} J_\ell(\kappa\sigma_0)\,\sigma_0\,d\sigma_0\,. \tag{5.23}$$

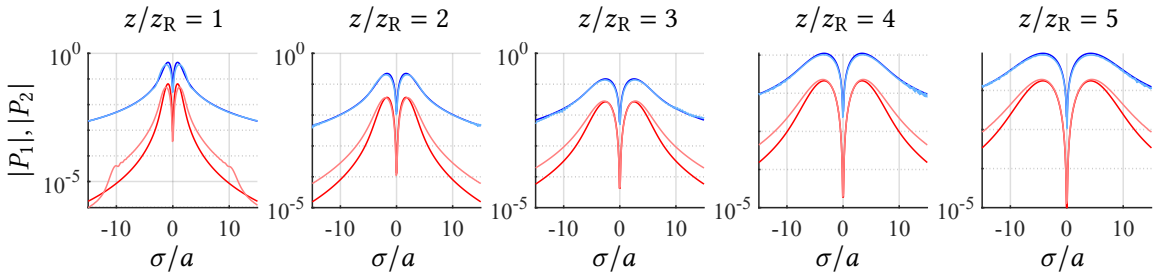

Figure 5.4: Comparison of the magnitude of the second harmonic given by Eq. (5.15) in combination with Eq. (5.19) (dark red curve) with the numerical solution based on operator splitting (light red curve) for $\ell = 1$ and $1 \leq z/z_R \leq 5$. The dark blue curve corresponds to the fundamental given by Eq. (5.14) in combination with Eq. (5.19), while the light blue curve is the fundamental predicted by the numerical solution. The solution for the second harmonic converges to the numerical solution of the Westervelt equation for $\ln(z/z_R) \gg 1$.

Evaluating the integral yields yields for $\ell > -2$

$$p_1 = -ik\rho_0 c_0 v_0 \frac{e^{i(kr-\omega t)}}{r} \kappa^{-2} e^{i\ell(\phi-\pi/2)} F_\ell(\kappa a)\,, \tag{5.24}$$

where the function F_ℓ is given by Eq. (4.7). Replacing κ with $k \sin\theta$, rearranging terms, and invoking Eq. (5.11) yields the directivity

$$D(\theta,\phi) = \frac{F_\ell(ka\sin\theta)}{\sin^2\theta} e^{i\ell(\phi-\pi/2)}\,, \quad \ell > -2\,. \tag{5.25}$$

For $\ell = 0$, $F_0(ka\sin\theta) = ka\sin(\theta) J_1(ka\sin\theta)$ from Eq. (4.8), and Eq. (5.25) combined with Eq. (5.11) recovers the familiar expression for the far-field pressure radiated by a baffled circular piston [9, Chap. 13, Eq. (B-2)],

$$p_1(r,\theta,\phi) = -\frac{i\rho_0 c_0 v_0 ka}{r/a} \frac{J_1(ka\sin\theta)}{ka\sin\theta} e^{i(kr-\omega t)}\,. \tag{5.26}$$

In terms of the normalized quantities introduced by Eqs. (5.13), the magnitude of Eq. (5.25) becomes

$$|D| = \frac{|F_\ell(KS/R)|}{S^2/R^2}. \tag{5.27}$$

In Fig. 5.5, Eqs. (5.14) and (5.15) in combination with Eq. (5.27) are compared to the fundamental and second harmonic predicted by the numerical solution of the Westervelt

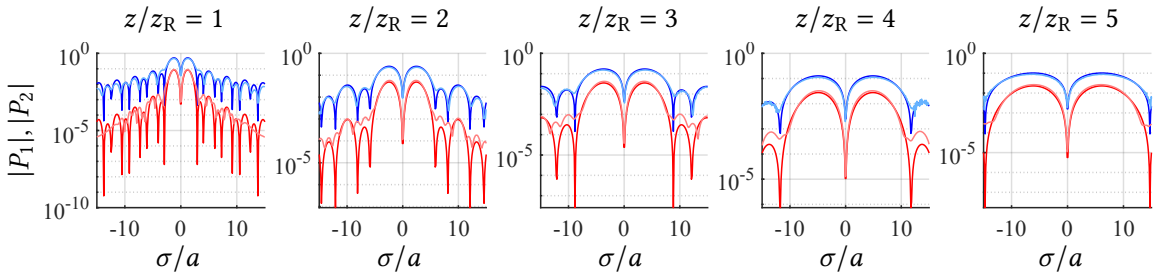

Figure 5.5: Comparison of the magnitude of the second harmonic given by Eq. (5.15) for D given by Eq. (5.25) (dark red curve) with the numerical solution based on operator splitting (light red curve) for $\ell = 1$ and $1 \leq z/z_R \leq 5$. The dark blue curve corresponds to the fundamental given by Eq. (5.14), while the light blue curve is the fundamental predicted by the numerical solution.

equation for $\ell = 1$. The parameters used are the same as those in Fig. 5.4. A similar comparison for $\ell = 2$ was performed and revealed similar agreement between the numerical and analytical solutions.

Figures 5.4 and 5.5 show that Eq. (5.12) accurately predicts the amplitudes and radii of the second harmonic vortex rings. The agreement between the analytical and numerical solutions improves for $\ln(z/z_R) \gg 1$, consistent with the far-field assumption underlying Eq. (5.11). In the future, the far fields of second harmonics generated by vortex beams may be measured experimentally and compared with Eq. (5.12). While Eq. (5.12) does not account for near-field effects [6, Eq. (8.33)], such effects may also be considered in the future.

Appendix A: Additional perspectives on ka

The limits $ka \to 0$, $ka \gg 1$, and $ka \to \infty$ of the Helmholtz equation [9, Chap. 1, Eq. (E-4)]

$$\nabla^2 \tilde{p} + k^2 \tilde{p} = 0 \tag{A.1}$$

are derived in Sec. A.1. Equation (A.1) follows from the linear acoustic wave equation [22, Eq. (1.6.1)]

$$\nabla^2 p - \frac{1}{c_0^2} \frac{\partial^2 p}{\partial t^2} = 0 \tag{A.2}$$

by assuming the time-harmonic solution

$$p(\mathbf{r}, t) = \mathrm{Re}[\tilde{p}(\mathbf{r}) e^{-i\omega t}] \,, \tag{A.3}$$

where c_0 is the speed of sound, ω is the angular frequency, t is time, and $k = \omega / c_0$ is the wavenumber. A conceptual representation of Fig. 1.1 is offered in Sec. A.2.

A.1 Limits of the Helmholtz equation

Laplace equation

Letting $k = 0$ in Eq. (A.1) immediately yields the Laplace equation,

$$\nabla^2 p = 0 \,. \tag{A.4}$$

Setting $k = 0$ is equivalent to setting $\omega = k c_0 = 0$, so $\tilde{p}$ introduced in Eq. (A.3) can be interchanged with p in Eq. (A.4). Setting $c_0 = \infty$ for a finite value of k in Eq. (A.2) also yields Eq. (A.4).

The Laplace equation appears more frequently in fluid mechanics in terms of the velocity potential ϕ, which is related to the fluid velocity $\mathbf{v}$ by [9, Chap. 1, Eq. (D-5)]

$$\mathbf{v} = \boldsymbol{\nabla} \phi \,. \tag{A.5}$$

Equation (A.5) restricts the fluid to irrotational motion, for which

$$\boldsymbol{\nabla} \times \mathbf{v} = \mathbf{0}\,. \tag{A.6}$$

Equation (A.6) is consistent with the assumptions leading to Eq. (A.2). The Laplace equation can be obtained in terms of ϕ by noting from the linearized state equation [9, Chap. 1, Eq. (C-56)]

$$\rho' = p/c_0^2 \tag{A.7}$$

that $\rho' \to 0$ as $c_0 \to \infty$. The linearized continuity equation [9, Chap. 1, Eq. (D-3)]

$$\frac{\partial \rho'}{\partial t} + \rho_0 \boldsymbol{\nabla} \cdot \mathbf{v} = 0 \tag{A.8}$$

therefore reduces to

$$\boldsymbol{\nabla} \cdot \mathbf{v} = 0\,, \tag{A.9}$$

where ρ' is the acoustic density and ρ_0 is the ambient density. Equation (A.9) in combination with Eq. (A.5) yields the Laplace equation in terms of ϕ:

$$\nabla^2 \phi = 0\,. \tag{A.10}$$

Equation (A.10) derived from the linearized state and continuity equations describes linearized incompressible flow in a homogeneous and incompressible fluid.

The relationship between Eq. (A.10) and nonlinear incompressible flow is elucidated by beginning with the exact momentum equation for a nonviscous fluid [9, Chap. 2, Eq. (A-47)],

$$\frac{\partial \mathbf{v}}{\partial t} + (\boldsymbol{\nabla}\mathbf{v})^{\mathrm{T}} \cdot \mathbf{v} + \frac{\boldsymbol{\nabla} P}{\rho} = \mathbf{0}\,, \tag{A.11}$$

where the transpose operation is defined by Eq. (D.3), and ρ and P are the fluid density and pressure, respectively. The assumption that the fluid is both homogeneous and incompressible implies that ρ is a constant in space and time, i.e., $\boldsymbol{\nabla}\rho$ and $\partial\rho/\partial t$ vanish

independently. The second term on the left-hand side of Eq. (A.11) can be recast by recalling the identity [230, p. 35, Item (iv)]

$$\boldsymbol{\nabla}(\mathbf{u}\cdot\mathbf{w}) = (\boldsymbol{\nabla}\mathbf{u})^{\mathrm{T}}\cdot\mathbf{w} + (\boldsymbol{\nabla}\mathbf{w})^{\mathrm{T}}\cdot\mathbf{u}\,,$$

which for $\mathbf{u} = \mathbf{w} = \mathbf{v}$ reduces to

$$\boldsymbol{\nabla}(v^2) = 2(\boldsymbol{\nabla}\mathbf{v})^{\mathrm{T}}\cdot\mathbf{v}\,, \tag{A.12}$$

where $v^2 = \mathbf{v}\cdot\mathbf{v}$. Equation (A.6) implies that $(\boldsymbol{\nabla}\mathbf{v})^{\mathrm{T}} = \boldsymbol{\nabla}\mathbf{v}$, and Eq. (A.12) therefore yields

$$(\boldsymbol{\nabla}\mathbf{v})\cdot\mathbf{v} = \tfrac{1}{2}\boldsymbol{\nabla}(v^2)\,. \tag{A.13}$$

Equation (A.11) can be expressed in terms of Eqs. (A.5) and (A.13) as

$$\boldsymbol{\nabla}\left(\frac{\partial\phi}{\partial t} + \tfrac{1}{2}|\boldsymbol{\nabla}\phi|^2 + \frac{P}{\rho}\right) = \mathbf{0}\,. \tag{A.14}$$

Integrating Eq. (A.14) over space yields the Bernoulli equation

$$\frac{\partial\phi}{\partial t} + \tfrac{1}{2}|\boldsymbol{\nabla}\phi|^2 + \frac{P}{\rho} = f(t)\,, \tag{A.15}$$

where $f(t)$ is an integration constant that depends on time. Neglecting the quadratic term in Eq. (A.15) and taking the Laplacian of both sides yields

$$\frac{\partial}{\partial t}\nabla^2\phi + \frac{1}{\rho}\nabla^2 P = 0\,, \tag{A.16}$$

where it has been noted that neither ρ nor f depends on space. The condition $\nabla^2\phi$ for incompressible flow in an irrotational and nonviscous medium [299, Eq. (10.6)] therefore implies in the linear approximation ($|\nabla\phi|^2 \ll |\partial\phi/\partial t| \sim P/\rho$) that

$$\nabla^2 P = 0\,. \tag{A.17}$$

Equation (A.17) is equivalent to Eq. (A.4) because $P = P_0 + p$, where P_0 is the constant ambient pressure, i.e., $\nabla^2 P_0 = 0$. The incompressible limit of the linear acoustic wave equation is therefore recovered by linearizing the exact theory of incompressible flow for a nonviscous fluid.

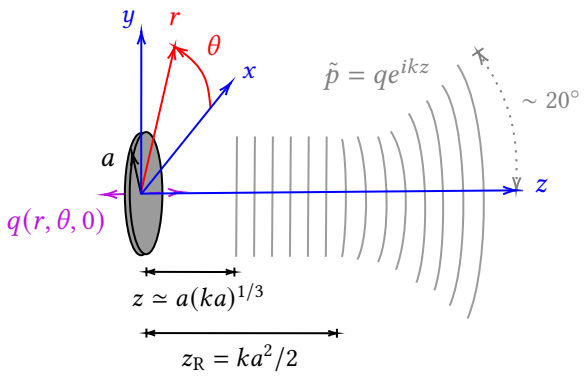

Figure A.1: Quasiplanar waves represented by $\tilde{p} = qe^{ikz}$ radiating from a source of radius a. The paraxial approximation is generally valid for $ka \gg 1$ [from Eq. (A.23)] and $z \gtrsim a(ka)^{1/3}$ [from Eq. (E.25)], although the vortex motion and focusing discussed in Chap. 4 place additional conditions on the validity of the approximation (see Sec. 4.5). The Rayleigh distance $z_R = ka^2/2$ is the distance from the source at which the intensity transitions from r^0 to r^{-2} spreading.

Solutions of Eq. (A.4) for the interior of a rigid spheroid [164] are used in Sec. 5.1 to calculate components of radiation forces exerted by plane progressive waves. The relevance of Eq. (A.4) to acoustics is discussed in greater detail by Ginsberg [7, pp. 337–338, 492–494]. Examples of other physical systems governed by the Laplace equation are provided by Feynman [163, Vol. II, Chap. 12].

Paraxial equation

For $ka \gg 1$, Eq. (A.1) is approximated by the evolution equation for the paraxial field. The paraxial equation is derived in Cartesian coordinates by inserting the solution

$$\tilde{p}(x, y, z) = q(x, y, z)e^{ikz} \tag{A.18}$$

into Eq. (A.1), where Eq. (A.18) describes a wave traveling primarily in the z direction, as depicted in Fig. A.1. The relevant second partial derivatives of Eq. (A.18) equal

$$\tilde{p}_{xx} = q_{xx}e^{ikz}, \tag{A.19}$$

$$\tilde{p}_{yy} = q_{yy}e^{ikz}, \tag{A.20}$$

$$\tilde{p}_{zz} = (q_{zz} + ikq_z)e^{ikz} + ik(q_z + ikq)e^{ikz} = (q_{zz} + i2kq_z - k^2q)e^{ikz}, \tag{A.21}$$

where the subscripts indicate partial differentiation with respect to the subscripted variable. In terms of Eqs. (A.19)–(A.21), Eq. (A.1) divided by the common factor e^{ikz} equals

$$q_{xx} + q_{yy} + q_{zz} + i2kq_z = 0\,. \tag{A.22}$$

The ratio of the magnitudes of the third and fourth terms in Eq. (A.22) is on the order of

$$\frac{|q_{zz}|}{2k|iq_z|} \sim \frac{|q|/z_\mathrm{R}^2}{k|q|/z_\mathrm{R}} \sim \frac{1}{kz_\mathrm{R}} \sim \frac{1}{(ka)^2}\,, \tag{A.23}$$

where $z_\mathrm{R} = ka^2/2$ is the Rayleigh distance. In the first similarity of Eq. (A.23), $|q_z|$ is approximated as $|q|/z_\mathrm{R}$ because the Rayleigh distance is the nominal distance over which q varies, as shown in Fig. A.1. Equation (A.23) shows that $|q_{zz}| \ll 2k|q_z|$ for

$$ka \gg 1\,. \tag{A.24}$$

If Eq. (A.24) is satisfied, Eq. (A.22) is therefore well approximated by

$$i2k\frac{\partial q}{\partial z} + \nabla_\perp^2 q = 0\,, \tag{A.25}$$

where the symbol $\nabla_\perp^2$ is the Laplacian in the plane perpendicular to the z axis [300, Eq. (3.6-10)]. In the study of diffraction, the transverse Laplacian is most frequently evaluated in Cartesian and cylindrical coordinates [301, Chap. 10, Sec. 9]:

$$\begin{aligned} \nabla_\perp^2 f &= \frac{\partial^2 f}{\partial x^2} + \frac{\partial^2 f}{\partial y^2} && \text{(Cartesian)} \\ &= \frac{1}{r}\frac{\partial}{\partial r}\left(r\frac{\partial f}{\partial r}\right) + \frac{1}{r^2}\frac{\partial^2 f}{\partial \theta^2}\,. && \text{(cylindrical)} \end{aligned}$$

The paraxial equation is used in Sec. 4.3 to study vortex beam diffraction for $ka \gg 1$.

Eikonal and transport equations

The partial differential equations governing geometrical acoustics in a homogeneous medium are obtained by taking the infinite-frequency limit of Eq. (A.1).[1] The solution of Eq. (A.1) is

[1] The following discussion details the procedure outlined in Sec. 8.5 of Ref. 22. The approach is attributed to Sommerfeld and Runge [302].

expressed as a product of an amplitude function P and a phase dependence $e^{i\omega\tau(\mathbf{r})}$, where τ defines a wavefront and $\boldsymbol{\nabla}\tau$ defines the direction of wave propagation [22, pp. 429]:

$$\tilde{p}(\mathbf{r}) = P(\mathbf{r},\omega)e^{i\omega\tau(\mathbf{r})}\,. \tag{A.26}$$

Inserting Eq. (A.26) into Eq. (A.1), writing $\nabla^2 = \boldsymbol{\nabla}\cdot\boldsymbol{\nabla}$, and evaluating the gradient yields

$$\boldsymbol{\nabla}\cdot[e^{i\omega\tau(\mathbf{r})}\boldsymbol{\nabla}P(\mathbf{r},\omega) + i\omega P(\mathbf{r},\omega)e^{i\omega\tau(\mathbf{r})}\boldsymbol{\nabla}\tau(\mathbf{r})] + k^2P(\mathbf{r},\omega)e^{i\omega\tau(\mathbf{r})} = 0\,. \tag{A.27}$$

Evaluating the divergence in Eq. (A.27) yields

$$\begin{aligned} &i\omega e^{i\omega\tau(\mathbf{r})}\boldsymbol{\nabla}\tau(\mathbf{r})\cdot\boldsymbol{\nabla}P(\mathbf{r},\omega) + e^{i\omega\tau(\mathbf{r})}\nabla^2P(\mathbf{r},\omega) + i\omega\boldsymbol{\nabla}[P(\mathbf{r},\omega)e^{i\omega\tau(\mathbf{r})}]\cdot\boldsymbol{\nabla}\tau(\mathbf{r}) \\ &\quad + i\omega P(\mathbf{r},\omega)e^{i\omega\tau(\mathbf{r})}\nabla^2\tau(\mathbf{r}) + k^2P(\mathbf{r},\omega)e^{i\omega\tau(\mathbf{r})} = 0\,, \end{aligned} \tag{A.28}$$

where the vector calculus identity

$$\boldsymbol{\nabla}\cdot[f(\mathbf{r})\boldsymbol{\nabla}g(\mathbf{r})] = \boldsymbol{\nabla}f(\mathbf{r})\cdot\boldsymbol{\nabla}g(\mathbf{r}) + f(\mathbf{r})\nabla^2g(\mathbf{r}) \tag{A.29}$$

has been used. Evaluating the gradient of the quantity in square brackets in Eq. (A.28) yields

$$\begin{aligned} &i\omega\boldsymbol{\nabla}\tau(\mathbf{r})\cdot\boldsymbol{\nabla}P(\mathbf{r},\omega) + \nabla^2P(\mathbf{r},\omega) + i\omega\boldsymbol{\nabla}P(\mathbf{r},\omega)\cdot\boldsymbol{\nabla}\tau(\mathbf{r}) \\ &\quad - \omega^2P(\mathbf{r},\omega)\boldsymbol{\nabla}\tau(\mathbf{r})\cdot\boldsymbol{\nabla}\tau(\mathbf{r}) + i\omega P(\mathbf{r},\omega)\nabla^2\tau(\mathbf{r}) + k^2P(\mathbf{r},\omega) = 0\,. \end{aligned} \tag{A.30}$$

Grouping common terms, writing $k = \omega/c_0$, and suppressing the functional dependencies yields [22, Eq. (8.5.1)]

$$\nabla^2P + i\omega(2\boldsymbol{\nabla}P\cdot\boldsymbol{\nabla}\tau + P\nabla^2\tau) - \omega^2P(|\boldsymbol{\nabla}\tau|^2 - c_0^{-2}) = 0\,. \tag{A.31}$$

Substituting the expansion $P(\mathbf{r},\omega) = P_0(\mathbf{r}) + \omega^{-1}P_1(\mathbf{r}) + \omega^{-2}P_2(\mathbf{r}) + \ldots$ into Eq. (A.31) yields

$$\begin{aligned} &\nabla^2[P_0(\mathbf{r}) + \omega^{-1}P_1(\mathbf{r}) + \omega^{-2}P_2(\mathbf{r}) + \ldots] \\ &\quad + i2\boldsymbol{\nabla}[\omega P_0(\mathbf{r}) + P_1(\mathbf{r}) + \omega^{-1}P_2(\mathbf{r}) + \ldots]\cdot\boldsymbol{\nabla}\tau \\ &\quad + i[\omega P_0(\mathbf{r}) + P_1(\mathbf{r}) + \omega^{-1}P_2(\mathbf{r}) + \ldots]\nabla^2\tau \\ &\quad - [\omega^2P_0(\mathbf{r}) + \omega P_1(\mathbf{r}) + P_2(\mathbf{r}) + \ldots](|\boldsymbol{\nabla}\tau|^2 - c_0^{-2}) = 0\,. \end{aligned} \tag{A.32}$$

If ω is very large, the terms of order ω^{-1}, ω^{-2}, and higher in Eq. (A.32) are very small, and

$$\omega P_0 \gg P_1\,, \qquad \omega^2 P_0 \gg \omega P_1 \gg P_2\,.$$

For large ω, Eq. (A.32) therefore equals

$$\nabla^2 P_0 + i\omega(2\boldsymbol{\nabla} P_0 \cdot \boldsymbol{\nabla}\tau + P_0\nabla^2\tau) - \omega^2 P_0(|\boldsymbol{\nabla}\tau|^2 - c_0^{-2}) = 0\,. \tag{A.33}$$

In the limit $\omega \to \infty$, Eq. (A.33) separates into three independent equations,

$$\nabla^2 P(\mathbf{r}) = 0\,, \qquad O(\omega^0)\,, \tag{A.34}$$

$$2\boldsymbol{\nabla} P \cdot \boldsymbol{\nabla}\tau + P\nabla^2\tau = 0\,, \qquad O(\omega^1)\,, \tag{A.35}$$

$$P(|\boldsymbol{\nabla}\tau|^2 - c_0^{-2}) = 0\,, \qquad O(\omega^2)\,, \tag{A.36}$$

where P_0 has been taken to be "an adequate approximation for P" [22, p. 455]. Equation (A.34) recovers the Laplace equation given by Eq. (A.17) and is associated with the zero-frequency limit. The ω^1 and ω^2 equations, in contrast, describe wave propagation at infinite frequencies. The ω^2 equation [22, Eq. (8.5.3a)]

$$|\boldsymbol{\nabla}\tau|^2 = \frac{1}{c_0^2} \tag{A.37}$$

determines the trajectories of rays and is known as the *eikonal equation.* Next, multiplying Eq. (A.35) by P yields [22, Eq. (8.5.3b)]

$$2P\boldsymbol{\nabla} P \cdot \boldsymbol{\nabla}\tau + P^2\nabla^2\tau = 0\,. \tag{A.38}$$

Noting that $2P\boldsymbol{\nabla} P = \boldsymbol{\nabla}(P^2)$ and invoking Eq. (A.29) allows Eq. (A.38) to be expressed as

$$\boldsymbol{\nabla} \cdot (P^2\boldsymbol{\nabla}\tau) = 0\,. \tag{A.39}$$

Equation (A.39) can be understood in terms of a collection of locally parallel rays that form a ray tube, as depicted in Fig. 8.17 of Ref. 22 for rays in an inhomogeneous medium and in Fig. 4.13 for rays radiated by a focused vortex source in a homogeneous medium. Suppose that rays in the neighborhood of the position $\mathbf{r}_0$ pass through a cross-sectional area $A(\mathbf{r}_0)$

and travel to position $\mathbf{r}$, where they pass through a cross-sectional area $A(\mathbf{r})$. The areas $A(\mathbf{r}_0)$ and $A(\mathbf{r})$ define the ends of the ray tube, where the sides of the tube are parallel to the direction of the rays. Let V denote the volume enclosed by the ray tube and S denote the corresponding surface. Integration of Eq. (A.39) over V yields $\int_V \boldsymbol{\nabla} \cdot (P^2 \boldsymbol{\nabla}\tau)\, dV = 0$, and application of the divergence theorem yields

$$\oint_S (P^2 \boldsymbol{\nabla}\tau) \cdot \mathbf{n}\, dS = 0\,, \tag{A.40}$$

where $\mathbf{n}$ is the outward unit normal vector to the surface of the ray tube. Since the walls of the ray tube are parallel to the direction of the rays, the only contributions to the surface integral in Eq. (A.40) are the values of the integrand at the ends, resulting in

$$(P^2 \boldsymbol{\nabla}\tau \cdot \mathbf{n})\big|_{\mathbf{r}}\, A(\mathbf{r}) - (P^2 \boldsymbol{\nabla}\tau \cdot \mathbf{n})\big|_{\mathbf{r}_0}\, A(\mathbf{r}_0) = 0\,. \tag{A.41}$$

The assumption that the medium is homogeneous implies that $\boldsymbol{\nabla}\tau \cdot \mathbf{n} = 1/c_0$ at both positions $\mathbf{r}_0$ and $\mathbf{r}$. Thus Eq. (A.41) becomes $P^2(\mathbf{r})A(\mathbf{r}) = P^2(\mathbf{r}_0)A(\mathbf{r}_0)$, or

$$P(\mathbf{r}) = P(\mathbf{r}_0)\sqrt{\frac{A(\mathbf{r}_0)}{A(\mathbf{r})}}\,. \tag{A.42}$$

Equation (A.42) describes how the pressure amplitude varies along a ray tube in a homogeneous medium [22, Eqs. (8.5.4)]. It appears as Eq. (4.99) in the infinite-frequency approximation of vortex beams.

While the analysis above (and that of Chap. 4) is restricted to linear wave phenomena, geometrical acoustics can be used to calculate nonlinear acoustic fields [303]. Recent ray calculations of high-frequency focused ultrasonic fields [304] may be generalized in the future to account for a vortex-phase dependence of the form of Eqs. (4.92) and (4.93).[2]

A.2 Conceptual rendering of the frequency spectrum

A conceptual rendering of the frequency spectrum is presented in Figure A.2, which shows more clearly how the Helmholtz equation relates to its approximations. In the limit of in-

[2] A preliminary analysis (not based on ray theory) of the second harmonic generated in the far field of vortex beams is offered in Sec. 5.3.

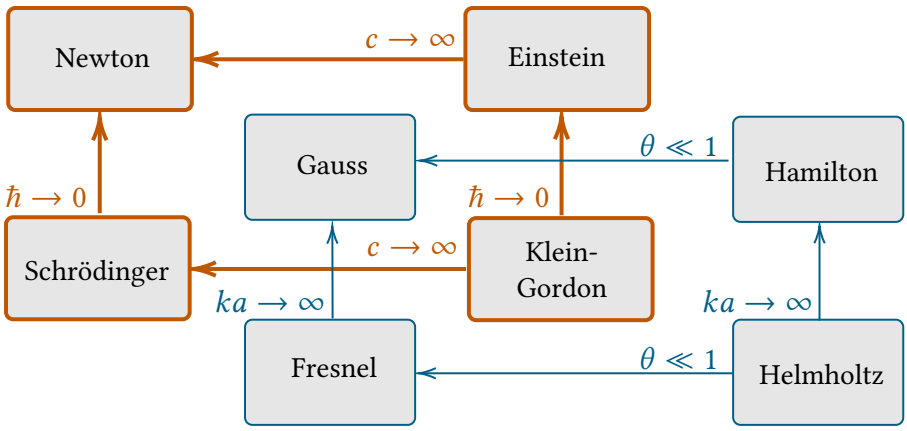

Figure A.2: Reduction of the Helmholtz equation to ray theory (associated with Hamilton), Gaussian optics, and the Fresnel approximation. The limits of the Helmholtz equation are analogous to the limits of the Klein-Gordon equation: Einstein's special relativity, Newtonian mechanics, and Schrödinger's nonrelativistic quantum mechanics [300, pp. 90–111].

finite frequency, the Helmholtz equation reduces to ray theory, which is associated with the pioneering work of W. R. Hamilton on geometrical optics [305]. For rays deviating from one another by small angles $\theta \ll 1$, ray theory reduces to Gaussian optics [300, Eq. (3.5-17)]. Meanwhile, the small-angle limit underlying the Fresnel approximation reduces the Helmholtz equation to the paraxial equation, the restriction for which is $ka \gg 1$ [22, p. 251].

Marcuse draws parallels between the three limits of the Helmholtz equation and the three limits of the Klein-Gordon equation of relativistic quantum mechanics [300, pp. 90–111], represented by the orange boxes in Fig. A.2. In the limit for which Planck's constant $\hbar$ vanishes, relativistic quantum mechanics recovers Einstein's special relativity. Special relativity in turn recovers Newtonian mechanics if the speed of light c is considered to be infinite. Meanwhile, the limit $c \to \infty$ of the Klein-Gordon equation recovers Schrödinger's non-relativistic quantum mechanics.

Figure A.2 suggests that ka and $\hbar$ serve similar roles: the limits $ka \to \infty$ and $\hbar \to 0$ reduce acoustic and quantum mechanical waves to rays and classical trajectories, respectively. Likewise, θ and c serve similar roles: the limits $\theta \ll 1$ and $c \to \infty$ reduce the Helmholtz and Klein-Gordon equations to the paraxial and Schrödinger equations by

confining the region of applicability to small angles in three-dimensional space and four-dimensional spacetime, respectively. The analogy between wave mechanics and particle dynamics is succinctly articulated by Gloge and Marcuse: “Maxwell’s theory can be considered as the quantum theory of a single photon and geometrical optics as the classical mechanics of this photon” [119].

The perspective offered by Fig. A.2 informs the study of acoustical phenomena by organizing the limits of wave mechanics in terms of their relation to the Helmholtz equation. If a phenomenon cannot be explained easily in terms of the Helmholtz equation, physical intuition and mathematical simplification may follow from considering its limits.

Appendix B: Notes on radiation force

The theory of acoustic radiation force is developed from first principles, synthesizing the perspectives of Westervelt [121, 177], Gor'kov [3], and Wang and Lee [288]. Kinetic and potential energy densities of fields predicted by linear acoustics are derived in Sec. B.1. The time-averaged conservation of momentum at quadratic order is derived in Sec. B.2 in terms of the acoustic radiation stress tensor. Diagonal elements of the matrix representation of this tensor are related to the mean excess pressure, which can be written in terms of energy densities. A simplified derivation of the Langevin radiation force is presented in Sec. B.3, and parallels are drawn to radiation forces exerted by electromagnetic waves, surface gravity waves, and waves on a string. Westervelt's far-field formulation for the radiation force is discussed in Sec. B.4. The integral for the radiation force in the far-field is simplified for incident progressive waves in Sec. B.5. For an alternative perspective on acoustic radiation force that parallels the quantum mechanical explanation of optical radiation force, see Ref. 306.

B.1 Energy densities

The exact acoustic potential and kinetic energy densities are

$$T = \tfrac{1}{2}\rho v^2\,, \tag{B.1}$$

$$U = -\frac{1}{V_0}\int_{V_0}^{V} p\,dV\,, \tag{B.2}$$

where $v^2 = \mathbf{v}\cdot\mathbf{v} = |\mathbf{v}|^2$ and $p = P - P_0$ is the difference between the total pressure P and ambient pressure P_0. Equation (B.1) follows from the definition of kinetic energy, and Eq. (B.2) is based on the thermodynamic definition of the compressional work done on a system [307, Eq. (1.29)]. In linear acoustics, the energy densities are quadratic in the wave variables p and $\mathbf{v}$. Equation (B.1) is reduced to quadratic order by introducing the perturbation density $\rho' = \rho - \rho_0$, where ρ_0 is the ambient density. Neglecting the cubic

term $\rho' v^2$ in Eq. (B.1) yields

$$T = \tfrac{1}{2}\rho_0 v^2 \,. \tag{B.3}$$

Reducing Eq. (B.2) to quadratic order is more challenging because dV is an inconvenient differential for the evaluation of the integral. To relate dV to the acoustic pressure p, first note that volume is related to density by $M = \rho V$, where M is mass. Writing $V = M/\rho$ allows for the calculation of the derivative

$$\frac{dV}{d\rho} = -\frac{M}{\rho^2} \,,$$

and solving for dV yields

$$dV = -\frac{M}{\rho^2}\, d\rho = -\frac{V}{\rho} d\rho \,, \tag{B.4}$$

where the fact that $M = \rho V$ has again been invoked to arrive at the second equality in Eq. (B.4). Since $d\rho = d(\rho_0 + \rho') = d\rho'$ and $V = V_0 + V'$, where V' is the perturbation volume, Eq. (B.4) becomes

$$dV = -(V_0 + V')(\rho_0 + \rho')^{-1} d\rho' \,, \tag{B.5}$$

where $1/\rho$ has been written as $(\rho_0 + \rho')^{-1}$. Since

$$(\rho_0 + \rho')^{-1} = \frac{(1 + \rho'/\rho_0)^{-1}}{\rho_0} \simeq \frac{1 - \rho'/\rho_0}{\rho_0} \,,$$

Eq. (B.5) becomes

$$\begin{aligned} dV &= -(V_0 + V')(1 - \rho'/\rho_0)\frac{d\rho'}{\rho_0} \\ &= -\frac{V_0}{\rho_0} d\rho' + \text{higher-order terms} \,. \end{aligned} \tag{B.6}$$

Inserting Eq. (B.6) in Eq. (B.2) and retaining only linear terms yields

$$U = \frac{1}{\rho_0} \int_0^{\rho'} p \, d\tilde{\rho}' \,, \tag{B.7}$$

where the integration variable is denoted $\tilde{\rho}'$ to maintain distinction from the upper limit of integration. Equation (B.7) is related to the acoustic pressure by appealing to the linearized equation of state given by Eq. (A.7). Equation (B.7) therefore becomes

$$U = \frac{1}{\rho_0 c_0^2} \int_0^{p} \tilde{p} \, d\tilde{p} = \frac{p^2}{2\rho_0 c_0^2} \,. \tag{B.8}$$

B.2 Traditional derivation of radiation force

A derivation of acoustic radiation force is provided in index notation by Wang and Lee [288, pp. 176–180]. The same result is obtained below symbolically, and intermediate steps are detailed. A momentum conservation theorem is derived in terms of the mean excess pressure, which is related to the energy densities derived in Sec. B.1. A simplified derivation of the Langevin radiation force is presented in Sec. B.3.

Conservation of momentum at quadratic order

Begin by considering the exact equation of conservation of momentum in the absence of viscosity [299, Eq. (2.3)]:

$$\rho \frac{\partial \mathbf{v}}{\partial t} + \rho \mathbf{v} \cdot \boldsymbol{\nabla} \mathbf{v} = -\boldsymbol{\nabla} P \,. \tag{B.9}$$

Meanwhile, the exact continuity equation is [299, Eq. (1.2)]

$$\frac{\partial \rho}{\partial t} + \boldsymbol{\nabla} \cdot (\rho \mathbf{v}) = 0 \,. \tag{B.10}$$

Adding Eqs. (B.9) to $\mathbf{v}$ times Eq. (B.10) yields

$$\rho \frac{\partial \mathbf{v}}{\partial t} + \mathbf{v} \frac{\partial \rho}{\partial t} + \rho \mathbf{v} \cdot \boldsymbol{\nabla} \mathbf{v} + \mathbf{v} \boldsymbol{\nabla} \cdot (\rho \mathbf{v}) = -\boldsymbol{\nabla} P \,.$$

Using the product rules $\rho \partial \mathbf{v}/\partial t + \mathbf{v} \partial \rho / \partial t = \partial(\rho \mathbf{v})/\partial t$ and $\rho \mathbf{v} \cdot \boldsymbol{\nabla} \mathbf{v} + \mathbf{v} \boldsymbol{\nabla} \cdot (\rho \mathbf{v}) = \boldsymbol{\nabla} \cdot (\rho \mathbf{v} \otimes \mathbf{v})$ yields[1]

$$\frac{\partial (\rho \mathbf{v})}{\partial t} + \boldsymbol{\nabla} \cdot (\rho \mathbf{v} \otimes \mathbf{v}) = -\boldsymbol{\nabla} P \,. \tag{B.11}$$

It is now assumed that ρ, $\mathbf{v}$, and P in Eq. (B.11) are time-harmonic. Taking the time average of Eq. (B.11) and noting that[2] $\langle \partial(\rho \mathbf{v})/\partial t \rangle = 0$ yields

$$-\langle \boldsymbol{\nabla} P + \boldsymbol{\nabla} \cdot \rho \mathbf{v} \otimes \mathbf{v} \rangle = \mathbf{0} \,. \tag{B.12}$$

[1] The second product rule follows from the identity $\boldsymbol{\nabla} \cdot (\mathbf{u} \otimes \mathbf{v}) = (\boldsymbol{\nabla} \mathbf{u}) \cdot \mathbf{v} + (\boldsymbol{\nabla} \cdot \mathbf{v}) \mathbf{u}$, where Eq. (D.1) defines the outer product.

[2] To show this, suppose $f(t) = \cos \omega t$ and $g(t) = \cos(\omega t + \phi)$, so $f(t) g(t) = [\cos(2\omega t + \phi) + \cos \phi]/2$. Thus $d[f(t)g(t)]/dt = -\omega \sin(2\omega t + \phi)$, the time average of which is zero.

Since

$$\underline{\mathbf{I}} \cdot \boldsymbol{\nabla} P = \boldsymbol{\nabla} \cdot (\underline{\mathbf{I}} P) - P \boldsymbol{\nabla} \cdot \underline{\mathbf{I}} ,$$

where $\underline{\mathbf{I}}$ is the identity tensor,[3] and since $\boldsymbol{\nabla} \cdot \underline{\mathbf{I}} = \mathbf{0}$, Eq. (B.12) becomes

$$\boldsymbol{\nabla} \cdot \langle -\underline{\mathbf{I}} P - \rho \mathbf{v} \otimes \mathbf{v} \rangle = \mathbf{0} , \tag{B.13}$$

where movement of the divergence outside the time average follows from the linearity of the time-average operation. Since P_0 is a constant, $\boldsymbol{\nabla} \cdot (\underline{\mathbf{I}} P)$ can be expressed as $\boldsymbol{\nabla} \cdot [\underline{\mathbf{I}} (P - P_0)]$. Retaining terms up to quadratic order in Eq. (B.13) therefore yields

$$\boldsymbol{\nabla} \cdot \langle -\underline{\mathbf{I}} (P - P_0) - \rho_0 \mathbf{v} \otimes \mathbf{v} \rangle = \mathbf{0} . \tag{B.14}$$

The quantity in the time average in Eq. (B.14) is identified as the *acoustic radiation stress tensor*:

$$\underline{\mathbf{S}} = -\underline{\mathbf{I}} (P - P_0) - \rho_0 \mathbf{v} \otimes \mathbf{v} . \tag{B.15}$$

In index notation, the components of Eq. (B.15) are[4]

$$S_{ij} = -\delta_{ij} (P - P_0) - \rho_0 v_i v_j , \tag{B.16}$$

where $\delta_{ij} = 1$ if $i = j$ and 0 if $i \neq j$. Equation (B.16) is reminiscent of the components of the Maxwell stress tensor of electrodynamics [8, Eq. (8.19)], an analogy that is made explicit in Sec. B.3. In terms of the acoustic radiation stress tensor, Eq. (B.14) becomes

$$\boldsymbol{\nabla} \cdot \langle \underline{\mathbf{S}} \rangle = \mathbf{0} . \tag{B.17}$$

Mean excess pressure

Attention is now turned to the *mean excess pressure* $\langle P - P_0 \rangle$ appearing in Eq. (B.15). Begin by expanding $P - P_0$ in w, the enthalpy per unit mass:

$$P - P_0 = \left(\frac{\partial P}{\partial w} \right)_{s,0} w + \frac{1}{2} \left(\frac{\partial^2 P}{\partial w^2} \right)_{s,0} w^2 + \dots . \tag{B.18}$$

[3] For a scalar ϕ and rank-2 tensor $\underline{\mathbf{T}}$, $\boldsymbol{\nabla} \cdot (\phi \underline{\mathbf{T}}) = \phi \, \boldsymbol{\nabla} \cdot \underline{\mathbf{T}} + \underline{\mathbf{T}} \cdot (\boldsymbol{\nabla} \phi)$.

[4] Wang and Lee identify the components of the acoustic radiation stress as the *time average* of Eq. (B.16) [288, Eq. (6.7)].

The differential enthalpy per unit mass is $dw = Tds + dP/\rho$, where T is temperature and s is entropy. For an isentropic process, $ds = 0$, so

$$dw = \frac{dP}{\rho}\,. \tag{B.19}$$

Rearrangement of Eq. (B.19) yields

$$\frac{dP}{dw} = \left(\frac{\partial P}{\partial w}\right)_{s,0} = \rho\,, \tag{B.20}$$

and Eq. (B.18) can therefore be expressed as

$$P - P_0 = \rho w + \frac{1}{2}\left(\frac{\partial \rho}{\partial w}\right)_{s,0} w^2 + \ldots\,. \tag{B.21}$$

Since

$$\frac{\partial \rho}{\partial w} = \frac{\partial \rho}{\partial P}\frac{\partial P}{\partial w} = \frac{1}{c^2}\frac{dP}{dw} = \frac{\rho}{c^2}\,,$$

where the last equality follows from Eq. (B.20), Eq. (B.21) becomes

$$P - P_0 = \rho_0 w + \frac{\rho_0}{2c_0^2} w^2 + \ldots\,. \tag{B.22}$$

While the excess pressure given by Eq. (B.15) can be written in terms of Eq. (B.22), the resulting expression in terms of w is inconvenient. To relate w and w^2 in Eq. (B.22) to more familiar acoustic variables, the gradient of minus Eq. (B.19) is taken, yielding

$$-\boldsymbol{\nabla} w = -\frac{\boldsymbol{\nabla} P}{\rho}\,. \tag{B.23}$$

Equation (B.23) is equated to the left-hand side of the momentum equation given by Eq. (B.9) divided by ρ:

$$-\boldsymbol{\nabla} w = -\frac{\boldsymbol{\nabla} P}{\rho} = \frac{\partial \mathbf{v}}{\partial t} + \mathbf{v}\cdot\boldsymbol{\nabla}\mathbf{v}\,. \tag{B.24}$$

Since spatial derivatives to not appear in in Eq. (B.21), it is desired to remove the gradient operator from Eq. (B.24) by integrating over volume. To facilitate this manipulation, the velocity potential ϕ is introduced, as defined by Eq. (A.5). No generality is lost because

Eq. (B.9) does not contain terms related to viscosity, i.e, the velocity field is irrotational as described by Eq. (A.6). In terms of ϕ, Eq. (B.24) becomes

$$-\boldsymbol{\nabla} w = \boldsymbol{\nabla}\frac{\partial \phi}{\partial t} + \boldsymbol{\nabla}\phi \cdot \boldsymbol{\nabla}\boldsymbol{\nabla}\phi \,. \tag{B.25}$$

Since by the product rule

$$\boldsymbol{\nabla}\phi \cdot \boldsymbol{\nabla}\boldsymbol{\nabla}\phi = \tfrac{1}{2}\boldsymbol{\nabla}(\boldsymbol{\nabla}\phi \cdot \boldsymbol{\nabla}\phi) = \tfrac{1}{2}\boldsymbol{\nabla}(|\boldsymbol{\nabla}\phi|^2)\,,$$

Eq. (B.25) becomes

$$\boldsymbol{\nabla} w = -\boldsymbol{\nabla}\left(\frac{\partial \phi}{\partial t} + \tfrac{1}{2}|\boldsymbol{\nabla}\phi|^2\right). \tag{B.26}$$

Equation (B.26) is integrated over space, resulting in the introduction of an arbitrary constant C':

$$w = -\frac{\partial \phi}{\partial t} - \tfrac{1}{2}|\boldsymbol{\nabla}\phi|^2 + C' \,. \tag{B.27}$$

Combining Eqs. (B.22) and (B.27) yields

$$P - P_0 = \rho_0\left(-\frac{\partial \phi}{\partial t} - \tfrac{1}{2}|\boldsymbol{\nabla}\phi|^2 + C'\right) + \frac{\rho_0}{2c_0^2}\left(-\frac{\partial \phi}{\partial t} - \tfrac{1}{2}|\boldsymbol{\nabla}\phi|^2 + C'\right)^2 + \ldots\,, \tag{B.28}$$

recovering Eq. (6.11) of Ref. 288. Taking the time average of Eq. (B.28) eliminates terms that are of odd powers, namely $\partial\phi/\partial t$. According to Wang and Lee, C' is a quadratic quantity, and thus it has a nonzero time average $\langle C'\rangle \equiv \rho_0 C$ [288, p. 178]. Removing from Eq. (B.28) quantities of quartic order and higher yields

$$\langle P - P_0\rangle = \frac{\rho_0}{2c_0^2}\left\langle(\partial\phi/\partial t)^2\right\rangle - \tfrac{1}{2}\rho_0\langle|\boldsymbol{\nabla}\phi|^2\rangle + C\,. \tag{B.29}$$

The fluid velocity $\mathbf{v}$ is now reinstated for $\boldsymbol{\nabla}\phi$. To relate $\partial\phi/\partial t$ to p and $\mathbf{v}$, it suffices to consider the linearized version of Eq. (B.9), since this quantity is squared in Eq. (B.29):

$$\boldsymbol{\nabla} p = -\rho_0\frac{\partial \mathbf{v}}{\partial t} = -\rho_0\boldsymbol{\nabla}\frac{\partial \phi}{\partial t}\,. \tag{B.30}$$

Integrating Eq. (B.30) over volume, noting that the integration constant is arbitrary (since the value of the potential ϕ can be set to 0 anywhere without changing the values of p and $\mathbf{v}$), and solving for $\partial\phi/\partial t$ yields the relation $\partial\phi/\partial t = -p/\rho_0$. Equation (B.29) thus becomes

$$\langle P - P_0 \rangle = \frac{1}{2\rho_0 c_0^2} \langle p^2 \rangle - \tfrac{1}{2}\rho_0 \langle v^2 \rangle + C\,, \tag{B.31}$$

recovering Eq. (6.13) of Ref. 288. Combining Eq. (B.31) with Eqs. (B.3) and (B.8) allows the mean excess pressure to be defined in terms of the Lagrangian density $L = T - U$:

$$\langle P - P_0 \rangle = -\langle L \rangle + C\,. \tag{B.32}$$

Equation (B.17) has units of stress per unit length, which equals force per unit volume. Integrating over volume V_s therefore results in quantity with dimensions of force. Since Eq. (B.17) was derived in free space, there is no change of mechanical linear momentum in the volume V_s per unit time. However, if a scatterer of sound lies within V_s, then the radiation force exerted on the scatterer equals

$$\mathbf{F} = \int_{V_\mathrm{s}} \boldsymbol{\nabla} \cdot \langle \underline{\mathbf{S}} \rangle \, dV_\mathrm{s}\,. \tag{B.33}$$

The calculation of radiation force exerted in an unconstrained medium in Sec. B.4 is performed by setting $C = 0$ in Eq. (B.32) [288, pp. 179–180]. Section B.3 offers a simplified derivation of Eq. (B.33) for the case $C = 0$ and draws parallels with other manifestations of radiation force.

B.3 Simplified derivation of Langevin radiation force

Radiation forces described by setting $C = 0$ and $C \neq 0$ in Eq. (B.32) are associated with Paul Langevin and Lord Rayleigh, respectively. Accessible discussions of the difference between the Rayleigh and Langevin forces are provided by Wang and Lee [288, pp. 179–180]

A portion of Sec. B.3 is currently under review for publication in the *Journal of the Acoustical Society of America*.

and Ostrovsky [308]. The present section shows that in the Langevin case, it is unnecessary to begin with the exact momentum and continuity equations given by Eqs. (B.9) and (B.10), respectively. Below, Eq. (B.33) is derived from the equations of linear acoustics, paralleling the derivation of momentum conservation for electromagnetic waves, surface gravity waves, and waves on a string.

Motivation for a simplified derivation

Radiation forces exerted by acoustic waves are generated by stresses that are quadratic in the wave variable, leading to the question of whether second-order equations must be used to calculate the field producing the force. This question has been discussed for over a century. Regarding his calculation of the radiation pressure in an adiabatic gas exerted by a plane progressive wave on a perfectly reflecting wall, Poynting wrote, "Lord Rayleigh kindly pulled me out of the pit into which I fell, pointing out that when we take into account second-order quantities the ordinary sound equation does not hold" [135]. Rayleigh's result [137] retains the quadratic term in the state equation in order to conserve mass [288, p. 181]. Poynting's neglect of this nonlinearity is not surprising given his background in electromagnetism [309], in which no such criterion arises, and for which the analogous radiation pressure equals twice the energy density of the incident wave [8, pp. 380–382].

Current interest in radiation force is motivated by, among other applications, acoustic tweezers and acoustofluidic devices [28, 141], for which constraints on the total mass or volume of the acoustic field are rarely imposed. In such cases, the nonlinearity considered by Rayleigh is irrelevant, and "the Rayleigh radiation force has no major practical importance" [124]. The neglect of these constraints is associated with the Langevin radiation force, which is the "usually measured" quantity that "can be observed down to the lowest sound intensities under certain conditions" [133].

Despite the prevalence of the Langevin radiation force, traditional derivations of acoustic radiation force begin with the exact momentum equation [310, Sec. 2.4.2], as re-

viewed in Sec. B.2, introducing unnecessary complications and obscuring the fact that the Langevin radiation force is a consequence of linear acoustics. The equations of linear acoustics are combined to derive the acoustic momentum conservation theorem in a homogeneous fluid. In the presence of a scatterer, the time average of the integral form of the conservation theorem equals the Langevin radiation force. Similar momentum conservation theorems for electromagnetic waves, surface gravity waves, and waves on a string are then derived, showing that analogous forces can be obtained from linear fields.

Acoustic momentum conservation theorem

Linear acoustic fields in a homogeneous fluid satisfy [9, Chap. 1, Eqs. (C-54)–(C-56)]

$$\frac{\partial \rho'}{\partial t} + \rho_0 \boldsymbol{\nabla} \cdot \mathbf{v} = 0\,, \tag{B.34}$$

$$\rho' - p/c_0^2 = 0\,, \tag{B.35}$$

$$\boldsymbol{\nabla} p + \rho_0 \frac{\partial \mathbf{v}}{\partial t} = \mathbf{0}\,. \tag{B.36}$$

Equations (B.34), (B.35), and (B.36) are the linearized continuity, state, and momentum equations, respectively, where ρ' is the density perturbation, ρ_0 is the ambient density, $\mathbf{v}$ is the fluid velocity, p is the acoustic pressure, and c_0 is the speed of sound. The conservation theorem derived below is formed from solutions of Eq. (A.2), which is obtained from Eqs. (B.34)–(B.36).

Multiplying Eq. (B.34) by $\mathbf{v}$ yields

$$\frac{\partial \rho'}{\partial t}\mathbf{v} + \rho_0 (\boldsymbol{\nabla} \cdot \mathbf{v})\mathbf{v} = \mathbf{0}\,. \tag{B.37}$$

Equation (B.37) is recast using the product rules[1]

$$\frac{\partial \rho'}{\partial t}\mathbf{v} = \frac{\partial (\rho' \mathbf{v})}{\partial t} - \rho' \frac{\partial \mathbf{v}}{\partial t}\,,$$
$$(\boldsymbol{\nabla} \cdot \mathbf{v})\mathbf{v} = \boldsymbol{\nabla} \cdot (\mathbf{v} \otimes \mathbf{v}) - (\boldsymbol{\nabla} \mathbf{v}) \cdot \mathbf{v}\,,$$

[1] See footnote 1 on p. 185.

resulting in

$$\frac{1}{c_0^2}\frac{\partial \mathbf{I}}{\partial t} - \frac{p}{c_0^2}\frac{\partial \mathbf{v}}{\partial t} + \rho_0[\boldsymbol{\nabla}\cdot(\mathbf{v}\otimes\mathbf{v}) - (\boldsymbol{\nabla}\mathbf{v})\cdot\mathbf{v}] = \mathbf{0}\,, \tag{B.38}$$

where Eq. (B.35) has been used to eliminate ρ' and $p\mathbf{v}$ has been identified as the instantaneous intensity $\mathbf{I}$ [22, Eq. (1.11.3)]. Solving Eq. (B.36) for $\partial\mathbf{v}/\partial t$ and multiplying by p shows that

$$p\frac{\partial \mathbf{v}}{\partial t} = -\frac{1}{\rho_0}p\boldsymbol{\nabla}p = -\frac{1}{2\rho_0}\boldsymbol{\nabla}(p^2)\,,$$

while the term $(\boldsymbol{\nabla}\mathbf{v})\cdot\mathbf{v}$ in Eq. (B.38) can be replaced with $\boldsymbol{\nabla}(v^2)/2$, as shown in Eq. (A.13). Equation (B.38) therefore becomes

$$\boldsymbol{\nabla}\left(\tfrac{1}{2}\rho_0 v^2 - \tfrac{1}{2}\beta_0 p^2\right) - \rho_0\boldsymbol{\nabla}\cdot(\mathbf{v}\otimes\mathbf{v}) = \frac{1}{c_0^2}\frac{\partial \mathbf{I}}{\partial t}\,, \tag{B.39}$$

where $\beta_0 = 1/\rho_0 c_0^2$ denotes the compressibility. Since $T = \frac{1}{2}\rho_0 v^2$ = kinetic energy density, $U = \frac{1}{2}\beta_0 p^2$ = potential energy density, and $L = T - U$ = Lagrangian density, [22] the gradient in Eq. (B.39) can be written as (see footnote 3 on p. 186)

$$\boldsymbol{\nabla}L = \underline{\mathbf{I}}\cdot\boldsymbol{\nabla}L = \boldsymbol{\nabla}\cdot(\underline{\mathbf{I}}L) - L\boldsymbol{\nabla}\cdot\underline{\mathbf{I}}\,, \tag{B.40}$$

where $\underline{\mathbf{I}}$ is the identity tensor. Since $\boldsymbol{\nabla}\cdot\underline{\mathbf{I}} = \mathbf{0}$, Eq. (B.40) reduces to $\boldsymbol{\nabla}L = \boldsymbol{\nabla}\cdot(\underline{\mathbf{I}}L)$, and Eq. (B.39) becomes

$$\boldsymbol{\nabla}\cdot(\underline{\mathbf{I}}L - \rho_0\mathbf{v}\otimes\mathbf{v}) = \frac{1}{c_0^2}\frac{\partial \mathbf{I}}{\partial t}\,. \tag{B.41}$$

Identifying

$$\mathbf{g} = \mathbf{I}/c_0^2 = \text{momentum density}, \tag{B.42}$$

$$\underline{\mathbf{S}} = \underline{\mathbf{I}}L - \rho_0\mathbf{v}\otimes\mathbf{v} = \text{acoustic radiation stress} \tag{B.43}$$

allows Eq. (B.41) to be expressed as

$$\boldsymbol{\nabla}\cdot\underline{\mathbf{S}} = \frac{\partial \mathbf{g}}{\partial t}\,, \tag{B.44}$$

which is the conservation theorem of acoustic momentum in a homogeneous fluid. An early form of Eq. (B.44) for $\boldsymbol{\nabla} \times \mathbf{v} \neq \mathbf{0}$ was obtained by Eckart, who suggested that "the acoustic momentum is related to acoustic energy in the same manner as the corresponding electromagnetic quantities," [311, Eq. (11)] as shown below. Morse and Ingard present Eq. (B.44) and state that $c_0\mathbf{g}$ "is the radiation pressure exerted by the wave," [122, p. 250] which is true only in the Langevin case for a plane wave incident on a perfectly absorbing wall [288].[2] An elastodynamic version of Eq. (B.44) was derived by Gurevich and Thellung [312]. It is also noted that Eq. (B.44) is reminiscent of the energy conservation theorem $\boldsymbol{\nabla} \cdot \mathbf{I} + \partial(T + U)/\partial t = 0$, which is obtained by multiplying Eq. (B.36) by $\mathbf{v}$ [22, pp. 38–39].

Integrating Eq. (B.44) over a volume V yields

$$\oint_A \underline{\mathbf{S}} \cdot d\mathbf{A} = \frac{d}{dt} \int_V \mathbf{g}\, dV\,, \tag{B.45}$$

where the divergence theorem has been applied to the left-hand side, and where $d\mathbf{A}$ is the outward-oriented differential area. Equation (B.45) states that the rate of change of momentum within a volume enclosed by the surface A in the acoustic field equals the sum of forces acting on the surface. If the acoustic field is time-harmonic, the time average of Eq. (B.45) yields[3]

$$\oint_A \langle \underline{\mathbf{S}} \rangle \cdot d\mathbf{A} = \mathbf{0}\,, \tag{B.46}$$

which is the integral form of Wang and Lee's Eq. (6.5) [288]. Equation (B.46) states that there is no change in momentum in the volume V enclosed by the surface A over an acoustic cycle if the enclosed fluid is lossless and homogeneous [121]. However, as discussed in Sec. B.2, if a scatterer lies within the surface, then $\oint_A \langle \underline{\mathbf{S}} \rangle \cdot d\mathbf{A}$ equals the rate at which momentum is transferred from the acoustic field to the scatterer, which is identified as

[2] Morse and Ingard's $\mathfrak{W}$ = Eq. (B.43) and $\mathbf{M}$ = −Eq. (B.42). Note on p. 250 that $-c\mathbf{M} = p\mathbf{v}/c$ (not $c\mathbf{M}$) is the instantaneous radiation pressure.

[3] If ω is the angular frequency, the time average of $f(t)$ is $\langle f \rangle = (\omega/2\pi)\int_0^{2\pi/\omega} f(t)\, dt$. Suppose $f(t) = \cos \omega t$ and $g(t) = \cos(\omega t + \phi)$, so $f(t)g(t) = [\cos(2\omega t + \phi) + \cos\phi]/2$. Thus $d[f(t)g(t)]/dt = -\omega \sin(2\omega t + \phi)$, the time average of which is zero.

the Langevin radiation force for $\underline{\mathbf{S}}$ given by Eq. (B.43):

$$\mathbf{F} = \oint_A \langle \underline{\mathbf{S}} \rangle \cdot d\mathbf{A} \,. \tag{B.47}$$

Equation (B.47) recovers Westervelt's Eq. (1) of Ref. 121 and Gor'kov's equation preceding Eq. (4) of Ref. 3.

The fact that Eq. (B.47) is formed from solutions of Eqs. (B.34)–(B.36) clarifies Gor'kov's statement that "for the calculation of the average force correct up to terms of the second order in the velocity, it is sufficient to find the solution of the linear scattering problem" [3]. Landau and Lifshitz similarly note that the mean excess pressure "can be expressed in terms of quantities calculated from the linear sound equations, so that it is not necessary to solve directly the nonlinear equations of motion" [299, p. 257]. Despite these statements, the connection between the linear fields and the quadratic quantities involved in the Langevin radiation force has not previously been made explicit.

The above derivation counters the statement that "nonlinear effects cause a small but nonzero magnitude to be associated with a physical entity, the existence of which the linear model precludes" [22, p. 649] as it applies to the Langevin radiation pressure. Linear acoustics predicts a nonzero radiation stress on the same order as the energy and intensity of an acoustic wave.

Analogous electromagnetic momentum theorem

Traditional derivations of the electromagnetic momentum conservation theorem in the presence of charges and currents are provided by Jackson [226, Eqs. (6.120)–(6.123)] and Griffiths [8, Sec. 8.2]. The following derivation parallels the derivation above by considering the Faraday and Ampère-Maxwell laws in the absence of charges and currents,

$$\boldsymbol{\nabla} \times \mathbf{E} + \mu \frac{\partial \mathbf{H}}{\partial t} = \mathbf{0} \,, \tag{B.48}$$

$$\boldsymbol{\nabla} \times \mathbf{H} - \epsilon \frac{\partial \mathbf{E}}{\partial t} = \mathbf{0} \,, \tag{B.49}$$

where the permittivity ϵ and permeability μ correspond to a linear, homogeneous, isotropic, and nondispersive medium. The linearity of Eqs. (B.48) and (B.49) in the electric field $\mathbf{E}$ and magnetic field $\mathbf{H}$ parallels the linearity of Eqs. (B.34)–(B.36) in ρ', $\mathbf{v}$, and p.

The cross product of $\epsilon\mathbf{E}$ and Eq. (B.48) equals

$$\epsilon\mathbf{E}\times(\boldsymbol{\nabla}\times\mathbf{E})+\frac{1}{c^2}\frac{\partial\mathbf{I}}{\partial t}-\frac{1}{c^2}\frac{\partial\mathbf{E}}{\partial t}\times\mathbf{H}=\mathbf{0}\,, \tag{B.50}$$

where it has been noted that $\mathbf{I}=\mathbf{E}\times\mathbf{H}$, $c^{-2}=\epsilon\mu$, and

$$\mathbf{E}\times\frac{\partial\mathbf{H}}{\partial t}=\frac{\partial\mathbf{I}}{\partial t}-\frac{\partial\mathbf{E}}{\partial t}\times\mathbf{H}\,.$$

The cross product of $\mu\mathbf{H}$ and Eq. (B.49) similarly equals

$$\mu\mathbf{H}\times(\boldsymbol{\nabla}\times\mathbf{H})+\frac{1}{c^2}\frac{\partial\mathbf{I}}{\partial t}+\frac{1}{c^2}\frac{\partial\mathbf{H}}{\partial t}\times\mathbf{E}=\mathbf{0}\,. \tag{B.51}$$

Adding Eqs. (B.50) and (B.51) and noting from Eqs. (B.48) and (B.49) that $\partial\mathbf{H}/\partial t=-\boldsymbol{\nabla}\times\mathbf{E}/\mu$ and $\partial\mathbf{E}/\partial t=\boldsymbol{\nabla}\times\mathbf{H}/\epsilon$ yields

$$\epsilon\mathbf{E}\times(\boldsymbol{\nabla}\times\mathbf{E})+\mu\mathbf{H}\times(\boldsymbol{\nabla}\times\mathbf{H})+\frac{1}{c^2}\frac{\partial\mathbf{I}}{\partial t}=\mathbf{0}\,. \tag{B.52}$$

The charge-free condition $\boldsymbol{\nabla}\cdot\mathbf{E}=0$ and absence of magnetic monopoles $\boldsymbol{\nabla}\cdot\mathbf{H}=0$ yield

$$\mathbf{E}\times(\boldsymbol{\nabla}\times\mathbf{E})=\tfrac{1}{2}\boldsymbol{\nabla}(E^2)-\boldsymbol{\nabla}\cdot(\mathbf{E}\otimes\mathbf{E})\,,$$
$$\mathbf{H}\times(\boldsymbol{\nabla}\times\mathbf{H})=\tfrac{1}{2}\boldsymbol{\nabla}(H^2)-\boldsymbol{\nabla}\cdot(\mathbf{H}\otimes\mathbf{H})\,,$$

respectively, allowing Eq. (B.52) to be expressed as

$$\boldsymbol{\nabla}\cdot\left[\epsilon\mathbf{E}\otimes\mathbf{E}+\mu\mathbf{H}\otimes\mathbf{H}-\underline{\mathbf{I}}\left(\tfrac{1}{2}\epsilon E^2+\tfrac{1}{2}\mu H^2\right)\right]=\frac{1}{c^2}\frac{\partial\mathbf{I}}{\partial t}. \tag{B.53}$$

Equation (B.53) can be written in terms of [8, pp. 345–356]

$$\mathbf{g}=\mathbf{I}/c^2=\text{momentum density}, \tag{B.54}$$
$$\underline{\mathbf{S}}=\epsilon\mathbf{E}\otimes\mathbf{E}+\mu\mathbf{H}\otimes\mathbf{H}-\underline{\mathbf{I}}(\tfrac{1}{2}\epsilon E^2+\tfrac{1}{2}\mu H^2)=\text{Maxwell stress} \tag{B.55}$$

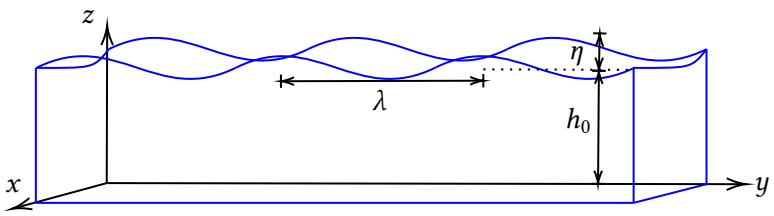

Figure B.1: Surface gravity waves of height $z = h$ as measured from the bottom, $z = 0$.

as

$$\boldsymbol{\nabla} \cdot \underline{\mathbf{S}} = \frac{\partial \mathbf{g}}{\partial t} \,. \tag{B.56}$$

Setting ϵ and μ equal to their free-space values given by ϵ_0 and μ_0, respectively, recovers the differential form of Eq. (6.121) of Ref. 226 and Eq. (8.21) of Ref. 8 in the absence of charges and currents. Electromagnetic radiation force is calculated in a manner similar to Eq. (B.47) [313, Eq. (6)].

Analogous theorem for surface gravity waves

Let the height of the fluid be

$$h(\mathbf{r}, t) = h_0 + \eta(\mathbf{r}, t) \,, \tag{B.57}$$

where h_0 is the depth as measured from the surface at rest to the bottom, and where η is the wave variable, as shown in Fig. B.1. The position vector $\mathbf{r}$ is represented by two coordinates in the plane perpendicular to the direction of the displacement, which is identified as the z direction, e.g., $\mathbf{r} = x\mathbf{e}_x + y\mathbf{e}_y$, where $\mathbf{e}_x$ and $\mathbf{e}_y$ are the Cartesian unit vectors. The bottom is defined by the plane $z = 0$, and the ambient surface corresponds to $z = h_0$.

The following analysis is placed on the same footing as the linear wave phenomena described in Sec. B.3 by let the analysis be confined to shallow waves, i.e., $h_0 \ll \lambda$, where λ is the wavelength. The velocity $\mathbf{v}$ of the fluid is then not a function of the depth, i.e., $\mathbf{v} = \mathbf{v}(\mathbf{r}) \neq \mathbf{v}(z)$, and $\mathbf{v}$ has no component in the z direction. It is also assumed that the fluid is incompressible, i.e., $\rho = \rho_0$. If P_0 is the atmospheric pressure, then the pressure in

the fluid at height z is

$$P(\mathbf{r}, z, t) = P_0 + \rho_0 g[\eta(\mathbf{r}, t) - z]\,, \tag{B.58}$$

where g is the acceleration due to gravity. These approximations allow for the fluid motion to be approximated by the linearized continuity and momentum equations, given by

$$h_0 \boldsymbol{\nabla} \cdot \mathbf{v} + \frac{\partial \eta}{\partial t} = 0\,, \tag{B.59}$$

$$g \boldsymbol{\nabla} \eta + \frac{\partial \mathbf{v}}{\partial t} = 0\,, \tag{B.60}$$

respectively. Combination of Eqs. (B.59) and (B.60) yields the linear wave equation $\nabla^2 \eta - c_0^{-2} \partial^2 \eta / \partial t^2 = 0$, where $c_0 = \sqrt{g h_0}$, where the corresponding kinetic energy density, potential energy density, and intensity equal

$$T = \tfrac{1}{2} \rho_0 v^2\,, \tag{B.61}$$

$$U = \tfrac{1}{2} \frac{\rho_0 g}{h_0} \eta^2\,, \tag{B.62}$$

$$\mathbf{I} = \rho_0 g \eta \mathbf{v}\,. \tag{B.63}$$

The $O(\eta^2)$ momentum conservation theorem is obtained by multiplying Eqs. (B.59) and Eq. (B.60) by $\mathbf{v}$ and η, respectively. Adding the resulting equations and noting that $\mathbf{v} \partial \eta / \partial t + \eta \partial \mathbf{v} / \partial t = \partial (\eta \mathbf{v}) / \partial t$ yields

$$h_0 \mathbf{v} \boldsymbol{\nabla} \cdot \mathbf{v} + g \eta \boldsymbol{\nabla} \eta + \frac{\partial (\eta \mathbf{v})}{\partial t} = 0\,. \tag{B.64}$$

The tensor calculus identity given by footnote 1 on p. 185 allows the quantity $\mathbf{v} \boldsymbol{\nabla} \cdot \mathbf{v}$ appearing in Eq. (B.64) to be written as

$$\mathbf{v} \boldsymbol{\nabla} \cdot \mathbf{v} = \boldsymbol{\nabla} \cdot (\mathbf{v} \otimes \mathbf{v}) - (\boldsymbol{\nabla} \mathbf{v}) \cdot \mathbf{v}\,,$$

insertion of which into Eq. (B.64) and multiplication through by ρ_0 / h_0 yields

$$\rho_0 [\boldsymbol{\nabla} \cdot (\mathbf{v} \otimes \mathbf{v}) - (\boldsymbol{\nabla} \mathbf{v}) \cdot \mathbf{v}] + \frac{\rho_0 g}{h_0} \eta \boldsymbol{\nabla} \eta + \frac{\rho_0}{h_0} \frac{\partial (\eta \mathbf{v})}{\partial t} = 0\,. \tag{B.65}$$

Invoking the tensor calculus identity

$$\boldsymbol{\nabla} \cdot (\underline{\mathbf{T}}^{\mathrm{T}} \cdot \mathbf{u}) = (\boldsymbol{\nabla} \cdot \underline{\mathbf{T}}) \cdot \mathbf{u} + \underline{\mathbf{T}} \cdot \boldsymbol{\nabla}\mathbf{u} \tag{B.66}$$

for the identity tensor $\underline{\mathbf{I}}$ and fluid velocity vector $\mathbf{v}$ yields

$$\boldsymbol{\nabla} \cdot (\underline{\mathbf{I}} \cdot \mathbf{v}) = \underline{\mathbf{I}} \cdot \boldsymbol{\nabla}\mathbf{v}\,,$$

where it has been noted that the transpose of $\underline{\mathbf{I}}$ is itself, i.e., $\underline{\mathbf{I}}^{\mathrm{T}} = \underline{\mathbf{I}}$, and that $\boldsymbol{\nabla} \cdot \underline{\mathbf{I}} = \mathbf{0}$. Thus the second term of Eq. (B.65) can be written as

$$-\rho_0(\boldsymbol{\nabla}\mathbf{v}) \cdot \mathbf{v} = -\rho_0(\underline{\mathbf{I}} \cdot \boldsymbol{\nabla}\mathbf{v}) \cdot \mathbf{v} = -\rho_0 \boldsymbol{\nabla} \cdot (\underline{\mathbf{I}} \cdot \mathbf{v}) \cdot \mathbf{v} = -\tfrac{1}{2}\rho_0 \boldsymbol{\nabla} \cdot (\underline{\mathbf{I}} v^2) = -\boldsymbol{\nabla} \cdot (\underline{\mathbf{I}} T)\,, \tag{B.67}$$

where the second-to-last equality holds by the product rule, and the last equality holds by Eq. (B.61). Meanwhile, in view of Eq. (B.62), the third term of Eq. (B.65) can be written as

$$\frac{\rho_0 g}{h_0}\eta\boldsymbol{\nabla}\eta = \tfrac{1}{2}\frac{\rho_0 g}{h_0}\boldsymbol{\nabla}\eta^2 = \boldsymbol{\nabla}U = \boldsymbol{\nabla} \cdot (\underline{\mathbf{I}} U)\,, \tag{B.68}$$

where the last equality holds by the identity given by footnote 3 on p. 186. Finally, in view of Eq. (B.63) and the fact that $c_0^2 = g h_0$, the last term of Eq. (B.65) can be written as $\partial\mathbf{g}/\partial t$, where

$$\mathbf{g} = \mathbf{I}/c_0^2 \tag{B.69}$$

is the momentum density. In view of Eqs. (B.67), (B.68), and (B.69), Eq. (B.65) becomes

$$\rho_0 \boldsymbol{\nabla} \cdot (\mathbf{v} \otimes \mathbf{v}) - \boldsymbol{\nabla} \cdot (\underline{\mathbf{I}} L) + \frac{\partial \mathbf{g}}{\partial t} = 0\,. \tag{B.70}$$

Rearranging terms yields the momentum conservation equation,

$$\boldsymbol{\nabla} \cdot \underline{\mathbf{S}} = \frac{\partial \mathbf{g}}{\partial t}\,, \tag{B.71}$$

where

$$\underline{\mathbf{S}} = \underline{\mathbf{I}} L - \rho_0 \mathbf{v} \otimes \mathbf{v} \tag{B.72}$$

is the radiation stress. Equation (B.71) has the same form as Eqs. (B.44) and (B.56) for acoustic and electromagnetic waves, respectively. The radiation force exerted on a scatterer enclosed by surface A is

$$\mathbf{F} = \int_A \langle \boldsymbol{\nabla} \cdot \underline{\mathbf{S}} \rangle \, dA = \oint \langle \underline{\mathbf{S}} \rangle \cdot \mathbf{e}_n \, dl \,, \tag{B.73}$$

where the second equality holds by Green's theorem and $\mathbf{e}_n$ is the outward normal to the surface.

Analogous theorem for waves on string

Waves on a string provide a one-dimensional analog of the theorems derived above. Let $\xi(x,t)$ denote the transverse displacement of a string of density ρ_0 under tension $\mathcal{T}$. For $|\partial\xi/\partial x| \ll 1$, the equation of motion is the linear wave equation [9, Chap. 1, Eq. (C-13)]

$$\frac{\partial^2 \xi}{\partial x^2} - \frac{1}{c_0^2} \frac{\partial^2 \xi}{\partial t^2} = 0 \,, \tag{B.74}$$

where $c_0 = \sqrt{\mathcal{T}/\rho_0}$ is the wave speed. Equation (B.74) is based on the assumption that the cross-sectional area of the string is vanishingly small, precluding the existence of longitudinal waves. A discussion of how longitudinal waves affect momentum conservation is provided by Rowland and Pask [314].[4]

To obtain the momentum conservation theorem, Eq. (B.74) is multiplied by $\partial\xi/\partial x$, yielding

$$\frac{1}{c_0^2} \frac{\partial}{\partial t} \left(\mathcal{T} \frac{\partial \xi}{\partial x} \frac{\partial \xi}{\partial t} \right) = \mathcal{T} \frac{\partial^2 \xi}{\partial x^2} \frac{\partial \xi}{\partial x} + \rho_0 \frac{\partial^2 \xi}{\partial t \partial x} \frac{\partial \xi}{\partial t} \,, \tag{B.75}$$

where it has been noted that

$$\frac{\partial \xi}{\partial x} \frac{\partial^2 \xi}{\partial t^2} = \frac{\partial}{\partial t} \left(\frac{\partial \xi}{\partial x} \frac{\partial \xi}{\partial t} \right) - \frac{\partial^2 \xi}{\partial t \partial x} \frac{\partial \xi}{\partial t} \,.$$

[4] Radiation force resolves Rowland and Pask's "Paradox 1": the time-averaged force applied by the wave at the interface connecting the two strings in Fig. 3 equals the restoring force exerted by the interface to maintain its position at $x = 0$.

Noting from the product rule that

$$\frac{\partial^2 \xi}{\partial x^2}\frac{\partial \xi}{\partial x} = \frac{1}{2}\frac{\partial}{\partial x}\left(\frac{\partial \xi}{\partial x}\right)^2 \quad \text{and} \quad \frac{\partial^2 \xi}{\partial t \partial x}\frac{\partial \xi}{\partial t} = \frac{1}{2}\frac{\partial}{\partial x}\left(\frac{\partial \xi}{\partial t}\right)^2$$

allows Eq. (B.75) to be written as

$$\frac{\partial S}{\partial x} = \frac{\partial g}{\partial t}\,, \tag{B.76}$$

where [9, 122]

$$I = -\mathcal{T}\frac{\partial \xi}{\partial x}\frac{\partial \xi}{\partial t} = \text{instantaneous intensity}, \tag{B.77}$$

$$g = I/c_0^2 = \text{momentum density}, \tag{B.78}$$

$$T = \tfrac{1}{2}\rho_0(\partial \xi/\partial t)^2 = \text{kinetic energy density}, \tag{B.79}$$

$$U = \tfrac{1}{2}\mathcal{T}(\partial \xi/\partial x)^2 = \text{potential energy density}, \tag{B.80}$$

$$L = T - U = \text{Lagrangian density}, \tag{B.81}$$

$$S = L - \rho_0(\partial \xi/\partial t)^2 = \text{radiation stress}. \tag{B.82}$$

Equation (B.76) recovers Morse and Ingard's in-line equation developed qualitatively on p. 106 of Ref. 122. Equation (B.77) can be understood by noting that the force exerted by an element of the string on an element to its right is $-\mathcal{T}\partial\xi/\partial x$; since power equals force times velocity $\partial\xi/\partial t$, the quantity in parentheses on the left-hand side of Eq. (B.75) is identified as minus the energy flux.

Integrating Eq. (B.76) over x from point x_1 to x_2, assuming that ξ is time-harmonic, and taking the time average yields

$$\langle S(x_2) - S(x_1)\rangle = 0\,. \tag{B.83}$$

Equation (B.83), which is analogous to Eq. (B.46) of the present work and Eq. (7) of Ref. 121, states that waves pass through the control length $x_2 - x_1$ with no change in momentum. If a mass lies between points x_1 and x_2, however, waves will generally reflect from and transmit through the mass. In such cases, the difference in $\langle S\rangle$ at points x_2 and x_1 equals the

rate at which momentum is transferred from the waves to the mass, which by Newton's second law equals the radiation force:

$$F = \langle S(x_2) - S(x_1) \rangle \,. \tag{B.84}$$

Since S contains squares of partial derivatives of ξ, calculation of the radiation force amounts to solving the linear scattering problem, as in the case for calculating the electromagnetic and acoustic Langevin radiation forces.

In summary, the acoustic momentum conservation theorem was derived from the equations of linear acoustics, paralleling Pierce's derivation of the acoustic energy corollary [22, pp. 38–39]. The derivation clarifies the linear origins of the Langevin radiation force and avoids the complications encountered in the traditional derivation reviewed in Sec. B.2, like distinctions between Eulerian and Lagrangian coordinates and expansions in the enthalpy [Eq. (B.18)]. The analogous theorems for electromagnetic waves, surface gravity waves, and waves on a string were derived, showing that radiation forces are calculated using linear wave fields. Section 5.1 outlines future research directions related to radiation forces exerted by one- and two-dimensional wave fields.

B.4 Far-field formulation

The following approach to simplify the volume integral for the radiation force given by Eq. (B.33) [which is equivalent to the surface integral given by Eq. (B.47)] is attributed to Westervelt [121, 177]. Consider a spherical surface A_s immediately surrounding an object (enclosing a corresponding volume V_s), and a much larger spherical surface A (enclosing a corresponding volume V and concentric with A_s), as shown in Fig. B.2. Wang and Lee summarize the procedure as follows, where their notation has been modified to be consistent with the present work [288, Sec. 3.1.2]:

> By integrating $\boldsymbol{\nabla} \cdot \langle \underline{\mathbf{S}} \rangle = 0$ over the space between [the surface] A_s and a much larger spherical surface A concentric with the sphere, and using Gauss's theorem, we obtain a surface integral of $\langle \underline{\mathbf{S}} \rangle \cdot \mathbf{e}_n$ over $A' = A_\mathrm{s} + A$, equated to

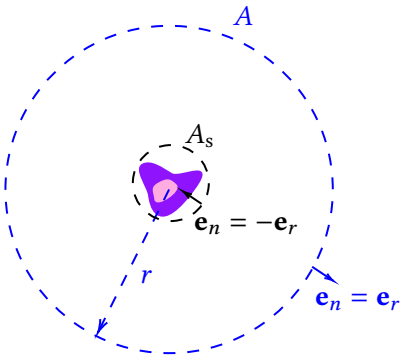

Figure B.2: Equation (B.17) is integrated over the volume within surface A but outside surface A_s. $\mathbf{e}_r$ is the radial unit vector, and r is sufficiently large such that $\underline{\mathbf{S}}$ can be evaluated in the far field.

> zero, where $\mathbf{e}_n$ is the normal unit vector on the surface A' pointing away from the enclosed space…[T]he integral over $-\langle\underline{\mathbf{S}}\rangle \cdot \mathbf{e}_n$ over A_s is the force acting on the sphere.

Equation (B.17) is integrated over the volume within surface A but outside surface A_s:

$$\int_V \boldsymbol{\nabla} \cdot \langle\underline{\mathbf{S}}(\mathbf{r})\rangle \, dV - \int_{V_s} \boldsymbol{\nabla} \cdot \langle\underline{\mathbf{S}}(\mathbf{r}_s)\rangle \, dV_s = \mathbf{0} \,. \tag{B.85}$$

Upon invoking the divergence theorem, the first term in Eq. (B.85) becomes $\oint_A \langle\underline{\mathbf{S}}(\mathbf{r})\rangle \cdot \mathbf{e}_r \, dA$, and the second term becomes $-\oint_{A_s} \langle\underline{\mathbf{S}}(\mathbf{r}_s)\rangle \cdot \mathbf{e}_r \, dA_s$, where $\mathbf{e}_r$ is the spherical radial unit vector:

$$\oint_A \langle\underline{\mathbf{S}}(\mathbf{r})\rangle \cdot \mathbf{e}_r \, dA - \oint_{A_s} \langle\underline{\mathbf{S}}(\mathbf{r}_s)\rangle \cdot \mathbf{e}_r \, dA_s = \mathbf{0} \,. \tag{B.86}$$

Since it is desired to define the radiation force on the object enclosed by A_s with respect to the *inward* normal, $\mathbf{e}_n$ is identified as $-\mathbf{e}_r$ on A_s, with $\mathbf{e}_n$ identified as $\mathbf{e}_r$ on A, as shown in Fig. B.2:

$$\oint_A \langle\underline{\mathbf{S}}(\mathbf{r})\rangle \cdot \mathbf{e}_n \, dA + \oint_{A_s} \langle\underline{\mathbf{S}}(\mathbf{r}_s)\rangle \cdot \mathbf{e}_n \, dA_s = \mathbf{0} \,. \tag{B.87}$$

Solving Eq. (B.87) for $-\oint_{A_s} \langle\underline{\mathbf{S}}(\mathbf{r}_s)\rangle \cdot \mathbf{e}_n \, dA_s$ yields the radiation force on the object enclosed by A_s:

$$\mathbf{F} = -\oint_{A_s} \langle\underline{\mathbf{S}}(\mathbf{r}_s)\rangle \cdot \mathbf{e}_n \, dA_s = \oint_A \langle\underline{\mathbf{S}}(\mathbf{r})\rangle \cdot \mathbf{e}_n \, dA \,. \tag{B.88}$$

The first equality of Eq. (B.88), when expressed in index notation, recovers the first equation (not numbered) of Ref. 3. When expressed in terms of Eq. (B.15), Eq. (B.88) equals

$$\mathbf{F} = -\oint_A \left\langle \underline{\mathbf{I}}(P - P_0) + \rho_0 \mathbf{v} \otimes \mathbf{v} \right\rangle \cdot \mathbf{e}_n \, dA \,, \tag{B.89}$$

the indicial form of which recovers Eq. (6.82) of Ref. 288. Equation (B.89) can be written in terms of the acoustic fields p and $\mathbf{v}$ by using Eq. (B.31), resulting in

$$\mathbf{F} = -\oint_A \left\langle \tfrac{1}{2}\underline{\mathbf{I}} p^2/\rho_0 c_0^2 - \tfrac{1}{2}\rho_0 \underline{\mathbf{I}} v^2 + \rho_0 \mathbf{v} \otimes \mathbf{v} \right\rangle \cdot \mathbf{e}_n \, dA \,, \tag{B.90}$$

where C has been set to zero to describe the Langevin force discussed in Sec. B.3 and on pp. 179–180 of Ref. 288.[5] When reduced to index notation and expressed in terms of velocity potential [Eq. (A.5)], Eq. (B.90) recovers the equation at the top of the second column on the first page of Ref. 3. Equation (B.90) reveals the utility of the surface integral over A in the second equality of Eq. (B.88): since the surface A can be arbitrarily large, the calculation of the radiation force $\mathbf{F}$ amounts to solving the far-field scattering problem. The algebraic relationship between p and $\mathbf{v}$ in the far field of a scattered spherical wave is exploited in Sec. B.5.

B.5 Simplification for progressive waves

Westervelt simplified Eq. (B.90) for incident progressive wave fields [121, 177]. The steps leading to Eq. (2) of Ref. 121 are reviewed, and the final step of Westervelt's derivation is elucidated by invoking energy conservation. Begin by expressing Eq. (B.90) in terms of the Lagrangian density given by Eq. (B.32):

$$\mathbf{F} = \oint_A \left\langle \underline{\mathbf{I}} L - \rho_0 \mathbf{v} \otimes \mathbf{v} \right\rangle \cdot \mathbf{e}_n \, dA \,. \tag{B.91}$$

Equation (B.91) is equivalent to Eq. (4) of Ref. 121. For both progressive and standing wave configurations, the pressure and particle velocity fields are written in terms of the

[5] Equation (B.90) is equivalent to Eq. (B.47) in combination with Eq. (B.43).

incident fields (subscripted "i") and scattered fields (subscripted "s"),

$$p = p_\mathrm{i} + p_\mathrm{s}\,, \tag{B.92}$$

$$\mathbf{v} = \mathbf{v}_\mathrm{i} + \mathbf{v}_\mathrm{s}\,, \tag{B.93}$$

and thus the Lagrangian density can be expanded as $L = L_\mathrm{i} + L_\mathrm{s} + L_\mathrm{is}$, where

$$L_\mathrm{i} = \tfrac{1}{2}\rho_0 v_\mathrm{i}^2 - p_\mathrm{i}^2/2\rho_0 c_0^2\,, \tag{B.94}$$

$$L_\mathrm{s} = \tfrac{1}{2}\rho_0 v_\mathrm{s}^2 - p_\mathrm{s}^2/2\rho_0 c_0^2\,, \tag{B.95}$$

$$L_\mathrm{is} = \rho_0 \mathbf{v}_\mathrm{i}\cdot\mathbf{v}_\mathrm{s} - p_\mathrm{i}p_\mathrm{s}/\rho_0 c_0^2 = \rho_0 v_\mathrm{i} v_\mathrm{s}\cos\psi - p_\mathrm{i}p_\mathrm{s}/\rho_0 c_0^2\,, \tag{B.96}$$

where ψ is the angle between $\mathbf{v}_\mathrm{i}$ and $\mathbf{v}_\mathrm{s}$.[6] Equations (B.94) and (B.95) are the "contributions to the flux of momentum from the incident and scattered waves respectively" [121]. Westervelt calls Eq. (B.96) the "interaction Lagrangian" since it contains the cross terms of the squares of Eq. (B.92) and (B.93). Similarly, the quantity $\mathbf{v}\otimes\mathbf{v}$ that appears in the second term in the integrand of Eq. (B.91) can be expanded as

$$\mathbf{v}\otimes\mathbf{v} = \mathbf{v}_\mathrm{i}\otimes\mathbf{v}_\mathrm{i} + \mathbf{v}_\mathrm{s}\otimes\mathbf{v}_\mathrm{s} + \mathbf{v}_\mathrm{i}\otimes\mathbf{v}_\mathrm{s} + \mathbf{v}_\mathrm{s}\otimes\mathbf{v}_\mathrm{i}\,. \tag{B.97}$$

In the absence of an object from which sound is scattered, Eqs. (B.92) and (B.93) reduce to $p = p_\mathrm{i}$ and $\mathbf{v} = \mathbf{v}_\mathrm{i}$. Equations (B.95) and (B.96) thus vanish, and $L = L_\mathrm{i}$. Similarly, Eq. (B.97) becomes $\mathbf{v}\otimes\mathbf{v} = \mathbf{v}_\mathrm{i}\otimes\mathbf{v}_\mathrm{i}$, and Eq. (B.91) becomes

$$\mathbf{F} = \oint_A \left\langle \underline{\mathbf{I}} L_\mathrm{i} - \rho_0 \mathbf{v}_\mathrm{i}\otimes\mathbf{v}_\mathrm{i}\right\rangle \cdot \mathbf{e}_n\, dA = \mathbf{0}\,, \tag{B.98}$$

which according to Westervelt "is simply a statement of the fact that the unperturbed incident wave loses no momentum in passing through the control surface $[A]$" [121]. Combining Eqs. (B.94)–(B.98) shows that Eq. (B.91) can be written as

$$\mathbf{F} = \oint_A \left\langle \underline{\mathbf{I}}(L_\mathrm{s} + L_\mathrm{is}) - \rho_0(\mathbf{v}_\mathrm{s}\otimes\mathbf{v}_\mathrm{s} + \mathbf{v}_\mathrm{i}\otimes\mathbf{v}_\mathrm{s} + \mathbf{v}_\mathrm{s}\otimes\mathbf{v}_\mathrm{i})\right\rangle \cdot \mathbf{e}_r\, dA\,, \tag{B.99}$$

[6] Westervelt uses θ instead of ψ, but θ is reserved for the spherical polar angle in Chap. 2. See Fig. 2.1.

where it has been noted that $\mathbf{e}_n$ equals $\mathbf{e}_r$ on the surface A (see Fig. B.2). Next, since the scattered wave is in the far field ($kr^2/2a \gg 1$),

$$\mathbf{v}_\mathrm{s} = p_\mathrm{s}\mathbf{e}_r/\rho_0 c_0\,, \tag{B.100}$$

where $\mathbf{k}_s = k\mathbf{e}_r$ is the scattered wave vector, i.e., the scattered wave is locally planar in the far field. Thus $\langle L_\mathrm{s}\rangle = 0$, because the kinetic and potential energy densities are equal in plane progressive waves. Making use of Eq. (D.1), Eq. (B.100), and the fact that $\mathbf{v}_\mathrm{i}\cdot\mathbf{e}_r = v_\mathrm{i}\cos\psi$, one obtains for the outer products in Eq. (B.99)

$$(\mathbf{v}_\mathrm{s}\otimes\mathbf{v}_\mathrm{s})\cdot\mathbf{e}_r\,dA = (\mathbf{v}_\mathrm{s}\cdot\mathbf{e}_r\,dA)\mathbf{v}_\mathrm{s} = p_\mathrm{s}v_\mathrm{s}\,\mathbf{e}_r\,dA/\rho_0 c_0\,, \tag{B.101}$$

$$(\mathbf{v}_\mathrm{i}\otimes\mathbf{v}_\mathrm{s})\cdot\mathbf{e}_r\,dA = (\mathbf{v}_\mathrm{s}\cdot\mathbf{e}_r\,dA)\mathbf{v}_\mathrm{i} = p_\mathrm{s}\mathbf{v}_\mathrm{i}\,dA/\rho_0 c_0\,, \tag{B.102}$$

$$(\mathbf{v}_\mathrm{s}\otimes\mathbf{v}_\mathrm{i})\cdot\mathbf{e}_r\,dA = (\mathbf{v}_\mathrm{i}\cdot\mathbf{e}_r\,dA)\mathbf{v}_\mathrm{s} = p_\mathrm{s}v_\mathrm{i}\cos\psi\,\mathbf{e}_r\,dA/\rho_0 c_0\,. \tag{B.103}$$

Similar manipulations show that Eq. (B.96) equals

$$L_\mathrm{is} = \frac{1}{c_0}(p_\mathrm{s}v_\mathrm{i}\cos\psi - p_\mathrm{i}v_\mathrm{s})\,. \tag{B.104}$$

Using Eqs. (B.101)–(B.104), along with the fact that $\underline{\mathbf{I}}\cdot\mathbf{e}_r = \mathbf{e}_r$, one obtains for Eq. (B.99)

$$\mathbf{F} = \frac{1}{c_0}\oint_A \langle p_\mathrm{s}v_\mathrm{i}\mathbf{e}_r\cos\psi - p_\mathrm{i}v_\mathrm{s}\mathbf{e}_r - p_\mathrm{s}v_\mathrm{s}\mathbf{e}_r - p_\mathrm{s}\mathbf{v}_\mathrm{i} - p_\mathrm{s}v_\mathrm{i}\mathbf{e}_r\cos\psi\rangle\; dA\,.$$

The first and last terms in the integrand cancel, recovering Eq. (12) of Ref. 121:

$$\mathbf{F} = -\frac{1}{c_0}\oint_A \langle p_\mathrm{i}v_\mathrm{s}\mathbf{e}_\mathrm{i} + p_\mathrm{s}v_\mathrm{i}\mathbf{e}_r + p_\mathrm{s}\mathbf{v}_\mathrm{s}\rangle\, dA\,. \tag{B.105}$$

The component of the force in the direction of the incident wave is obtained by taking the inner product of both sides of Eq. (B.105) with $\mathbf{e}_\mathrm{i}$, moving $\mathbf{e}_\mathrm{i}$ inside the surface integral, and denoting $\mathbf{e}_r\cdot\mathbf{e}_\mathrm{i} = \cos\psi$:

$$F_\parallel = -\frac{1}{c_0}\oint_A \langle p_\mathrm{i}v_\mathrm{s} + (p_\mathrm{s}v_\mathrm{i} + p_\mathrm{s}v_\mathrm{s})\cos\psi\rangle\, dA\,. \tag{B.106}$$

While unit vectors cannot in general be moved inside integrals [8, p. 39], the operation leading to Eq. (B.106) is justified because the incident wave is assumed to be planar. Thus

$\mathbf{e}_\mathrm{i}$ can always be represented by a linear combination of Cartesian unit vectors, which, unlike curvilinear unit vectors, do not depend on position $\mathbf{r}$. Equation (B.106) recovers Eq. (13) of Ref. 121, from which Westervelt obtains Eq. (2) of Ref. 121 [Eq. (B.113) of the present work] by resorting to Lamb's argument that the surface integral in the far field over $\langle p_\mathrm{i}\mathbf{v}_\mathrm{s} + p_\mathrm{s}\mathbf{v}_\mathrm{i}\rangle$ equals "the total rate at which energy is withdrawn from the [incident] waves, in consequence of the presence of the obstacle" [315, p. 658, Eq. (10)]. The connection between Lamb's statement and Eq. (14) of Ref. 121 is not immediately clear, motivating the following discussion in which Eq. (2) of Ref. 121 is obtained from Eq. (B.106) by appealing to energy conservation.

In the absence of acoustic sources and sinks, energy conservation requires that [22, Eq. (1.11.2)]

$$\boldsymbol{\nabla}\cdot\mathbf{I} + \frac{\partial E}{\partial t} = 0\,, \tag{B.107}$$

where $\mathbf{I} = p\mathbf{v}$ is the instantaneous intensity and $E = T + U$ is the total instantaneous acoustic energy density. Integrating Eq. (B.107) over the volume enclosed by A, invoking the divergence theorem, and taking the time average yields

$$\oint_A \langle\mathbf{I}\rangle \cdot d\mathbf{A} = 0\,, \tag{B.108}$$

which has exploited the fact that the time average of the time derivative of a product of two time-harmonic functions vanishes (see footnote 3 on p. 193). Equation (B.108) states that the energy flux through surface A is zero in the absence of sources and sinks in the volume enclosed by A. Two scenarios based on Eq. (B.108) are now considered. The first scenario, shown in Fig. B.3(a), features an incident plane progressive wave that originates from outside the surface A propagating in the absence of the scatterer. In such a case, no scattered waves are generated, and Eq. (B.108) combined with Eqs. (B.92) and (B.93) yields

$$\oint_A \langle p_\mathrm{i}\mathbf{v}_\mathrm{i}\rangle \cdot d\mathbf{A} = 0\,. \tag{B.109}$$

In the second scenario a scatterer is introduced, as shown in Fig. B.3(b), resulting in scattered waves. In this case, Eq. (B.108) combined with Eqs. (B.92) and (B.93) yields

$$\oint_A \langle p_\mathrm{i}\mathbf{v}_\mathrm{i} + p_\mathrm{s}\mathbf{v}_\mathrm{s} + p_\mathrm{s}\mathbf{v}_\mathrm{i} + p_\mathrm{i}\mathbf{v}_\mathrm{s}\rangle \cdot d\mathbf{A} = 0\,. \tag{B.110}$$

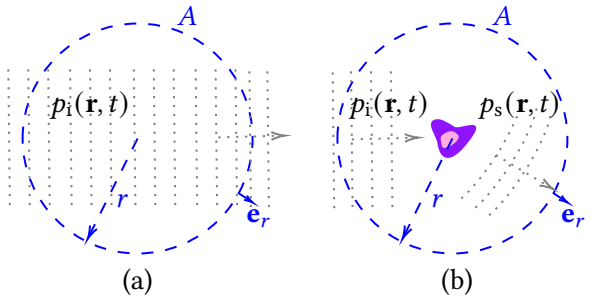

Figure B.3: (a) In the absence of a scatterer, the incident plane progressive wave p_i, which originates from outside the region enclosed by surface A, propagates unperturbed through A. The energy flux through A is given by Eq. (B.109). (b) In the presence of a scatterer, some of the incident wave is perturbed, generating the scattered wave p_s. The energy flux through A is given by Eq. (B.111).

Equations (B.109) and (B.110) are equal because the scatterer is passive; introduction of the scatterer therefore does not contribute to the energy flux through A.

Combining Eqs. (B.109) and (B.110) and recalling that $d\mathbf{A} = \mathbf{e}_r\, dA$, $\mathbf{v}_s = v_s\mathbf{e}_r$, and $\mathbf{v}_i = v_i\mathbf{e}_i$ yields

$$\oint_A \langle p_i v_s + p_s v_i \cos\psi + p_s v_s \rangle\, dA = 0\,. \tag{B.111}$$

Subtracting $\oint_A \langle p_s v_s\rangle(1-\cos\psi)dA$ from both sides of Eq. (B.111) and dividing by $-c_0$ yields

$$\frac{1}{c_0}\oint_A \langle p_s v_s\rangle(1-\cos\psi)\, dA = -\frac{1}{c_0}\oint_A \langle p_i v_s + (p_s v_i + p_s v_s)\cos\psi\rangle\, dA\,. \tag{B.112}$$

Comparing Eqs. (B.106) and (B.112) yields

$$F_{\parallel} = \frac{1}{c_0}\oint_A \langle p_s v_s\rangle(1-\cos\psi)\, dA\,, \tag{B.113}$$

which recovers Eq. (2) of Ref. 121 for a lossless scatterer. Equation (B.113) also recovers Eq. (8') of Ref. 3 upon noting that $p_s v_s/c_0 = \rho_0 v_s^2$ in the far field.

In terms of the complex-valued functions used to represent time-harmonic wave fields in Secs. 2.2, the pressure and fluid velocity of the scattered wave can be represented in the far field by Eq. (2.10) and

$$\tilde{v}_s = \frac{p_0}{\rho_0 c_0}\frac{e^{ikr}}{r}\Phi(\mathbf{k}_s)\,, \tag{B.114}$$

respectively, where the physical pressure and fluid velocity fields are given by Eq. (A.3) and $\mathbf{v}(\mathbf{r},t) = \mathrm{Re}[\tilde{\mathbf{v}}(\mathbf{r})e^{-i\omega t}]$, respectively. The time average of the scattered intensity appearing in Eq. (B.113) therefore equals

$$\langle p_\mathrm{s} v_\mathrm{s} \rangle = \frac{p_0^2}{2\rho_0 c_0} \frac{|\Phi(\mathbf{k}_\mathrm{s})|^2}{r^2}, \tag{B.115}$$

insertion of which into Eq. (B.113) yields Eq. (2.1), where $d\Omega = r^{-2} dA$ is the differential solid angle.

A qualitative derivation of Eq. (2.1) in terms of the scattering cross section, equal to $\oint |\Phi|^2 d\Omega$ of the present work, is provided van de Hulst [23, pp. 13–14]. Alternative perspectives on Westervelt's integral can be found in Ref. 182, in which the axisymmetric form of Eq. (2.1) is obtained, and in Ref. 156, in which the same result is obtained using the optical theorem. More insight into the physical meaning of the cross terms $\langle p_\mathrm{i}\mathbf{v}_\mathrm{s} + p_\mathrm{s}\mathbf{v}_\mathrm{i} \rangle$ is provided by Marston and Zhang [316]. A generalized form of Westervelt's result appropriate for Bessel beams is provided by Zhang and Marston [110, 317].

Appendix C: Notes on scattering

The theory of acoustic scattering is developed from first principles. The approach below is based on the Green's function solution of the inhomogeneous Helmholtz equation. Green's functions are defined in Sec. C.1, and the free-space Green's functions of the one- and three-dimensional inhomogeneous Helmholtz equations are obtained. The Helmholtz-Kirchhoff integral theorem is derived in Sec. C.2. A wave equation that accounts for the presence of scatterers is derived in Sec. C.3, the integral form of which is obtained in Sec. C.4. The dipole-order expansion is introduced in Sec. C.5 and is used in Sec. C.6 to calculate the radiation force exerted by progressive waves on rigid spheroids. The results of Chap. 2 are compared to previous studies in Sec. C.7. The methods discussed below are similar to methods used in quantum mechanical scattering, an accessible introduction to which is provided by Griffiths [153, Chap. 11].

C.1 Green's functions

Definition

Consider a linear differential operator $\mathcal{L}$ (e.g., $\nabla^2 + k^2$). A Green's function g satisfies[1]

$$\mathcal{L}\{g(\mathbf{r}|\mathbf{r}_0)\} = -\delta(\mathbf{r} - \mathbf{r}_0)\,. \tag{C.1}$$

The Green's function can be used to solve more general inhomogeneous differential equations, like

$$\mathcal{L}\{\phi(\mathbf{r})\} = -f(\mathbf{r})\,. \tag{C.2}$$

[1]The "−" sign in Eq. (C.1) is motivated by electrostatics. Gauss's law states that $\boldsymbol{\nabla}\cdot\mathbf{E} = \rho/\epsilon_0$, where $\mathbf{E}$ is the electric field, ρ is the charge density, and ϵ_0 is the permittivity of free space. The electric field is defined in terms of the electric potential V by $\mathbf{E} = -\boldsymbol{\nabla}V$. Combining these equations leads to Poisson's equation, which has a negative right-hand side: $\nabla^2 V = -\rho/\epsilon_0$. It is therefore convenient in electrostatics to let $g(\mathbf{r}|\mathbf{r}_0)$ solve the inhomogeneous Poisson equation with negative right-hand side.

Exploiting the sifting property of the Dirac delta function δ allows the right-hand side of Eq. (C.2) to be expressed as an integral:

$$f(\mathbf{r}) = \int f(\mathbf{r}_0)\delta(\mathbf{r} - \mathbf{r_0})\, dV_0\,. \tag{C.3}$$

In terms of Eq. (C.3), Eq. (C.2) becomes

$$\mathcal{L}\{\phi(\mathbf{r})\} = -\int f(\mathbf{r}_0)\delta(\mathbf{r} - \mathbf{r_0})\, dV_0\,. \tag{C.4}$$

Replacing $-\delta(\mathbf{r} - \mathbf{r}_0)$ in Eq. (C.4) with the right-hand side of Eq. (C.1) allows Eq. (C.2) to be written as

$$\mathcal{L}\{\phi(\mathbf{r})\} = \int f(\mathbf{r}_0)\mathcal{L}\{g(\mathbf{r}|\mathbf{r}_0)\}\, dV_0\,. \tag{C.5}$$

The linearity of the integral allows $\mathcal{L}$ in Eq. (C.5) to be removed from the integral:

$$\mathcal{L}\{\phi(\mathbf{r})\} = \mathcal{L}\left\{\int f(\mathbf{r}_0)g(\mathbf{r}|\mathbf{r}_0)\, dV_0\right\}. \tag{C.6}$$

Equation (C.6) shows that the particular solution of Eq. (C.2) is

$$\phi(\mathbf{r}) = \int f(\mathbf{r_0})g(\mathbf{r}|\mathbf{r}_0)dV_0\,, \tag{C.7}$$

where $g(\mathbf{r}|\mathbf{r}_0)$ is the *free-space Green's function* defined by Eq. (C.1). The free-space Green's function satisfies $\mathcal{L}\{g(\mathbf{r}|\mathbf{r}_0)\} = 0$ everywhere except at $\mathbf{r} = \mathbf{r}_0$.

The one- and three-dimensional free-space Green's functions of the Helmholtz equation are now derived. The former is used in Chap. 3, and the latter is used in Chaps. 2 and 4.

One-dimensional Green's function

The inhomogeneous Helmholtz equation in one dimension is

$$\frac{d^2g}{dx^2} + k^2 g = -\delta(x - x_0)\,. \tag{C.8}$$

The solution $g(x|x_0)$ has the form

$$g(x|x_0) = \begin{cases} Ae^{ik(x-x_0)}, & x > x_0 \\ Ae^{-ik(x-x_0)}, & x < x_0\,, \end{cases} \tag{C.9}$$

which can be written as

$$g(x|x_0) = Ae^{ik|x-x_0|}, \quad x \neq x_0\,. \tag{C.10}$$

To calculate the constant A, Eq. (C.8) is integrated in the vicinity of x_0, where the right-hand side of Eq. (C.8) integrates to -1 because of the definition of the delta function:

$$\left.\frac{dg}{dx}\right|_{x_0-\varepsilon}^{x_0+\varepsilon} + k^2 \int_{x_0-\varepsilon}^{x_0+\varepsilon} g\,dx = -1\,. \tag{C.11}$$

The first term in Eq. (C.11) is found by differentiating Eq. (C.9):

$$\begin{aligned} \left.\frac{dg}{dx}\right|_{x_0-\varepsilon}^{x_0+\varepsilon} &= ikAe^{ik\varepsilon} - (-ik)Ae^{ik\varepsilon} \\ &\longrightarrow 2ikA\,, \quad \varepsilon \longrightarrow 0\,. \end{aligned}$$

The second integral in Eq. (C.11) becomes

$$\begin{aligned} \int_{x_0-\varepsilon}^{x_0+\varepsilon} g\,dx &= \int_{x_0-\varepsilon}^{x_0} g\,dx + \int_{x_0}^{x_0+\varepsilon} g\,dx \\ &= \frac{A}{ik}(1 - e^{ik\varepsilon}) - \frac{A}{ik}(e^{-ik\varepsilon} - 1) \\ &\longrightarrow 0\,, \quad \varepsilon \longrightarrow 0\,. \end{aligned}$$

Equation (C.11) therefore reduces to $A = i/2k$. According to Eq. (C.10), the Green's function of the one-dimensional Helmholtz equation is therefore

$$g(x|x_0) = \frac{i}{2k}e^{ik|x-x_0|}\,. \tag{C.12}$$

Three-dimensional Green's function

Now consider the inhomogeneous Helmholtz equation in three dimensions [122, pp. 319–320]:

$$\nabla^2 g + k^2 g = -\delta(\mathbf{r} - \mathbf{r}_0)\,. \tag{C.13}$$

The solution is supposed to have the form

$$g(\mathbf{r}|\mathbf{r}_0) = A\frac{e^{ikR}}{R}\,, \tag{C.14}$$

where $R = |\mathbf{r} - \mathbf{r}_0|$. As in the case for the Green's function of the one-dimensional Helmholtz equation, the constant A is determined by integrating Eq. (C.13), this time over the volume of a sphere of radius ε centered at $\mathbf{r} = \mathbf{r}_0$:

$$\int \nabla^2 g\, dV + k^2 \int g\, dV = -1\,. \tag{C.15}$$

Since $\nabla^2 = \boldsymbol{\nabla}\cdot\boldsymbol{\nabla}$, the first integral on the left-hand side of Eq. (C.15) may be written as

$$\int \nabla^2 g\, dV = \int \boldsymbol{\nabla}\cdot\boldsymbol{\nabla} g\, dV = A\int \boldsymbol{\nabla}\cdot(-R^{-2} + ikR^{-1})e^{ikR}\mathbf{e}_R\, dV\,.$$

Since the spherical radial unit vector $\mathbf{e}_R$ is the outward normal of the spherical surface of radius ε enclosing the volume of integration, the divergence theorem is invoked:

$$\begin{aligned}\int \nabla^2 g\, dV &= A\oint (-\varepsilon^{-2} + ik\varepsilon^{-1})e^{ik\varepsilon}\, dS \\ &= 4\pi\varepsilon^2 A\left(-\frac{1}{\varepsilon^2} + \frac{ik}{\varepsilon}\right)e^{ik\varepsilon} \\ &= 4\pi A(-1 + ik\varepsilon)e^{ik\varepsilon} \\ &\to -4\pi A\,, \quad \varepsilon \to 0\,,\end{aligned} \tag{C.16}$$

where it is noted in the second line that $dS = \varepsilon^2 \sin\theta\, d\theta\, d\phi$, where θ and ϕ are the spherical polar and azimuthal coordinates, respectively. The second integral in Eq. (C.15) is evaluated in spherical coordinates (R, θ, ϕ), for which the differential volume dV equals $R^2 \sin\theta\, d\theta\, d\phi\, dR$. Since there is no dependence on θ and ϕ, $dV = 4\pi R^2 dR$, and evaluation of the second integral in Eq. (C.15) yields

$$\begin{aligned}\int \nabla^2 g\, dV &= 4\pi A\int_0^{\varepsilon} e^{ikR} R\, dR \\ &= -4\pi A k^{-2}(1 + ik\varepsilon e^{ik\varepsilon} - e^{ik\varepsilon}) \\ &\to 0\,, \quad \varepsilon \to 0\,.\end{aligned} \tag{C.17}$$

Combining Eqs. (C.14)–(C.17) shows that $A = 1/4\pi$. The Green's function of the 3D Helmholtz equation is therefore

$$g(\mathbf{r}|\mathbf{r}_0) = \frac{e^{ik|\mathbf{r}-\mathbf{r}_0|}}{4\pi|\mathbf{r}-\mathbf{r}_0|} = \frac{e^{ikR}}{4\pi R}\,. \tag{C.18}$$

For a derivation of Eq. (C.18) that does not begin with the assumed form given by Eq. (C.14), see pp. 408–411 of Ref. 153. Equation (11.65) differs from Eq. (C.18) by a minus sign because a minus sign is included in Eq. (C.13) but is not included in the corresponding Eq. (11.52) of Ref. 153.

C.2 Helmholtz-Kirchhoff integral

When the inhomogeneous term in the Helmholtz equation represents a surface or volume of scattering or radiating elements, the Helmholtz-Kirchhoff integral serves as an appropriate starting point for deriving a solution. In the absence of boundaries, the Helmholtz-Kirchhoff integral reduces to the free-space Green's function solution given by Eq. (C.7) in combination with Eq. (C.18), as shown below.[2]

Begin by considering two inhomogeneous Helmholtz equations, where G is a Green's function more general than Eq. (C.18) that accounts for the presence of boundaries [122, pp. 320–322]:

$$(\nabla^2 + k^2)\tilde{p}(\mathbf{r}) = -f(\mathbf{r})\,, \tag{C.19}$$

$$(\nabla^2 + k^2)G(\mathbf{r}|\mathbf{r}_0) = -\delta(\mathbf{r}-\mathbf{r}_0)\,. \tag{C.20}$$

Subtracting Eq. (C.20) times $\tilde{p}$ from Eq. (C.19) times G yields

$$G(\mathbf{r}|\mathbf{r}_0)\nabla^2\tilde{p}(\mathbf{r}) - \tilde{p}(\mathbf{r})\nabla^2 G(\mathbf{r}|\mathbf{r}_0) = -G(\mathbf{r}|\mathbf{r}_0)f(\mathbf{r}) + \tilde{p}(\mathbf{r})\delta(\mathbf{r}-\mathbf{r}_0)\,. \tag{C.21}$$

[2] The derivation that follows is adapted from the discussion leading to Eq. (7.1.17) of Ref. 122. See pp. 473–476 of Ref. 9 for an alternative derivation.

Now interchange $\mathbf{r}$ and $\mathbf{r}_0$ in Eq. (C.21), noting that $G(\mathbf{r}|\mathbf{r}_0) = G(\mathbf{r}_0|\mathbf{r})$ and $\delta(\mathbf{r} - \mathbf{r}_0) = \delta(\mathbf{r}_0 - \mathbf{r})$. Taking the volume integral of the resulting equation yields

$$\begin{aligned}\int [G(\mathbf{r}|\mathbf{r}_0)\nabla_0^2\tilde{p}(\mathbf{r}_0) - \tilde{p}(\mathbf{r}_0)\nabla_0^2 G(\mathbf{r}|\mathbf{r}_0)]dV_0 \\ = -\int G(\mathbf{r}|\mathbf{r}_0)f(\mathbf{r}_0)dV_0 + \int \tilde{p}(\mathbf{r}_0)\delta(\mathbf{r} - \mathbf{r}_0)dV_0\,. \end{aligned} \tag{C.22}$$

Gauss's theorem is used to convert the volume integral on the left-hand side of Eq. (C.22) to a surface integral:

$$\tilde{p}(\mathbf{r}) = \int f(\mathbf{r})G(\mathbf{r}|\mathbf{r}_0)dV_0 + \oint \left[G(\mathbf{r}|\mathbf{r}_0)\frac{\partial\tilde{p}(\mathbf{r}_0)}{\partial n_0} - \tilde{p}(\mathbf{r_0})\frac{\partial G(\mathbf{r}|\mathbf{r}_0)}{\partial n_0}\right]dA_0\,, \tag{C.23}$$

where $\mathbf{n}$ is the outward unit normal, and Eq. (C.23) is observed to be an implicit solution for $\tilde{p}$. In free space, the surface integral vanishes, $G = g$, and Eq. (C.23) reduces to the explicit solution

$$\tilde{p}(\mathbf{r}) = \int f(\mathbf{r}_0)g(\mathbf{r}|\mathbf{r}_0)dV_0\,.$$

Equation (C.23) is used in Sec. C.4 to develop the scattering solution that forms the basis for Chap. 2. Equation (C.23) is also a traditional starting point for the derivation of the Rayleigh integral and diffraction phenomena [22, Sec. 5.2.1], as mentioned in Sec. 4.2.

C.3 Wave equation for inhomogeneous media

To describe the scattering of acoustic waves from heterogeneities, a wave equation for an inhomogeneous medium must be developed. The following derivation combines the approaches taken by Morse and Ingard [122, pp. 407–409] and Pierce [22, Sec. 9.1.4]. While Morse and Ingard allow the spatial heterogeneities to vary in time, Pierce does not; the latter assumption is made here.

Let $\rho_s(\mathbf{r})$ be the spatially dependent ambient density and $\rho'(\mathbf{r}, t)$ be the linear acoustic field quantity. Pierce provides the appropriate equation of state [22, p. 15]:

If the ambient state is inhomogeneous, $p = p(\rho, s_0)$ cannot be used and one falls back on $p = p(\rho, s)$, $Ds/Dt = 0$ as a starting point. If $p_0(\mathbf{x})$ and $\rho_0(\mathbf{x})$ are independent of t, these lead to

$$\frac{\partial p'}{\partial t} + \mathbf{v}' \cdot \boldsymbol{\nabla} p_0 = c^2 \left(\frac{\partial \rho'}{\partial t} + \mathbf{v}' \cdot \boldsymbol{\nabla} \rho_0 \right)$$

as the linear equation that replaces $[p' = c^2 \rho', c^2 = (\partial p/\partial \rho)_0]$.

Using the notation of the present work, noting that $\boldsymbol{\nabla} p_0 = \mathbf{0}$ in the present work, and solving for $\partial \rho'/\partial t$ yields

$$\frac{\partial \rho'}{\partial t} = \frac{1}{c^2} \frac{\partial p}{\partial t} - \mathbf{v} \cdot \boldsymbol{\nabla} \rho_s(\mathbf{r}) \,. \tag{C.24}$$

Equation (C.24) is used to eliminate the perturbation density from the systems of partial differential equations that follow.

The exact mass conservation equation in an inhomogeneous medium is

$$\frac{\partial}{\partial t} [\rho_s(\mathbf{r}) + \rho'(\mathbf{r}, t)] + \boldsymbol{\nabla} \cdot \{ [\rho_s(\mathbf{r}) + \rho'(\mathbf{r}, t)] \mathbf{v} \} = 0 \,.$$

Neglecting the nonlinear term $\rho'(\mathbf{r}, t)\mathbf{v}$ and expanding the divergence of the product $\rho_s(\mathbf{r})\mathbf{v}$ yields

$$\frac{\partial \rho'(\mathbf{r}, t)}{\partial t} + \rho_s(\mathbf{r}) \boldsymbol{\nabla} \cdot \mathbf{v} + \mathbf{v} \cdot \boldsymbol{\nabla} \rho_s(\mathbf{r}) = 0 \,.$$

Inserting the linearized state equation given by Eq. (C.24) results in

$$\frac{1}{c^2} \frac{\partial p}{\partial t} - \mathbf{v} \cdot \boldsymbol{\nabla} \rho_s(\mathbf{r}) + \rho(\mathbf{r}) \boldsymbol{\nabla} \cdot \mathbf{v} + \mathbf{v} \cdot \boldsymbol{\nabla} \rho_s(\mathbf{r}) = 0 \,.$$

The $\mathbf{v} \cdot \boldsymbol{\nabla} \rho_s(\mathbf{r})$ terms cancel, resulting in

$$\boldsymbol{\nabla} \cdot \mathbf{v} = -\beta_s(\mathbf{r}) \frac{\partial p}{\partial t} \,. \tag{C.25}$$

Conservation of momentum requires that

$$\boldsymbol{\nabla} p + \frac{\partial}{\partial t} \{ [\rho_s(\mathbf{r}) + \rho'(\mathbf{r}, t)] \mathbf{v} \} = \mathbf{0} \,.$$

Neglecting the nonlinear term $\rho'\mathbf{v}$ yields

$$\boldsymbol{\nabla} p + \frac{\partial}{\partial t}[\rho_s(\mathbf{r})\mathbf{v}] = \mathbf{0}\,.$$

Since ρ is not a function of time, it can be removed from the time derivative:

$$\boldsymbol{\nabla} p + \rho_s(\mathbf{r})\frac{\partial \mathbf{v}}{\partial t} = \mathbf{0}\,.$$

Solving for $\partial\mathbf{v}/\partial t$ gives

$$\frac{\partial \mathbf{v}}{\partial t} = -\frac{1}{\rho_s(\mathbf{r})}\boldsymbol{\nabla} p\,. \tag{C.26}$$

The wave equation for an inhomogeneous medium is derived by taking the time derivative of Eq. (C.25) and the divergence of Eq. (C.26). Subtracting the resulting equations yields

$$\frac{\partial}{\partial t}(\boldsymbol{\nabla}\cdot\mathbf{v}) - \boldsymbol{\nabla}\cdot\left[\frac{\partial \mathbf{v}}{\partial t}\right] = -\beta_s(\mathbf{r})\frac{\partial^2 p}{\partial t^2} + \boldsymbol{\nabla}\cdot\left[\frac{1}{\rho_s(\mathbf{r})}\boldsymbol{\nabla} p\right].$$

The left-hand side of the above equation vanishes, resulting in

$$\boldsymbol{\nabla}\cdot\left[\frac{\boldsymbol{\nabla} p}{\rho_s(\mathbf{r})}\right] = \beta_s(\mathbf{r})\frac{\partial^2 p}{\partial t^2}\,. \tag{C.27}$$

Denoting the density and compressibility of the background medium as ρ_0 and β_0, respectively, allows Eq. (C.27) to be written as

$$\boldsymbol{\nabla}\cdot\left[\left(\frac{1}{\rho_s(\mathbf{r})} - \frac{1}{\rho_0}\right)\boldsymbol{\nabla} p + \frac{\boldsymbol{\nabla} p}{\rho_0}\right] = [\beta_s(\mathbf{r}) - \beta_0]\frac{\partial^2 p}{\partial t^2} + \beta_0\frac{\partial^2 p}{\partial t^2}\,,$$

rearrangement of which yields

$$\frac{1}{\rho_0}\nabla^2 p - \beta_0\frac{\partial^2 p}{\partial t^2} = [\beta_s(\mathbf{r}) - \beta_0]\frac{\partial^2 p}{\partial t^2} - \boldsymbol{\nabla}\cdot\left\{\left[\frac{1}{\rho_s(\mathbf{r})} - \frac{1}{\rho_0}\right]\boldsymbol{\nabla} p\right\}.$$

The equation above is rearranged further in preparation to identify dimensionless spatially dependent contrast factors:

$$\nabla^2 p - \beta_0\rho_0\frac{\partial^2 p}{\partial t^2} = -\beta_0\rho_0\left[1 - \frac{\beta_s(\mathbf{r})}{\beta_0}\right]\frac{\partial^2 p}{\partial t^2} - \boldsymbol{\nabla}\cdot\left\{\left[\frac{\rho_0}{\rho_s(\mathbf{r})} - 1\right]\boldsymbol{\nabla} p\right\}.$$

In terms of the sound speed c_0 of the background medium and Eqs. (2.3), the preceding equation becomes

$$\nabla^2 p - \frac{1}{c_0^2}\frac{\partial^2 p}{\partial t^2} = \frac{\gamma_\beta(\mathbf{r})}{c_0^2}\frac{\partial^2 p}{\partial t^2} + \boldsymbol{\nabla}\cdot\left[\gamma_\rho(\mathbf{r})\boldsymbol{\nabla} p\right] . \tag{C.28}$$

Equation (C.28) recovers Morse and Ingard's Eq. (8.1.11) for material contrast factors that are not functions of time [122]. Assuming a time-harmonic solution [Eq. (A.3)] reduces Eq. (C.28) to Eq. (2.2).

C.4 Exact integral solution

Equation (2.2) can be written as

$$\nabla^2\tilde{p} + k^2\tilde{p} = -h(\mathbf{r}) ,$$

where

$$h(\mathbf{r}) = k^2\gamma_\beta\tilde{p} - \boldsymbol{\nabla}\cdot(\gamma_\rho\boldsymbol{\nabla}\tilde{p}) . \tag{C.29}$$

The particular solution of an inhomogeneous Helmholtz equation is given by Eq. (C.23),

$$\tilde{p}(\mathbf{r}) = \int h(\mathbf{r}_\mathrm{s})G(\mathbf{r}|\mathbf{r}_\mathrm{s})dV_\mathrm{s} + \oint\left[G(\mathbf{r}|\mathbf{r}_\mathrm{s})\frac{\partial\tilde{p}(\mathbf{r}_\mathrm{s})}{\partial n_\mathrm{s}} - \tilde{p}(\mathbf{r}_\mathrm{s})\frac{\partial G(\mathbf{r}|\mathbf{r}_\mathrm{s})}{\partial n_\mathrm{s}}\right]dA_\mathrm{s} , \tag{C.30}$$

where $G(\mathbf{r}|\mathbf{r}_\mathrm{s})$ is the appropriate Green's function [122, Eq. (7.1.15)], $\mathbf{r}_\mathrm{s}$ is the spatial integration coordinate, and n_s denotes the normal component of the gradient operator $\boldsymbol{\nabla}_\mathrm{s}$. The volume integral in Eq. (C.30) is taken "over the whole volume occupied by the medium," and the surface integral is evaluated "on the surface bounding the medium" [122, p. 319–322]. Assuming that the volume occupied by the medium is unbounded reduces $G(\mathbf{r}|\mathbf{r}_\mathrm{s})$ to the free-space Green's function given by Eq. (C.18), notated here as

$$g(\mathbf{r}|\mathbf{r}_\mathrm{s}) = \frac{e^{ik|\mathbf{r}-\mathbf{r}_\mathrm{s}|}}{4\pi|\mathbf{r}-\mathbf{r}_\mathrm{s}|} . \tag{C.31}$$

The solution of Eq. (2.2) in terms of Eq. (C.29) is then

$$\tilde{p}(\mathbf{r}) = \tilde{p}(\mathbf{r}\to\infty) + \int h(\mathbf{r}_\mathrm{s})g(\mathbf{r}|\mathbf{r}_\mathrm{s})dV_\mathrm{s} , \tag{C.32}$$

where

$$\tilde{p}(\mathbf{r} \to \infty) = \oint \left[g(\mathbf{r}|\mathbf{r}_\mathrm{s}) \frac{\partial \tilde{p}(\mathbf{r}_\mathrm{s})}{\partial n_\mathrm{s}} - \tilde{p}(\mathbf{r}_\mathrm{s}) \frac{\partial g(\mathbf{r}|\mathbf{r}_\mathrm{s})}{\partial n_\mathrm{s}} \right] dA_\mathrm{s} \,.$$

The pressure field infinitely far away from the scatterer is simply the field due to the incident wave $\tilde{p}_\mathrm{i}(\mathbf{r})$, so $\tilde{p}(\mathbf{r} \to \infty) = \tilde{p}_\mathrm{i}(\mathbf{r})$. Therefore, the total field given by Eq. (C.32) becomes

$$\tilde{p}(\mathbf{r}) = \tilde{p}_\mathrm{i}(\mathbf{r}) + \tilde{p}_\mathrm{s}(\mathbf{r}) \,, \tag{C.33}$$

where

$$\tilde{p}_\mathrm{s}(\mathbf{r}) = \int \left\{ k^2 \gamma_\beta(\mathbf{r}_\mathrm{s}) p(\mathbf{r}_\mathrm{s}) - \boldsymbol{\nabla}_\mathrm{s} \cdot \left[\gamma_\rho(\mathbf{r}_\mathrm{s}) \boldsymbol{\nabla}_\mathrm{s} p(\mathbf{r}_\mathrm{s}) \right] \right\} g(\mathbf{r}|\mathbf{r}_\mathrm{s}) dV_\mathrm{s} \,. \tag{C.34}$$

Noting from the product rule of divergences that

$$\begin{aligned} &\boldsymbol{\nabla}_\mathrm{s} \cdot [\gamma_\rho(\mathbf{r}_\mathrm{s}) \boldsymbol{\nabla}_\mathrm{s} \tilde{p}(\mathbf{r}_\mathrm{s})] g(\mathbf{r}_\mathrm{s}|\mathbf{r}_\mathrm{s}) \\ &\quad = \boldsymbol{\nabla}_\mathrm{s} \cdot \{\gamma_\rho(\mathbf{r}_\mathrm{s}) [\boldsymbol{\nabla}_\mathrm{s} \tilde{p}(\mathbf{r}_\mathrm{s})] g(\mathbf{r}|\mathbf{r}_\mathrm{s})\} - \gamma_\rho(\mathbf{r}_\mathrm{s}) \boldsymbol{\nabla}_\mathrm{s} \tilde{p}(\mathbf{r}_\mathrm{s}) \cdot \boldsymbol{\nabla}_\mathrm{s} g(\mathbf{r}|\mathbf{r}_\mathrm{s}) \end{aligned} \tag{C.35}$$

allows Eq. (C.34) to be written as

$$\begin{aligned} \tilde{p}_\mathrm{s}(\mathbf{r}) = &\int k^2 \gamma_\beta(\mathbf{r}_\mathrm{s}) \tilde{p}(\mathbf{r}_\mathrm{s}) g(\mathbf{r}|\mathbf{r}_\mathrm{s}) dV_\mathrm{s} - \int \boldsymbol{\nabla}_\mathrm{s} \cdot \{\gamma_\rho(\mathbf{r}_\mathrm{s}) [\boldsymbol{\nabla}_\mathrm{s} \tilde{p}(\mathbf{r}_\mathrm{s})] g(\mathbf{r}|\mathbf{r}_\mathrm{s})\} dV_\mathrm{s} \\ &+ \int \gamma_\rho(\mathbf{r}_\mathrm{s}) \boldsymbol{\nabla}_\mathrm{s} \tilde{p}(\mathbf{r}_\mathrm{s}) \cdot \boldsymbol{\nabla}_\mathrm{s} g(\mathbf{r}|\mathbf{r}_\mathrm{s}) dV_\mathrm{s} \,. \end{aligned} \tag{C.36}$$

Invoking the divergence theorem allows the second integral of Eq. (C.36) to be written as

$$- \int \boldsymbol{\nabla}_\mathrm{s} \cdot \{\gamma_\rho(\mathbf{r}_\mathrm{s}) [\boldsymbol{\nabla}_\mathrm{s} \tilde{p}(\mathbf{r}_\mathrm{s})] g(\mathbf{r}|\mathbf{r}_\mathrm{s})\} dV_\mathrm{s} = - \oint \gamma_\rho(\mathbf{r}_\mathrm{s}) \frac{\partial \tilde{p}}{\partial n_\mathrm{s}} g(\mathbf{r}|\mathbf{r}_\mathrm{s}) dS_\mathrm{s},$$

which vanishes on the surface at ∞ because $\gamma_\rho = 0$ at ∞. The first and third terms of Eq. (C.36) therefore yield Eq. (2.7).

C.5 Dipole-order expansion

The dipole-order expansion of the scattered pressure given by Eq. (2.19) is derived from first principles by obtaining expressions for volume and force sources, replacing the integrand in Eq. (2.7) with those expressions, and representing an extended scatterer as a point scatterer.

Consider a sphere of radius a centered at the origin that pulsates radially with time-harmonic velocity amplitude v_0. The general form of the radiated pressure field is [9]

$$\tilde{p}(r) = B\frac{e^{ikr}}{r}, \tag{C.37}$$

where the constant B is determined by substituting Eq. (C.37) into the linearized momentum equation $\partial\tilde{p}/\partial r = -i\omega\rho_0 v_0$ evaluated at $r = a$:

$$B = -\frac{ika^2\rho_0 c_0 v_0}{1 - ika}e^{-ika}. \tag{C.38}$$

Combining Eqs. (C.37) and (C.38) and assuming $ka \ll 1$ yields

$$\tilde{p}(r) = -ik\rho_0 c_0 Q\frac{e^{ikr}}{4\pi r}, \tag{C.39}$$

where $Q = 4\pi a^2 v_0$ is the volume velocity. If the center of the sphere is translated from the origin $\mathbf{0}$ to another location $\mathbf{r}_s$, then r in Eq. (C.39) is replaced with $R = |\mathbf{r} - \mathbf{r}_s|$. In view of the free-space Green's function given by Eq. (2.8), the pressure field due to a monopole at $\mathbf{r} = \mathbf{r}_s$ can be expressed as

$$\tilde{p}(\mathbf{r}|\mathbf{r}_s) = -ik\rho_0 c_0 Q g(\mathbf{r}|\mathbf{r}_s), \tag{C.40}$$

recovering the second of Pierce's Eqs. (4-3.1), where it is noted that Pierce's "monopole amplitude" $\hat{S}$ equals $-ik\rho_0 c_0 \hat{Q}_s/4\pi$ [22].

The field radiated by a dipole is described by two out-of-phase monopoles separated along the z axis by a distance h:

$$\tilde{p}(\mathbf{r}) = -ik\rho_0 c_0 Q[g(\mathbf{r}|z_s = h/2) - g(\mathbf{r}|z_s = -h/2)]. \tag{C.41}$$

In the $h \to 0$ limit, Eq. (C.41) becomes

$$\tilde{p}(\mathbf{r}) = \rho_0 \dot{Q} h[\partial g/\partial z_s]_{r_s=0}, \tag{C.42}$$

where $\dot{Q} = -ikc_0 Q$ is the time derivative of the volume velocity. Following Blackstock's discussion on p. 369 of Ref. 9, the quantity $\rho_0 \dot{Q} h$ is identified as a time harmonic force

F exerted in the z direction. If the separation between the monopoles in Eq. (C.41) is not restricted to the z axis and is instead denoted by a separation vector $\mathbf{h}$ extending from the negative monopole to the positive monopole defining the dipole, then the partial derivative of the Green's function with respect to z in Eq. (C.42) generalizes to the gradient of the Green's function with respect to $\mathbf{r}_s$. Equation (C.42) then becomes

$$\tilde{p}(\mathbf{r}|\mathbf{r}_s) = \mathbf{F} \cdot \boldsymbol{\nabla}_s g(\mathbf{r}|\mathbf{r}_s)\,, \tag{C.43}$$

where $\mathbf{F} = \rho_0 \dot{Q}\mathbf{h}$. Equation (C.43) recovers Pierce's Eq. (4-4.1), [22] where the identification of the force vector recovers Pierce's discussion in Sec. 4.4 of Ref. 22, in which $\mathbf{F} = -ik\rho_0 c_0 4\pi a^2 v_0 \mathbf{h} = \rho_0 \dot{Q}\mathbf{h}$. In Pierce's notation, the identification is expressed as $\mathbf{F} = 4\pi\hat{\mathbf{d}} = 4\pi\hat{S}\mathbf{d}$, where $\hat{S}$ is the "monopole amplitude" defined below Eqs. (4.3.1) for a point source as $-i\omega\rho a^2 \hat{v}_s$.

The integrand of Eq. (2.7) can be interpreted as the contribution of volume and force sources given by Eqs. (C.40) and (C.43), respectively. Setting $k^2\gamma_\beta p\Delta V = -ik\rho_0 c_0 Q$ and $\gamma_\rho \boldsymbol{\nabla} p\Delta V = \mathbf{F}$ yields the identifications

$$q(\mathbf{r}) = \frac{Q}{\Delta V} = \frac{ik}{\rho_0 c_0}\gamma_\beta(\mathbf{r})\tilde{p}(\mathbf{r})\,, \tag{C.44}$$

$$\mathbf{f}(\mathbf{r}) = \frac{\mathbf{F}}{\Delta V} = \gamma_\rho(\mathbf{r})\boldsymbol{\nabla}\tilde{p}(\mathbf{r})\,. \tag{C.45}$$

In terms of Eqs. (C.44) and (C.45), Eq. (2.7) can be expressed as

$$\tilde{p}_s(\mathbf{r}) = -ik\rho_0 c_0 \int q(\mathbf{r}_s) g(\mathbf{r}|\mathbf{r}_s)\, dV_s + \int \mathbf{f}(\mathbf{r}_s) \cdot \boldsymbol{\nabla}_s g(\mathbf{r}|\mathbf{r}_s)\, dV_s\,. \tag{C.46}$$

Equation (C.46) recovers the second of Eqs. (A2) of Sieck et al. [13] upon replacing kc_0 with ω and noting that the gradient in Eq. (C.46) is evaluated over the scatterer's coordinates $\mathbf{r}_s$. The evaluation by Sieck et al. of the gradient over the field coordinate $\mathbf{r}$ causes the second term of the second of Eqs. (A2) in Ref. 13 to differ in sign from the second integral in Eq. (C.46).

The field at $\mathbf{r}$ due to a point scatterer located at the origin $\mathbf{0}$ is obtained by letting $q = -ikc_0 m\delta(\mathbf{r}_s)$ and $\mathbf{f} = ikc_0 \mathbf{d}(\mathbf{r}_s)\delta(\mathbf{r}_s)$ in Eq. (C.46), where these definitions are identical

to those introduced by Sieck et al. on p. 18 of Ref. 13:

$$\tilde{p}_{\mathrm{s}}(\mathbf{r}) = ik\rho_0 c_0 \int ikc_0 m\delta(\mathbf{r}_{\mathrm{s}}) g(\mathbf{r}|\mathbf{r}_{\mathrm{s}})\, dV_{\mathrm{s}} + ikc_0 \int \mathbf{d}(\mathbf{r}_{\mathrm{s}})\delta(\mathbf{r}_{\mathrm{s}}) \cdot \boldsymbol{\nabla}_{\mathrm{s}} g(\mathbf{r}|\mathbf{r}_{\mathrm{s}})\, dV_{\mathrm{s}} \,. \tag{C.47}$$

Using the sifting property of the delta function yields Eq. (2.19), which recovers the second of Eqs. (19) of Sieck et al. [13] The second term of Eq. (2.19) differs in sign from the dipole term of the second of Eqs. (19) of Ref. 13 due to the choice of coordinate with respect to which the gradient is evaluated, as illustrated by Pierce's Eq. (4-4.2). [22]

C.6 Radiation force on rigid subwavelength spheroids

As discussed in Sec. 2.3, if the compressibility and density of a scatterer are even functions of position $\mathbf{r}$, the scattered pressure is represented in the Born approximation by Eq. (2.10) in combination with

$$\Phi = \frac{k^2}{4\pi}(\alpha_{\mathrm{m}} + \mathbf{e}_r \cdot \underline{\boldsymbol{\alpha}}_{\mathrm{d}} \cdot \mathbf{e}_{\mathrm{i}}) \,. \tag{C.48}$$

Sections 2.2 and 2.3 show that the Born approximation simplifies the calculation of the polarizabilities to volume integrals over the scatterer's material properties [Eqs. (2.27)–(2.29)]. This simplification is used in Sec. 2.4 to calculate the radiation force exerted by plane progressive waves on subwavelength objects. Although the Born approximation facilitates the calculation of fields scattered from fairly complicated scatterers, Born scatterers do not experience transverse radiation forces at dipole order because the scattered dipole field is parallel to the incident velocity field [7, p. 491], i.e., $\underline{\boldsymbol{\alpha}}_{\mathrm{d}} = \alpha_{\mathrm{d}}\underline{\mathbf{I}}$, where $\underline{\mathbf{I}}$ is the identity tensor. A consequence of the fact that $\underline{\boldsymbol{\alpha}}_{\mathrm{d}} = \alpha_{\mathrm{d}}\underline{\mathbf{I}}$ for Born scatterers is that radiation forces perpendicular to the incident wave vanish in the subwavelength limit, as demonstrated by the inhomogeneous cube considered in Sec. 2.4.

Meanwhile, scatterers with large material contrasts are characterized by a dipole polarizability tensor that is generally not proportional to $\underline{\mathbf{I}}$. The objective of the following discussion is to calculate radiation forces due to progressive waves on such scatterers. Scattering solutions for rigid subwavelength spheroids depicted in Fig. C.1 and defined in

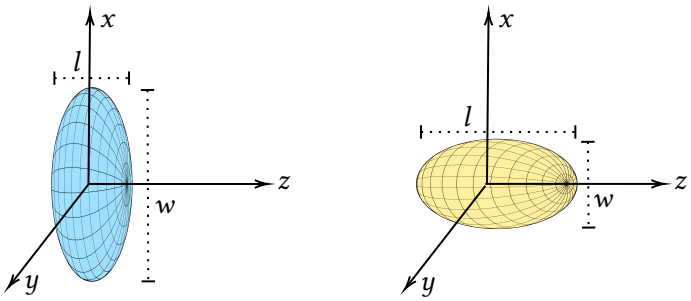

(a) Oblate spheroid (b) Prolate spheroid

Figure C.1: Geometry of (a) an oblate spheroid, for which $l < w$ in Eq. (C.49), and (b) a prolate spheroid, for which $l > w$. The z axis is oriented in the rightward direction. Diagram of spheroids adapted from Ref. 318.

Cartesian coordinates (x, y, z) by

$$\frac{x^2 + y^2}{(w/2)^2} + \frac{z^2}{(l/2)^2} = 1 \tag{C.49}$$

are combined with Westervelt's far-field integrals for the radiation force parallel and perpendicular to $\mathbf{e}_i$, given by Eqs. (2.1) and (2.32), respectively. The field scattered by an oblate spheroid ($l < w$) as a function of rotation angle about the y axis is presented in terms of α_m and $\underline{\boldsymbol{\alpha}}_d$, and Eqs. (2.1) and (2.32) are used to calculate the corresponding radiation forces exerted on the spheroid. The analysis is then repeated for a prolate spheroid ($l > w$).

Oblate spheroid

Consider a rigid oblate spheroid defined by Eq. (C.49) with the aspect ratio $l/w = 1/2$. The volume of the spheroid is $V = \pi w^3/12$, and the directivity of the scattered wave is given by Eq. (C.48), where

$$\alpha_m = -V\,, \quad \underline{\boldsymbol{\alpha}}_d = \underline{\mathbf{M}} \tag{C.50}$$

and $\underline{\mathbf{M}}$ is a quantity adapted from electromagnetic scattering by Senior [164]. Methods of obtaining matrix representations of $\underline{\mathbf{M}}$ are discussed in Refs. 319 and 320; it suffices to note in the present discussion that Eqs. (C.50) in combination with Eqs. (C.48) and (2.10) satisfy Eq. (A.4) inside the spheroid and Eq. (A.1) outside the spheroid. For the orientation

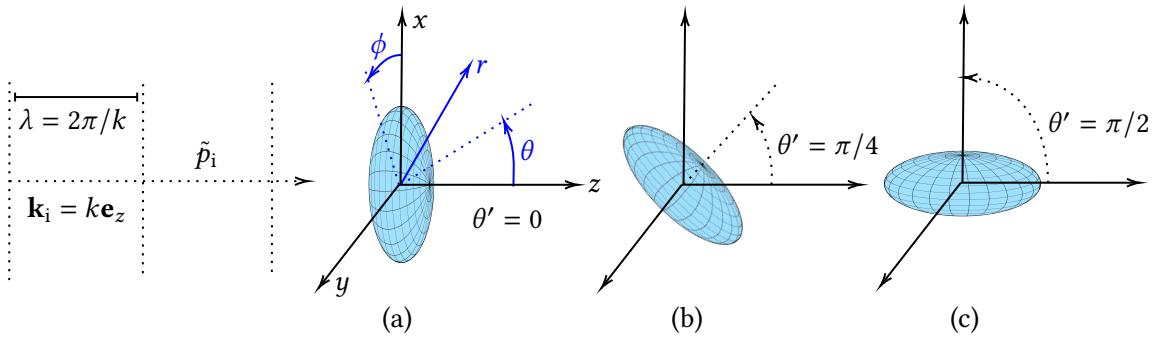

Figure C.2: Geometry of oblate spheroid with respect to the incident wave $\tilde{p}_\mathrm{i}$ for three angles of rotation about the y axis: (a) $\theta' = 0$, (b) $\theta = \pi/4$, and (c) $\theta = \pi/2$. Diagram of oblate spheroid adapted from Ref. 318.

and axes shown in Fig. C.2(a), $\mathbf{e}_\mathrm{i}$ and $\underline{\mathbf{M}}$ are represented in Cartesian coordinates (x, y, z) by

$$[e_z] = \begin{pmatrix} 0 \\ 0 \\ 1 \end{pmatrix}, \quad [M] = V \begin{pmatrix} 1 & 0 & 0 \\ 0 & 1 & 0 \\ 0 & 0 & 2 \end{pmatrix}, \tag{C.51}$$

respectively, where the matrix components are determined from Fig. 1 of Ref. 164.[3]

To consider rotations of the spheroid about the y axis by an angle θ' (see Fig. C.2), the rotation matrix

$$[R_y] = \begin{pmatrix} \cos\theta' & 0 & \sin\theta' \\ 0 & 1 & 0 \\ -\sin\theta' & 0 & \cos\theta' \end{pmatrix} \tag{C.52}$$

is used to transform $[M]$ given by Eq. (C.51) according to the formula $[M]' = [R_y][M][R_y]^\mathrm{T}$ for active rotations [153, Eq. (A.64)], yielding

$$[M]' = V \begin{pmatrix} 1 + \sin^2\theta' & 0 & \frac{1}{2}\sin 2\theta' \\ 0 & 1 & 0 \\ \frac{1}{2}\sin 2\theta' & 0 & 1 + \cos^2\theta' \end{pmatrix}. \tag{C.53}$$

In terms of Eqs. (C.50) and (C.53), Eq. (C.48) equals

$$\Phi = -\frac{k^2 V}{4\pi}\left[1 - \tfrac{1}{2}\sin 2\theta' \sin\theta\cos\phi - (1 + \cos^2\theta')\cos\theta\right], \tag{C.54}$$

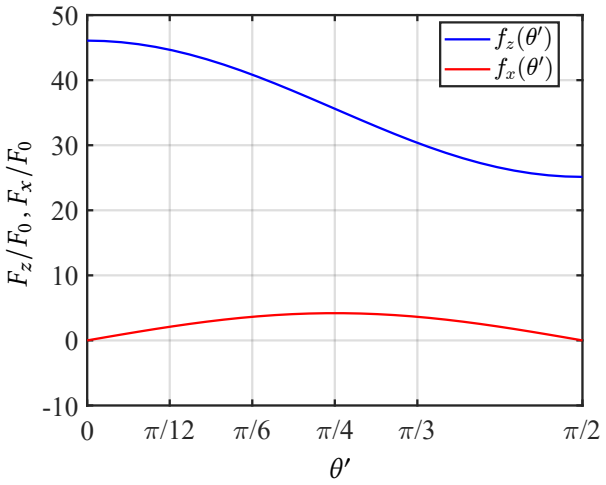

Figure C.3: Dimensionless radiation forces $F_z/F_0 = f_z(\theta')$ and $F_x/F_0 = f_x(\theta')$ exerted by a plane progressive wave on an oblate spheroid as functions of the angle of rotation θ' about the y axis.

where it has been noted that $\mathbf{e}_r \cdot \mathbf{e}_x = \sin\theta\cos\phi$ and $\mathbf{e}_r \cdot \mathbf{e}_z = \cos\theta$.

According to Eq. (2.1), the radiation force in the z direction corresponding to Eq. (C.54) is

$$F_z = \frac{p_0^2}{2\rho_0 c_0^2}\int_0^{2\pi}\int_0^{\pi} |\Phi|^2(1-\cos\theta)\sin\theta\, d\theta\, d\phi = F_0 f_z(\theta')\,, \tag{C.55}$$

while from Eq. (2.32) the radiation force in the x direction is

$$F_x = -\frac{p_0^2}{2\rho_0 c_0^2}\int_0^{2\pi}\int_0^{\pi} |\Phi|^2\,\sin^2\theta\,\cos\phi\, d\theta\, d\phi = F_0 f_x(\theta')\,, \tag{C.56}$$

where

$$F_0 = \frac{p_0^2 A}{2\rho_0 c_0^2}\frac{(kw)^4}{576\pi} \tag{C.57}$$

is the normalization factor. The factor of area A in Eq. (C.57) equals $\pi(w/2)^2$, which corresponds to the cross-sectional area of the oblate spheroid for $\theta' = 0$, as shown in Fig. C.2(a). Equations (C.55) and (C.56) are plotted as functions of θ' in Fig. C.3. The component F_z

[3] See also Fig. 9-2 of Ref. 22.

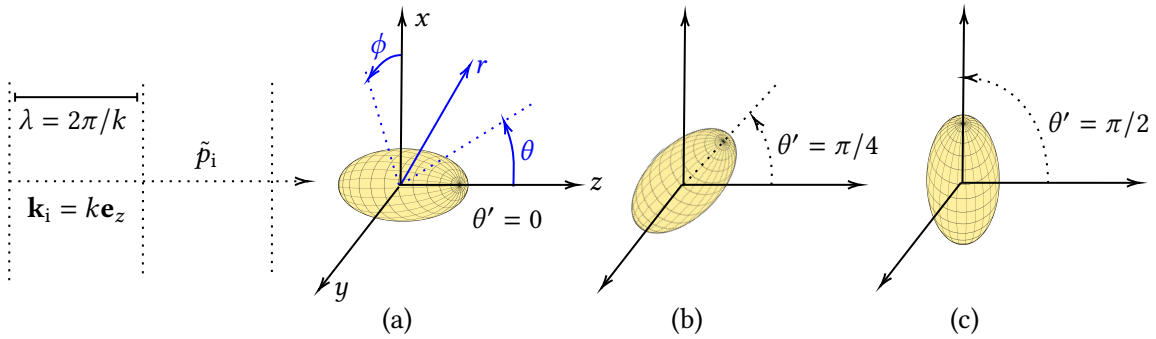

Figure C.4: Geometry of prolate spheroid with respect to the incident wave $\tilde{p}_\mathrm{i}$ for three angles of rotation about the y axis: (a) $\theta' = 0$, (b) $\theta = \pi/4$, and (c) $\theta = \pi/2$. Diagram of prolate spheroid adapted from Ref. 318.

decreases monotonically in θ' because the cross-sectional area accompanying the counterclockwise rotation decreases from $0 < \theta' < \pi/2$. By symmetry, the radiation force in the x direction vanishes for $\theta' = 0$ and $\theta' = \pi/2$, as can be intuited from Figs. C.2(a) and (c). For intermediate values of θ', F_x is predicted in the positive x direction. Such forces were studied previously by Smagin et al. and have been called the "lateral recoil force" [32]. Meanwhile, the y component of the force, obtained by replacing the factor of $\cos\phi$ in Eq. (C.56) with $\sin\phi$, is zero for all θ' due to symmetry.

Prolate spheroid

Considered next is a prolate spheroid defined by Eq. (C.49) for $l/w = 5$. In this case, $V = 5\pi w^3/6$, and the matrix representation of $\underline{\mathbf{M}}$ for the spheroid oriented in Fig. C.4(a) is [164]

$$[M] = V\begin{pmatrix} 2 & 0 & 0 \\ 0 & 2 & 0 \\ 0 & 0 & 1 \end{pmatrix}, \tag{C.58}$$

In this case, $[M]' = [R_y][M][R_y]^\mathrm{T}$ yields

$$[M]' = V\begin{pmatrix} 1+\cos^2\theta' & 0 & -\frac{1}{2}\sin 2\theta' \\ 0 & 2 & 0 \\ -\frac{1}{2}\sin 2\theta' & 0 & 1+\sin^2\theta' \end{pmatrix}. \tag{C.59}$$

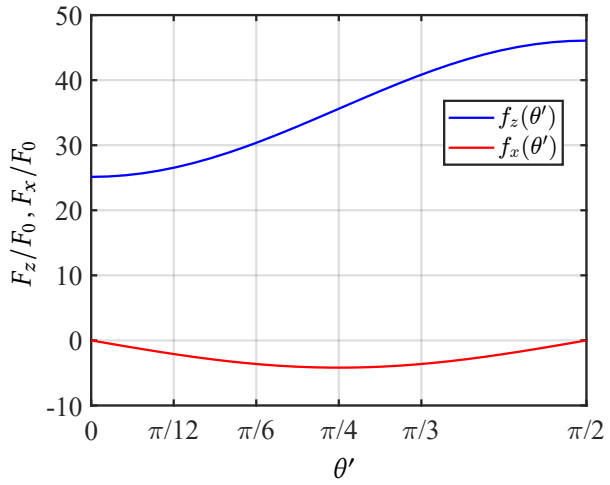

Figure C.5: Dimensionless radiation forces $F_z/F_0 = f_z(\theta')$ and $F_x/F_0 = f_x(\theta')$ exerted by a plane progressive wave on an prolate spheroid as functions of the angle of rotation θ'.

In terms of Eqs. (C.50) and (C.59), Eq. (C.48) equals

$$\Phi = -\frac{k^2 V}{4\pi}\left[1 + \tfrac{1}{2}\sin 2\theta' \sin\theta\cos\phi - (1 + \sin^2\theta')\cos\theta\right]. \tag{C.60}$$

Evaluating Eqs. (C.55) and (C.56) for Φ given by Eq. (C.60) yields $F_z = F_0 f_z(\theta')$ and $F_x = F_0 f_x(\theta')$, respectively, where the normalization factor is now

$$F_0 = \frac{p_0^2 A}{2\rho_0 c_0^2}\frac{25(kw)^4}{144\pi} \tag{C.61}$$

and A corresponds to the the cross-sectional area of the prolate spheroid for $\theta' = 0$, as shown in Fig. C.4(a). Similar to Fig. C.3, F_x vanishes for $\theta' = 0$ and $\theta' = \pi/2$ by symmetry, as can be seen in Figs. C.4(a) and (c). In contrast with Fig. C.3, negative values of F_x are predicted for intermediate values of θ' due to the orientation of the prolate spheroid with respect to the incident wave. As in Sec. C.6, the y component of the radiation force is zero by symmetry.

Future work related to rigid subwavelength scatterers may involve considering the limits $l \ll w$ and $l \gg w$, which approximate a rigid disk and rod, respectively. The radiation forces presented in Figs. C.3 and C.5 may also be compared with results obtained using the finite element method.

C.7 Comments on previous polarizability-based calculations

The results of the present work are compared with those obtained by Sepehrirahnama et al. [33], in which alternative conventions introduced by Quan et al. [56] are used. For clarity, equations numbers from Ref. 33 are labeled with an "S." To relate Eqs. (2.27)–(2.29) to the polarizabilities α_{pp}, $\boldsymbol{\alpha}_{pv}$, $\boldsymbol{\alpha}_{vp}$, and $\underline{\boldsymbol{\alpha}}_{vv}$ used in Ref. 33, it is first necessary to relate the monopole strength m and dipole moment $\mathbf{d}$ of the present work to the monopole strength and dipole moment used in Ref. 33, denoted m' and $\mathbf{d}'$, respectively. The dipole-order expansion used in Ref. 33 is given by the first of Eqs. (S5), which is the far-field approximation of

$$\tilde{p}_\mathrm{s}(\mathbf{r}) = -k^2 c_0^2 m' g(\mathbf{r}|\mathbf{r}_\mathrm{s}) + k^2 c_0^2 \mathbf{d}' \cdot \boldsymbol{\nabla} g(\mathbf{r}|\mathbf{r}_\mathrm{s}) \,, \tag{C.62}$$

where $\mathbf{d}'$ has been removed from the divergence because $\boldsymbol{\nabla} \cdot \mathbf{d}' = 0$. Meanwhile, the dipole-order expansion used in the present work is given by Eq. (2.19), which for a scatterer located at position $\mathbf{r}_\mathrm{s}$ is

$$\tilde{p}_\mathrm{s}(\mathbf{r}) = -k^2 \rho_0 c_0^2 m g(\mathbf{r}|\mathbf{r}_\mathrm{s}) + ikc_0 \mathbf{d} \cdot \boldsymbol{\nabla} g(\mathbf{r}|\mathbf{r}_\mathrm{s}) \,. \tag{C.63}$$

Comparing Eqs. (C.62) and (C.63) shows that

$$m' = \rho_0 m \,, \quad \mathbf{d}' = i\mathbf{d}/kc_0 \,. \tag{C.64}$$

The polarizabilities used in Ref. 33 are defined by Eqs. (S7):

$$m' = \alpha_{pp} \tilde{p} + \boldsymbol{\alpha}_{pv} \cdot \tilde{\mathbf{u}} \,, \tag{C.65}$$

$$\mathbf{d}' = \boldsymbol{\alpha}_{pv} \tilde{p} + \underline{\boldsymbol{\alpha}}_{vv} \cdot \tilde{\mathbf{u}} \,. \tag{C.66}$$

Inserting Eqs. (2.20), (2.21), (C.65), and (C.66) into Eq. (C.64) yields the relations

$$\alpha_{pp} = -\alpha_\mathrm{m}/c_0^2 \,, \quad \underline{\boldsymbol{\alpha}}_{vv} = i\rho_0 \underline{\boldsymbol{\alpha}}_\mathrm{d}/kc_0 \,, \tag{C.67}$$

$$\boldsymbol{\alpha}_{pv} = -i\rho_0 \boldsymbol{\alpha}_\mathrm{c}/c_0 = -ik\rho_0 c_0 \boldsymbol{\alpha}_{vp} \,, \tag{C.68}$$

where j has been replaced with i because the convention $j(kx - \omega t)$ is used in Ref. 33.

Considered first is the radiation force for cases in which $\boldsymbol{\alpha}_\mathrm{c} = \mathbf{0}$. The present formulation predicts the radiation force given by Eq. (2.31), which in Sec. 2.4 is shown to recover Gor'kov's analytical result and agree with solutions based on spherical wave expansions for homogeneous and layered spheres. The radiation force exerted by progressive waves is given in Ref. 33 by the first of their Eqs. (S28). Combining Eq. (2.27) for α_m with Eq. (C.67) shows that α_{pp} is real-valued; thus the first of their Eqs. (S28), the first term of which is proportional to $\mathrm{Im}(\alpha_{pp})$, reduces to only a single term. Therefore the radiation force due to progressive waves predicted by the first of Eqs. (S28) of Ref. 33 does not recover Gor'kov's Eq. (10), which contains three terms [3].

Moreover, substituting Eq. (S27) into Eq. (S17) does not lead to the first of Eqs. (S28), as is claimed in Ref. 33. Noting from Eq. (S28) that

$$\boldsymbol{\nabla} p_\mathrm{i}^2 = \mathrm{Re}[2ikP_a^2 e^{2i(kz-\omega t)}]\mathbf{e}_z \tag{C.69}$$

shows that the first term of Eq. (S17) is proportional to

$$\langle \boldsymbol{\nabla} p_\mathrm{i}^2 \rangle = \tfrac{1}{2}\,\mathrm{Re}(2ikP_a^2)\mathbf{e}_z = \mathbf{0}\,. \tag{C.70}$$

It is unclear why α_{pp} appears in the first of Eqs. (S28) in view of Eq. (C.70).

While it does not appear to affect the calculation of the first of Eqs. (S28), another inconsistency can be found in Eq. (S27), in which the gradient of the incident pressure field should not contain the minus sign.

Attention is now turned to the case in which $\boldsymbol{\alpha}_\mathrm{c}$ is nonzero. It is concluded in Ref. 33 that "the direct contribution of the Willis coupling terms $\boldsymbol{\alpha}_{pv}$ and $\boldsymbol{\alpha}_{vp}$ to the force under [a] traveling wave is zero," whereas the presence of $\boldsymbol{\alpha}_\mathrm{c} = ic_0\boldsymbol{\alpha}_{pv}/\rho_0 = -kc_0^2\boldsymbol{\alpha}_{vp}$ in Φ given by Eq. (2.26) shows that the coupled polarizability does in general contribute to the radiation force through Westervelt's integral given by Eq. (2.1). An example of an object in which the coupled polarizabilities contribute solely to the radiation force are the inhomogeneous cubes considered in Sec. 2.4, for which radiation forces on the order of $(ka)^6$ are predicted.

As suggested in Sec. 2.3, errors in Eq. (S28) of may be due to the fact that Eq. (S17) does not contain terms that are proportional to the momentum of the scattered wave.

While forces due to standing waves are not the focus of the present work, it should be noted that Eqs. (S10) and (S20), which are related to the radiation force on a sphere in a standing wave, also contain errors. In terms of the notation of Ref. 33, the top-left element of the matrix in Eq. (S10) should appear as $\Omega f_\beta/c_\mathrm{f}^2$, and the first term of Eq. (S20) should appear as $f_\beta \tilde{p}_\mathrm{i}^2/2\kappa_\mathrm{f}$, as is now shown. Invoking the relation $\tilde{p}_\mathrm{s} = i\omega\rho_\mathrm{f}\phi_s$ allows Eq. (S4) to be expressed as

$$\tilde{p}_\mathrm{s} = -\frac{i\omega a_\mathrm{s}^3}{3} f_\beta \frac{\partial \rho_\mathrm{i}}{\partial t}\frac{e^{ikr}}{r} - \tfrac{1}{2} i\omega\rho_\mathrm{f} a_\mathrm{s}^3 \boldsymbol{\nabla}\cdot(f_\rho \tilde{\mathbf{u}}_\mathrm{i} e^{ikr}/r)\,. \tag{C.71}$$

Noting that $\partial\rho_\mathrm{i}/\partial t = -i\omega\rho_\mathrm{i} = -i\omega\tilde{p}_\mathrm{i}/c_\mathrm{f}^2$ and $G = e^{ikr}/4\pi r$ yields

$$\tilde{p}_\mathrm{s} = -\tfrac{4}{3}\pi a_\mathrm{s}^3 \frac{\omega^2}{c_\mathrm{f}^2} f_\beta \tilde{p}_\mathrm{i} G - \omega^2 \boldsymbol{\nabla}\cdot(2\pi i a_\mathrm{s}^3 \rho_\mathrm{f} f_\rho \tilde{\mathbf{u}}_\mathrm{i} G/\omega)\,. \tag{C.72}$$

To determine the corresponding polarizabilities, Eq. (C.72) of Ref. 33 is equated to the scattered field described by the multipole expansion to dipole order [Eq. (S5)]:

$$\tilde{p}_\mathrm{s} = -\omega^2 \Omega M G + \omega^2 \boldsymbol{\nabla}\cdot(\Omega \mathbf{D} G)\,. \tag{C.73}$$

Substituting the monopole strength and dipole moment

$$M = m'/\Omega\,, \quad \mathbf{D} = d'/\Omega \tag{C.74}$$

defined by Eqs. (S7) into Eq. (C.73) yields

$$\tilde{p}_\mathrm{s} = -\omega^2(\alpha_{pp}\tilde{p}_\mathrm{i} + \boldsymbol{\alpha}_{pv}\cdot\tilde{\mathbf{u}}_\mathrm{i})G + \omega^2\boldsymbol{\nabla}\cdot\left[(\boldsymbol{\alpha}_{vp}\tilde{p}_\mathrm{i} + \underline{\boldsymbol{\alpha}}_{vv}\cdot\tilde{\mathbf{u}}_\mathrm{i})G\right]. \tag{C.75}$$

Equation (C.72) is now equated to Eq. (C.75). Since $\tilde{p}_\mathrm{i}$ and $\boldsymbol{\nabla}\cdot\tilde{\mathbf{u}}_\mathrm{i}$ (and not $\boldsymbol{\nabla}\tilde{p}_\mathrm{i}$ and $\tilde{\mathbf{u}}_\mathrm{i}$) appear in Eq. (C.72), it is concluded that $\boldsymbol{\alpha}_{pv} = \mathbf{0}$ and $\boldsymbol{\alpha}_{vp} = \mathbf{0}$. Equation (C.75) therefore reduces to

$$\tilde{p}_\mathrm{s} = -\omega^2\alpha_{pp}\tilde{p}_\mathrm{i} G + \omega^2\boldsymbol{\nabla}\cdot(\underline{\boldsymbol{\alpha}}_{vv}\cdot\tilde{\mathbf{u}}_\mathrm{i} G)\,. \tag{C.76}$$

Comparing Eqs. (C.72) and (C.76) and noting for a sphere that $\Omega = 4\pi a_\mathrm{s}^3/3$ yields expressions for the monopole and dipole polarizabilities:

$$\alpha_{pp} = \Omega \frac{f_\beta}{c_\mathrm{f}^2} \quad \text{and} \quad \underline{\boldsymbol{\alpha}}_{vv} = -\frac{3i\Omega}{2\omega} \rho_\mathrm{f} f_\rho \underline{\mathbf{I}}. \tag{C.77}$$

While the second of Eqs. (C.77) matches the bottom-right element of the 2×2 block matrix in Eq. (S10), the first of Eqs. (C.77) does not match the top-left element of the block matrix. The error in Eq. (S10) propagates to Eq. (S20). The correct form of the equation is obtained by substituting Eq. (C.77) into Eq. (S19) and noting that $\mathbf{F} = -\boldsymbol{\nabla} G$, yielding

$$G = \frac{4\pi a^3}{3} \left\langle \frac{f_\beta}{2\kappa_\mathrm{f}} p_\mathrm{i}^2 - \frac{3 f_\rho}{4} \rho_\mathrm{f} u_\mathrm{i}^2 \right\rangle, \tag{C.78}$$

whereas the first term of Eq. (S20) is given incorrectly by $f_\beta \kappa_\mathrm{f} \tilde{p}_\mathrm{i}^2/2$.

Finally, it is noted that the quantity $\kappa_\mathrm{f} = \rho_\mathrm{f} c_\mathrm{f}^2$ is incorrectly called the "fluid compressibility" on p. 2 of Ref. 33. While $\rho_\mathrm{f} c_\mathrm{f}^2$ is in fact the bulk modulus of the fluid, Eqs. (S10) and (S20) would be correct if κ_f were the compressibility, which equals $1/\rho_\mathrm{f} c_\mathrm{f}^2$.

Appendix D: Tensor transpositions

The present appendix discusses vector and tensor operations relevant to Sec. 3.3. More complete discussions of the algebra and calculus of vectors and tensors are provided by Refs. 227, 230, and 321.

D.1 Outer products

Definition

The outer product $\otimes$ is defined in terms of three vectors $\mathbf{u}$, $\mathbf{v}$, and $\mathbf{w}$:

$$(\mathbf{u} \otimes \mathbf{v}) \cdot \mathbf{w} = (\mathbf{v} \cdot \mathbf{w})\mathbf{u} \,. \tag{D.1}$$

Associativity

The outer product is associative:

$$(\mathbf{u} \otimes \mathbf{v}) \otimes \mathbf{w} = \mathbf{u} \otimes (\mathbf{v} \otimes \mathbf{w}) \,. \tag{D.2}$$

To prove Eq. (D.2), the inner product is taken between the left-hand side of Eq. (D.2) and a fourth arbitrary vector $\mathbf{x}$:

$$[(\mathbf{u} \otimes \mathbf{v}) \otimes \mathbf{w}] \cdot \mathbf{x} = (\mathbf{u} \otimes \mathbf{v})(\mathbf{w} \cdot \mathbf{x}) = \mathbf{u} \otimes (\mathbf{w} \cdot \mathbf{x})\mathbf{v} = \mathbf{u} \otimes (\mathbf{v} \otimes \mathbf{w}) \cdot \mathbf{x} \,.$$

Equation (D.1) has been used in the first and third equalities above, and the fact that $\mathbf{w} \cdot \mathbf{x}$ is a scalar is used to magnify $\mathbf{v}$ in the second equality. Since $\mathbf{x}$ is an arbitrary vector, the proof of Eq. (D.2) is complete.

D.2 Rank-2 tensors

Definition of transpose

The transpose of a rank-2 tensor $\underline{\mathbf{a}}$ is defined by [227, Eq. (1.119)]

$$(\underline{\mathbf{a}}^{\mathrm{T}} \cdot \mathbf{u}) \cdot \mathbf{v} = (\underline{\mathbf{a}} \cdot \mathbf{v}) \cdot \mathbf{u} \,, \tag{D.3}$$

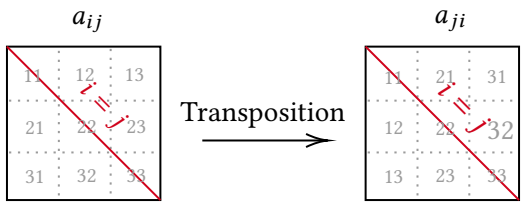

Figure D.1: The transposition of a rank-2 tensor is conceptualized as exchanging the elements of its matrix representation across the red line along which $i = j$. If a_{ij} are the elements of the matrix representing $\underline{\mathbf{a}}$ in a given basis, then a_{ji} are the elements of the matrix representation of $\underline{\mathbf{a}}^{\mathrm{T}}$. If $a_{ij} = a_{ji}$, the matrix is symmetric.

where $\mathbf{u}$ and $\mathbf{v}$ are two arbitrary vectors. A rank-2 tensor is symmetric if $\underline{\mathbf{a}} = \underline{\mathbf{a}}^{\mathrm{T}}$. The tensor $\underline{\mathbf{a}}$ can be represented in index notation as a_{ij}, which is the ijth component of the matrix representing $\underline{\mathbf{a}}$ in a particular basis. In index notation, Eq. (D.3) is expressed as

$$a_{ji}u_j v_i = a_{ij}v_j u_i \,. \tag{D.4}$$

Equation (D.4) shows that in index notation, transposition of a rank-2 tensor involves interchanging indices $j \leftrightarrow i$. Since each factor of Eq. (D.4) is a scalar, the commutative property can be used to equivalently express the left-hand side as $a_{ji}v_i u_j$, $u_j a_{ji} v_i$, $v_i u_j a_{ji}$, or $u_j v_i a_{ji}$. If $a_{ij} = a_{ji}$, the matrix representation of $\underline{\mathbf{a}}$ is symmetric. In Fig. D.1, the transposition of the matrix representation of a rank-2 tensor is illustrated as the exchange of matrix elements elements across the main diagonal.

Transpose of the transpose

The transpose of the transpose of a rank-2 tensor is itself. To prove this, consider two arbitrary vectors $\mathbf{u}$ and $\mathbf{v}$ and invoke Eq. (D.3) twice:

$$[(\underline{\mathbf{a}}^{\mathrm{T}})^{\mathrm{T}} \cdot \mathbf{u}] \cdot \mathbf{v} = (\underline{\mathbf{a}}^{\mathrm{T}} \cdot \mathbf{v}) \cdot \mathbf{u} = (\underline{\mathbf{a}} \cdot \mathbf{u}) \cdot \mathbf{v} \,.$$

Since $\mathbf{u}$ and $\mathbf{v}$ are arbitrary,

$$(\underline{\mathbf{a}}^{\mathrm{T}})^{\mathrm{T}} = \underline{\mathbf{a}} \,. \tag{D.5}$$

Transpose of a product

The transpose of a product of rank-2 tensors equals the product of the transposed tensors in reverse order, as can be shown by introducing three arbitrary vectors, $\mathbf{b}$, $\mathbf{u}$, and $\mathbf{v}$:

$$\begin{aligned}
[(\underline{\mathbf{a}} \cdot \underline{\mathbf{b}})^{\mathrm{T}} \cdot \mathbf{u}] \cdot \mathbf{v} &= [(\underline{\mathbf{a}} \cdot \underline{\mathbf{b}}) \cdot \mathbf{v}] \cdot \mathbf{u} \\
&= [\underline{\mathbf{a}} \cdot (\underline{\mathbf{b}} \cdot \mathbf{v})] \cdot \mathbf{u} \\
&= (\underline{\mathbf{b}} \cdot \mathbf{v}) \cdot (\underline{\mathbf{a}}^{\mathrm{T}} \cdot \mathbf{u}) \\
&= [\underline{\mathbf{b}}^{\mathrm{T}} \cdot (\underline{\mathbf{a}}^{\mathrm{T}} \cdot \mathbf{u})] \cdot \mathbf{v} \\
&= [(\underline{\mathbf{b}}^{\mathrm{T}} \cdot \underline{\mathbf{a}}^{\mathrm{T}}) \cdot \mathbf{u}] \cdot \mathbf{v} \,.
\end{aligned}$$

The definition of transpose given by Eq. (D.3) has been used in the first, third, and fourth lines, and the composition property has been used in the second and final lines [230, p. 11]. Since the vectors introduced are arbitrary, it has been shown that

$$(\underline{\mathbf{a}} \cdot \underline{\mathbf{b}})^{\mathrm{T}} = \underline{\mathbf{b}}^{\mathrm{T}} \cdot \underline{\mathbf{a}}^{\mathrm{T}} \,. \tag{D.6}$$

Transpose of an outer product

It is sometimes convenient to express a rank-2 tensor as an outer product of two vectors, e.g., $\mathbf{u} \otimes \mathbf{v}$. The transpose of such a tensor is obtained by reversing the order of the vectors in the outer product, i.e., $(\mathbf{u} \otimes \mathbf{v})^{\mathrm{T}} = \mathbf{v} \otimes \mathbf{u}$. To prove this, two arbitrary vectors $\mathbf{a}$ and $\mathbf{d}$ are introduced, and the commutativity of the inner product between two vectors is used:

$$[(\mathbf{u} \otimes \mathbf{v})^{\mathrm{T}} \cdot \mathbf{d}] \cdot \mathbf{a} = \mathbf{a} \cdot [(\mathbf{u} \otimes \mathbf{v})^{\mathrm{T}} \cdot \mathbf{d}] = [(\mathbf{u} \otimes \mathbf{v}) \cdot \mathbf{a}] \cdot \mathbf{d}$$

The definition of the transpose operation is invoked in the second equality. Invoking the definition of outer product allows the above equation to be written as

$$\begin{aligned}
[(\mathbf{u} \otimes \mathbf{v})^{\mathrm{T}} \cdot \mathbf{d}] \cdot \mathbf{a} &= [(\mathbf{v} \cdot \mathbf{a})\mathbf{u}] \cdot \mathbf{d} \\
&= (\mathbf{u} \cdot \mathbf{d})(\mathbf{v} \cdot \mathbf{a}) \\
&= [(\mathbf{u} \cdot \mathbf{d})\mathbf{v}] \cdot \mathbf{a} \\
&= (\mathbf{v} \otimes \mathbf{u}) \cdot \mathbf{d} \cdot \mathbf{a} \,.
\end{aligned}$$

Since $\mathbf{a}$ and $\mathbf{d}$ are arbitrary vectors, it has been shown that

$$(\mathbf{u} \otimes \mathbf{v})^{\mathrm{T}} = (\mathbf{v} \otimes \mathbf{u})\,. \tag{D.7}$$

D.3 Rank-3 tensors

While there is only one transposition of a rank-2 tensor [Eq. (D.3)], there are *five* transpositions of a rank-3 tensor, three of which are called "minor" and two of which are called "major."

Minor transpositions

The three minor transpositions of a rank-3 tensor $\underset{\sim}{\mathbf{a}}$ are defined by

$$[(\underset{\sim}{\mathbf{a}}^{\mathrm{t1}} \cdot \mathbf{u}) \cdot \mathbf{v}] \cdot \mathbf{w} = [(\underset{\sim}{\mathbf{a}} \cdot \mathbf{u}) \cdot \mathbf{w}] \cdot \mathbf{v}\,, \tag{D.8a}$$

$$[(\underset{\sim}{\mathbf{a}}^{\mathrm{t2}} \cdot \mathbf{u}) \cdot \mathbf{v}] \cdot \mathbf{w} = [(\underset{\sim}{\mathbf{a}} \cdot \mathbf{v}) \cdot \mathbf{u}] \cdot \mathbf{w}\,, \tag{D.8b}$$

$$[(\underset{\sim}{\mathbf{a}}^{\mathrm{t3}} \cdot \mathbf{u}) \cdot \mathbf{v}] \cdot \mathbf{w} = [(\underset{\sim}{\mathbf{a}} \cdot \mathbf{w}) \cdot \mathbf{v}] \cdot \mathbf{u}\,. \tag{D.8c}$$

Equations (D.8a) and (D.8b) can be expressed alternatively by invoking the definition of the transpose of rank-2 tensors given by Eq. (D.3). Replacing $\underset{\sim}{\mathbf{a}}^{\mathrm{t1}} \cdot \mathbf{u}$ with $\underline{\mathbf{b}}$ allows Eq. (D.8a) to be written as

$$(\underline{\mathbf{b}} \cdot \mathbf{v}) \cdot \mathbf{w} = (\underline{\mathbf{b}}^{\mathrm{T}} \cdot \mathbf{w}) \cdot \mathbf{v} = [(\underset{\sim}{\mathbf{a}} \cdot \mathbf{u}) \cdot \mathbf{w}] \cdot \mathbf{v}\,,$$

where Eq. (D.3) has been used to obtain the first equality. According to the second equality, $\underline{\mathbf{b}}^{\mathrm{T}} = \underset{\sim}{\mathbf{a}} \cdot \mathbf{u}$. Reinstating $\underline{\mathbf{b}} = \underset{\sim}{\mathbf{a}}^{\mathrm{t1}} \cdot \mathbf{u}$ shows that

$$(\underset{\sim}{\mathbf{a}}^{\mathrm{t1}} \cdot \mathbf{u})^{\mathrm{T}} = \underset{\sim}{\mathbf{a}} \cdot \mathbf{u}\,.$$

Taking the transpose of the equation above yields

$$[(\underset{\sim}{\mathbf{a}}^{\mathrm{t1}} \cdot \mathbf{u})^{\mathrm{T}}]^{\mathrm{T}} = (\underset{\sim}{\mathbf{a}} \cdot \mathbf{u})^{\mathrm{T}}\,,$$

and application of Eq. (D.5) shows that the first minor transpose of a rank-3 tensor can be defined by

$$\underset{\sim}{\mathbf{a}}^{\mathrm{t1}} \cdot \mathbf{u} = (\underset{\sim}{\mathbf{a}} \cdot \mathbf{u})^{\mathrm{T}}\,. \tag{D.9}$$

The matrix representation of Eq. (D.8a) is

$$a_{jik}u_k v_j w_i = a_{ijk}u_k w_j v_i \,, \tag{D.10}$$

i.e., the first minor transpose amounts to permuting the *first* two indices ($i \leftrightarrow j$).

The second minor transpose of a rank-3 tensor given by Eq. (D.8b) can similarly be expressed in terms of the transpose of a rank-2 tensor. Using the definition of the outer product allows Eq. (D.8b) to be written as

$$[\underset{\sim}{\mathbf{a}}^{\mathrm{t2}} : (\mathbf{v} \otimes \mathbf{u})] \cdot \mathbf{w} = [\underset{\sim}{\mathbf{a}} : (\mathbf{u} \otimes \mathbf{v})] \cdot \mathbf{w} \,.$$

Identifying $\mathbf{v} \otimes \mathbf{u}$ as an arbitrary rank-2 tensor $\underline{\mathbf{x}}$ and recalling Eq. (D.7) shows that

$$(\underset{\sim}{\mathbf{a}}^{\mathrm{t2}} : \underline{\mathbf{x}}) \cdot \mathbf{w} = (\underset{\sim}{\mathbf{a}} : \underline{\mathbf{x}}^{\mathrm{T}}) \cdot \mathbf{w} \,,$$

so the second minor transpose of a rank-3 tensor can be defined by

$$\underset{\sim}{\mathbf{a}}^{\mathrm{t2}} : \underline{\mathbf{x}} = \underset{\sim}{\mathbf{a}} : \underline{\mathbf{x}}^{\mathrm{T}} \,. \tag{D.11}$$

The indicial representation of Eq. (D.8b) is

$$a_{ikj}u_k v_j w_i = a_{ijk}v_k u_j w_i \tag{D.12}$$

which amounts to permuting the *second* two indices ($j \leftrightarrow k$).

The third minor transpose given by Eq. (D.8c) is not of relevance to Sec. 3.3, but it is noted that its matrix representation corresponds to exchanging the first and third indices ($k \leftrightarrow i$):

$$a_{kji}u_k v_j w_i = a_{ijk}w_k v_j u_i \,. \tag{D.13}$$

Figure D.2 illustrates the matrix representations of the three minor transposition operations of a rank-2 tensor. Whereas matrix elements were exchanged about a *line* in the matrix representation of the transpose of a rank-2 tensor (see Fig. D.1), the elements are exchanged about *planes* in the matrix representation of the transposes of a rank-3 tensor, where the line along which $i = j = k$ lies in each plane.

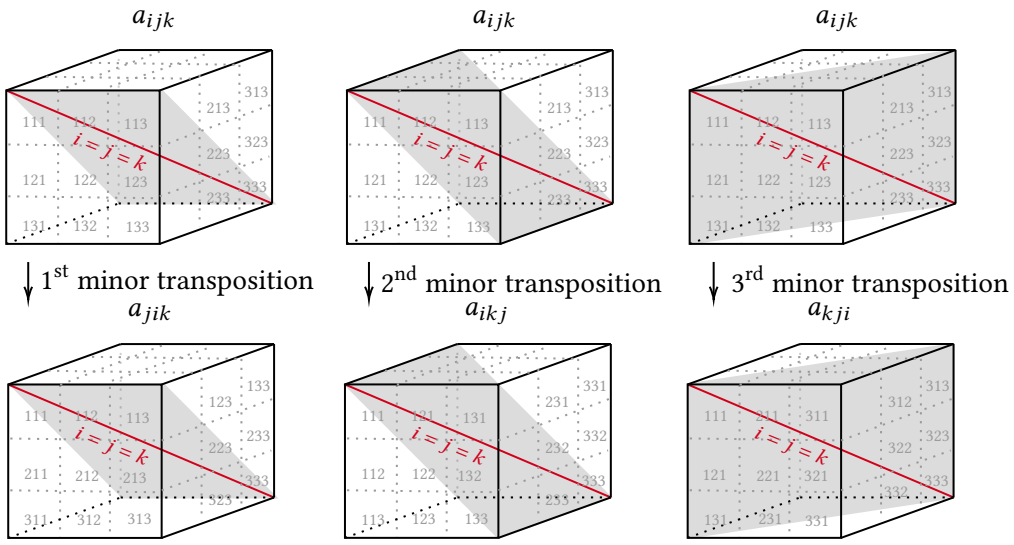

Figure D.2: The minor transpositions of a rank-3 tensor given symbolically by Eqs. (D.8a), (D.8b), and (D.8c) are often represented in index notation by Eqs. (D.10), (D.12), and (D.13). Similar to the exchange of elements in Fig. D.1, the transpose operations for rank-3 tensors corresponds to exchanges of elements across the main diagonal (shown in red above).

Major transpositions

The two major transposes of a rank-3 tensor are defined by

$$[(\underset{\sim}{\mathbf{a}}^{\mathrm{T1}} \cdot \mathbf{u}) \cdot \mathbf{v}] \cdot \mathbf{w} = [(\underset{\sim}{\mathbf{a}} \cdot \mathbf{w}) \cdot \mathbf{u}] \cdot \mathbf{v} \tag{D.14}$$

$$[(\underset{\sim}{\mathbf{a}}^{\mathrm{T2}} \cdot \mathbf{u}) \cdot \mathbf{v}] \cdot \mathbf{w} = [(\underset{\sim}{\mathbf{a}} \cdot \mathbf{v}) \cdot \mathbf{w}] \cdot \mathbf{u}\,. \tag{D.15}$$

Like the minor transposes, the major transposes can be written in terms of rank-2 tensors and vectors. Invoking the definition of the outer product allows Eq. (D.14) to be written as

$$[\underset{\sim}{\mathbf{a}}^{\mathrm{T1}} : (\mathbf{v} \otimes \mathbf{u})] \cdot \mathbf{w} = (\underset{\sim}{\mathbf{a}} \cdot \mathbf{w}) : (\mathbf{v} \otimes \mathbf{u})\,.$$

Denoting $\mathbf{v} \otimes \mathbf{u} = \underline{\mathbf{b}}$ yields

$$(\underset{\sim}{\mathbf{a}}^{\mathrm{T1}} : \underline{\mathbf{b}}) \cdot \mathbf{w} = (\underset{\sim}{\mathbf{a}} \cdot \mathbf{w}) : \underline{\mathbf{b}}\,. \tag{D.16}$$

In index notation, Eq. (D.14) can be expressed as

$$a_{jki} u_k v_j w_i = a_{ijk} w_k u_j v_i\,, \tag{D.17}$$

showing that the first major transpose corresponds to the permutations $i \mapsto j$, $j \mapsto k$, and $k \mapsto i$.

Similarly, the second major transpose defined by Eq. (D.15) can be written as

$$(\underset{\sim}{\mathbf{a}}^{\mathrm{T2}} \cdot \mathbf{u}) : (\mathbf{w} \otimes \mathbf{v}) = [\underset{\sim}{\mathbf{a}} : (\mathbf{w} \otimes \mathbf{v})] \cdot \mathbf{u}\,.$$

Denoting $\mathbf{w} \otimes \mathbf{v} = \underline{\mathbf{c}}$ yields

$$(\underset{\sim}{\mathbf{a}}^{\mathrm{T2}} \cdot \mathbf{u}) : \underline{\mathbf{c}} = [\underset{\sim}{\mathbf{a}} : \underline{\mathbf{c}}] \cdot \mathbf{u}\,. \tag{D.18}$$

In index notation, Eq. (D.15) may be expressed as

$$a_{kij} u_k v_j w_i = a_{ijk} v_k w_j u_i\,, \tag{D.19}$$

showing that the second major transpose corresponds to the permutations $i \mapsto k$, $j \mapsto i$, and $k \mapsto j$.

Unlike Eq. (D.5) for rank-2 tensors, $(\underset{\sim}{\mathbf{a}}^{\mathrm{T1}})^{\mathrm{T1}} \neq \underset{\sim}{\mathbf{a}}$ and $(\underset{\sim}{\mathbf{a}}^{\mathrm{T2}})^{\mathrm{T2}} \neq \underset{\sim}{\mathbf{a}}$. Instead, for an arbitrary vector $\mathbf{u}$ and rank-2 tensor $\underline{\mathbf{c}}$,

$$[(\underset{\sim}{\mathbf{a}}^{\mathrm{T2}})^{\mathrm{T1}} : \underline{\mathbf{c}}] \cdot \mathbf{u} = [\underset{\sim}{\mathbf{a}}^{\mathrm{T1}} \cdot \mathbf{u}] : \underline{\mathbf{c}} = (\underset{\sim}{\mathbf{a}} : \underline{\mathbf{c}}) \cdot \mathbf{u}\,, \tag{D.20a}$$

$$[(\underset{\sim}{\mathbf{a}}^{\mathrm{T1}})^{\mathrm{T2}} \cdot \mathbf{u}] : \underline{\mathbf{c}} = [\underset{\sim}{\mathbf{a}}^{\mathrm{T2}} : \underline{\mathbf{c}}] \cdot \mathbf{u} = (\underset{\sim}{\mathbf{a}} \cdot \mathbf{u}) : \underline{\mathbf{c}}\,, \tag{D.20b}$$

showing that $(\underset{\sim}{\mathbf{a}}^{\mathrm{T2}})^{\mathrm{T1}} = (\underset{\sim}{\mathbf{a}}^{\mathrm{T1}})^{\mathrm{T2}} = \underset{\sim}{\mathbf{a}}$.

Figure D.3 shows that the indicial representations of both major transpositions of rank-3 tensors consists of exchanges of matrix elements with respect to two planes, and that the order of the exchanges determines the type of major transposition that arises. The first major transposition given by Eq. (D.17) corresponds to performing the first and third minor transpositions consecutively on the matrix representation of $\underset{\sim}{\mathbf{a}}$, while the second major transposition given by Eq. (D.19) corresponds to performing the third and first minor transpositions consecutively. Figure D.3 suggests that a rank-3 tensor possessing first and third minor symmetries necessarily possesses both major symmetries.

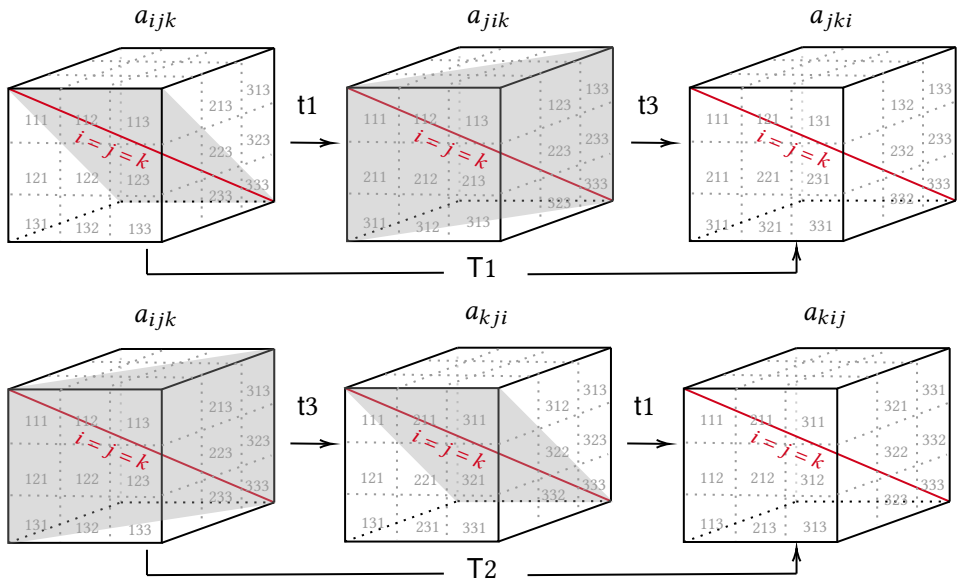

Figure D.3: The major transpositions T1 and T2 of a rank-3 tensor given symbolically by Eqs. (D.14) and (D.15) can be represented in index notation by Eqs. (D.17) and (D.19). The major transpose operation is decomposed into two minor transpose operations t1 and t3 given in index notation by Eqs. (D.10) and (D.13).

D.4 Rank-4 tensors

A rank-4 tensor can be transposed in many ways, but only the three transpositions that appear in Sec. 3.3 are discussed below.[1] The two minor transpositions and one major transposition of interest are

$$\{[(\mathbb{A}^{\mathrm{t1}} \cdot \mathbf{u}) \cdot \mathbf{v}] \cdot \mathbf{w}\} \cdot \mathbf{x} = \{[(\mathbb{A} \cdot \mathbf{u}) \cdot \mathbf{v}] \cdot \mathbf{x}\} \cdot \mathbf{w}, \tag{D.21}$$

$$\{[(\mathbb{A}^{\mathrm{t2}} \cdot \mathbf{u}) \cdot \mathbf{v}] \cdot \mathbf{w}\} \cdot \mathbf{x} = \{[(\mathbb{A} \cdot \mathbf{v}) \cdot \mathbf{u}] \cdot \mathbf{w}\} \cdot \mathbf{x}, \tag{D.22}$$

$$\{[(\mathbb{A}^{\mathrm{T}} \cdot \mathbf{u}) \cdot \mathbf{v}] \cdot \mathbf{w}\} \cdot \mathbf{x} = \{[(\mathbb{A} \cdot \mathbf{w}) \cdot \mathbf{x}] \cdot \mathbf{u}\} \cdot \mathbf{v}, \tag{D.23}$$

where $\mathbf{u}$, $\mathbf{v}$, $\mathbf{w}$, and $\mathbf{x}$ are arbitrary vectors.

[1] Itskov discusses only two of the possible transpositions, acknowledging that "in contrast to second-order tensors allowing for the unique transposition operation, one can define for fourth-order tensors various transpositions. We confine our attention here to the following two operations $(\cdot)^{\mathrm{T}}$ and $(\cdot)^{\mathrm{t}}$ defined by $\mathbb{A}^{\mathrm{T}} : \underline{\mathbf{x}} = \underline{\mathbf{x}} : \mathbb{A}$ [and] $\mathbb{A}^{\mathrm{t}} : \underline{\mathbf{x}} = \mathbb{A} : \underline{\mathbf{x}}^{\mathrm{T}}$" [227, p. 128].

Relevant minor transpositions

As for rank-3 tensors, it is convenient to write Eqs. (D.21), (D.22), and (D.23) in terms of the transposes of rank-2 tensors. Denoting $(\mathbb{A}^{\mathrm{t1}} \cdot \mathbf{u}) \cdot \mathbf{v} = \mathbb{A}^{\mathrm{t1}} : (\mathbf{v} \otimes \mathbf{u}) = \underline{\mathbf{b}}$ and $\mathbb{A} : (\mathbf{v} \otimes \mathbf{u}) = \underline{\mathbf{c}}$ allows for the first minor transposition of a rank-4 tensor given by Eq. (D.21) to be expressed as

$$(\underline{\mathbf{b}} \cdot \mathbf{w}) \cdot \mathbf{x} = (\underline{\mathbf{c}} \cdot \mathbf{x}) \cdot \mathbf{w} \,.$$

Invoking the definition of the outer product yields

$$\underline{\mathbf{b}} : (\mathbf{x} \otimes \mathbf{w}) = \underline{\mathbf{c}} : (\mathbf{w} \otimes \mathbf{x}) \,.$$

Denoting $\mathbf{x} \otimes \mathbf{w} = \underline{\mathbf{d}}$ and invoking Eq. (D.7) reduces above equation to

$$\underline{\mathbf{b}} : \underline{\mathbf{d}} = \underline{\mathbf{c}} : \underline{\mathbf{d}}^{\mathrm{T}} \,. \tag{D.24}$$

The ijth component of $\underline{\mathbf{c}} : \underline{\mathbf{d}}^{\mathrm{T}}$ can be written in index notation as $(\underline{\mathbf{c}})_{ij} : (\underline{\mathbf{d}}^{\mathrm{T}})_{ji}$. Since $(\underline{\mathbf{c}})_{ij} = (\underline{\mathbf{c}}^{\mathrm{T}})_{ji}$ and $(\underline{\mathbf{d}}^{\mathrm{T}})_{ji} = (\underline{\mathbf{d}})_{ij}$, the quantity $\underline{\mathbf{c}} : \underline{\mathbf{d}}^{\mathrm{T}}$ can be written as $(\underline{\mathbf{c}}^{\mathrm{T}})_{ji}(\underline{\mathbf{d}})_{ij} = \underline{\mathbf{c}}^{\mathrm{T}} : \underline{\mathbf{d}}$ [227, Eq. (1.154)], so Eq. (D.24) becomes

$$\underline{\mathbf{b}} : \underline{\mathbf{d}} = \underline{\mathbf{c}}^{\mathrm{T}} : \underline{\mathbf{d}} \,.$$

Denoting $\mathbf{v} \otimes \mathbf{u} = \underline{\mathbf{e}}$ and reinstating $\underline{\mathbf{b}} = \mathbb{A}^{\mathrm{t1}} : (\mathbf{v} \otimes \mathbf{u})$ and $\underline{\mathbf{c}} = \mathbb{A} : (\mathbf{v} \otimes \mathbf{u})$ allows for the first minor transpose of a rank-4 tensor to be expressed in terms of the transpose of a rank-2 tensor:

$$\mathbb{A}^{\mathrm{t1}} : \underline{\mathbf{e}} = (\mathbb{A} : \underline{\mathbf{e}})^{\mathrm{T}} \,. \tag{D.25}$$

In index notation, Eq. (D.21) corresponds to the permutation $i \leftrightarrow j$:

$$a_{jikl} u_l v_k w_j x_i = a_{ijkl} u_l v_k x_j w_i \,. \tag{D.26}$$

The second minor transposition of a rank-4 tensor given by Eq. (D.22) can be expressed similarly as

$$\{[\mathbb{A}^{\mathrm{t2}} : (\mathbf{v} \otimes \mathbf{u})] \cdot \mathbf{w}\} \cdot \mathbf{x} = \{[\mathbb{A} : (\mathbf{u} \otimes \mathbf{v})] \cdot \mathbf{w}\} \cdot \mathbf{x} \,.$$

Denoting $\mathbf{v} \otimes \mathbf{u} \equiv \underline{\mathbf{y}}$ and invoking Eq. (D.7) yields

$$\{[\mathbb{A}^{\mathrm{t2}} : \underline{\mathbf{y}}] \cdot \mathbf{w}\} \cdot \mathbf{x} = \{[\mathbb{A} : \underline{\mathbf{y}}^{\mathrm{T}}] \cdot \mathbf{w}\} \cdot \mathbf{x} \,.$$

Denoting $\mathbb{A}^{\mathrm{t2}} : \underline{\mathbf{y}} = \underline{\mathbf{b}}$ and $\mathbb{A} : \underline{\mathbf{y}}^{\mathrm{T}} = \underline{\mathbf{c}}$ allows for the above equation to be expressed as

$$(\underline{\mathbf{b}} \cdot \mathbf{w}) \cdot \mathbf{x} = (\underline{\mathbf{c}} \cdot \mathbf{w}) \cdot \mathbf{x} \,.$$

Invoking the definition of the outer product yields

$$\underline{\mathbf{b}} : (\mathbf{x} \otimes \mathbf{w}) = \underline{\mathbf{c}} : (\mathbf{x} \otimes \mathbf{w}) \,.$$

Reinstating $\underline{\mathbf{b}} = \mathbb{A}^{\mathrm{t2}} : \underline{\mathbf{y}}$ and $\underline{\mathbf{c}} = \mathbb{A} : \underline{\mathbf{y}}^{\mathrm{T}}$ allows for the first minor transpose to be defined by

$$\mathbb{A}^{\mathrm{t2}} : \underline{\mathbf{y}} = \mathbb{A} : \underline{\mathbf{y}}^{\mathrm{T}} \,, \tag{D.27}$$

which recovers the second of Eqs. (5.45) in Ref. 227. In index notation, the second minor transposition of a rank-4 tensor corresponds to the permutation $k \leftrightarrow l$:

$$a_{ijlk} v_k u_l v_j x_i = a_{ijkl} v_l u_k w_j x_i \,. \tag{D.28}$$

Relevant major transposition

To express Eq. (D.23) in terms of operations involving rank-2 tensors, Eq. (D.23) is first expressed in terms of outer products as

$$\{[\mathbb{A}^{\mathrm{T}} : (\mathbf{v} \otimes \mathbf{u})] \cdot \mathbf{w}\} \cdot \mathbf{x} = \{[\mathbb{A} : (\mathbf{w} \otimes \mathbf{x})] \cdot \mathbf{u}\} \cdot \mathbf{v} \,.$$

Calling $\mathbb{A}^{\mathrm{T}} : (\mathbf{u} \otimes \mathbf{v}) = \underline{\mathbf{b}}$ and $\mathbb{A} : (\mathbf{w} \otimes \mathbf{x}) = \underline{\mathbf{c}}$ yields

$$(\underline{\mathbf{b}} \cdot \mathbf{w}) \cdot \mathbf{x} = (\underline{\mathbf{c}} \cdot \mathbf{u}) \cdot \mathbf{v} \,.$$

Invoking the definition of the outer product given by Eq. (D.1) results in

$$\underline{\mathbf{b}} : (\mathbf{w} \otimes \mathbf{x}) = \underline{\mathbf{c}} : (\mathbf{u} \otimes \mathbf{v}) \,.$$

Reinstating $\underline{\mathbf{b}} = \mathbb{A}^{\mathrm{T}} : (\mathbf{u} \otimes \mathbf{v})$ and $\underline{\mathbf{c}} = \mathbb{A} : (\mathbf{w} \otimes \mathbf{x})$ yields

$$[\mathbb{A}^{\mathrm{T}} : (\mathbf{u} \otimes \mathbf{v})] : (\mathbf{w} \otimes \mathbf{x}) = [\mathbb{A} : (\mathbf{w} \otimes \mathbf{x})] : (\mathbf{u} \otimes \mathbf{v}) \,.$$

Denoting $\mathbf{u} \otimes \mathbf{v} = \underline{\mathbf{y}}$ and $\mathbf{w} \otimes \mathbf{x} = \underline{\mathbf{z}}$ allows the above equation to be expressed as

$$(\mathbb{A}^{\mathrm{T}} : \underline{\mathbf{y}}) : \underline{\mathbf{z}} = (\mathbb{A} : \underline{\mathbf{z}}) : \underline{\mathbf{y}} \,, \tag{D.29}$$

which matches the first of Eqs. (5.45) of Ref. 227. Equation (D.29) is analogous to the definition of the transpose of a rank-2 tensor given by Eq. (D.3), where the rank-2 tensor in Eq. (D.3) has been replaced by a rank-4 tensor in Eq. (D.29), the single inner product has been replaced by the double inner product, and the vectors have been replaced by rank-2 tensors. The major transpose operation defined by Eq. (D.23) is expressed using index notation as

$$a_{klij} u_l v_k w_j x_i = a_{ijkl} w_l x_k u_j v_i \,. \tag{D.30}$$

The present section concludes with a few useful properties involving rank-4 tensors.

Major transpose of the major transpose

The major transpose of the major transpose of a rank-4 tensor is itself, a fact that is reminiscent of Eq. (D.5) for rank-2 tensors. Two arbitrary rank-2 tensors $\underline{\mathbf{u}}$ and $\underline{\mathbf{v}}$ are introduced, and Eq. (D.29) is applied twice, completing the proof:

$$[(\mathbb{A}^{\mathrm{T}})^{\mathrm{T}} : \underline{\mathbf{u}}] \cdot \mathbf{v} = (\mathbb{A}^{\mathrm{T}} \cdot \underline{\mathbf{v}}) : \underline{\mathbf{u}} = (\mathbb{A} : \underline{\mathbf{u}}) \cdot \underline{\mathbf{v}} \,. \tag{D.31}$$

Major transpose of a product

The major transpose of the double inner product of two rank-4 tensors equals the product of the major-transposed tensors in reverse order. The following derivation parallels that of Eq. (D.6) for rank-2 tensors. Auxiliary rank-2 tensors $\underline{\mathbf{u}}$ and $\underline{\mathbf{w}}$ are introduced, and the

definition of transpose given by Eq. (D.29) is used in the first, third, and fourth lines below:

$$\begin{aligned}
[(\mathbb{A} : \mathbb{B})^{\mathrm{T}} : \underline{\mathbf{u}}] : \underline{\mathbf{w}} &= [(\mathbb{A} : \mathbb{B}) : \underline{\mathbf{w}}] : \underline{\mathbf{u}} \\
&= [\mathbb{A} : (\mathbb{B} : \underline{\mathbf{w}})] : \underline{\mathbf{u}} \\
&= (\mathbb{B} : \underline{\mathbf{w}}) : (\mathbb{A}^{\mathrm{T}} : \underline{\mathbf{u}}) \\
&= [\mathbb{B}^{\mathrm{T}} : (\mathbb{A}^{\mathrm{T}} : \underline{\mathbf{u}})] : \underline{\mathbf{w}} \\
&= [(\mathbb{B}^{\mathrm{T}} : \mathbb{A}^{\mathrm{T}}) : \underline{\mathbf{u}}] : \underline{\mathbf{w}} \,.
\end{aligned}$$

The composition property is used in the second and final lines above. Since $\underline{\mathbf{u}}$ and $\underline{\mathbf{w}}$ are arbitrary, it has been shown that

$$(\mathbb{A} : \mathbb{B})^{\mathrm{T}} = \mathbb{B}^{\mathrm{T}} : \mathbb{A}^{\mathrm{T}} \,. \tag{D.32}$$

Inverse of a product

The inverse of the double inner product of two rank-4 tensors is the double inner product of the inverses in reverse order. The steps of the proof are provided for clarity:

$$\begin{aligned}
(\mathbb{A} : \mathbb{B})^{-1} : \underline{\mathbf{u}} &= (\mathbb{A} : \mathbb{B})^{-1} : \mathbb{I} : \underline{\mathbf{u}} && \text{(identity property } \mathbb{I} : \underline{\mathbf{u}} = \underline{\mathbf{u}}) \\
&= (\mathbb{A} : \mathbb{B})^{-1} : \mathbb{I} : \mathbb{I} : \underline{\mathbf{u}} && \text{(same as above)} \\
&= (\mathbb{A} : \mathbb{B})^{-1} : \mathbb{I} : \mathbb{A} : \mathbb{A}^{-1} : \underline{\mathbf{u}} && \text{(since } \mathbb{A} : \mathbb{A}^{-1} = \mathbb{I}) \\
&= (\mathbb{A} : \mathbb{B})^{-1} : \mathbb{A} : \mathbb{I} : \mathbb{A}^{-1} : \underline{\mathbf{u}} && \text{(since } \mathbb{A} : \mathbb{I} = \mathbb{I} : \mathbb{A}) \\
&= (\mathbb{A} : \mathbb{B})^{-1} : \mathbb{A} : (\mathbb{B} : \mathbb{B}^{-1}) : \mathbb{A}^{-1} : \underline{\mathbf{u}} && \text{(since } \mathbb{B} : \mathbb{B}^{-1} = \mathbb{I}) \\
&= (\mathbb{A} : \mathbb{B})^{-1} : (\mathbb{A} : \mathbb{B}) : \mathbb{B}^{-1} : \mathbb{A}^{-1} : \underline{\mathbf{u}} && \text{(composition property)} \\
&= \mathbb{B}^{-1} : \mathbb{A}^{-1} : \underline{\mathbf{u}} && \text{(since } (\mathbb{A} : \mathbb{B})^{-1} : (\mathbb{A} : \mathbb{B}) = \mathbb{I})
\end{aligned}$$

Since $\underline{\mathbf{u}}$ is arbitrary, it has been shown that

$$(\mathbb{A} : \mathbb{B})^{-1} = \mathbb{B}^{-1} : \mathbb{A}^{-1} \,. \tag{D.33}$$

Inverse of the identity tensor

The major transpose of the rank-4 identity tensor is itself, a fact that can be proved by invoking two arbitrary rank-2 tensors $\underline{\mathbf{u}}$ and $\underline{\mathbf{w}}$. First note that the double inner product of two rank-2 tensors is commutative:

$$\underline{\mathbf{u}} : \underline{\mathbf{w}} = \underline{\mathbf{w}} : \underline{\mathbf{u}} \,.$$

By the existence of the identity element, the above equation can be written as

$$(\mathbb{I} : \underline{\mathbf{u}}) : \underline{\mathbf{w}} = (\mathbb{I} : \underline{\mathbf{w}}) : \underline{\mathbf{u}} \,.$$

The right-hand side of the above equation can be written in terms of the major transpose defined by Eq. (D.29):

$$(\mathbb{I} : \underline{\mathbf{u}}) : \underline{\mathbf{w}} = (\mathbb{I}^{\mathrm{T}} : \underline{\mathbf{u}}) : \underline{\mathbf{w}} \,.$$

Since $\underline{\mathbf{u}}$ and $\underline{\mathbf{w}}$ are arbitrary, it is concluded that

$$\mathbb{I}^{\mathrm{T}} = \mathbb{I} \,. \tag{D.34}$$

Inverse of the inverse

The inverse of the inverse of a rank-4 tensor is itself. Begin by considered the existence of the identity element in the rank-4 tensor space:

$$\mathbb{A}^{-1} : \mathbb{A} = \mathbb{I} \,. \tag{D.35}$$

The inverse of both sides of Eq. (D.35) is taken:

$$(\mathbb{A}^{-1} : \mathbb{A})^{-1} = \mathbb{I}^{-1} \,.$$

Invoking Eq. (D.33) and noting from Eq. (D.34) that the inverse of the identity element is itself yields

$$\mathbb{A}^{-1} : (\mathbb{A}^{-1})^{-1} = \mathbb{I} \,.$$

Taking the double inner product with $\mathbb{A}$ on the left, applying the composition property, and again invoking Eq. (D.35) yields

$$(\mathbb{A}^{-1})^{-1} = \mathbb{A} \,. \tag{D.36}$$

Major transpose of the inverse

The major transpose of the inverse of a rank-4 tensor equals the inverse of the major transpose of the tensor. To prove this, consider the major transpose of Eq. (D.35), and note that $\mathbb{I}^{\mathrm{T}} = \mathbb{I}$ from Eq. (D.34):

$$(\mathbb{A}^{-1} : \mathbb{A})^{\mathrm{T}} = \mathbb{I}^{\mathrm{T}} = \mathbb{I}\,.$$

Applying Eq. (D.32) yields

$$\mathbb{A}^{\mathrm{T}} : (\mathbb{A}^{-1})^{\mathrm{T}} = \mathbb{I}\,.$$

Taking the double inner product on the left of both sides with $(\mathbb{A}^{\mathrm{T}})^{-1}$, applying the associativity of the inner product, and noting that $(\mathbb{A}^{\mathrm{T}})^{-1} : \mathbb{I} = (\mathbb{A}^{\mathrm{T}})^{-1}$ yields

$$[(\mathbb{A}^{\mathrm{T}})^{-1} : \mathbb{A}^{\mathrm{T}}] : (\mathbb{A}^{-1})^{\mathrm{T}} = (\mathbb{A}^{\mathrm{T}})^{-1}\,.$$

Since $(\mathbb{A}^{\mathrm{T}})^{-1} : \mathbb{A}^{\mathrm{T}} = \mathbb{I}$, the above equation shows that the transpose of the inverse of a rank-4 tensor equals the inverse of the transpose of the tensor:

$$(\mathbb{A}^{-1})^{\mathrm{T}} = (\mathbb{A}^{\mathrm{T}})^{-1}\,. \tag{D.37}$$

D.5 Hermitian conjugation

The Hermitian conjugate of a rank-2 tensor $\underline{\mathbf{a}}$ is defined by

$$(\underline{\mathbf{a}}^{\mathrm{T}*} \cdot \mathbf{u}) \cdot \mathbf{v} = (\underline{\mathbf{a}} \cdot \mathbf{v}) \cdot \mathbf{u}\,, \tag{D.38}$$

where the asterisk denotes the complex conjugate. The relevant minor [Eqs. (D.39a), (D.39b)] and major [Eqs. (D.39c), (D.39d)] Hermitian conjugates of a rank-3 tensor $\underset{\sim}{\mathbf{a}}$ are

$$\underset{\sim}{\mathbf{a}}^{\mathrm{t1}*} \cdot \mathbf{u} = (\underline{\mathbf{a}} \cdot \mathbf{u})^{\mathrm{T}*}\,, \tag{D.39a}$$

$$\underset{\sim}{\mathbf{a}}^{\mathrm{t2}*} : \underline{\mathbf{x}} = \underline{\mathbf{a}} : \underline{\mathbf{x}}^{\mathrm{T}*}\,, \tag{D.39b}$$

$$(\underset{\sim}{\mathbf{a}}^{\mathrm{T1}*} : \underline{\mathbf{b}}) \cdot \mathbf{w} = (\underline{\mathbf{a}} \cdot \mathbf{w}) : \underline{\mathbf{b}}\,, \tag{D.39c}$$

$$(\underset{\sim}{\mathbf{a}}^{\mathrm{T2}*} \cdot \mathbf{u}) : \underline{\mathbf{c}} = (\underline{\mathbf{a}} : \underline{\mathbf{c}}) \cdot \mathbf{u}\,, \tag{D.39d}$$

and the relevant major [Eq. (D.40a)] and minor [Eqs. (D.40b), (D.40c)] Hermitian conjugates of a rank-4 tensor $\mathbb{A}$ are

$$(\mathbb{A}^{\mathrm{T}*} : \underline{\mathbf{y}}) : \underline{\mathbf{z}} = (\mathbb{A} : \underline{\mathbf{z}}) : \underline{\mathbf{y}}, \tag{D.40a}$$

$$(\mathbb{A}^{\mathrm{t1}*} : \underline{\mathbf{e}}) : \underline{\mathbf{d}} = (\mathbb{A} : \underline{\mathbf{e}}) : \underline{\mathbf{d}}^{\mathrm{T}}, \tag{D.40b}$$

$$\mathbb{A}^{\mathrm{t2}*} : \underline{\mathbf{y}} = \mathbb{A} : \underline{\mathbf{y}}^{\mathrm{T}}. \tag{D.40c}$$

Appendix E: Notes on diffraction

E.1 Fourier acoustics

In Cartesian coordinates, the Helmholtz equation [Eq. (A.1)] takes the form

$$\nabla^2 \tilde{p} + k^2 \tilde{p} = \left(\frac{\partial^2}{\partial x^2} + \frac{\partial^2}{\partial y^2} + \frac{\partial^2}{\partial z^2} + k^2 \right) \tilde{p} = 0 \,. \tag{E.1}$$

Equation (E.1) can be solved by using the two-dimensional spatial Fourier transform and its inverse, given by

$$\hat{f}(k_x, k_y) = \mathcal{F}_{xy}[f(x,y)] = \iint_{-\infty}^{\infty} f(x,y) e^{-i(k_x x + k_y y)} dx\, dy \tag{E.2}$$

$$f(x,y) = \mathcal{F}_{xy}^{-1}[f(k_x, k_y)] = \frac{1}{(2\pi)^2} \iint_{-\infty}^{\infty} f(k_x, k_y) e^{i(k_x x + k_y y)} dk_x\, dk_y \,, \tag{E.3}$$

respectively. Begin by noting that the mth derivative of $f(x,y)$ with respect to x can be expressed as

$$\frac{\partial^m f(x,y)}{\partial x^m} = \frac{\partial^m}{\partial x^m} \mathcal{F}_{xy}^{-1}[\hat{f}(k_x, k_y)] \tag{E.4}$$

because $f(x,y) = \mathcal{F}_{xy}^{-1}\{\mathcal{F}_{xy}[f(x,y)]\}$. Writing the inverse 2D Fourier transform in Eq. (E.4) in terms of Eq. (E.3) yields

$$\frac{\partial^m f(x,y)}{\partial x^m} = \frac{1}{(2\pi)^2} \frac{\partial^m}{\partial x^m} \iint_{-\infty}^{\infty} \hat{f}(k_x, k_y) e^{i(k_x x + k_y y)} dk_x\, dk_y \,. \tag{E.5}$$

Moving the partial derivatives $\partial^m / \partial x^m$ inside the integral in Eq. (E.5) and noting that $\partial^m (e^{ik_x x}) / \partial x^m = (ik_x)^m e^{ik_x x}$ yields

$$\frac{\partial^m f(x,y)}{\partial x^m} = \mathcal{F}_{xy}^{-1}[(ik_x)^m \hat{f}(k_x, k_y)]. \tag{E.6}$$

Taking the Fourier transform of Eq. (E.6) yields

$$\mathcal{F}_{xy}\left[\frac{\partial^m f(x,y)}{\partial x^m} \right] = \mathcal{F}_{xy}\left\{ \mathcal{F}_{xy}^{-1}\left[(ik_x)^m \hat{f}(k_x, k_y) \right] \right\} = (ik_x)^m \hat{f}(k_x, k_y) \,, \tag{E.7}$$

where the second equality follows from the fact that $\mathcal{F}_{xy}$ and $\mathcal{F}_{xy}^{-1}$ are inverses. Similarly,

$$\mathcal{F}_{xy}\left[\frac{\partial^m f(x,y)}{\partial y^m}\right] = (ik_y)^m \hat{f}(k_x,k_y)\,. \tag{E.8}$$

Taking the 2D spatial Fourier transform of Eq. (E.1) and applying Eqs. (E.7) and (E.8) for $m = 2$ yields

$$0 = \mathcal{F}_{xy}\left(\frac{\partial^2\tilde{p}}{\partial x^2} + \frac{\partial^2\tilde{p}}{\partial y^2} + \frac{\partial^2\tilde{p}}{\partial z^2} + k^2\tilde{p}\right) = \left(-k_x^2 - k_y^2 - \frac{\partial^2}{\partial z^2} + k^2\right)\hat{p}(k_x,k_y,z)\,. \tag{E.9}$$

Since

$$k^2 = k_x^2 + k_y^2 + k_z^2\,, \tag{E.10}$$

the quantity $k^2 - k_x^2 - k_y^2$ in Eq. (E.9) is identified as k_z^2. Since $\hat{p}$ is not a function of k_z, Eq. (E.9) becomes an ordinary differential equation,

$$\frac{d^2\hat{p}}{dz^2} + k_z^2\hat{p} = 0\,, \tag{E.11}$$

the solution of which for propagation in the $+z$ direction is

$$\hat{p}(k_x,k_y,k_z) = \mathcal{F}_{xy}[\tilde{p}(x,y,0)]e^{ik_z z}\,, \tag{E.12}$$

where $\tilde{p}(x,y,0)$ is the source condition. The solution of the Helmholtz equation is found by taking the inverse Fourier transform of Eq. (E.12):

$$\tilde{p}(x,y,z) = \mathcal{F}_{xy}^{-1}\{\mathcal{F}_{xy}[\tilde{p}(x,y,0)]e^{ik_z z}\}\,. \tag{E.13}$$

where $k_z = (k^2 - k_x^2 - k_y^2)^{1/2}$ from Eq. (E.10).

Now suppose that the source condition is given by a velocity rather than a pressure, as in Sec. 4.2. For time-harmonic quantities, velocity is related to pressure through the linearized momentum equation

$$\tilde{\mathbf{v}} = \frac{1}{ik\rho_0 c_0}\boldsymbol{\nabla}\tilde{p}\,. \tag{E.14}$$

Expressing $\tilde{p}$ in Eq. (E.14) as $\mathcal{F}_{xy}^{-1}\{\mathcal{F}_{xy}[\tilde{p}(x,y,z)]\}$ yields

$$\tilde{\mathbf{v}} = (ik\rho_0 c_0)^{-1}\mathcal{F}_{xy}^{-1}\{\mathcal{F}_{xy}[\boldsymbol{\nabla}\tilde{p}(x,y,z)]\}\,, \tag{E.15}$$

where the gradient operator in Eq. (E.14) has been moved inside the Fourier transforms. Since

$$\mathcal{F}_{xy}(\partial\tilde{p}/\partial x) = ik_x\hat{p}\,, \qquad \mathcal{F}_{xy}(\partial\tilde{p}/\partial y) = ik_y\hat{p}\,, \qquad \mathcal{F}_{xy}(\partial\tilde{p}/\partial z) = ik_z\hat{p}\,, \tag{E.16}$$

where the third relation follows from Eqs. (E.11) and (E.12), Eq. (E.15) becomes

$$\tilde{\mathbf{v}} = (\rho_0 c_0)^{-1}\mathcal{F}_{xy}^{-1}\{\mathcal{F}_{xy}[\tilde{p}(x,y,z)]\mathbf{k}/k\}\,. \tag{E.17}$$

In the source plane $z = 0$, the z component of Eq. (E.17) may be expressed as

$$\tilde{v}_z(x,y,0) = (\rho_0 c_0)^{-1}\mathcal{F}_{xy}^{-1}\{\mathcal{F}_{xy}[\tilde{p}(x,y,0)]k_z/k\}\,. \tag{E.18}$$

Equation (E.18) is solved for $\mathcal{F}_{xy}^{-1}\{\mathcal{F}_{xy}[\tilde{p}(x,y,0)]$ by taking the 2D Fourier transform and multiplying by $(k/k_z)\rho_0 c_0$:

$$\mathcal{F}_{xy}^{-1}\{\mathcal{F}_{xy}[\tilde{p}(x,y,0)] = \rho_0 c_0 \mathcal{F}_{xy}[\tilde{v}_z(x,y,0)k/k_z]\,. \tag{E.19}$$

Inserting Eq. (E.19) in Eq. (E.13) yields

$$\tilde{p}(x,y,z) = k\rho_0 c_0 \mathcal{F}_{xy}^{-1}\{\mathcal{F}_{xy}[\tilde{v}_z(x,y)]e^{ik_z z}/k_z\}\,, \tag{E.20}$$

where $\tilde{v}_z(x,y,0)$ is understood to be the source condition $\tilde{v}_z(x,y)$.

For a comprehensive treatment of Fourier acoustics, see Ref. 322.

E.2 Fresnel diffraction integral

The Fresnel diffraction integral is an exact solution of Eq. (A.25). The integral can be derived from the Rayleigh integral [Eq. (4.2)], the magnitude of the displacement vector equals

$$|\mathbf{r} - \mathbf{r}_0| = R = \sqrt{(x-x_0)^2 + (y-y_0)^2 + z^2} \tag{E.21}$$

in Cartesian coordinates. Factoring out z from Eq. (E.21) yields

$$R = z\left[1 + \frac{(x-x_0)^2}{z^2} + \frac{(y-y_0)^2}{z^2}\right]^{1/2}. \tag{E.22}$$

For small angles from the z axis, the quadratic terms in Eq. (E.22) can be considered to be small, warranting the use of the binomial expansion:

$$R \simeq z + \frac{(x-x_0)^2}{2z} + \frac{(y-y_0)^2}{2z}. \tag{E.23}$$

The quantity kR that appears in the exponent is approximately

$$kR = kz + \frac{k}{2z}\left[(x-x_0)^2 + (y-y_0)^2\right]. \tag{E.24}$$

Note that the next higher order term in Eq. (E.24) is $O(z^{-3}) \sim ka^4/8z^3$, which in Eq. (E.24) has been assumed to be much smaller than π, i.e., the $O(z^{-3})$ term does not contribute significantly to the phase of e^{ikR} if

$$(z/a)^3 \gg ka/8\pi. \tag{E.25}$$

Equation (E.25) can be written as $z/a \gtrsim (ka)^{1/3}$, which corresponds to a region defined by a ~20° angle from the z axis. The denominator of the integrand of Eq. (4.2) is approximated as the first term of Eq. (E.23), while the phase in Eq. (4.2) is approximated as Eq. (E.24). Equation (4.2) therefore becomes

$$\tilde{p}(x,y,z) = -\frac{ik\rho_0 c_0}{2\pi}\frac{e^{ikz}}{z}\iint_{-\infty}^{\infty} v_z(x_0,y_0)e^{ik[(x-x_0)^2+(y-y_0)^2]/2z}\,dx_0\,dy_0. \tag{E.26}$$

Equation (E.26) results in Eq. (4.47) upon recalling that $\tilde{p} = qe^{ikz}$, where the relation $v_z = p/\rho_0 c_0$ has been used in Eq. (4.47) to replace the particle velocity with pressure [268].

While Eqs. (A.24) and (E.25) establish the traditional criteria for the validity of the paraxial approximation, additional criteria arise due to nonzero orbital numbers and focusing, as discussed in Sec. 4.5. More information about the paraxial approximation is provided by Pierce [22, Sec. 5.2.2].

E.3 Spherical focusing

A source condition proportional to

$$\frac{e^{-ik\sqrt{x^2+y^2+d^2}}}{\sqrt{x^2+y^2+d^2}} \tag{E.27}$$

in the plane $z = 0$ produces a spherical wave with a focus $z = d$ [9, Chap. 1, Eq. (D–13)]. The phase of expression (E.27) is approximated as

$$-ikd\left[1+\frac{x^2+y^2}{d^2}\right]^{1/2} \simeq -ikd - ik\frac{x^2+y^2}{2d},$$

and the magnitude of expression (E.27) is approximated as

$$\frac{1}{d}[1+(x^2+y^2)/d^2]^{-1/2} \simeq \frac{1}{d}.$$

In the paraxial approximation, a focused wave is proportional to $e^{-ikd}e^{-ik(x^2+y^2)/2d}/d$; accounting for focusing therefore amounts to multiplication of the source condition by $e^{-ik(x^2+y^2)/2d}$. In polar coordinates, the focusing factor is $e^{-ikr^2/2d}$.

E.4 Recovery of Gaussian beam

Equation (4.72) allows Eq. (4.67) for $\ell = 0$ to be expressed as

$$q(r,z) = -ip_0\underline{\frac{k}{2z}\left[\frac{1}{a^2}-\frac{ik}{2}\left(\frac{1}{z}-\frac{1}{d}\right)\right]^{-1}} \times \underline{\underline{\exp\left\{-\left(\frac{kr}{2z}\right)^2\left[\frac{1}{a^2}-\frac{ik}{2}\left(\frac{1}{z}-\frac{1}{d}\right)\right]^{-1}+\frac{ikr^2}{2z}\right\}}}. \tag{E.28}$$

Denoting $G = ka^2/2d$ allows the single-underlined factor in Eq. (E.28) to be written as

$$\frac{k}{2z}\left[\frac{1}{a^2}-\frac{ik}{2}\left(\frac{1}{z}-\frac{1}{d}\right)\right]^{-1} = \frac{i}{1-(1-iG^{-1})z/d}, \tag{E.29}$$

and the double-underlined factor of Eq. (E.28) becomes

$$\exp\left\{-\left(\frac{kr}{2z}\right)^2\left[\frac{1}{a^2}-\frac{ik}{2}\left(\frac{1}{z}-\frac{1}{d}\right)\right]^{-1}+\frac{ikr^2}{2z}\right\} = \exp\left[-\frac{i(G-i)r^2/a^2}{1-(1-iG^{-1})z/d}\right]. \tag{E.30}$$

In terms of Eqs. (E.29) and (E.30), Eq. (E.28) becomes

$$q(r,z) = \frac{p_0}{1-(1-iG^{-1})z/d} \exp\left[-\frac{(1+iG)(r/a)^2}{1-(1-iG^{-1})z/d}\right]. \tag{E.31}$$

Equations (E.31) and Eq. (8.37) of Ref. 6 differ by only the time convention, i.e., replacing the complex unit i in Eq. (E.31) with $-j$ recovers Eq. (8.37) of Ref. 6.

E.5 Laguerre-Gauss expansion

Laguerre-Gaussian modes are eigenfunctions of Eq. (A.25) in cylindrical coordinates [107, Eq. (A3)]. Since these modes form a complete orthogonal set [323], they can be used to describe directional radiation from a source plane with any amplitude and phase distribution that satisfies the restrictions on the paraxial approximation. Presented here for comparison with Eq. (4.67) is a common alternative solution for vortex beams based on an expansion in terms of Laguerre-Gaussian modes. The comparison is restricted to unfocused Gaussian sources with vorticity described by Eq. (4.63). While the focused source condition given by Eq. (4.63) is recovered by replacing a^2 in Eq. (4.63) with the complex quantity $\tilde{a}^2 = a^2/(1+ika^2/2d)$, focusing introduces complications in the standard Laguerre-Gauss formulation that are unnecessary for the purpose of comparing the expansions with Eq. (4.67). Specifically, it is demonstrated below that for all $\ell \neq 0$, an infinite number of Laguerre-Gaussian modes is required to describe the radiated field corresponding to the source condition in Eq. (4.63).

The solution of the paraxial equation [Eq. (A.25)] is sought in terms of the expansion

$$q(r,\theta,z) = \sum_{n,m} A_n^m \mathrm{LG}_{nm}(r,\theta,z) \tag{E.32}$$

with the Laguerre-Gaussian modes expressed in the standard form

$$\begin{aligned}\mathrm{LG}_{nm}(r,\theta,z) = {} & \frac{N_n^m}{w(z)}\left(\frac{\sqrt{2}r}{w(z)}\right)^{|m|} L_n^{|m|}\left(\frac{2r^2}{w^2(z)}\right)\exp\left(-\frac{r^2}{w^2(z)}\right) \\ & \times \exp\left\{i\left[m\theta + \frac{kr^2}{2R(z)} - (2n+|m|+1)\phi(z)\right]\right\},\end{aligned} \tag{E.33}$$

where L_n^m are the Laguerre polynomials. The quantities

$$w(z) = w_0\sqrt{1 + (z/z_w)^2}\,, \qquad R(z) = z[1 + (z_w/z)^2]\,, \qquad \phi(z) = \arctan(z/z_w)\,,$$

are functions of distance relative to the diffraction length $z_w = kw_0^2/2$ associated with the characteristic beam radius w_0, and $N_n^m = \{2n!/[\pi(n + |m|)!]\}^{1/2}$ is a normalization factor that yields

$$\int_0^{2\pi}\int_0^{\infty} \mathrm{LG}_{nm}(r,\theta,z)\mathrm{LG}^*_{n'm'}(r,\theta,z)\, r\, dr d\theta = \delta_{nn'}\delta_{mm'} \tag{E.34}$$

for the orthogonality integral, where $\delta_{\alpha\beta}$ is the Kronecker delta and the asterisk indicates complex conjugate.

The expansion coefficients in Eq. (E.32) are obtained as follows. Equation (E.33) is evaluated at $z = 0$:

$$\mathrm{LG}_{nm}(r,\theta,0) = N_n^m \frac{1}{w_0}\left(\frac{\sqrt{2}r}{w_0}\right)^{|m|} L_n^{|m|}\left(\frac{2r^2}{w_0^2}\right) e^{-r^2/w_0^2} e^{im\theta}\,. \tag{E.35}$$

Equations (4.63) and (E.35) are substituted into Eq. (E.32), and both sides are multiplied by $\mathrm{LG}^*_{n'm'}$. The resulting equation is integrated over the plane $z = 0$, and the orthogonality relation given by Eq. (E.34) is invoked. Noting that $\int_0^{2\pi} e^{i(\ell - m')\theta} d\theta = 2\pi\delta_{\ell m'}$ yields

$$A_n^\ell = 2\pi N_n^\ell \frac{p_0}{w_0}\int_0^{\infty}\left(\frac{\sqrt{2}r}{w_0}\right)^{|\ell|} L_n^{|\ell|}\left(\frac{2r^2}{w_0^2}\right) e^{-(a^{-2}+w_0^{-2})r^2}\, r\, dr \tag{E.36}$$

for the coefficients in the resulting summation over the single index n:

$$q(r,\theta,z) = \sum_{n=0}^{\infty} A_n^\ell \mathrm{LG}_{n\ell}(r,\theta,z)\,. \tag{E.37}$$

The expansion coefficients given by Eq. (E.36) are simplified by setting $w_0 = a$ and letting $x = 2r^2/a^2$, yielding

$$A_n^\ell = \frac{\pi}{2} N_n^\ell B_n^\ell p_0 a\,, \tag{E.38}$$

where the integral in Eq. (E.36) becomes

$$B_n^\ell = \int_0^\infty x^{|\ell|/2} L_n^{|\ell|}(x) e^{-x}\, dx = \frac{\Gamma(1+\ell/2)\Gamma(n+\ell/2)}{n!\,\Gamma(\ell/2)}\,, \tag{E.39}$$

and Γ is the gamma function. The Laguerre-Gaussian modes in Eq. (E.33) are thus evaluated with $m = \ell$, $w_0 = a$, and $z_w = z_R = ka^2/2$, making Eq. (E.37) equivalent to Eq. (4.67) with $d = \infty$ in Eq. (4.68).

For $\ell = 0$, Eq. (E.39) yields

$$B_n^0 = \frac{\Gamma(1)\Gamma(n)}{n!\,\Gamma(0)} = \delta_{n0}\,, \tag{E.40}$$

and therefore $B_0^0 = 1$ and $B_n^0 = 0$ for all $n > 0$ because $\Gamma(0) = \infty$. The summation in Eq. (E.37) thus reduces to the single term $n = 0$,

$$q(r,z) = A_0^0\, \mathrm{LG}_{00}(r,z), \quad \ell = 0\,. \tag{E.41}$$

Although less compact with LG_{00} expressed as in Eq. (E.33), Eq. (E.41) is equivalent to Eq. (4.73). For this degenerate case ($\ell = 0$, no vorticity), involving only one mode in the expansion ($n = 0$), there is no advantage to using Eq. (4.67).

However, Eq. (E.39) reveals that for all nonzero values of ℓ, B_n^ℓ is nonzero for all n, and therefore all modes in Eq. (E.37) are required for $\ell \neq 0$. For example, with $\ell = 1$, 2, and 3, one obtains

$$B_n^1 = \frac{\Gamma(3/2)\Gamma(n+1/2)}{n!\,\Gamma(1/2)} = \frac{\sqrt{\pi}(2n)!}{2(4^n)(n!)^2}\,, \tag{E.42}$$

$$B_n^2 = \frac{\Gamma(2)\Gamma(n+1)}{n!\,\Gamma(1)} = 1\,, \tag{E.43}$$

$$B_n^3 = \frac{\Gamma(2)\Gamma(n+1)}{n!\,\Gamma(1)} = 1\,, \tag{E.44}$$

and Eq. (E.37) yields

$$q(r,\theta,z) = p_0 e^{i\theta} \frac{r/a}{|\zeta(z)|^2} \exp\left(-\frac{r^2/a^2}{\zeta(z)}\right) \times \sqrt{\pi/2} \sum_{n=0}^{\infty} \frac{(2n)!\, e^{-i(2n+2)\phi_R(z)}}{4^n (n+1)(n!)^2} L_n^1\left(\frac{2r^2/a^2}{|\zeta(z)|^2}\right), \qquad \ell = 1, \tag{E.45}$$

$$q(r,\theta,z) = p_0 e^{i2\theta} \frac{r^2/a^2}{|\zeta(z)|^3} \exp\left(-\frac{r^2/a^2}{\zeta(z)}\right) \times 2 \sum_{n=0}^{\infty} \frac{e^{-i(2n+3)\phi_R(z)}}{(n+1)(n+2)} L_n^2\left(\frac{2r^2/a^2}{|\zeta(z)|^2}\right), \qquad \ell = 2, \tag{E.46}$$

$$q(r,\theta,z) = p_0 e^{i3\theta} \frac{r^3/a^3}{|\zeta(z)|^4} \exp\left(-\frac{r^2/a^2}{\zeta(z)}\right) \times 3\sqrt{2\pi} \sum_{n=0}^{\infty} \frac{(2n+2)! e^{-i(2n+4)\phi_R(z)}}{4^{n+1}(n+1)!(n+3)!} L_n^3\left(\frac{2r^2/a^2}{|\zeta(z)|^2}\right), \qquad \ell = 3, \tag{E.47}$$

where $\zeta(z) = 1 + iz/z_R$, $\phi_R(z) = \arctan(z/z_R)$, and $z_R = ka^2/2$.

In addition to the complexity of the Laguerre-Gauss expansions for $\ell \neq 0$ compared with Eq. (4.67), the number of terms required for convergence increases with ℓ. For $\ell = 1$, 2, and 3, approximately 10, 20, and 30 terms, respectively, are required for the magnitude of Eq. (E.37) to achieve reasonable agreement with Eq. (4.70) at distances $z/z_R \gtrsim 0.2$. Significantly more terms are required for comparable agreement in phase. The analytical solutions developed in Sec. 4.3 provide insights into the structure of the field that remained concealed by the summations involved in the Laguerre-Gauss expansions above.

Another benefit of the analytical solution obtained from the Fresnel diffraction integral is that the amplitude distribution in the source plane is unaltered by changes in the orbital number ℓ, permitting the consequences of varying ℓ to be decoupled from variations in other source parameters. In contrast, changing the value of ℓ for a field described by a single Laguerre-Gaussian mode alters the amplitude distribution corresponding to that mode in the source plane. Decoupling the source amplitude from the value of ℓ is also relevant to configurations in which a single source is employed and ℓ is changed by inserting a different phase screen in front of that source, as in the experiments with focused acoustic vortex beams reported by Terzi et al. [101].

The reader is referred to Pan et al. [106] for numerical evaluations of the Laguerre-Gauss expansion coefficients corresponding to the source condition in Eq. (4.63), rather than the explicit analytical expressions presented in Eqs. (E.36) and (E.39).

Works Cited

[1] P. W. Anderson. More is different. *Science*, 177:393–396, 1972.

[2] Lord Rayleigh. On the transmission of light through an atmosphere containing small particles in suspension, and on the origin of the blue of the sky. *Philos. Mag.*, 47:375–384, 1899.

[3] L. P. Gor'kov. On the forces acting on a small particle in an acoustical field in an ideal fluid. *Sov. Phys. Dokl.*, 6:773–775, 1962.

[4] A.-J. Fresnel. Mémoire sur la diffraction de la lumière. *Annales de Chimie et de Physique*, 2:239–281, 1816.

[5] K. S. Thorne and R. D. Blandford. *Modern Classical Physics: Optics, Fluids, Plasmas, Elasticity, Relativity, and Statistical Physics.* Princeton University Press, Princeton, New Jersey, 2017.

[6] M. F. Hamilton, "Sound Beams," M. F. Hamilton and D. T. Blackstock, editors. *Nonlinear Acoustics.* Springer, Cham, Switzerland, 3rd edition, 2024. Chap. 8.

[7] J. H. Ginsberg. *Acoustics: A Textbook for Engineers and Physicists*, volume 2. Springer, Cham, Switzerland, 2018.

[8] D. J. Griffiths. *Introduction to Electrodynamics.* Pearson, Upper Saddle River, New Jersey, 3rd edition, 1999.

[9] D. T. Blackstock. *Fundamentals of Physical Acoustics.* Wiley, New York, 2000.

[10] B. T. Hefner and P. L. Marston. An acoustical helicoidal wave transducer with applications for the alignment of ultrasonic and underwater systems. *J. Acoust. Soc. Am.*, 106:3313–3316, 1999.

[11] T. S. Jerome and M. F. Hamilton. Born approximation of acoustic radiation force and torque on inhomogeneous objects. *J. Acoust. Soc. Am.*, 150:3417–3427, 2021.

[12] A. Alù. First-principles homogenization theory for periodic metamaterials. *Phys. Rev. B.*, 84:075153, 2011.

[13] C. F. Sieck, A. Alù, and M. R. Haberman. Origins of Willis coupling and acoustic bianisotropy in acoustic metamaterials through source-driven homogenization. *Phys. Rev. B.*, 96:104303, 2017.

[14] A. J. Lawrence. *On Acoustic Multiple Scattering from Willis Media.* Ph.D. dissertation, University of Texas at Austin, 2024.

[15] P. Curie. Sur la symétrie dans les phénomènes physiques, symétrie d'un champ électrique et d'un champ magnétique. *J. Phys. Théor. Appl.*, 3:393–415, 1894.

[16] P. Curie, translated by A. Ziólkowski. On symmetry in physical phenomena, symmetry of an electric field and of a magnetic field. *Stud. Hist. Sci.*, 23:23–67, 2024.

[17] A. Bedard Jr. and T. M. Georges. Atmospheric infrasound. *Phys. Today*, 53:32–37, 2000.

[18] Lord Rayleigh. On the light from the sky, its polarization and colour. *Philos. Mag.*, 41:107–120, 1871.

[19] Lord Rayleigh. On the scattering of light by small particles. *Philos. Mag.*, 41:375–384, 1871.

[20] Lord Rayleigh. Investigation of the disturbance produced by a spherical obstacle on the waves of sound. *Proc. Lond. Math. Soc.*, 4:253–283, 1872.

[21] M. R. Haberman and M. D. Guild. Acoustic metamaterials. *Phys. Today*, 69:42–48, 2016.

[22] A. D. Pierce. *Acoustics: An Introduction to Its Physical Principles and Applications*. Springer, Cham, Switzerland, 2019.

[23] H. C. van de Hulst. *Light Scattering by Small Particles*. Wiley, New York, 1957.

[24] G. Mie. Beiträge zur Optik trüber Medien, speziell kolloidaler Metallösungen. *Ann. Phys.*, 330:377–445, 1908.

[25] National Oceanic and Atmospheric Administration. The Color of Clouds. https://www.noaa.gov/jetstream/clouds/color-of-clouds, 2023. Last updated April 20, 2023.

[26] J. W. Caruthers. On Rayleigh and Mie scattering. *Proc. Mtgs. Acoust.*, 14:070001, 2011.

[27] R. H. Silliman. Fresnel and the emergence of physics as a discipline. *Hist. Stud. Phys. Sci.*, 4:137–162, 1974.

[28] P. L. Marston and D. B. Thiessen. Manipulation of fluid objects with acoustic radiation pressure. *Ann. N. Y. Acad. Sci.*, 1027:414–434, 2004.

[29] H. Bruus, "Acoustic radiation force on small particles," T. Laurell and A. Lenshof, editors. *Microscale Acoustofluidics*. Royal Society of Chemistry, London, 2014.

[30] E. B. Lima and G. T. Silva. Mean acoustic fields exerted on a subwavelength axisymmetric particle. *J. Acoust. Soc. Am.*, 150:376–384, 2021.

[31] T. S. Jerome, Yu. A. Ilinskii, E. A. Zabolotskaya, and M. F. Hamilton. Acoustic radiation torque on a compressible spheroid. *J. Acoust. Soc. Am.*, 149:2081–2088, 2021.

[32] M. Smagin, I. Toftul, K. Y. Bliokh, and M. Petrov. Acoustic lateral recoil force and stable lift of anisotropic particles. *Phys. Rev. Appl.*, 22:064041, 2024.

[33] S. Sepehrirahnama, S. Oberst, Y. K. Chiang, and D. A. Powell. Acoustic radiation force and radiation torque beyond particles: Effects of nonspherical shape and Willis coupling. *Phys. Rev. E*, 104:065003, 2021.

[34] S. Sepehrirahnama and S. Oberst. Acoustic radiation force and torque acting on asymmetric objects in acoustic Bessel beam of zeroth order within Rayleigh scattering limit. *AIP Conf. Proc.*, 10:897648, 2022.

[35] S. Sepehrirahnama, S. Oberst, Y. K. Chiang, and D. A. Powell. Willis coupling-induced acoustic radiation force and torque reversal. *Phys. Rev. Lett.*, 129:174501, 2022.

[36] T. Tang and L. Huang. An efficient semi-analytical procedure to calculate acoustic radiation force and torque for axisymmetric irregular bodies. *J. Sound Vib.*, 532:117012, 2022.

[37] T. Tang, Y. Zhang, B. Dong, and L. Huang. Computation of acoustic scattered fields and derived radiation force and torque for axisymmetric objects at arbitrary orientations. *J. Acoust. Soc. Am.*, 156:2767–2782, 2024.

[38] A. A. Doinikov. Acoustic radiation forces: Classical theory and recent advances. *Recent Res. Dev. Acoust*, 1:39–67, 2003.

[39] G. Destgeer, B. H. Ha, J. H. Jung, and H. J. Sung. Submicron separation of microspheres via travelling surface acoustic waves. *Lab Chip*, 14:4665–4672, 2014.

[40] B. W. Drinkwater. A perspective on acoustical tweezers—devices, forces, and biomedical applications. *Appl. Phys. Lett.*, 117:180501, 2020. Fig. 1.

[41] M. R. Haberman and A. N. Norris. Acoustic metamaterials. *Acoustics Today*, 12:31–38, 2016.

[42] J. R. Willis. Variational principles for dynamic problems for inhomogeneous elastic media. *Wave Motion*, 3:1–11, 1981.

[43] J. R. Willis. Effective constitutive relations for waves in composites and metamaterials. *Proc. R. Soc. A*, 467:1865–1879, 2011.

[44] M. B. Muhlestein and M. R. Haberman. A micromechanical approach for homogenization of elastic metamaterials with dynamic microstructure. *Proc. R. Soc. A*, 472:20160438, 2016.

[45] M. B. Muhlestein, B. M. Goldsberry, A. N. Norris, and M. R. Haberman. Acoustic scattering from a fluid cylinder with Willis constitutive properties. *Proc. R. Soc. A*, 474:20180571, 2018.

[46] H. Nassar, X. C. Xu, A. N. Norris, and G. L. Huang. Modulated phononic crystals: Non-reciprocal wave propagation and Willis materials. *J. Mech. Phys. Solids*, 101:10–29, 2017.

[47] H. Esfahlani, Y. Mazor, and A. Alú. Homogenization and design of acoustic Willis metasurfaces. *Phys. Rev. B*, 103:054306, 2021.

[48] Y. Meng, Y. Hao, S. Guenneau, S. Wang, and J. Li. Willis coupling in water waves. *New J. Phys.*, 23:073004, 2021.

[49] T. Wiest, C. C. Seepersad, and M. R. Haberman. Robust design of an asymmetrically absorbing Willis acoustic metasurface subject to manufacturing-induced dimensional variations. *J. Acoust. Soc. Am.*, 151:216–231, 2022.

[50] Z. Li, P. Han, and G. Hu. Willis dynamic homogenization method for acoustic metamaterials based on multiple scattering theory. *J. Mech. Phys. Solids*, 189:105692, 2024.

[51] M. B. Muhlestein, C. F. Sieck, P. S. Wilson, and M. R. Haberman. Experimental evidence of Willis coupling in one-dimensional effective material element. *Nat. Commun.*, 8:15625, 2017.

[52] J. Li, C. Shen, A. Díaz-Rubio, S. A. Tretyakov, and S. A. Cummer. Systematic design and experimental demonstration of bianisotropic metasurfaces for scattering-free manipulation of acoustic wavefronts. *Nat. Commun.*, 9:1342, 2018.

[53] A. Melnikov, Y. K. Chiang, L. Quan, S. Oberst, A. Alù, S. Marburg, and D. Powell. Acoustic meta-atom with experimentally verified maximum Willis coupling. *Nat. Commun.*, 10:3148, 2019.

[54] J. Gu, Y. Tang, X. Wang, and Z. Huang. Laminated plate-type acoustic metamaterials with Willis coupling effects for broadband low-frequency sound insulation. *Compos. Struct.*, 292:115689, 2022.

[55] C. Cho, X. Wen, N. Park, and J. Li. Acoustic Willis meta-atom beyond the bounds of passivity and reciprocity. *Commun. Phys.*, 4:82, 2021.

[56] L. Quan, Y. Ra'di, D. L. Sounas, and A. Alù. Maximum Willis coupling in acoustic scatterers. *Phys. Rev. Lett.*, 120:254301, 2018.

[57] X. Su and A. N. Norris. Retrieval method for the bianisotropic polarizability tensor of Willis acoustic scatterers. *Phys. Rev. B*, 98:174305, 2018.

[58] M. Tsimokha, V. Igoshin, A. Nikitina, I. Toftul, K. Frizyuk, and M. Petrov. Acoustic resonators: Symmetry classification and multipolar content of the eigenmodes. *Phys. Rev. B*, 105:165311, 2022.

[59] D. L. Colton and R. Kress. *Inverse Acoustic and Electromagnetic Scattering Theory*. Springer, Cham, Switzerland, 4th edition, 2019.

[60] R. Pernas-Salomón and G. Shmuel. Symmetry breaking creates electro-momentum coupling in piezoelectric metamaterials. *J. Mech. Phys. Solids*, 134:103770, 2020.

[61] M. A. Casali. Material property extraction procedure for electromomentum coupled metamaterials. M. S. thesis, University of Texas at Austin, 2023.

[62] R. Pernas-Salomón, M. R. Haberman, A. N. Norris, and G. Shmuel. The electromomentum effect in piezoelectric Willis scatterers. *Wave Motion*, 106:102797, 2021.

[63] J.-H. Lee, Z. Zhang, and G. X. Gu. Dynamic homogenization of heterogeneous piezoelectric media: a polarization approach using infinite-body Green's function. *J. Mech. Phys. Solids*, 181:105442, 2023.

[64] H. Danawe and S. Tol. Electro-momentum coupling tailored in piezoelectric metamaterials with resonant shunts. *APL Materials*, 11:091118, 2023.

[65] A. Muhafra, M. Kosta, D. Torrent, R. Pernas-Salomón, and G. Shmuel. Homogenization of piezoelectric planar Willis materials undergoing antiplane shear. *Wave Motion*, 106:102833, 2021.

[66] K. Muhafra, M. R. Haberman, and G. Shmuel. Discrete one-dimensional models for the electromomentum coupling. *Phys. Rev. Appl.*, 20:014042, 2023.

[67] S. P. Wallen, M. A. Casali, B. M. Goldsberry, and M. R. Haberman. Polarizability of electromomentum coupled scatterers. *Proc. Mtgs. Acoust.*, 46:065002, 2022.

[68] J. Lee, Z. Zhang, and G. X. Gu. Maximum electro-momentum coupling in piezoelectric metamaterial scatterers. *J. Appl. Phys.*, 132:125108, 2022.

[69] J. Kong. Theorems of bianisotropic media. *Proc. IEEE*, 60:1036–1046, 1972.

[70] M. B. Muhlestein, C. F. Sieck, A. Alù, and M. R. Haberman. Reciprocity, passivity and causality in Willis materials. *Proc. R. Soc. A*, 472:20160604, 2016.

[71] S. Guo, Z. Ya, P. Wu, and M. Wan. A review on acoustic vortices: Generation, characterization, applications and perspectives. *J. Appl. Phys.*, 132:210701, 2022.

[72] S. T. Kang and C. K. Yeh. Potential-well model in acoustic tweezers. *IEEE Trans. Ultrason. Ferroelectr. Freq. Control*, 57:1451–1459, 2010.

[73] L. Zhang and P. L. Marston. Angular momentum flux of nonparaxial acoustic vortex beams and torques on axisymmetric objects. *Phys. Rev. E*, 84:065601, 2011.

[74] A. Anhäuser, R. Wunenburger, and E. Brasselet. Acoustic rotational manipulation using orbital angular momentum transfer. *Phys. Rev. Lett.*, 109:034301, 2012.

[75] D. Baresch, J. L. Thomas, and R. Marchiano. Spherical vortex beams of high radial degree for enhanced single-beam tweezers. *J. Appl. Phys.*, 113:184901, 2013.

[76] R. Wunenburger, J. I. V. Lozano, and E. Brasselet. Acoustic orbital angular momentum transfer to matter by chiral scattering. *New J. Phys.*, 17:103022, 2015.

[77] Z. Hong, J. Zhang, and B. W. Drinkwater. Observation of orbital angular momentum transfer from Bessel-shaped acoustic vortices to diphasic liquid-microparticle mixtures. *Phys. Rev. Lett.*, 114:214301, 2015.

[78] T. Wang, M. Ke, W. Li, Q. Yang, C. Qiu, and Z. Liu. Particle manipulation with acoustic vortex beam induced by a brass plate with spiral shape structure. *Appl. Phys. Lett.*, 109:112209, 2016.

[79] M. Baudoin, J.-C. Gerbedoen, A. Riaud, O. B. Matar, N. Smagin, and J.-L. Thomas. Folding a focalized acoustical vortex on a flat holographic transducer: Miniaturized selective acoustical tweezers. *Sci. Adv.*, 5:1967, 2019.

[80] Z. Gong and M. Baudoin. Particle assembly with synchronized acoustic tweezers. *Phys. Rev. Appl.*, 12:024045, 2019.

[81] A. Marzo and B. W. Drinkwater. Holographic acoustic tweezers. *Proc. Nat. Acad. Sci. U.S.A.*, 116:84–89, 2019.

[82] A. Ozcelik, J. Rufo, F. Guo, Y. Gu, P. Li, J. Lata, and T. J. Huang. Acoustic tweezers for the life sciences. *Nat. Methods*, 15:1021–1028, 2018.

[83] S. Jiménez-Gambín, N. Jiménez, and F. Camarena. Transcranial focusing of ultrasonic vortices by acoustic holograms. *Phys. Rev. App.*, 14:054070, 2020.

[84] S. Guo, Z. Ya, P. Wu, L. Zhang, and M. Wan. Enhanced sonothrombolysis induced by high-intensity focused acoustic vortex. *Ultrasound Med. Biol.*, 48:1907–1917, 2022.

[85] T. M. Marston and P. L. Marston. Modulated helicity for acoustic communications and helicity-selective acoustic receivers. *J. Acoust. Soc. Am.*, 127:1856, 2010.

[86] V. Bollen, D. J. Zartman, T. M. Marston, and P. L. Marston. Measured scattering of a first-order vortex beam by a sphere: Cross-helicity and helicity-neutral near-forward scattering and helicity modulation. *Proc. Mtgs. Acoust.*, 19:070075, 2013.

[87] C. Shi, M. Dubois, Y. Wang, and X. Zhang. High-speed acoustic communication by multiplexing orbital angular momentum. *Proc. Nat. Acad. Sci. U.S.A.*, 114:7250–7253, 2017.

[88] X. Jiang, B. Liang, J. C. Cheng, and C. W. Qiu. Twisted acoustics: Metasurface-enabled multiplexing and demultiplexing. *Adv. Mater.*, 30:1800257, 2018.

[89] X. Jiang, C. Shi, Y. Wang, J. Smalley, J. Cheng, and X. Zhang. Nonresonant metasurface for fast decoding in acoustic communications. *Phys. Rev. App.*, 13:014014, 2020.

[90] Z. Sun, Y. Shi, X. Sun, H. Jia, Z. Jin, K. Deng, and J. Yang. Underwater acoustic multiplexing communication by pentamode metasurface. *J. Phys. D: Appl. Phys.*, 54:205303, 2021.

[91] M. E. Kelly and C. Shi. Design and simulation of acoustic vortex wave arrays for long-range underwater communication. *JASA Express Lett.*, 3:076001, 2023.

[92] N. Jiménez, J.-P. Groby, and V. Romero-García. Spiral sound-diffusing metasurfaces based on holographic vortices. *Sci. Rep.*, 11:10217, 2021.

[93] X. Jiang, J. Zhao, S. L. Liu, B. Liang, X. Y. Zou, J. Yang, C. W. Qiu, and J. C. Cheng. Broadband and stable acoustic vortex emitter with multi-arm coiling slits. *Appl. Phys. Lett.*, 108:203501, 2016.

[94] D.-C. Chen, Q.-W. Zhou, X.-F. Zhu, Z. Xu, and D.-J. Wu. Focused acoustic vortex by an artificial structure with two sets of discrete Archimedean spiral slits. *Appl. Phys. Lett.*, 115:083501, 2019.

[95] J.-F. Zeng, X. Zhang, F.-G. Wu, L.-X. Han, Q. Wangand Z.-F. Mu, H.-F. Dong, and Y.-W. Yao. Phase modulation of acoustic vortex beam with metasurfaces. *Phys. Lett. A*, 383:2640–2644, 2019.

[96] Y.-R. Jia, W.-Q. Ji, D.-J. Wu, and X.-J. Liu. Metasurface-enabled airborne fractional acoustic vortex emitter. *Appl. Phys. Lett.*, 113:173502, 2018.

[97] X. Jiang, D. Ta, and W. Wang. Modulation of orbital-angular-momentum symmetry of nondiffractive acoustic vortex beams and realization using a metasurface. *Phys. Rev. App.*, 14:034014, 2020.

[98] Z. Guo, H. Liu, H. Zhou, K. Zhou, S. Wang, F. Shen, Y. Gong, J. Gao, S. Liu, and K. Guo. High-order acoustic vortex field generation based on a metasurface. *Phys. Rev. E*, 100:053315, 2019.

[99] S. Gao, Y. Li, C. Ma, Y. Cheng, and X. Liu. Emitting long-distance spiral airborne sound using low-profile planar acoustic antenna. *Nat. Commun.*, 12:2006, 2021.

[100] N. Jiménez, V. Romero-García, L. M. García-Raffi, F. Camarena, and K. Staliunas. Sharp acoustic vortex focusing by Fresnel-spiral zone plates. *Appl. Phys. Lett.*, 112:204101, 2018.

[101] M. E. Terzi, S. A. Tsysar, P. V. Yuldashev, M. M. Karzova, and O. A. Sapozhnikov. Generation of a vortex ultrasonic beam with a phase plate with an angular dependence of the thickness. *Moscow University Physics Bulletin*, 72:61–67, 2017.

[102] H. Zhou, J. Li, K. Guo, and Z. Guo. Generation of acoustic vortex beams with designed Fermat's spiral diffraction grating. *J. Acoust. Soc. Am.*, 146:4237–4243, 2019.

[103] V. Bollen and P. L. Marston. Phase and amplitude evolution of backscattering by a sphere scanned through an acoustic vortex beam: Measured helicity projections. *J. Acoust. Soc. Am.*, 148:135–140, 2020. Eq. (1).

[104] N. Jiménez, J. Ealo, R. D. Muelas-Hurtado, A. Duclos, and V. Romero-García. Sub-wavelength acoustic vortex beams using self-demodulation. *Phys. Rev. Appl.*, 15:054027, 2021.

[105] R. Marchiano and J. L. Thomas. Synthesis and analysis of linear and nonlinear acoustical vortices. *Phys. Rev. E*, 71:066616, 2005.

[106] X. Pan, J. Wu, Z. Li, C. Zhang, C. Deng, Z. Zhang, H. Wen, Q. Gao, J. Yang, Z. Yi, M. Yu, L. Liu, F. Chi, and P. Bai. Laguerre-Gaussian mode purity of Gaussian vortex beams. *Optik*, 230:166320, 2021.

[107] C. A. Gokani, M. R. Haberman, and M. F. Hamilton. Paraxial and ray approximations of acoustic vortex beams. *J. Acoust. Soc. Am.*, 155:2707–2723, 2024.

[108] P. L. Marston. Scattering of a Bessel beam by a sphere: II. Helicoidal case and spherical shell example. *J. Acoust. Soc. Am.*, 124:2905–2910, 2008.

[109] P. L. Marston. Radiation force of a helicoidal Bessel beam on a sphere. *J. Acoust. Soc. Am.*, 125:3539–3547, 2009.

[110] L. Zhang and P. L. Marston. Geometrical interpretation of negative radiation forces of acoustical Bessel beams on spheres. *Phys. Rev. E*, 84:035601, 2011.

[111] N. Jiménez, V. J. Sánchez-Morcillo, R. Pico, L. M Garcia-Raffi, V. Romero-Garcia, and K. Staliunas. High-order acoustic Bessel beam generation by spiral gratings. *Physics Procedia*, 70:245–248, 2015.

[112] N. Jiménez, R. Picó, V. Sánchez-Morcillo, V. Romero-García, L. M. García-Raffi, and K. Staliunas. Formation of high-order acoustic Bessel beams by spiral diffraction gratings. *Phys. Rev. E*, 94:053004, 2016.

[113] M. R. Lapointe. Review of non-diffracting Bessel beam experiments. *Opt. Laser Technol.*, 24:315–321, 1992.

[114] V. A. Soifer, S.I. Kharitonov, S. N. Khonina, and S. G. Volotovsky. Caustics of vortex optical beams. *Dokl. Phys.*, 64:276–279, 2019.

[115] S. I. Kharitonov, S. N. Khonina, S. G. Volotovskiy, and N. L. Kazanskiy. Caustics of the vortex beams generated by vortex lenses and vortex axicons. *J. Opt. Soc. Am. A*, 37:476–482, 2020.

[116] S. N. Khonina, S. I. Kharitonov, S. G. Volotovskiy, and V. A. Soifer. Caustics of non-paraxial perfect optical vortices generated by toroidal vortex lenses. *Photonics*, 8:259, 2021.

[117] N. Xiao, C. Xie, E. Jia, J. Li, R. Giust, F. Courvoisier, and M. Hu. Caustic interpretation of the abruptly autofocusing vortex beams. *Opt. Express*, 29:19975, 2021.

[118] E. Jia, C. Xie, Y. Yang, N. Xiao, and M. Hu. Abruptly autofocusing vortex beams for rapid controllable femtosecond two-photon polymerization. *Materials*, 16:4625, 2023.

[119] D. Gloge and D. Marcuse. Formal quantum theory of light rays. *J. Opt. Soc. Am.*, 59:1629–1631, 1969.

[120] S. Yves, R. Fleury, G. Shmuel, M. Fruchart, V. Vitelli, M. R. Haberman, and A. Alù. Symmetry-driven phononic metamaterials. *Nat. Rev. Mater.*, 11:156–180, 2026.

[121] P. J. Westervelt. Acoustic radiation pressure. *J. Acoust. Soc. Am.*, 29:26–29, 1957.

[122] P. M. Morse and K. U. Ingard. *Theoretical Acoustics*. Princeton University Press, Princeton, New Jersey, 1968.

[123] R. Pernas-Salomón and G. Shmuel. Fundamental principles for generalized Willis metamaterials. *Phys. Rev. Applied*, 14:064005, 2020.

[124] G. R. Torr. The acoustic radiation force. *Am. J. Phys.*, 52:402–408, 1984.

[125] F. Mignard. On the radiation forces. In *Interrelations Between Physics and Dynamics for Minor Bodies in the Solar System*, pages 419–451. Editions Frontières, Gif-sur-Yvette, 1992.

[126] J. Needham and C. A. Ronan. *The Shorter Science and Civilisation in China*, volume 3. Cambridge University Press, 1978.

[127] J. R. Christianson. Tycho Brahe's German treatise on the comet of 1577: A study in science and politics. *Isis*, 70:110–140, 1979.

[128] D. Seargent. *The Greatest Comets in History: Broom Stars and Celestial Scimitars*. Springer, New York, 2009.

[129] A. Koestler. *The Sleepwalkers*. Hutchinson, London, 1959.

[130] J. Kepler. *De Cometis Libelli Tres*. A Apergeri, AvgvstæVindelicorvum, 1619.

[131] J. Dalibard. Atoms and radiation. *La lettre du Collège de France*, 8:10, 2014.

[132] L. Euler. *Mem. Acad. R. Sci. Classe Math. Berlin*, 117, 1746.

[133] R. T. Beyer. Radiation pressure—the history of a mislabeled tensor. *J. Acoust. Soc. Am.*, 63:1025–1030, 1978.

[134] J. C. Maxwell. *A Treatise on Electricity and Magnetism*. Clarendon Press, Oxford, 1873.

[135] J. H. Poynting. Radiation pressure. *Philos. Mag.*, 9:393–406, 1905.

[136] J. H. Poynting. The wave motion of a revolving shaft, and a suggestion as to the angular momentum in a beam of circularly polarised light. *Proc. R. Soc. A*, 82:560–567, 1909.

[137] Lord Rayleigh. On the momentum and pressure of gaseous vibrations, and on the connection with the virial theorem. *Philos. Mag.*, 3:364–374, 1905.

[138] A. Kundt. Über eine neue Art akustischer Staubfiguren und über die Anwendung derselben zur Bestimmung der Schallgeschwindigkeit in festen körpern und Gasen. *Ann. Phys.*, 203:497–523, 1866.

[139] Lord Rayleigh. On the pressure of vibrations. *Philos. Mag.*, 3:338–346, 1902.

[140] L. Brillouin. On radiation stresses. *Ann. Phys.*, 4:528–586, 1925.

[141] J. Rufo, F. Cai, J. Friend, M. Wiklund, and T. J. Huang. Acoustofluidics for biomedical applications. *Nat. Rev. Methods Primers*, 2:30, 2022.

[142] S. Yang, J. Rufo, Y. Chen, C. Chen, B. W. Drinkwater, L. P. Lee, and T. J. Huang. Acoustic tweezers for advancing precision biology and medicine. *Nat. Rev. Methods Primers*, 5:49, 2025.

[143] P. Mishra, P. Glynne-Jones, R. J. Boltryk, and M. Hill. Efficient finite element modeling of acoustic radiation forces on inhomogeneous elastic particles. *J. Acoust. Soc. Am.*, 1433:753–756, 2012.

[144] T. S. Jerome, Yu. A. Ilinskii, E. A. Zabolotskaya, and M. F. Hamilton. Born approximation of acoustic radiation force and torque on soft objects of arbitrary shape. *J. Acoust. Soc. Am.*, 145:36–44, 2019.

[145] R. M. Abraham-Ekeroth, M. Lester, and D. Torrent. Control and sorting of inhomogeneous dielectric core–shell nanoparticles using two counter-propagating plane waves. *Eur. Phys. J. Plus*, 140:1–12, 2025.

[146] T. S. Jerome, Yu. A. Ilinskii, E. A. Zabolotskaya, and M. F. Hamilton. Acoustic radiation force on a compressible spheroid. *J. Acoust. Soc. Am.*, 148:2403–2415, 2020.

[147] Z. Ma, D. J. Collins, J. Guo, and Y. Ai. Mechanical properties based particle separation via traveling surface acoustic wave. *Anal. Chem.*, 88:11844–11851, 2016.

[148] T. J. Matula, O. A. Sapozhnikov, L. A. Ostrovsky, A. A. Brayman, J. Kucewicz, B. E. MacConaghy, and D. De Raad. Ultrasound-based cell sorting with microbubbles: A feasibility study. *J. Acoust. Soc. Am.*, 144:41–52, 2018.

[149] K. Mutafopulos, P. Spink, C. D. Lofstrom, P. J. Lu, H. Lu, J. C. Sharpe, T. Franke, and D. A. Weitz. Traveling surface acoustic wave (TSAW) microfluidic fluorescence activated cell sorter (μFACS). *Lab Chip*, 19:2435–2443, 2019.

[150] D. Zhang and C. Ma. Acoustic metamaterials for remote manipulation of large objects in water. *Mater. Horiz.*, 54:4639–4647, 2025.

[151] M. I. Mishchenko, W. J. Wiscombe, J. W. Hovenier, and L. D. Travis. Overview of scattering by nonspherical particles. In M. I. Mishchenko, J. W. Hovenier, and L. D. Travis, editors, *Light Scattering by Nonspherical Particles: Theory, Measurements, and Applications*. Academic Press, San Diego, 2000. Chap. 8.

[152] L. Zhang and P. L. Marston. Acoustic radiation force expressed using complex phase shifts and momentum-transfer cross sections. *J. Acoust. Soc. Am.*, 140:EL178–EL183, 2016.

[153] D. J. Griffiths. *Introduction to Quantum Mechanics*. Pearson, Upper Saddle River, New Jersey, 2nd edition, 2005.

[154] R. Löfstedt and S. Putterman. Theory of long wavelength acoustic radiation pressure. *J. Acoust. Soc. Am.*, 90:2027–2033, 1991.

[155] L. Zhang and P. L. Marston. Acoustic radiation torque and the conservation of angular momentum (L). *J. Acoust. Soc. Am.*, 129:1679–1680, 2011.

[156] P. A. Martin. On the far-field computation of acoustic radiation forces. *J. Acoust. Soc. Am.*, 142:2094–2100, 2017. Eq. (18).

[157] P. L. Marston, S. G. Goosby, D. S. Langley, and S. E. LoPorto-Arione. Resonances, radiation pressure and optical scattering phenomena of drops and bubbles. In *Proceedings of the Second International Colloquium on Drops and Bubbles*, pages 166–174, Pasadena, CA, 1982. Jet Prop. Lab.

[158] T. Leighton. *The Acoustic Bubble*. Academic Press, London, 1994.

[159] L. Ostrovsky. Concentration of microparticles and bubbles in standing waves. *J. Acoust. Soc. Am.*, 138:3607–3612, 2015.

[160] O. A. Sapozhnikov and M. R. Bailey. Radiation force of an arbitrary acoustic beam on an elastic sphere in a fluid. *J. Acoust. Soc. Am.*, 133:661–676, 2013.

[161] S. Moskow and J. C. Schotland. Convergence and stability of the inverse scattering series for diffuse waves. *Inverse Probl.*, 24:065005, 2008.

[162] X.-D. Fan and L. Zhang. Phase shift approach for engineering desired radiation force: Acoustic pulling force example. *J. Acoust. Soc. Am.*, 150:102–110, 2021.

[163] R. P. Feynman. *Feynman Lectures on Physics*. Basic Books, New York, 2013. https://www.feynmanlectures.caltech.edu/.

[164] T. B. A. Senior. Low-frequency scattering. *J. Acoust. Soc. Am.*, 53:742–747, 1973.

[165] A. F. Stevenson. Solution of electromagnetic scattering problems as power series in the ratio (dimension of scatterer)/wavelength. *J. Appl. Phys.*, 24:1134–1142, 1953.

[166] P. L. Marston. Phase-shift derivation of expansions for material and frequency dependence of progressive-wave radiation forces and backscattering by spheres. *J. Acoust. Soc. Am.*, 145:EL39–EL44, 2019.

[167] P. L. Marston. Finite-size radiation force correction for inviscid spheres in standing waves. *J. Acoust. Soc. Am.*, 142:1167–1170, 2017.

[168] P. L. Marston. Contrast factor for standing-wave radiation forces on spheres: Series expansion in powers of sphere radius. *JASA Express Lett.*, 4:074001, 2024.

[169] P. L. Marston and L. Zhang. Relationship of scattering phase shifts to special radiation force conditions for spheres in axisymmetric wave-fields. *J. Acoust. Soc. Am.*, 141:3042–3049, 2017.

[170] P. L. Marston. Concentric fluid spheres: Scattering and radiation forces and the lowest monopole resonance of bubble shells. *JASA Express Lett.*, 5:094002, 2025.

[171] P. L. Marston. Born approximation for scattering by evanescent waves: Comparison with exact scattering by an infinite fluid cylinder. *J. Acoust. Soc. Am.*, 115:2473, 2004.

[172] L. Quan, S. Yves, Y. Peng, H. Esfahlani, and A. Alù. Odd Willis coupling induced by broken time-reversal symmetry. *Nat. Commun.*, 12:2615, 2021.

[173] P. L. Marston. Acoustic radiation force and scattering series expansions for spheres at low frequencies. In *APS Division of Fluid Dynamics Meeting Abstracts*, pages Q06–001, 2019.

[174] S. T. Thornton and J. B. Marion. *Clasical Dynamics of Particles and Systems*. Brooks/Cole, Belmont, California, 5th edition, 2004.

[175] A. Srivastava and S. Nemat-Nasser. On the limit and applicability of dynamic homogenization. *Wave Motion*, 51:1045–1054, 2014.

[176] A. Srivastava. Elastic metamaterials and dynamic homogenization: a review. *Int. J. Smart Nano Mat.*, 6:41–60, 2015.

[177] P. J. Westervelt. The theory of steady forces caused by sound waves. *J. Acoust. Soc. Am.*, 23:312–315, 1951.

[178] Y.-Y. Wang, J. Yao, X.-W. Wu, D.-J. Wu, and X.-J. Liu. Influences of the geometry and acoustic parameter on acoustic radiation forces on three-layered nucleate cells. *J. Appl. Phys.*, 122:094902, 2017.

[179] Yu. A. Ilinskii, E. A. Zabolotskaya, B. C. Treweek, and M. F. Hamilton. Acoustic radiation force on an elastic sphere in a soft elastic medium. *J. Acoust. Soc. Am.*, 144:568–576, 2018.

[180] NIST Digital Library of Mathematical Functions. https://dlmf.nist.gov/. F. W. J. Olver, A. B. Olde Daalhuis, D. W. Lozier, B. I. Schneider, R. F. Boisvert, C. W. Clark, B. R. Miller, B. V. Saunders, H. S. Cohl, and M. A. McClain, eds.

[181] B. C. Treweek. *Acoustic Radiation Force Due to Sound Beams Incident on Spherical Scatterers in Soft Tissue-Like Media.* Ph.D. dissertation, University of Texas at Austin, 2019.

[182] P. L. Marston. Axial radiation force of a Bessel beam on a sphere and direction reversal of the force. *J. Acoust. Soc. Am.*, 120:3518–3524, 2006.

[183] P. L. Marston. Scattering of a Bessel beam by a sphere. *J. Acoust. Soc. Am.*, 121:753–758, 2007.

[184] P. L. Marston, T. D. Daniel, A. R. Fortuner, I. P. Kirsteins, and A. T. Abawi. Specular-reflection contributions to static and dynamic radiation forces on circular cylinders. *J. Acoust. Soc. Am.*, 149:3042–3051, 2021.

[185] P. L. Marston, T. D. Daniel, and A. R. Fortuner. Specular reflection contributions to dynamic radiation forces on highly reflecting spheres (L). *J. Acoust. Soc. Am.*, 150:25–28, 2021.

[186] P. A. Chinnery, V. F. Humphrey, and J. Zhang. Low-frequency acoustic scattering by a cube: Experimental measurements and theoretical predictions. *J. Acoust. Soc. Am.*, 101:2571–2582, 1997.

[187] D. H. Napper. A diffraction theory approach to the total scattering by cubes. *Kolloid-Zeitschrift und Zeitschrift für Polymere*, 218:41–46, 1967.

[188] A. Masłowska, P. J. Flatau, and G. L. Stephens. On the validity of the anomalous diffraction theory to light scattering by cubes. *Opt. Commun.*, 107:35–40, 1994.

[189] M. W. Ospel. Iterative path expansion for Helmholtz scattering with Neumann boundary conditions. *J. Acoust. Soc. Am.*, 159:600–609, 2026.

[190] A. Papoulis. *Systems and Transforms with Applications in Optics*. McGraw-Hill, New York, 1968.

[191] X. Peng, W. He, F. Xin, G. M. Genin, and T. J. Lu. Standing surface acoustic waves, and the mechanics of acoustic tweezer manipulation of eukaryotic cells. *J. Mech. Phys. Solids*, 145:104134, 2020.

[192] C. A. Gokani, T. S. Jerome, M. R. Haberman, and M. F. Hamilton. Born approximation of acoustic radiation force used for acoustofluidic separation. *Proc. Mtgs. Acoust.*, 48:045002, 2022.

[193] A. Smirnov, S. Chugunov, A. Kholodkova, M. Isachenkov, A. Vasin, and I. Shishkovsky. Progress and challenges of 3D-printing technologies in the manufacturing of piezoceramics. *Ceram. Int.*, 47:10478–10511, 2021.

[194] C. A. Gokani and M. R. Haberman. Acousto-electromagnetic media: Homogenization and constraints. In *2025 Nineteenth International Congress on Artificial Materials for Novel Wave Phenomena (Metamaterials)*, pages X135–X137, 2025.

[195] C. J. Naify, A. Titovich, and M. R. Haberman. What is an acoustic metamaterial? *Proc. Mtgs. Acoust.*, 51:065002, 2023.

[196] G. Atay, Z. Sü Gül, and O. Önen. The acoustical characterization of clay pots in Ottoman architecture through experimental and numerical analysis. *J. Acoust. Soc. Am.*, 154:1389–1400, 2023.

[197] M. I. Hussein, M. J. Leamy, and M. Ruzzene. Dynamics of phononic materials and structures: Historical origins, recent progress, and future outlook. *Appl. Mech. Rev.*, 66:040802, 2014.

[198] S. A. Cummer, J. Christensen, and A. Alù. Controlling sound with acoustic metamaterials. *Nat. Rev. Mater.*, 1:16001, 2016.

[199] K. Fan and W. J. Padilla. Dynamic electromagnetic metamaterials. *Mater. Today*, 18:39–50, 2015.

[200] J. B. Pendry. Negative refraction makes a perfect lens. *Phys. Rev. Lett.*, 85:3966–3969, 2000.

[201] T. Brunet, J. Leng, and O. Mondain-Monval. Soft acoustic metamaterials. *Science*, 342:323–324, 2013.

[202] T. Brunet, A. Merlin, B. Mascaro, K. Zimny, J. Leng, O. Poncelet, C. Aristégui, and O. Mondain-Monval. Soft 3D acoustic metamaterial with negative index. *Nat. Mater.*, 14:384–388, 2015.

[203] D. K. Cheng and J. Kong. Covariant descriptions of bianisotropic media. *Proc. IEEE*, 56:248–251, 1968.

[204] F. R. Prudencio, S. A. Matos, and C. R. Paiva. A geometrical approach to duality transformations for Tellegen media. *IEEE T. Microw. Theory*, 62:1417–1428, 2014.

[205] A. J. Lawrence, B. M. Goldsberry, S. P. Wallen, and M. R. Haberman. Numerical study of acoustic focusing using a bianisotropic acoustic lens. *J. Acoust. Soc. Am.*, 148:EL365–EL369, 2020.

[206] G. W. Milton, M. Briane, and J. R. Willis. On cloaking for elasticity and physical equations with a transformation invariant form. *New J. Phys*, 8:248–248, 2006.

[207] G. W. Milton and J. R. Willis. On modifications of Newton's second law and linear continuum elastodynamics. *Proc. R. Soc. A*, 463:855–880, 2007.

[208] V. S. Asadchy, A. Díaz-Rubio, and S. A. Tretyakov. Bianisotropic metasurfaces: physics and applications. *Nanophotonics*, 7:1069–1094, 2018.

[209] IEEE Ultrasonics, Ferroelectrics, and Frequency Control Society. *Standard on Magnetostrictive Materials: Piezomagnetic Nomenclature*. IEEE Std. 319-1990, 1990.

[210] eFunda Engineering Fundamentals. All constitutive forms. https://www.efunda.com/materials/piezo/piezo_math/transforms.cfm.

[211] G. Shmuel. The electromomentum coupling. https://doi.org/10.52843/meta-mat.qb6tvw, 2025. MetaMAT Weekly Seminars.

[212] F. C. Moon. Scattering of waves by a cylindrical piezoelectric inclusion. *J. Acoust. Soc. Am.*, 48:253–262, 1970.

[213] J. Venn. *Symbolic Logic*. MacMillan, London, 1881.

[214] A. N. Norris, A. L. Shuvalov, and A. A. Kutsenko. Analytical formulation of three-dimensional dynamic homogenization for periodic elastic systems. *P. Roy. Soc. A: Math. Phys.*, 468:1629–1651, 2012.

[215] P. S. Piva, A. L. Gower, and I. D. Abrahams. Designing band gaps with randomly distributed sub-wavelength Helmholtz resonators. *NPJ Acoust.*, 2:10, 2026.

[216] R. C. McPhedran, N. A. Nicorovici, L. C. Botten, and K.-D. Bao. Green's function, lattice sums and Rayleigh's identity for a dynamic scattering problem. In *Wave Propagation in Complex Media*, pages 155–186. Springer, New York, 1998.

[217] W. A. Schwalm and M. K. Schwalm. Extension theory for lattice Green functions. *Phys. Rev. B*, 37:9524, 1988.

[218] A. Alù, A. D. Yaghjian, R. A. Shore, and M. G. Silveirinha. Causality relations in the homogenization of metamaterials. *Phys. Rev. B*, 83:054305, 2011.

[219] A. Alù. Restoring the physical meaning of metamaterial constitutive parameters. *Phys. Rev. B*, 83:081102, 2011.

[220] J. R. Willis, "Dynamics of Composites," P. Suquet, editor. *Continuum Micromechanics.* Springer, Cham, Switzerland, 1997.

[221] C. F. Sieck. *Bianisotropy in Passive Acoustic Metamaterials.* Ph.D. dissertation, University of Texas at Austin, 2017.

[222] A. Bedford and D. S. Drumheller. *Introduction to Elastic Wave Propagation.* Springer, Cham, Switzerland, 2023.

[223] B. A. Auld. *Acoustic Fields and Waves in Solids.* Wiley, New York, 1973.

[224] J. F. Havlice, W. L. Bond, and L. B. Wigton. 'Elastic' Poynting Vector in a Piezoelectric Medium. *IEEE Trans. Ultrason. Ferroelectr. Freq. Control*, 17:246–248, 1970.

[225] J. D. Achenbach. *Reciprocity in Elastodynamics.* Cambridge University Press, Cambridge, UK, 2003.

[226] J. D. Jackson. *Classical Electrodynamics.* Wiley, Hoboken, New Jersey, 3rd edition, 1999.

[227] M. Itskov. *Tensor Algebra and Tensor Analysis for Engineers.* Springer, Cham, Switzerland, 2007.

[228] A. Srivastava and S. Nemat-Nasser. Overall dynamic properties of three-dimensional periodic elastic composites. *Proc. R. Soc. A*, 468:269–287, 2012.

[229] A. Srivastava. Causality and passivity in elastodynamics. *Proc. R. Soc. A*, 471:20150256, 2015.

[230] M. Stern. An Introduction to Nonlinear Continuum Mechanics, 2004. Unpublished lecture notes, University of Texas at Austin.

[231] C. A. Gokani, M. R. Haberman, and M. F. Hamilton. Analytical solutions for acoustic vortex beam radiation from planar and spherically focused circular pistons. *JASA Express Lett.*, 4:124001, 2024.

[232] C. A. Gokani, R. P. Williams, M. R. Haberman, and M. F. Hamilton. An alternative approach to modeling radiation from baffled circular pistons (L). *J. Acoust. Soc. Am.*, 158:2642–2646, 2025.

[233] L. Allen, M. W. Beijersbergen, R. J. C. Spreeuw, and J. P. Woerdman. Orbital angular momentum of light and the transformation of Laguerre-Gaussian laser modes. *Phys. Rev. A*, 45:8185–8189, 1992.

[234] Y. Shen, X. Wang, Z. Xie, C. Min, X. Fu, Q. Liu, M. Gong, and X. Yuan. Optical vortices 30 years on: OAM manipulation from topological charge to multiple singularities. *Light–Sci. Appl.*, 8:90, 2019.

[235] P. Coullet, L. Gil, and F. Rocca. Optical vortices. *Opt. Commun.*, 73:403–408, 1989.

[236] H. von Helmholtz. On integrals of the hydrodynamical equations, which express vortex-motion. *Philos. Mag.*, 33:485–512, 1867.

[237] D. Baresch, J. L. Thomas, and R. Marchiano. Observation of a single-beam gradient force acoustical trap for elastic particles: Acoustical tweezers. *Phys. Rev. Lett.*, 116:024301, 2016.

[238] A. Marzo, S. Seah, B. W. Drinkwater, D. R. Sahoo, B. Long, and S. Subramanian. Holographic acoustic elements for manipulation of levitated objects. *Nat. Commun.*, 6:8661, 2015.

[239] Y. Jin, R. Kumar, O. Poncelet, O. Mondain-Monval, and T. Brunet. Flat acoustics with soft gradient-index metasurfaces. *Nat. Commun.*, 10:143, 2019.

[240] J. Li, A. Crivoi, X. Peng, L. Shen, Y. Pu, Z. Fan, and S. A. Cummer. Three dimensional acoustic tweezers with vortex streaming. *Commun. Phys.*, 4:113, 2021.

[241] X. Jiang, Y. Li, B. Liang, J.-C. Cheng, and L. Zhang. Convert acoustic resonances to orbital angular momentum. *Phys. Rev. Lett.*, 117:034301, 2016.

[242] Y. Luo, Y. Jia, J. Yao, D. Wu, and X. Liu. Enhanced fractional acoustic vortices by an annulus acoustic metasurface with multi-layered rings. *Adv. Mater. Tech.*, 5:2000356, 2020.

[243] H. Esfahlani, H. Lissek, and J. R. Mosig. Generation of acoustic helical wavefronts using metasurfaces. *Phys. Rev. B*, 95:024312, 2017.

[244] C. J. Naify, C. A. Rohde, T. P. Martin, M. Nicholas, M. D. Guild, and G. J. Orris. Generation of topologically diverse acoustic vortex beams using a compact metamaterial aperture. *Appl. Phys. Lett.*, 108:223503, 2016.

[245] C. A. Rohde and C. J. Naify. Detecting acoustic chirality with matched metamaterial vortex wave antennas. *J. Acoust. Soc. Am.*, 154:721–729, 2023.

[246] Y. Chen and G. Hu. Broadband and high-transmission metasurface for converting underwater cylindrical waves to plane waves. *Phys. Rev. App.*, 12:044046, 2019.

[247] C. W. Cushing, M. J. Kelsten, X. Su, P. S. Wilson, M. R Haberman, and A. N. Norris. Design and characterization of a three-dimensional anisotropic additively manufactured pentamode material. *J. Acoust. Soc. Am.*, 151:168–179, 2022.

[248] H. T. O'Neil. Theory of focusing radiators. *J. Acoust. Soc. Am.*, 21:516–526, 1949.

[249] M. J. Padgett and L. Allen. The Poynting vector in Laguerre-Gaussian laser modes. *Opt. Commun.*, 121:36–40, 1995.

[250] J. E. Curtis and D. G. Grier. Structure of optical vortices. *Phys. Rev. Lett.*, 90:485–487, 2003.

[251] D. Baresch and V. Garbin. Acoustic trapping of microbubbles in complex environments and controlled payload release. *Proc. Natl. Acad. Sci.*, 117:15490–15496, 2020.

[252] C. Zhou, Q. Wang, S. Pu, Y. Li, G. Guo, H. Chu, Q. Ma, J. Tu, and D. Zhang. Focused acoustic vortex generated by a circular array of planar sector transducers using an acoustic lens, and its application in object manipulation. *J. Appl. Phys.*, 128:084901, 2020.

[253] W. Lo, C. Fan, Y. Ho, C. Lin, and C. Yeh. Tornado-inspired acoustic vortex tweezer for trapping and manipulating microbubbles. *Proc. Nat. Acad. Sci. U.S.A.*, 118:e2023188118, 2021.

[254] D. Zhao, J.-L. Thomas, and R. Marchiano. Generation of spherical vortex beams to trap large particles for enhanced axial force. *Ultrasonics*, 111:106296, 2021.

[255] T. D. Daniel, F. Gittes, I. P. Kirsteins, and P. L. Marston. Bessel beam expansion of linear focused ultrasound. *J. Acoust. Soc. Am.*, 144:3076–3083, 2018.

[256] I. S. Gradshteyn and I. M. Ryzhik. *Table of Integrals, Series, and Products*. Academic Press, New York, 4th edition, 1980.

[257] M. Abramowitz and I. A. Stegun, editors. *Handbook of Mathematical Functions*. Dover Publications, New York, 4th edition, 1972.

[258] J. Durnin. Exact solutions for nondiffracting beams. I. The scalar theory. *J. Opt. Soc. Am. A*, 4:651–654, 1987.

[259] L. V. King. On the acoustic radiation field of the piezo-electric oscillator and the effect of viscosity on transmission. *Can. J. Res.*, 11:135–155, 1934.

[260] M. C. Junger and D. Feit. *Sound, Structures, and Their Interaction*, volume 225. MIT Press, Cambridge, MA, 1986.

[261] J. D. Jackson. *Classical Electrodynamics, 1st edition*. Wiley, Hoboken, New Jersey, 1962.

[262] G. N. Watson. *A Treatise on the Theory of Bessel Functions*. Cambridge University Press, Cambridge, UK, 2nd edition, 1944.

[263] L. T. Brekhovskikh. *Waves in Layered Media*. Academic Press, Cambridge, Massachusetts, 2nd edition, 1980.

[264] E. G. Williams and J. D. Maynard. Numerical evaluation of the Rayleigh integral for planar radiators using the FFT. *J. Acoust. Soc. Am.*, 72:2020–2030, 1982.

[265] P. Wu, R. Kazys, and T. Stepinski. Analysis of the numerically implemented angular spectrum approach based on the evaluation of two-dimensional acoustic fields. Part I. Errors due to the discrete Fourier transform and discretization. *J. Acoust. Soc. Am.*, 99:1339–1348, 1996.

[266] J. Blackmore, R. O. Cleveland, and J. Mobley. Spatial filters suppress ripple artifacts in the computation of acoustic fields with the angular spectrum method. *J. Acoust. Soc. Am.*, 144:2947–2951, 2018.

[267] R. Lirette and J. Mobley. Ultrasonic near-field based acoustic tweezers for the extraction and manipulation of hydrocarbon droplets. *Appl. Phys. Lett.*, 121:1–6, 2022.

[268] E. A. Zabolotskaya and R. V. Khokhlov. Quasi-plane waves in the nonlinear acoustics of confined beams. *Sov. Phys. Acoust.*, 15:35–40, 1969.

[269] A. Marzo, M. Caleap, and B. W. Drinkwater. Acoustic virtual vortices with tunable orbital angular momentum for trapping of Mie particles. *Phys. Rev. Lett.*, 120:044301, 2018.

[270] Z. S. Sacks, D. Rozas, and G. A. Swartzlander, Jr. Holographic formation of optical-vortex filaments. *J. Opt. Soc. Am. B*, 15:2226–2234, 1998.

[271] R. Marchiano, F. Coulouvrat, L. Ganjehi, and J.-L. Thomas. Numerical investigation of the properties of nonlinear acoustical vortices through weakly heterogeneous media. *Phys. Rev. E*, 77:016605, 2008.

[272] V. V. Kotlyar, A. A. Almazov, S. N. Khonina, V. A. Soifer, H. Elfstrom, and J. Turunen. Generation of phase singularity through diffracting a plane or Gaussian beam by a spiral phase plate. *J. Opt. Soc. Am. A*, 22:849–861, 2005.

[273] J. W. Goodman. *Introduction to Fourier Optics*. Roberts & Company, Englewood, Colorado, 3rd edition, 2005.

[274] N. Jiménez, J. Ealo, R. D. Muelas-Hurtado, A. Duclos, and V. Romero-García. A helicoidal parametric antenna for subwavelength vortex generation. *Proc. Mtgs. Acoust.*, 48:045001, 2022.

[275] S. Gspan, A. Meyer, S. Bernet, and M. Ritsch-Marte. Optoacoustic generation of a helicoidal ultrasonic beam. *J. Acoust. Soc. Am.*, 115:1142–1146, 2004.

[276] Y. Li, P. Li, N. Ding, G. Guo, Q. Ma, J. Tu, and D. Zhang. Weak-focused acoustic vortex generated by a focused ring array of planar transducers and its application in large-scale rotational object manipulation. *Chinese Phys. B*, 30:044302, 2021.

[277] G. Richard, H. S. Lay, D. Giovannini, S. Cochran, G. C. Spalding, and M. P. J. Lavery. Twisting waves increase the visibility of nonlinear behaviour. *New J. Phys.*, 22:063021, 2020.

[278] Y. Li, Q. Wang, G. Guo, H. Chu, Q. Ma, J. Tu, and D. Zhang. Pulling force of acoustic-vortex beams on centered elastic spheres based on the annular transducer model. *Chinese Phys. B*, 29:054302, 2020.

[279] M. Baudoin, J.-L. Thomas, R. A. Sahely, J.-C. Gerbedoen, Z. Gong, A. Sivery, O. B. Matar, N. Smagin, P. Favreau, and A. Vlandas. Spatially selective manipulation of cells with single-beam acoustical tweezers. *Nat. Commun.*, 11:4244, 2020.

[280] G. Maidanik. Torques due to acoustical radiation pressure. *J. Acoust. Soc. Am.*, 30:620–623, 1958.

[281] Y. Harada and T. Asakura. Radiation forces on a dielectric sphere in the Rayleigh scattering regime. *Opt. Commun.*, 124:529–541, 1996.

[282] X. Fan and L. Zhang. Born approximation of trapping forces by acoustical Bessel and vortex fields. *J. Acoust. Soc. Am.*, 154:3354–3363, 2023.

[283] M. C. Jo and R. Guldiken. Active density-based separation using standing surface acoustic waves. *Sensor Actuat. A-Phys.*, 187:22–28, 2012.

[284] C. A. Gokani, M. R. Haberman, and M. F. Hamilton. Radiation force exerted by progressive waves on a string in terms of polarizability. *J. Acoust. Soc. Am.*, 158:A191, 2025.

[285] P. L. Marston. Geometrical and catastrophe optics methods in scattering. In *Physical Acoustics*, volume 21, pages 1–234. Academic Press, Cambridge, Massachusetts, 1992.

[286] P. L. Marston and T. D. Daniel. Geometric approximation of radiation stress projections for canonical objects. *J. Acoust. Soc. Am.*, 143:1718, 2018.

[287] S. P. Wallen, B. M. Goldsberry, C. A. Gokani, and M. R. Haberman. Computational analysis of sub-wavelength scatterers exhibiting electro-momentum coupling. *J. Acoust. Soc. Am.*, 153:A120, 2023.

[288] T. G. Wang and C. P. Lee, "Radiation Pressure and Acoustic Levitation," M. F. Hamilton and D. T. Blackstock, editors. *Nonlinear Acoustics*. Springer, Cham, Switzerland, 3rd edition, 2024. Chap. 6.

[289] M. Stocker. Fish, mollusks and other sea animals' use of sound, and the impact of anthropogenic noise in the marine acoustic environment. *J. Acoust. Soc. Am.*, 112:2431, 2002.

[290] X.-D. Fan, Z. Zou, and L. Zhang. Acoustic vortices in inhomogeneous media. *Phys. Rev.*, 1:032014, 2019.

[291] G. Guo, X. Li, Z. Chen, T. Meng, Y. Li, and Q. Ma. Nonlinear fields of focused acoustic-vortex beams. *Appl. Acoust.*, 221:110022, 2024.

[292] T. Brunet, J.-L. Thomas, R. Marchiano, and F. Coulouvrat. Experimental observation of azimuthal shock waves on nonlinear acoustical vortices. *New J. Phys.*, 11:013002, 2009.

[293] K. B. Cunningham and M. F. Hamilton. Bessel beams of finite amplitude in absorbing fluids. *J. Acoust. Soc. Am.*, 108:519–525, 2000.

[294] D. T. Blackstock, M. F. Hamilton, and A. D. Pierce, "Progressive Waves in Lossless and Lossy Fluids," M. F. Hamilton and D. T. Blackstock, editors. *Nonlinear Acoustics*. Springer, Cham, Switzerland, 3rd edition, 2024. Chap. 6.

[295] P. J. Westervelt and J. Radue. Nonlinear diverging waves. *J. Acoust. Soc. Am.*, 33:1672, 1961.

[296] M. A. Averkiou and M. F. Hamilton. Measurements of harmonic generation in a focused finite-amplitude sound beam. *J. Acoust. Soc. Am.*, 98:3439–3442, 1995.

[297] P. V. Yuldashev and V. A. Khokhlova. Simulation of three-dimensional nonlinear fields of ultrasound therapeutic arrays. *Acoust. Phys*, 57:334–343, 2011.

[298] R. P. Williams, C. A. Gokani, and M. F. Hamilton. Measurement and analysis of second-harmonic generation in focused vortex beams. *J. Acoust. Soc. Am.*, 158:A374, 2025.

[299] L. D. Landau and E. M. Lifshitz. *Fluid Mechanics*. Pergamon Press, Oxford, 2nd edition, 1987.

[300] D. Marcuse. *Light Transmission Optics*. Van Nostrand Reinhold, New York, 1982.

[301] M. L. Boas. *Mathematical Methods in the Physical Sciences*. John Wiley & Sons, 3rd edition, 1980.

[302] A. Sommerfeld and J. Runge. The application of vector calculus to the foundations of geometrical optics. *Ann. Phys.*, 340:277–298, 1911.

[303] C. L. Morfey and F. D. Cotaras, "Propagation in Inhomogeneous Media (Ray Theory)," M. F. Hamilton and D. T. Blackstock, editors. *Nonlinear Acoustics*. Springer, Cham, Switzerland, 3rd edition, 2024. Chap. 12.

[304] M. Foster. *Weakly Nonlinear Ray Tracing Approximations for Focused Ultrasound*. PhD thesis, University College London, 2025.

[305] W. R. Hamilton. Theory of systems of rays. *Trans. R. Ir. Acad.*, pages 69–174, 1828. Edited by D. R. Wilkins.

[306] M. Sato and T. Fujii. Quantum mechanical representation of acoustic streaming and acoustic radiation pressure. *Phys. Rev. E*, 64:026311, 2001.

[307] D. V. Schroeder. *An Introduction to Thermal Physics*. Oxford University Press, Oxford, 2020.

[308] L. A. Ostrovsky. Notes on the Acoustic Radiation Force. *Radiophysics and Quantum Electronics*, 66:421–430, 2023.

[309] P. L. Marston. James Clerk Maxwell: Life and science. *J. Quant. Spectrosc. Ra.*, 178:50–65, 2016.

[310] O. A. Sapozhnikov. High-intensity ultrasonic waves in fluids: Nonlinear propagation and effects. In *Power Ultrasonics*, pages 7–22. Woodhead Publishing, Cambridge, MA, 2023.

[311] C. Eckart. Vortices and streams caused by sound waves. *Phys. Rev.*, 73:68–76, 1948.

[312] V. L. Gurevich and A. Thellung. Quasimomentum in the theory of elasticity and its conservation. *Phys. Rev. B*, 42:7345, 1990.

[313] X. Wu, Y. Liu, S. Jin, and M. Yu. Particle dynamics in optical tweezer systems. *Rev. Chem. Eng.*, 41:197–223, 2025.

[314] D. R. Rowland and C. Pask. The missing wave momentum mystery. *Am. J. Phys.*, 67:378–388, 1999.

[315] H. Lamb. *Hydrodynamics*. Dover, New York, 6th edition, 1945.

[316] P. L. Marston and L. Zhang. Unphysical consequences of negative absorbed power in linear passive scattering: Implications for radiation force and torque. *J. Acoust. Soc. Am.*, 139:3139–3144, 2016.

[317] L. Zhang and P. L. Marston. Axial radiation force exerted by general non-diffracting beams. *J. Acoust. Soc. Am.*, 131:329–335, 2012.

[318] T. Ruen. Spheroids with vertical rotation axes. https://upload.wikimedia.org/wikipedia/commons/e/e6/Spheroids.svg. Licenced under CC BY-SA 4.0.

[319] J. B. Keller, R. E. Kleinman, and T. B. A. Senior. Dipole moments in Rayleigh scattering. *J. Inst. Appl. Maths*, 9:14–22, 1972.

[320] R. E. Kleinman and T. B. A. Senior. Rayleigh Scattering. In *Low and High Frequency Asymptotics*, volume 2, pages 2–70. Elsevier, Amsterdam, 1986.

[321] S. Bechtel and R. Lowe. *Fundamentals of Continuum Mechanics: With Applications to Mechanical, Thermomechanical, and Smart Materials*. Academic Press, Cambridge, Massachusetts, 2014.

[322] E. G. Williams. *Fourier Acoustics*. Academic Press, San Diego, 1999.

[323] H. Kogelnik and T. Li. Laser beams and resonators. *Appl. Opt.*, 5:1550–1567, 1966.

Vita

Chirag A. Gokani was born in 1999. He graduated in 2021 with a B.S. in physics and a minor in music from the University of Texas at Dallas. He began his graduate studies at the University of Texas at Austin in fall 2021.

Address: chiragokani@utexas.edu

This dissertation was set in Libertinus using the LaTeX package newtx.